

66

# Advanced Modeling and Inversion Techniques for Three-dimensional Geoelectrical Surveys

by

Weiqun Shi

B.S., Physics  
Nanking University, 1987

M.S., Marine Physics  
University of Miami, 1993

Submitted to the Department of  
Earth, Atmospheric, and Planetary Sciences  
in partial fulfillment of the requirements for the degree of  
Doctor of Philosophy in Geophysics

at the

MASSACHUSETTS INSTITUTE OF TECHNOLOGY

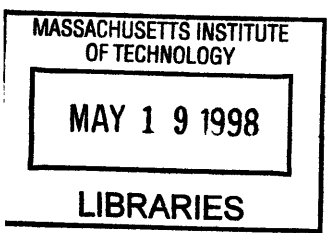
June 1998

© MASSACHUSETTS INSTITUTE OF TECHNOLOGY  
All rights reserved

Signature of Author.....  
Department of Earth, Atmospheric, and Planetary Sciences  
May 1, 1998

Certified by.....  
F. Dale Morgan  
Professor of Geophysics  
Thesis Advisor

Accepted by.....  
Thomas H. Jordan  
Chairman  
Department of Earth, Atmospheric, and Planetary Sciences



Lindgren

# Advanced Modeling and Inversion Techniques for Three-dimensional Geoelectrical Surveys

by

Weiqun Shi

Submitted to the Department of Earth, Atmospheric, and Planetary Sciences  
on May 1, 1998, in partial fulfillment of the requirements for the degree of  
Doctor of Philosophy

## Abstract

This thesis develops an integrated methodology for high resolution geoelectrical surveys including a physically meaningful inversion method, an efficient inversion algorithm, a resolution and uncertainty analysis technique, and an effective data acquisition geometry. The methodology is applied to three important geoelectrical inverse problems: 3-D d.c. electrical resistivity, 3-D electrical induced polarization, and 3-D electrical self-potential.

The 3-D d.c. electrical resistivity inversion recovers the subsurface bulk resistivity distribution from static electrical potential measurements obtained on the surface of the earth or in boreholes. This is an ill-posed problem in the sense that a large number of solutions to the inverse problem exist due to incomplete and uncertain data. To reduce the ill-posedness, this thesis investigates inversion algorithms based on the Tikhonov regularization method which solves a minimization problem to find models that fit the data and also have minimum structure. Different smoothness constraints are investigated to obtain the minimum structure. A smoothness operator that employs the second-order spatial derivatives (the Laplacian) is found to be most effective in yielding a stable inversion solution and eliminating surface artifacts.

To implement the regularized inversion on a 3-D resistivity model, one faces a computational challenge owing to the nonlinear nature of the resistivity problem and the large number of model parameters and data which can possibly exist in a moderate 3-D model. This thesis develops an efficient numerical algorithm based on the nonlinear conjugate gradient method with pre-conditioning to minimize the objective functional and solve the inverse problem. Different pre-conditioners are investigated and their efficiency are compared. By using a pre-conditioner based on the approximate form of the Hessian matrix of the objective function, the nonlinear

conjugate gradient method results in a tremendous time saving over the conventional Gauss-Newton approach.

The nonlinear regularized inversion methodology is then extended to solve the inverse problem of 3-D electrical Induced Polarization (IP). The subsurface complex resistivity distribution is reconstructed from the measurements of the amplitude and phase of the electrical potential in the frequency domain. Given a complex resistivity structure, the forward modeling which predicts the complex electrical potential distribution is solved by a bi-conjugate gradient method. Because the linear system of the equation for the forward modeling has a complex symmetric conductance matrix, the bi-conjugate gradient method is simplified to a special form which is comparable to the (real) conjugate gradient method that is used in the d.c. resistivity forward modeling. While in the IP inversion, the imaginary component of the complex resistivity is much smaller than the real part, the objective function is constructed in a complex form, and the minimization is solved directly in the complex domain using a bi-conjugate gradient method. This approach makes the inversion of 3-D Induced Polarization efficient because the computational cost is similar to that of the d.c. resistivity problem.

The inversion methodology is also extended to the inverse problem of 3-D electrical Self-Potential (SP), here the subsurface electrical current source distribution induced by underground mechanical and electrochemical activities is recovered. The SP inverse problem is inherently non-unique, in fact one can obtain a perfect data fit by appropriately adjusting the location, magnitude, and dimension of the electrical current source in many combinations. To reduce the nonuniqueness, the regularization constraints are justified and extended to a broader range of formulation including constraints on the resistivity structure and constraints on position, orientation, magnitude, or dimension of the SP source geometry.

Usually, the inversion reconstruction is evaluated in terms of how well the data are fit, but the suitability of the solution is better judged through uncertainty and resolution analysis. This thesis introduces an uncertainty and resolution analysis to quantify the variance and resolution length as a function of position for the geoelectrical inversion. It appeals to the Bayesian framework whereby both variance and resolution are inferred from the *a posteriori* covariance associated with the Tikhonov regularization method. The *a posteriori* covariance matrix is first calculated on an optimal nonlinear regularization solution by inverting the associated Hessian matrix or a Monte Carlo sampling method to give a local estimate of uncertainties about the optimal solution. Such resulted uncertainty does not possess an accurate measure for every model parameter. Therefore, the only uncertainties extracted are the ones associated with deterministically resolved model parameters. Then these uncertainties are calibrated from a sensitivity analysis. The uncertainty associated with the other

model parameters are thus obtained. To measure the resolution power of the inversion technique, a Monte Carlo method is used to invert realizations of perturbed data and obtain the *a posteriori* model correlation. For computational efficiency the resolution is also analyzed through the Modulation Transfer Function, borrowed from the optical imaging community. The numerical analysis of synthetic data demonstrates that the method gives resolution and variance information that correlates well with the electrical current coverage and the character of the associated reconstruction.

In order to increase the accuracy of the geoelectrical imaging technique, a new survey geometry which employs a spatially varying source dipole is designed. This new survey geometry is investigated with sensitivity analysis and model correlation estimation, and it appears to be more effective than traditional pseudo-section acquisition geometry in cases where structure has an extended lateral variation.

Finally, our inversion techniques are successfully applied to various geoelectric field measurements. The first example applies the 3-D d.c. resistivity tomography to characterize subsurface soil properties in an effort to understand the transport mechanisms that have been involved in drinking water contamination in the Aberjona River of Woburn, Massachusetts. The inversion result correlates well with other geophysical results at the site (GPR sections and cone penetrometer logs) and extrapolates the sparse stratigraphic information into a full 3-D model of the study area. The second example uses the 3-D d.c. resistivity tomography to monitor changes in subsurface electrical resistivity caused by the movement of water and the conversion of water to steam in the Larderello-Valle Secolo geothermal field in Italy. Comparisons of the resistivity anomalies obtained from two surveys conducted in 1991 and 1993 indicate a correlation between the changes in resistivity and the water re-injection history. The results show that it is possible to evaluate and detect the re-injection of fluid through systematic observation of electrical resistivity at the site. The third example uses the 3-D d.c. resistivity tomography to map underground limestone caves in Barbados, West Indies. The inversion successfully identifies the known caves and a previously undiscovered cave. In the last example, the 3-D electrical Self-Potential tomography is used to investigate groundwater contamination associated with a jet-fuel leakage at Massachusetts Military Reservation in Cape Cod, Massachusetts. The inversion locates and describes the shape of the contaminant plume which matches well the plume geometry obtained from drill-hole samples.

Thesis supervisor: F. Dale Morgan  
Title: Professor of Geophysics

## Acknowledgment

There are many people whom I wish to thank for their influence on my life and research. My first debt of gratitude is to my thesis advisor, Prof. F. Dale Morgan, who encouraged me to develop a broad range of research interests and stimulated me with endless scientific curiosity. His effort has also brought me unique opportunities to get involved in some worldwide scientific interactions especially those with colleagues in the Caribbean islands with whom I shared not only environmental geophysics knowledge but also the joy of life. Over the course of my thesis research, his advice on every aspect of my research, such as selecting the topic, pursuing the goal, and presenting the work, made the completion of this thesis possible.

I am also indebted to Prof. Nafi Toksöz who supervised my research during the first two years of my study. His ceaseless efforts have provided the students and staff at ERL a unique research and educational environment. His support and encouragement during my first two years of study were invaluable. I owe another debt of gratitude to Dr. Bill Rodi who was always there to offer advice when my work needed help. Almost every aspect of the geophysical inverse theory I have learned in the past years was a great result of working with Bill. His broad range of experience and knowledge in the inverse theory was critical to the progress of my research. His scientific curiosity contributed greatly to the development of this thesis.

I would like to take this opportunity to thank other members of my dissertation committee, Prof. Harold Hemond and Prof. Robert Van Der Hilst, for their friendly attitudes, encouragement, and helpful feedback. I am also grateful to Prof. Tom Jordan, Prof. Ted Madden, and Prof. John Southard, for the great scientific guidance, conscientious support, and endless patience they provided during my general exam period. Their insight into a wide range of scientific problems opened my eyes. I will benefit from their influence throughout my entire scientific career.

As a full-time student I was sponsored by a numerous funding resources including the Department of Energy, the Environmental Protection Agency, and the Borehole Acoustics and Logging Consortium at ERL.

Thanks also go to Dr. Randy Mackie for his great help and friendship during my first two years of research. His guidance was critical to the progress of my general paper. I am also grateful to Dr. Arthur Cheng who brought me to the ERL and offered much advice on my research.

I am thankful for the friendship of fellow ERLers (past and present); Abdulfattah Al-Dajani, Sara Brydges, Dan Burns, Naida Buckingham, Wei Chen, Ningya Cheng, Chantal Chauvelier, David Cist, Wenjie Dong, Chuck Doll, Bob Greaves, Matthijs

Haartsen, Liz Henderson, Xiaojun Huang, Matthias Imhof, Jonathan Kane, David Lesmes, Yingping Li, Mary Krasovec, Bertram Nolte, Jane Maloof, Joe Matarese, Oleg Mikhailov, John Olson, Chengbin Peng, Rama Rao, Rob Reilinger, Philip Rappert, Shirley Rieven, Francesca Scappuzzo, Feng Shen, Roque Szeto, John Sogade, Sue Turbak, Roger Turpening, Yervant Vichabian, Lori Weldon, Zhenya Zhu, Xiang Zhu, Jie Zhang, and Xiaomin Zhao. Specifically, I would like to thank Ms. Kate Jesdale for reviewing my thesis manuscript.

My greatest debt of gratitude is to those who are closest to me. My mother, father, and sister always have offered me endless care and love. Their tremendous support and sacrifices are the foundations of my life and work. George Theophanis, my father-in-law, is one of the most insightful scientists I have known, he is capable of discussing almost any scientific issue. Susan Theophanis, my mother-in-law, is always passionate and supportive. Nana Olga, and Ari and Maia Theophanis, have been a great source of love for me. Most of all, I wish to acknowledge my husband, Stephen, who has been a great inspiration to me throughout our years together. His tremendous help, scientific insight, and stimulating discussion cannot be measured in the preparation of this document. His brave attitude towards life encourages me to face any challenge.

# Contents

<b>1</b>	<b>Introduction</b>	<b>11</b>
1.1	Background . . . . .	11
1.2	Objectives . . . . .	16
1.3	Thesis Plan . . . . .	17
<b>2</b>	<b>Inversion of D.C. Electrical Resistivity Data – Theory</b>	<b>20</b>
2.1	Introduction . . . . .	20
2.2	Formulation of the Inverse Problem . . . . .	25
2.3	Nonlinear Inversion Using Tikhonov Regularization . . . . .	27
2.3.1	Comparison of Stabilizing Functionals . . . . .	29
2.4	Nonlinear Minimization Algorithm . . . . .	33
2.4.1	Gauss-Newton Method . . . . .	34
2.4.2	Nonlinear Conjugate Gradient Method . . . . .	35
2.4.3	Numerical Comparison . . . . .	38
2.5	Conclusions . . . . .	39

<b>3</b>	<b>Inversion of d.c. Electrical Resistivity Data – Applications</b>	<b>53</b>
3.1	Introduction . . . . .	53
3.2	Imaging Aberjona Contamination Site . . . . .	54
3.2.1	Introduction . . . . .	54
3.2.2	Inversion Results . . . . .	55
3.2.3	Conclusion . . . . .	57
3.3	Imaging Larderello Geothermal Field . . . . .	58
3.3.1	Introduction . . . . .	58
3.3.2	Geoelectrical Survey at Larderello-Valle Secolo . . . . .	59
3.3.3	Inversion Procedure . . . . .	60
3.3.4	Inversion Results and Interpretation . . . . .	63
3.3.5	Conclusions . . . . .	64
3.4	Imaging A Limestone Cavern System in Barbados, West Indies . . . . .	65
3.4.1	Introduction . . . . .	65
3.4.2	Data Acquisition . . . . .	66
3.4.3	Inversion Results . . . . .	66
3.4.4	Conclusion . . . . .	68
<b>4</b>	<b>Inversion of Electrical Induced Polarization Data</b>	<b>92</b>
4.1	Introduction . . . . .	92
4.2	Formulation of the Problem . . . . .	96
4.3	Forward Modeling . . . . .	97



4.4	Extension of Nonlinear Inverse Theory to the Complex Domain . . .	98
4.5	Bi-Conjugate Gradient Method . . . . .	103
4.6	Example . . . . .	105
4.7	Conclusion . . . . .	106
<b>5</b>	<b>Inversion of Electrical Self-Potential Data</b>	<b>114</b>
5.1	Introduction . . . . .	114
5.2	Formulation of the Forward Modeling . . . . .	116
5.3	Inversion Method . . . . .	118
5.4	Non-uniqueness . . . . .	119
5.5	Field Example . . . . .	121
5.6	Conclusion . . . . .	124
<b>6</b>	<b>Uncertainty and Resolution Analysis</b>	<b>141</b>
6.1	Introduction . . . . .	141
6.2	Uncertainty Analysis via Bayesian Parameter Estimation and Monte Carlo Method . . . . .	146
6.3	Uncertainty Analysis via Tikhonov Regularization and Monte Carlo Method . . . . .	150
6.4	Augmented Uncertainty Analysis In Tikhonov Regularization . . . . .	152
6.5	Resolution Analysis Via Model Correlation and The Modulation Transfer Function . . . . .	155
6.6	Numerical Results . . . . .	158
6.7	Conclusions . . . . .	163

<b>7</b>	<b>Optimizing The Electrical Survey</b>	<b>176</b>
7.1	Introduction . . . . .	176
7.2	Tomographic Data Acquisition Geometry . . . . .	177
7.3	Tomographic Vs. Pseudo-Section Acquisition . . . . .	178
7.4	Sensitivity Analysis . . . . .	179
7.5	Model Correlation Analysis . . . . .	180
7.6	Conclusion . . . . .	181
<b>8</b>	<b>Summary and Conclusions</b>	<b>189</b>
8.1	Conclusions and Contributions . . . . .	189
8.2	Future Work . . . . .	193

# Chapter 1

## Introduction

### 1.1 Background

Geophysical surveys are used to remotely sense the physical properties of the earth to provide specific knowledge of the subsurface for a wide range of applications such as oil exploration, mineral prospecting, groundwater mapping, and environmental contamination detection to name a few. There are many geophysical surveying methods available to determine different physical properties of the earth which include geoelectrical, seismic, gravity, magnetic, electromagnetic, and radar methods. Geoelectrical surveys distinguish themselves from these other techniques through the detection of surface electrical fields produced by electric current flow in the ground.

Geoelectrical survey methods include d.c. electrical resistivity, electrical induced polarization (IP), and electrical self-potential (SP) methods. These methods can be classified by the type of electric source involved in the survey. The d.c electrical resistivity and the IP method attempt to map subsurface properties using an artificially applied current source, while the SP method relies on naturally induced current

sources. This thesis will address issues of modeling and inversion techniques, as well as the optimization of survey geometry as applied to these three methods.

In the problem of d.c. electrical resistivity, one is interested in finding the subsurface bulk resistivity distribution from static electrical measurements obtained on the boundary of the domain, usually the surface of the earth. It is the most commonly used geoelectrical method due to the enormous variation in electrical resistivity found in earth material and to its cost effectiveness . This problem has extensive applications in mineral deposits prospecting, underground facility identification, groundwater exploration, geothermal studies, and engineering construction projects.

In the problem of Induced Polarization, one is interested in finding the distribution of the complex character of low-frequency resistivity in the subsurface. The name induced polarization is derived from the analogy to the polarization of electrodes that occurs when an electric current is passed between an electrode and a surrounding ionic conducting fluid (Madden and Cantwell, 1967). It has been observed that when a current is applied to the ground, the ground behaves much like a capacitor, storing some of the applied current as a charge that is dissipated upon removal of the current. In this process, both capacitative and electrochemical effects are responsible. In comparison with the d.c. resistivity measurements, the IP method measures the transient (short-term) variations in electrical potential as the current is initially applied to or removed from the ground. IP is commonly used to detect concentrations of clay and electrically conductive metallic mineral grains, and it has recently been applied to the detection of underground environmental contaminant plumes.

In the problem of electrical Self-Potential, one is interested in finding the distribution of subsurface induced current sources, which may be caused by concealed geological features of economic or other interests, from the measurement of the electrical potential field made on the surface of the earth. The induced current sources

are driven by subsurface electrochemical, electrokinetic, and thermoelectric energies. The method thus bears a close relationship to the IP method. Measurements that utilize SP have been found in association with studies of groundwater movement related to leakage of dams, dikes, canals, reservoir floors, and other contaminant structures (Corwin, 1990). Other examples of SP investigations include the evaluation of heat flow associated with geothermal activity and certain biologic processes.

While each technique is designed to detect different information about the subsurface earth material, the physical phenomena of these three geoelectrical techniques are coherent and can be modeled jointly using Ohm's law and the conservation of current. This transfers into a second-order elliptic equation with either a spatially variable coefficient corresponding to the resistivity (bulk resistivity in the d.c. resistivity case; complex resistivity in the IP case) or a variable source term (in the SP case). Under this model, the inverse problem is defined as the determination of the variable coefficient representing the d.c resistivity, the complex resistivity (IP), or the variable source term representing SP as functions of position given the discrete measurement of electrical potential and certain boundary conditions. This has long been a difficult problem in the geophysics community.

The common difficulties among the three methods resemble many other geophysics inverse problems. The nonuniqueness is by far the most prominent factor to be considered. The solutions of geoelectrical inverse problems are necessarily nonunique. Consider for instance the problem of estimating the the spatially varying resistivity structure as a function of position. Because the resistivity is a continuous function which, in principal, consists of an infinite number of variables, it is impossible to define a unique solution solely from information of a finite number of potential measurements on the surface. The nonuniqueness also arises from the lack of knowledge which accounts for the complexity of the real earth: observed potential data always have experimental uncertainty, and the physical theories allowing the solution of the

forward problem are always approximations of a more complex reality.

Geoelectrical inverse problems also exhibit a nonlinear and numerically extensive nature. The electrical potential is nonlinearly dependent on the resistivity structure. Further, the number of parameters in the model must be large enough to allow an accurate simulation of the real earth, and the number of data associated with a moderate sized experiment is usually quite large. Thus many theoretical and computational challenges are involved in the successful application of these techniques.

The potential benefit through the application of geoelectrical techniques prompted a long history of extensive modeling and inversion developments for each of these three methods. The following paragraphs will briefly describe the interpretation history of each method, more detailed discussion is reserved for later chapters.

From the pioneering work of the early 1930's through the present day, there has been steady evolution in d.c electrical resistivity inversion technology. In early work between the 1930's and 1950's, efforts were made primarily on the interpretation of resistivity data over a 1-D layered earth using a curve matching technique based on Hankel's Fourier-Bessel formula (Slichter, 1933; Pekeris, 1940; Vozoff, 1958). Issues of the uniqueness and stability were not considered. Later, numerical algorithms using inversion methods on a trial-and-error basis was introduced to 1-D and 2-D resistivity interpretation (Madden, 1967; Coggon, 1971; Mufti, 1976; Dey and Morrison, 1979). Beginning in the late 1970's, more sophisticated numerical modeling for 2-D and 3-D earth models which permitted higher accuracy and resolution were developed. They include the integral equation approach to solve for simple prismatic inhomogeneities (Hohman, 1975; Yang and Ward, 1985; Eloranta, 1986; Beasley and Ward, 1986), the alpha center approach for solving uncomplicated structures (Petrick *et al.*, 1981; Shima, 1990), the finite-element approach (Sasaki, 1992), the finite-difference approach (Dey and Morrison, 1979; Park and Van, 1991; Ellis and Oldenburg, 1994b),

and the network analogy approach (Zhang *et al.*, 1995) for inhomogeneous media. These methods emphasized the ability to calculate the anomalies caused by complex 2-D or 3-D structures, they usually required extensive computation and a large number of iterations based on a Newton-type scheme. Even with the approved development of the mathematical theory in handling complex structure, they are still limited by the computational burden. Some of these methods touched on the use of damping or smoothness to get a stable solution in dealing with the nonuniqueness, but how to properly constrain the model was not fully understood.

The interpretation of IP data was developed in conjunction with the d.c. resistivity interpretation, but with far less success. Until fairly recently IP interpretation was mainly qualitative. Attempts were usually made to plot the change of apparent bulk resistivity with frequency but ignoring the phase shift associated with IP effect (Hallof, 1957; Madden, 1967). Methods for numerically inverting IP data were found to be sparse in the literature. The most common approach was to invert time domain IP data into an intrinsic chargeability distribution, defined as the ratio of the secondary voltage measured immediately after the current is turned off to the primary voltage measured while the current is on (Pelton *et al.*, 1978; Rijo, 1984, Oldenburg and Li, 1994). There was no successful inversion technique available which could extract more information from the IP data.

Methods for Self-Potential data interpretation were developed independently from the d.c resistivity or IP in past decades. Older methods were mostly based on polarized simple geometry bodies (de Witt, 1948; Yungul, 1965; Paul, 1965). After Marshall and Madden (1959) and Nourbehecht (1963) who related the solution of electrical potential to the primary coupled flows, research was focused on deriving the potential anomalies produced by the suspected thermoelectric, electrochemical, and electrokinetic sources by taking them as simple dipping dipoles contained in a medium with a simple resistivity structure (Sill, 1983; Fitterman, 1984). All of

these methods were limited to forward modeling, there was no inversion technique available at the time. This slow progress can be partly attributed to the lack of practical techniques for the inversion mostly caused by questions of how to constrain nonuniqueness.

The focus of today's research in geoelectrical imaging has been the development of efficient inversion algorithms for generating 3-D images of subsurface resistivity or current source structure. Relatively little work has been done on the problem of quantifying the accuracy and resolution of such images, i.e. to what degree do the images represent the actual medium. These accuracy and precision questions must be answered for geoelectrical imaging to become a practical technology. To further enhance the geoelectrical imaging method, optimization of the survey geometry is also a key issue, however, relatively little work has been done on this topic in the past.

## 1.2 Objectives

The objectives of this thesis are the following:

- Develop a better inversion method for 3-D d.c. electrical resistivity.
- Extend this inversion method to the 3-D electrical Induced-Polarization and the 3-D electrical Self-Potential inverse problems.
- Characterize uncertainty and resolution associated with the inversion.
- Develop an optimized electrode array to enhance the resolution and accuracy of the geoelectrical surveys and thus to increase the efficiency of the method.



- Bridge the gap between geoelectrical inversion theory and the applications by applying our inversion algorithms to various real geophysics problems.

## 1.3 Thesis Plan

The topics presented in the objectives will be covered in the individual chapters of the thesis as follows:

Chapter 2 discusses the generalized inversion methods used to treat the nonlinearity and nonuniqueness of the 3-D electrical inverse problem. I approach the solution to the inverse problems in two parts. First, I present the generalized inverse theory used as a framework to solve for the unknown electrical parameters. A minimization condition is defined which combines the misfit between observed and calculated data with an imposed smoothness constraint on the reconstructed model. This yields a model with minimum structure: i.e. it is the most featureless structure that fits the data. I implement this minimum structure approach using the method of Tikhonov regularization with a differential operator. I examine the possible form of the differential operator and will show that, for the electrical resistivity inversion, the best explicit form of the operator performs a second derivative operator over the region of the model. I demonstrate the type of regularization which produces minimum structure models that can vary in the degree of smoothness versus the fit to data. The second part of the solution is to develop an efficient numerical technique to solve the inverse problem. I present a nonlinear iterative method using the nonlinear conjugate gradient method and compare its efficiency with the commonly used Gauss-Newton method. I show that the efficiency of the method depends on the preconditioning, which controls the search direction of the minimization scheme, and experiment with a variety of preconditioners.

Chapter 3 details the implementation of nonlinear electrical tomography for the d.c resistivity problem. From the application point of view, perhaps the most important objective is to demonstrate that the method can be applied to the real earth. I therefore apply nonlinear 3-D d.c. resistivity tomography to three field data sets. The first data set was collected from the Aberjona River in Woburn, Massachusetts. The goal of the resistivity survey is to characterize the soil structure around the river in order to understand the transport mechanisms that have been involved in the contamination of drinking water. Inversion results from the resistivity survey is correlated with ground penetrating radar data and cone penetrometer information. The second experiment was performed in the Laderallo Geothermal Field in Italy. The objective is to relate the variations in resistivity with position and time to the re-injection history. A particular inversion procedure will be developed to extract the variation of resistivity as a function of time. The third experiment was performed at the Harrison's cave in Barbados, West Indies. The objective of the study is to detect underground limestone caves in an effort to understand the cavern structure in order to facilitate surface construction activities. I invert data from this experiment and show that our resistivity tomography technique can be very useful for cave or other underground facility mapping.

In chapter 4 I extend the theory of 3-D d.c. electrical resistivity tomography to Induced Polarization inversion. The parameters that are used to describe the IP effect are complex resistivity values. Under this definition the inversion will be carried out in the complex domain. From a synthetic example, with the 'true' complex resistivity value measured from a laboratory experiment, I show that IP tomography can be utilized to detect contaminant plumes, even with weak concentration, where d.c resistivity is not effective.

In chapter 5 I extend the inversion theory to the electrical self-potential problem and develop an inversion algorithm for reconstruction of underground current sources

generated by fluid flow or other origins. I investigate the strong nonuniqueness properties of the problem, and provide means to reduce the nonuniqueness by various constraints. The method is then applied to map a jet fuel contamination plume at the Massachusetts Military Reservation in Cape Cod, Massachusetts.

An inversion is incomplete without the analysis of uncertainty and resolution. This topic is discussed in chapter 6 where I develop a methodology to assess the uncertainty and resolution analysis of electrical inversion methods.

As a consequence, chapter 7 discusses the optimization of electrical surveys. Sensitivity analysis combined with the uncertainty and resolution analysis provide guidelines for the design of geoelectrical field surveys.

I summarize the work and results of the thesis in chapter 8, and discuss future work directions which could utilize and enhance the capability of our nonlinear 3-D electrical tomography techniques.

# Chapter 2

## Inversion of D.C. Electrical Resistivity Data – Theory

### 2.1 Introduction

The d.c. electrical resistivity method is a principal geophysical exploration technique which has been used extensively for subsurface characterization. The implementation of the method consists of injecting current into the ground, measuring the electrical potential at intervals on the surface or in boreholes, and from those measurements deducing the subsurface resistivity distribution. Because the instrumentation is simple and the data acquisition is straightforward, the method is extremely cost effective. Important applications include mineral deposits prospecting (Keller and Frischknecht, 1966; Burger, 1992), groundwater exploration (McNeill, 1990; Medeiros and Lima, 1990), geothermal studies (Burger, 1992) and engineering construction projects (Bogoslovsky *et al.*, 1979; Shima, 1992). Recently, this method increasingly has been applied to environmental protection surveys because of its non-invasive

property. The applications include general hydro-geological mapping (Okko,1993), monitoring contaminated fluid migration (Blum, 1989; Van *et al.*, 1992; Spies and El-lisi, 1995), mapping the extent of landfill areas (Carpenter *et al*, 1990) and detection of contaminant plumes (Mazac *et al.*, 1990; Buselli *et al*, 1991)

The electrical resistivity of geological materials depends on mineralogy, clay content, pore fluid, permeability, conducting metal content, and other properties of the materials. The resistivity value of different geological materials can vary from  $10^{-4}\Omega.m$ (Pyrrhotite) to  $10^{14}\Omega.m$  (dry limestone), a range in values that may be the widest of any common physical property of earth materials. The electrical resistivity method is ideally suited for the task of detection of chemical contamination. The resistivity of some chemical contaminants may be much in contrast with the surrounding natural materials, this contrast makes the resistivity method the most sensitive in discerning contaminants from groundwater. Even when the resistivity image does not reveal the presence of chemical contaminants directly, it can provide valuable information on soil properties that control the transport of chemical contaminants.

The task of the d.c. electrical resistivity inversion is to solve for the subsurface resistivity distribution using the measurements of electrical potential on the earth's surface or in boreholes. This is a difficult problem on many levels. One major difficulty encountered is that such an inverse problem is ill-posed. The ill-posedness comes from the fact that the number of measurements is always finite while the unknown subsurface electrical property distribution is a continuous function which contains in principle an infinite number of variables. It is impossible to construct a solution that is stable and unique based on fitting data alone. Therefore solutions must incorporate some *a priori* information or be regularized in order to be stable and meaningful against the noise in the data. Since such *a priori* information or regularization is usually difficult to obtain directly from the geological reality, it is subjected to personal bias. Deciding which *a priori* assumption or regularization criterion is appropriate for

the geoelectrical inversion remains a problem. The other major difficulty associated with the inversion is a result of the problem's nonlinear and numerically intensive nature. Since, in practice, a 3-D model always involves a large number of model parameters and data sets, the forward modeling entails solving many matrix systems. Further, for the d.c. electrical resistivity problem, because the observed electrical potential data are nonlinearly dependent on the subsurface resistivity parameters, iterative methods are needed to obtain the inversion solutions. Owing to this computational difficulty, methods for geoelectrical inversion were mostly restricted to 1-D (Inman, 1975; Parker, 1984) or 2-D (Pelton *et al.*, 1978; Tripp *et al.*, 1984; Smith and Vozoff, 1984) earth models in the past decades, only a few 3-D model inversions were found in recent literature (Park and Van, 1991; Ellis and Oldenburg, 1994; Zhang *et al.*, 1995).

There has been no great success in overcoming the uniqueness problem associated with practical data. A very common approach is restriction of the solution to the class of models consisting of a small number of parameters. In the past, most methods for d.c. resistivity inversion (e.g. Inman, 1975; Vozoff and Jupp, 1975) used coarsely parameterized models (e.g. large layers or blocks) to make the problem well-posed. These solutions suppress significant structures and can hardly match the geological reality. A more objective approach that allows finely parameterized model was developed by Parker (1984) using bilayer expansion of Green's function on a 1-D earth model. He introduced some smoothness constraints to eliminate the rapid unstable oscillation of the resistivity values that are caused by the non-uniqueness of the problem. Since the bilayer expansion was formulated based on a simple layered model, his approach was limited to 1-D earth models. Park and Van (1991) and Zhang *et al.* (1995) developed a 3-D resistivity inversion based on the maximum likelihood method (Tarantola and Valette, 1982) using statistical information to constrain the models. The method philosophically requires full statistical knowledge of the model parameters. However, in practice, such information is often unattainable. Therefore

the statistical information was often replaced by a uniform damping weighted on each model parameter which makes the method effectively the same as the conventionally damped least square method.

The approach presented in this paper is based on Tikhonov regularization (Tikhonov, 1977). The method finds solutions by emphasizing the importance of the spatial correlation of the model parameters. It seeks spatially smooth (or "minimum structure") solutions of the inverse problem. The basic motivation for seeking smooth models is that we do not wish to be misled by features that appear in the model but are not essential in matching the observations. Other models which satisfy observations but contain more complicated structures will be far more provocative and attractive than reality. This approach thus provides a low bound of the model complexity. It guarantees that the real profile must be as rich in structure as the inversion solution but never less complex in structure.

The quest for simple solution is well founded in literature. In the early fourteenth century William of Occam wrote that "it is vain to do with more what can be done with fewer" (Constable *et al*, 1987). What has become known as Occam's razor has also become a fundamental tenet of modern science: hypotheses should be neither unnecessarily complicated nor unnecessarily numerous. The minimum structure approach has been taken by many others. For example, it was taken by Rodi (1989) in 2-D magnetotellurics and seismic data, by Pilkington and Todoschuk (1992) in cross-hole seismic tomography, by Scales *et al* (1990) in refraction seismic profile, by Matarese (1995) in nonlinear travelttime tomography, and by Jiracek *et al.* (1987), Rodi (1989), deGroot-Hedlin and Constable (1990) in 2D magnetotellurics.

Additionally, we have justification in physics. Due to the diffusive nature of the electrical energy, the resistivity measurement does not possess high resolution on sharp contrasts. Therefore the minimum structure models are reasonable representa-

tions of the real earth.

When minimum structure models are sought, the inversion requires insertion of some smoothness constraints which are used to minimize the model roughness. One objective in this chapter is to investigate the effect of the smoothness constraints used in the Tikhonov regularization method. We will compare three commonly used smoothness constraints, i.e. the zeroth, the first and the second order spatial derivatives of model parameters. We will show that their effect on the stability of the solution relies on the behavior of the sensitivity function, which is a measure of how the electrical potential outputs change due to a small perturbation in the resistivity model parameters.

The difficulty of implementing such minimum structure regularization on a 3-D inversion depends, in part, on the numerical algorithm used for minimization. For d.c. electrical resistivity, because of the nonlinearity of the forward problem, iterative minimization schemes are needed to obtain solutions. The nonlinearity may also induce multiple local minima in the objective function used to find minimum structure models that fit the data. Therefore it may be necessary to repeat the iterative procedure by varying initial models for the minimization algorithm. Further, due to the non-uniqueness and uncertainty of the problem, it is desirable to find the full set of acceptable solutions or, at least, find as many solutions that fit the data as possible. In doing so, one needs to repeat the iteration algorithm by varying the *a priori* model or the smoothness constraint. Most current resistivity inversion algorithms are solved by an iterative linearized procedure which corresponds to the Gauss-Newton method (e.g. Park and Van, 1991; Zhang, *et al*, 1995). It starts from an initial model, then estimates a perturbation of the current model based upon the Taylor expansion. This process is then repeated until the solution converges. This method suffers from slow convergence at the early stage of iterations. It has been shown that it may take tens of hours of CPU time on a high speed workstation to find



a single inversion solution on a small (20x20x10) model (Ellis, 1995). A faster and more robust algorithm is very desirable for extensively studying the uncertainty and the resolution of the problem and to benefit the 3D geoelectrical method in future environmental and engineering application.

The second objective in this chapter is to investigate a more efficient algorithm based on the conjugate gradient method to solve the nonlinear minimization. We will show that with an appropriate pre-conditioner our algorithm requires fewer computer resources than the Gauss-Newton method, and its superiority will become important when the initial model varies widely from the true model.

## 2.2 Formulation of the Inverse Problem

A practical d.c. electrical resistivity inverse problem may be defined as: given a set of electrical potential measurements  $d = (d_1, d_2, \dots, d_M)$  made at the surface or in boreholes, determine as much information as possible about the subsurface electrical resistivity. This may be written via an equation,

$$d = \mathbf{G}(m) + e \tag{2.1}$$

where  $d \in E^M$  is a vector representing data in the Euclidean space of dimension M,  $m = m(\mathbf{x})$ , is the unknown resistivity function,  $\mathbf{G}$  is a forward modeling operator which maps the model space to the data space, and  $e$  is an error vector. To allow general spatial variations in resistivity and, at the same time, force resistivity to be positive everywhere, we may define  $m$  as a function of 3-D position,  $\mathbf{x}$ , whose values are the logarithm of resistivity, i.e.  $m(\mathbf{x}) = \log \rho(\mathbf{x})$ . In practice, the function  $m$  is sampled on a dense grid,  $m \in E^N$ .

Resistivity surveys inject current into the ground via a positive and negative

electrode and the source current density  $j(\mathbf{x})$  can be written

$$j(\mathbf{x}) = J_0 [e_+(\mathbf{x}) - e_-(\mathbf{x})] \quad (2.2)$$

where  $J_0$  is the total source current and where  $e_+$  and  $e_-$  represent the spatial distribution of the two electrodes. Typically, each electrode is small compared to the spacing between electrodes and  $e_+$  and  $e_-$  are each taken to be concentrated at a point, e.g.,

$$e_+(\mathbf{x}) = \delta(\mathbf{x} - \mathbf{x}_0) \quad (2.3)$$

where  $(\mathbf{x}_0)$  is the electrode position, and  $\delta$  is the Dirac distribution.

The forward modeling operator,  $G$ , is defined implicitly by the current-conservation equation

$$\nabla \cdot \left( \frac{1}{\rho(\mathbf{x})} \nabla V(\mathbf{x}) \right) = -I(\mathbf{x}) \quad (2.4)$$

where  $I(\mathbf{x})$  is the current source and  $V(\mathbf{x})$  is the electric potential field. Electrical potential  $V(x, y, z)$  is subject to appropriate boundary conditions. On the surface of the earth, it is necessary to use the Neumann boundary condition,  $\partial v / \partial \hat{n} = 0$ , where  $n$  is the direction normal to the boundary. On portions of the boundary inside the earth, an exact boundary condition is not available but various approximate boundary conditions including Dirichlet and mixed boundary conditions (Day and Morrison, 1979; Zhang *et al.*, 1995) can be used. For numerical simplicity, we assume that the model boundaries are far from the source and receiver so that a Dirichlet boundary condition,  $v = 0$ , can be used.

To solve Equation 2.4 numerically, we use the transmission network analog developed by Madden (1972) to discretize the 3-D model into a network that consists of network node, boundary nodes, and impedance branches (Figure 2-1). We define voltage nodes at the top center of each medium block, and the impedance elements,

$R_x$ ,  $R_y$ , and  $R_z$ , at the network branch.  $R_x$ ,  $R_y$ , and  $R_z$  are functions of the resistivity and the dimension of the network cells. Current sources can be placed at any network nodes and the potential is defined at every node. The governing equation (Equation 2.4) applied to the network results in a linear system of equations:

$$\mathbf{K}v = s \quad (2.5)$$

where  $v$  is a vector of the potentials at the network nodes,  $s$  is the current source vector, and  $\mathbf{K}$  is a real, symmetric, and positive-definite matrix which depends on the resistivities and dimensions of the network cells. For a potential measurement  $d$  at receiver number  $ir$ , we can write,

$$d = \mathbf{G}(m) = C_{ir}v \quad (2.6)$$

where  $C_{ir} = (0, \dots, 0, 1, 0, \dots, 0)$ , 1 is  $ir$ -th the component which corresponds to the location of the receiver. To efficiently solve the forward problem (Equation 2.5), a linear conjugate gradient algorithm with incomplete Cholesky decomposition is used (Zhang *et al.*, 1995).

Since  $d$  is finite-dimensional while (in theory)  $m$  is infinite-dimensional, the inverse problem (Equation 2.4) is ill-posed, i.e. unique, stable solutions cannot be obtained solely on the basis of fitting the data. It is necessary to incorporate *a priori* data or preferences in order to define a unique solution.

## 2.3 Nonlinear Inversion Using Tikhonov Regularization

There is little success in overcoming the uniqueness problem associated with practical data. The Monte Carlo method, in which a huge number of randomly generated

models are tested against the data, has been used for resistivity (Sternberg, 1979) and magnetotelluric (MT) (Jones and Hutton, 1979b) soundings in an attempt to characterize all models which agree with the observations. Such computations can never be exhaustive.

Another approach to overcome the nonuniqueness is to incorporate some *priori* information in order to define a unique solution. Classical remedies that advocate *a priori* preference into the model fall under two classes. One class assumes that the model parameters are random variables so that statistical information can be introduced to constrain the model. Important approaches include: Bayesian inference (Duijndam, 1988); stochastic inversion (Franklin, 1970), and the maximum likelihood method (Tarantola and Valette, 1982). The second class assumes some "regularity" properties of the solution such as a constraint on the spatial smoothness of the model parameter. This idea is familiar from the modern methods of data interpolation. For example, cubic spline interpolation describes the curve passing through a given series of measurement points with the smallest possible roughness. The original idea of a penalty for complexity seems to be due to Tikhonov, who named the general procedure "regularization", introducing it in order to overcome mathematical difficulties in the theory of ill-posed problems. (Tikhonov and Arsenin, 1977).

Tikhonov regularization defines a solution of the inverse problem that fits the data but also has minimum possible structure. It is our contention that regularization has enormous practical benefits in the interpretation of experimental data. In the case of the highly non-unique problems, this technique is very useful because it provides the simplest, or "minimum structure", solutions (Constable et al, 1987). It is also important to note that the methods in the first class, such as Bayesian inference, stochastic inversion, and the maximum likelihood method, philosophically require full statistical knowledge of the model parameters. However, often in practice, when such information is unavailable, these methods impose some smoothness constraints

which makes them effectively the same as Tikhonov regularization.

Using a least-square criterion, Tikhonov regularization defines a solution that is a joint minimization of data misfit and a "stabilizing functional":

$$\Psi = (d - \mathbf{G}(m))^T \mathbf{R}_{dd}^{-1} (d - \mathbf{G}(m)) + \tau (m - m_0)^T \mathbf{L}^T \mathbf{L} (m - m_0) = \min \quad (2.7)$$

where  $\Psi$  is the objective functional to be minimized,  $\mathbf{R}_{dd}$  is data covariance matrix,  $\mathbf{L}$  is a linear operator,  $\tau$  is a positive number known as the regularization parameter, and  $m_0$  is a *a priori* model. The first term of  $\Psi$  is the chi-squared measure of the data misfit. The second term defines the stabilizing functional which measures the spatial roughness of the model. In the stochastic or the maximum likelihood inversion,  $m_0$  is taken to be the *a priori* mean of  $m$  and  $\mathbf{L}$  is chosen such that  $(\mathbf{L}^T \mathbf{L})^{-1} = \mathbf{R}_{mm}$  is an *a priori* covariance of  $m$ . In a minimum structure approach,  $\mathbf{L}$  is a differential operator and  $m_0$  is taken to be a simple *a priori* model. In practice it is desirable to vary  $m_0$  so that multiple solutions can be obtained.

Conventionally, the most commonly used stabilizing functionals are:

$$1, \quad \mathbf{L} = I, \quad (m - m_0)^T \mathbf{L}^T \mathbf{L} (m - m_0) = \int dx dy dz |m - m_0|^2 \quad (2.8)$$

$$2, \quad \mathbf{L} = \nabla, \quad (m - m_0)^T \mathbf{L}^T \mathbf{L} (m - m_0) = \int dx dy dz |\nabla(m - m_0)|^2 \quad (2.9)$$

$$3, \quad \mathbf{L} = \nabla^2, \quad (m - m_0)^T \mathbf{L}^T \mathbf{L} (m - m_0) = \int dx dy dz |\nabla^2(m - m_0)|^2 \quad (2.10)$$

It is not certain whether any of these options guarantees a well-posed minimization in geoelectrical inversion. In the next section we will discuss this issue.

### 2.3.1 Comparison of Stabilizing Functionals

Among proponents of the minimum-structure approach, there is no consensus on the best smoothing operator  $\mathbf{L}$  to use (at least for 1-D models) (Bache *et al.* 1978).

Constable *et al.* (1987), Smith and Booker (1988) defined  $\mathbf{L}$  in terms of the first derivative, as in equation (Equation 2.9). Scales *et al.* (1990) defined  $\mathbf{L}$  in terms of the second derivative, as in Equation 2.10. Jiracek *et al.* (1987), Ellis and Oldenburg (1994) defined  $\mathbf{L}$  as a combination of both the first and the second derivatives. To investigate their influences on the 3D resistivity problem, we compare the three stabilizing functionals described in Equation 2.8 - Equation 2.10 both theoretically and numerically.

We know that in equation (Equation 2.7), when  $\Psi$  is minimized, its first order partial derivative with respect to  $m$  is zero yielding,

$$\mathbf{A}^T \mathbf{R}_{dd}^{-1} (d - \mathbf{G}\hat{m}) + \tau \mathbf{L}^T \mathbf{L} (\hat{m} - m_0) = 0 \quad (2.11)$$

where  $\hat{m}$  is the solution at which  $\Psi(\hat{m})$  is minimized.  $\mathbf{A}$  is the sensitivity operator, or Fréchet derivative which measures how data changes to a change of resistivity model. For a discrete model,  $\mathbf{A}$  is the matrix

$$\mathbf{A}_{ij} = \frac{\partial \mathbf{G}_i}{\partial m^j} \quad (2.12)$$

Park *et al.* (1991) derived that the sensitivity matrix is given by the inner product of the current density ( $J_s$ ) from a point source at the transmitter and the current density ( $J_r$ ) from a point source at the receiver integrated over the perturbed volume,

$$\mathbf{A}_{ij} \sim \int_V \rho J_s \cdot J_r d^3 \vec{x} \quad (2.13)$$

In the 3-D problem, since the current distribution from a point source approaches infinity at the source, this sensitivity function has singularities at the location of source and receivers. These singularities could result in a large variation in model space given a small perturbation in the data. This aspect of the physics must be accounted for in the regularization method.

Using Equation 2.11, we obtain the following relationship between the regularized

solution model  $\hat{m}$  and the sensitivity matrix  $\mathbf{A}$ ,

$$\mathbf{L}^T \mathbf{L} \hat{m} = \mathbf{L}^T \mathbf{L} m_0 + \tau^{-1} \mathbf{A} \mathbf{R}_{dd}^{-1} (d - \mathbf{G} \hat{m}) \quad (2.14)$$

Therefore, when  $\mathbf{L}$  is an identity, the solution model  $\hat{m}$  equals  $m_0$  plus a linear combination of the sensitivity matrix multiplied by the data residual. When  $\mathbf{L}$  is the first order spatial derivative operator, the Laplacian of  $\hat{m}$  is a linear combination of the sensitivity matrix multiplied by the data residue. When  $\mathbf{L}$  is the second order spatial derivative operator, the Laplacian squared of  $\hat{m}$  are a linear combination of the sensitivity matrix multiplied by the data residual. To test which choice of the stabilizing functional yields a stable solution, we design a simple synthetic test problem.

The model is a conductive block ( $1\Omega.m$ ) buried in a homogeneous half space ( $100\Omega.m$ ) (Figure 2-2). The model is parameterized as  $Log_{10}$  resistivity and discretized into  $21 \times 21 \times 15$  elements with 10 m spacing. The ( $1\Omega.m$ ) conductive block is discretized into  $7 \times 7 \times 3$  elements. 25 receiver electrodes are placed on the surface using the pole-pole configuration, among which nine of them are also used as current electrodes. A total of ( $9 \times 24 = 216$ ) observations are produced by forward modeling and 3% random Gaussian noise is added to the data.

To investigate which smoothness operator gives a better minimum structure model, we compare inversion results obtained by different smoothness operators, all fit data equally ( $\chi^2 = 216$ ). The results for an inversion obtained using the zeroth, the first and the second order regularization are shown in (Figure 2-6). The one with the zeroth order regularization has large resistivity variations in the vicinity of source and receivers indicating that the singularities in the sensitivity functions are not suppressed by this stabilizing functional. The first order regularization yields better results; however, the surface artifacts are still seen in the resulting model. The second order regularization successfully suppresses the surface artifacts, giving the smoothest result.

For a given stabilizing functional, the amount of smoothing done is more or less arbitrary and left to subjective judgment. Previous studies (Backus and Gilbert, 1970; Parker, 1984) indicate that when noise contaminates the data there is a trade-off between the data misfit and the model roughness. By varying the regularization parameter  $\tau$ , a trade-off curve (Figure 2-3) is generated using stabilizing functional Equation 2.10 as an example. Three points,  $\tau_1, \tau_2$  and  $\tau_3$ , are selected from the curve and their associated models are reconstructed and shown in (Figure 2-4). It is found that when the model is too smooth (when  $\tau = 5.5$ ), it can not fit the data very well ( $\chi^2 = 275$ ). As  $\tau$  is lowered ( $\tau = 1.1$ ), the model has a smooth structure and provides a better reconstruction ( $\chi^2 = 176$ ). Over-fitting data ( $\chi^2 = 130$  at  $\tau = 0.1$ ) results in a rough model which contains incorrect surface anomalies.

We now ask ourselves, which  $\tau$  is the optimum choice? To answer this question, we display the RMS misfit between the solution and the true model and the RMS  $\chi^2$  data misfit as functions of  $\tau$  in Figure 2-5. It is found that there is a minimum model misfit with the corresponding value of  $\tau = 1.1$  (top). Because this value of  $\tau$  gives the lowest model misfit, it is considered to be an optimum choice. Unfortunately in practice such comparison of the RMS model misfit is not available because true models are not known. Therefore one must seek other means for choosing the regularization parameter  $\tau$ . If we look at the curve of  $\chi^2$  data misfit against the regularization parameter  $\tau$  (middle) we find there is a slope change in the data misfit curve when  $\tau$  reaches its optimal value. By integrating the  $\chi^2$  data misfit with respect to  $\tau$  the change in slope is enhanced, as shown in the same figure (bottom). For the segments of the  $\chi^2$  data misfit curve that are below this point relatively unconstrained solutions are obtained for the inversion indicating a leakage of data noise into the solution. Even though the data misfit is small, the solution is unreliable and the associated model misfit may be large. For the segments of the  $\chi^2$  data misfit curve above this point, especially for a very large  $\tau$ , inversion solutions are highly constrained and over smoothed, which may result in poor model fitting. This change in slope in the



data misfit curve may serve as a good indicator for picking the optimal regularization parameter,  $\tau$ . In solving a travelttime tomographic problem, Philips and Fehler (1991) have found a similar behavior of the optimal regularization coefficient.

In the case where data contain random Gaussian noise, the expected value of  $\chi^2$  would be equal to the number of independent data. When  $\chi^2$  is greater than the number of independent data, the data have not been fully explained by the hypothesized model. This implies that either the inversion scheme is not applicable or the geometry of the model cells is inappropriate. More detail in the data may be fitted if a more complex model is used. In contrary, if  $\chi^2$  is smaller than the number of independent data, either the estimated variances of the observations have been overestimated (Wiggins, 1972; Inman, 1975) or the inversion is fitting the noise in the data (Inman, 1975).

## 2.4 Nonlinear Minimization Algorithm

In the preceding sections we have defined the solution of the resistivity inverse problem by minimizing the objective function  $\Psi$  in Equation 2.7. Since the forward modeling operator  $\mathbf{G}$  depends nonlinearly on  $m$ ,  $\Psi$  is non-quadratic and an iterative minimization is required.

In this section we will investigate two algorithms for minimizing the objective functional, i.e. the Gauss-Newton method, and a nonlinear conjugate gradients method.

### 2.4.1 Gauss-Newton Method

The Gauss-Newton method is based on expanding  $\mathbf{G}$  in a Taylor series and calculating the model correction at each iteration on the assumption of local linearity. By Taylor expansion, we have

$$\mathbf{G}(m + \delta m) = \mathbf{G}(m) + \mathbf{A}\delta m \quad (2.15)$$

where we have ignored higher order derivatives. Thus the value of  $\Psi$  predicted by Equation 2.7 is

$$\begin{aligned} \Psi(m + \delta m) = & (d - \mathbf{G}(m) - \mathbf{A}\delta m)^T \mathbf{R}_{dd}^{-1} (d - \mathbf{G}(m) - \mathbf{A}\delta m) + \\ & \tau(m - m_0 + \delta m)^T \mathbf{L}^T \mathbf{L} (m - m_0 + \delta m) \end{aligned} \quad (2.16)$$

With this approximation,  $\Psi$  depends quadratically on  $\delta m$  and is minimized by setting  $\partial\Psi/\partial\delta m = 0$ . Thus  $\delta m$  is found by solving

$$\delta m = (\mathbf{A}^T \mathbf{R}_{dd}^{-1} \mathbf{A} + \tau \mathbf{L}^T \mathbf{L})^{-1} (\mathbf{A}^T \mathbf{R}_{dd}^{-1} (d - \mathbf{G}(m)) + \tau \mathbf{L}^T \mathbf{L} (m_0 - m)) \quad (2.17)$$

The Gauss-Newton method thus constructs a sequence of the models by

$$m_{k+1} = m_k + \delta m_k \quad (2.18)$$

where  $\delta m_k$  is given by

$$\delta m_k = (\mathbf{A}_k^T \mathbf{R}_{dd}^{-1} \mathbf{A}_k + \tau \mathbf{L}^T \mathbf{L})^{-1} (\mathbf{A}_k^T \mathbf{R}_{dd}^{-1} (d - \mathbf{G}(m_k)) + \tau \mathbf{L}^T \mathbf{L} (m_0 - m_k)) \quad (2.19)$$

and a repetition of this process yields successive estimates  $m_1, m_2, \dots, m_k$  until the minimum is found.

Solving this system by computing the inverse of the Hessian,  $(\mathbf{A}^T \mathbf{R}_{dd}^{-1} \mathbf{A} + \tau \mathbf{L}^T \mathbf{L})$ , requires a tremendous amount of computing resources. Zhang *et al.* (1995) suggested that one can solve for  $\delta m$  without direct computation of the Hessian matrix by applying a linear conjugate gradient scheme. This approach significantly reduces the

amount of computing resources needed and makes the 3-D resistivity inversion using the Gauss-Newton method practical.

The Gauss-Newton method has the desirable feature of rapid convergence if the initial guess is close to the solution, especially if, in the neighborhood of the solution the objective function appears to become quadratic, then Gauss-Newton method will find the solution in one step. Unavoidably, an initial guess that is far from the solution may lead to difficulty. The convergence may reveal overshooting and unstable features. Therefore in practice a small damping is often added to the Hessian in order to secure the stability.

## 2.4.2 Nonlinear Conjugate Gradient Method

As shown in the previous section, we are able to solve for a minimum of  $\Psi$  by substituting a linearization of  $\mathbf{G}(m_k)$  about a perturbed  $m_k$  into Equation 2.16 and solve the inversion iteratively with each model update expressed in Equation 2.19. This Gauss-Newton type linearization procedure may result in a slow convergence for the nonlinear inverse problem when  $\Psi$  is far from a quadratic function. Another potentially more efficient algorithm for minimizing  $\Psi(m)$  is developed in this chapter. This method, the nonlinear conjugate gradient (NLCG) method, will solve Equation 2.7 directly.

All conjugate gradient methods were originally invented and analyzed for the purely quadratic optimization problem. Fletcher and Reeves (1959) extended the conjugate gradient to the general nonlinear minimization problem. Conjugate gradient methods use updated model vectors which are conjugate versions of each successive gradient vector: this means that the directions of updates are not specified *a priori*, but are determined sequentially as linear combinations of previous direction vectors.

Use of these conjugate directions helps the minimization procedure to make uniform progress towards convergence which is not so important in quadratic problems, but can be of crucial importance in non-quadratic problems (e.g. nonlinear inversion). NLCG method yields an alternative minimization of a nonlinear function directly without making any assumptions about its linearity. It has been implemented by Thompson (1995), Reiter and Rodi (1996) in a nonlinear waveform tomography, and by Matarese (1995) in a nonlinear travelttime tomography.

The framework of NLCG we use is from the Numerical Recipes library (Press *et al.*, 1989). It is outlined as follows:

- (a) Choose  $m_1$ , and set  $g_1 = -\nabla\Psi(m_1)$ ,  $h_1 = Cg_1$
- (b) Find  $\alpha = \alpha_k$  which minimizes  $\Psi_k(\alpha) = \Psi(m_k + \alpha h_k)$
- (c)  $m_{k+1} = m_k + \alpha_k h_k$ ,  $g_{k+1} = -\nabla\Psi(m_{k+1})$
- (d)  $h_{k+1} = Cg_{k+1} + \beta_k h_k$ , where  $\beta_k = \frac{(g_{k+1}-g_k)\cdot(Cg_{k+1})}{(g_k)\cdot(Cg_k)}$

In the algorithm,  $g_k$  is the gradient of the objective functional,  $h_k$  is the direction along which the parameter  $\alpha_k$  is searched to minimize  $\Psi(m_k + \alpha h_k)$ ,  $C$  is a preconditioning operator which we will discuss later, and the formula for  $h_k$  and  $g_k$  above imply the basic CG-relation

$$g_i \cdot h_j = 0, \quad (i \neq j) \quad (2.20)$$

This general NLCG scheme must be modified for use in our resistivity inversion. Two important procedures can aid in the convergence of the algorithm. First, in step (b) there is a line minimization required so as to find a single variable  $\alpha$  which minimizes  $\Psi(m_k + \alpha h_k)$ . At the earlier stage of the iterations, the surface of  $\Psi$  tends to be more distorted due to a relatively large amount of nonlinearity of  $\mathbf{G}$ , while at the later stage of the iterations it becomes more quadratic in the vicinity of the minimum.

This behavior of  $\Psi$  leads us to design a line minimization routine that is adequate for both the earlier and the later iterations. The strategy is: at every iteration  $k$ , try the first step of the line minimization based on a quadratic assumption,  $\alpha = -\Psi'_\alpha/\Psi''_\alpha$ , where  $\Psi'_\alpha$  and  $\Psi''_\alpha$  are the first and the second partial derivatives of  $\Psi$  with respect to  $\alpha$ . After a minimum is bracketed, then estimate the minimum point and estimate its value by using a cubic interpolation. Such a strategy not only would work at the earlier stage of iteration but also would guarantee a rapid quadratic convergence at the later stage of the iterations.

Secondly, we can also aid in the convergence of the algorithm by modifying the gradient direction in some sensible way through some *a priori* knowledge or constraint. This modification process is termed preconditioning: it can take many different forms depending on the problem being solved. A good preconditioner may help to decrease the objective function more quickly in the early iterations. If the problem were linear (quadratic  $\Psi$ ), a perfect preconditioner would be the inverse of the Hessian matrix

$$C = (\nabla^2\Psi)^{-1} = \frac{1}{2}(\mathbf{A}^T\mathbf{R}_{dd}^{-1}\mathbf{A} + \tau\mathbf{L}^T\mathbf{L})^{-1} \quad (2.21)$$

It is probably safe to assume that this preconditioner works well in the nonlinear problem too. However, applying it requires extensive computing resources. Hence we explore an improved preconditioner that approximates Equation 2.21 and can be implemented quickly. We suggest the use of the following formula as our preconditioner,

$$C = (\tau L^T L + \varepsilon I)^{-1} \quad (2.22)$$

where

$$\varepsilon = \frac{(\mathbf{A}u)^T\mathbf{R}_{dd}^{-1}\mathbf{A}u}{u^T u} \quad (2.23)$$

in which

$$u = [\log\rho_0, \log\rho_0, \log\rho_0, \dots, \log\rho_0] \quad (2.24)$$

is an uniform model vector with constant resistivity  $\rho_0$ .

The substitution of Equation 2.23 for Equation 2.21, in fact, maintains the d.c. component of the term  $\mathbf{A}^T \mathbf{R}_{dd}^{-1} \mathbf{A}$ . Numerically, the constant  $\varepsilon$  defined by Equation 2.23 is easy to calculate by integrating Equation 2.12 over the uniform vector  $u$ ,

$$(\mathbf{A}u)_i = (\mathbf{G}(m))_i \quad (2.25)$$

which is the response of the constant model and can be obtained with no computation beyond the forward calculation.

Another important issue needs to be addressed. Because of the strong nonlinearity of the resistivity problem, the objective function  $\Psi$  may have not only a global minimum but also some undesired local minimums. Although both the Gauss-Newton and NLCG methods solve the nonlinear minimization problem and will find a minimum, they can not guarantee that the minimum found is the global minimum. Finding the global minimum is, in general, a very difficult problem. A widely used method is to repeat the algorithm starting from different initial models, find minimums, and then pick the most extreme of them (if they are not all the same) (Press *et al.*, 1992). A faster algorithm will be benefit for this repeating procedure.

### 2.4.3 Numerical Comparison

We conducted a number of convergence tests for the Gauss-Newton and the nonlinear conjugate gradient method using the same synthetic model described above (Figure 2-2). The Gauss-Newton minimization scheme we compared to was developed by Zhang *et al.* (1995). It uses a linear conjugate gradient method for the purpose of efficiently computing the inverse of the Hessian matrix. It does not compute the inverse of Hessian matrix.

Choosing a starting model with a homogeneous resistivity value of  $200 \Omega.m$ , the convergence results for each optimization method are shown in (Figure 2-7). Here 'NLCG' denotes the NLCG method with the improved preconditioner Equation 2.22, 'NLCG-1' denotes the NLCG method without preconditioning ( $C=identity$ ), and 'NLCG-2' denotes the NLCG with the Hessian Equation 2.21. From these results it is clear that the convergence rate of the NLCG method depends strongly on the preconditioner: NLCG is the most efficient method in terms of the CPU time, and NLCG-2 is the least efficient method. We also see that NLCG-2 makes larger decreases in  $\Psi$  per iteration but takes more CPU time. The Gauss-Newton method interpolates between NLCG and NLCG-2. When all of the methods converge, they find the same solution (Figure 2-8).

If the initial model is chosen to be close to the true model ( $m_0 = 50\Omega.m$  inside the conductive block and  $m_0 = 100\Omega.m$  else where), the Gauss-Newton method is as efficient as that of the NLCG method (Figure 2-9). This result demonstrates that the Gauss-Newton method has a fast convergence rate in the neighborhood of the solution. Both methods find the same solution (Figure 2-10).

When the initial model is far from the solution,  $m_0 = 500\Omega.m$ , the NLCG method has a much faster convergence than the Gauss-Newton method (Figure 2-11). Both methods finally find the same solution (Figure 2-12).

## 2.5 Conclusions

In this paper, we have presented a method for solving the nonlinear geoelectrical inverse problem. To deal with the ill-posedness of the problem, the method uses Tikhonov regularization to obtain a solution which has the least structure necessary to fit the data to specified error bonds. We have investigated three different smooth-

ness constraints and concluded that it is necessary to constrain second order spatial derivatives of the resistivity function to obtain smooth, stable solutions. This result can be understood in terms of the sensitivity functions for 3-D resistivity data and the fact that they are singular at source and receiver positions.

To implement Tikhonov regularization numerically, we have developed a fast and efficient algorithm based on conjugate gradient with preconditioning to solve the nonlinear minimization problem. Using a simple preconditioning operator, the NLCG algorithm results in a tremendous time savings over the conventional Gauss-Newton approach, especially when the initial guess is far from the solution.



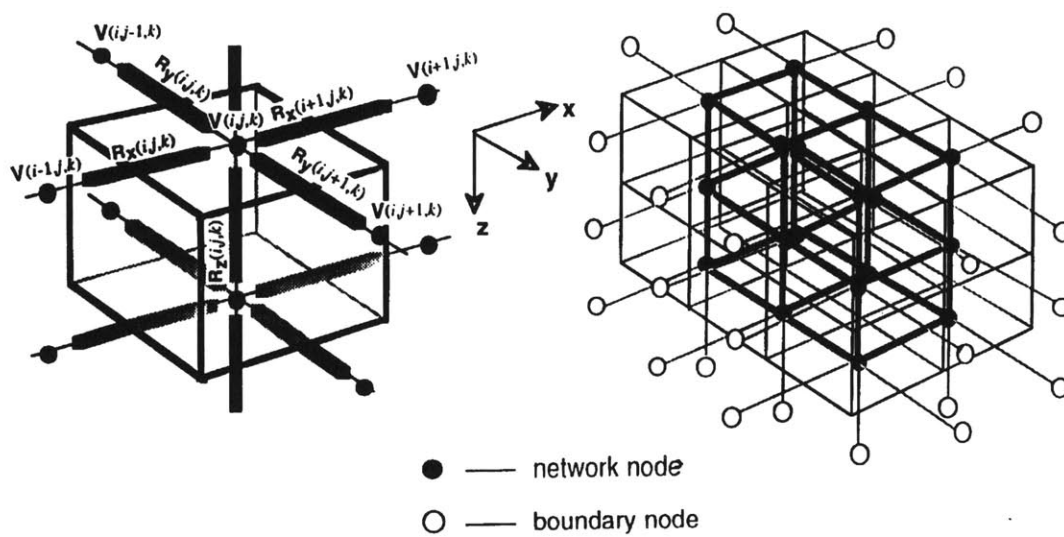


Figure 2-1: The 3-D electrical model is discretized into a network which consists of network nodes, boundary nodes, and impedance branches.

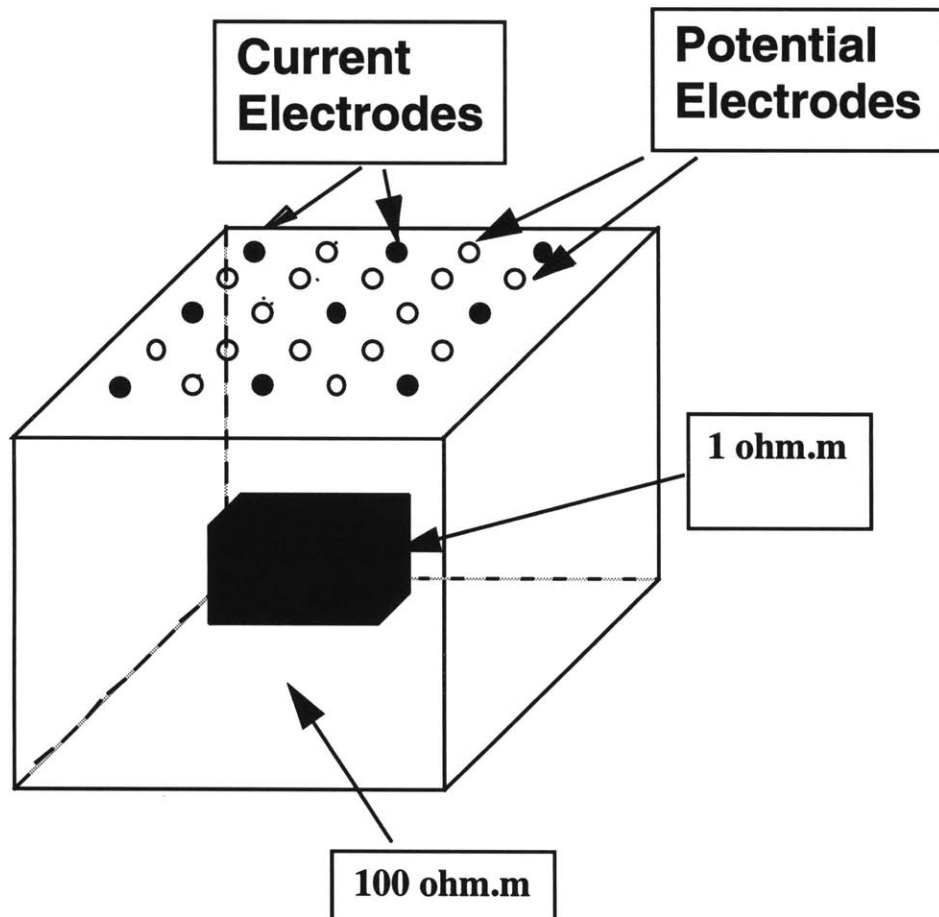


Figure 2-2: The synthetic model consists of a  $7 \times 7 \times 3$  prism ( $\rho = 1 \Omega.m$ ) inside a  $21 \times 21 \times 15$  background ( $\rho = 100 \Omega.m$ ). The data are defined on a  $5 \times 5$  electrode array and comprise 24 potential field measurements for each of nine pole current sources.

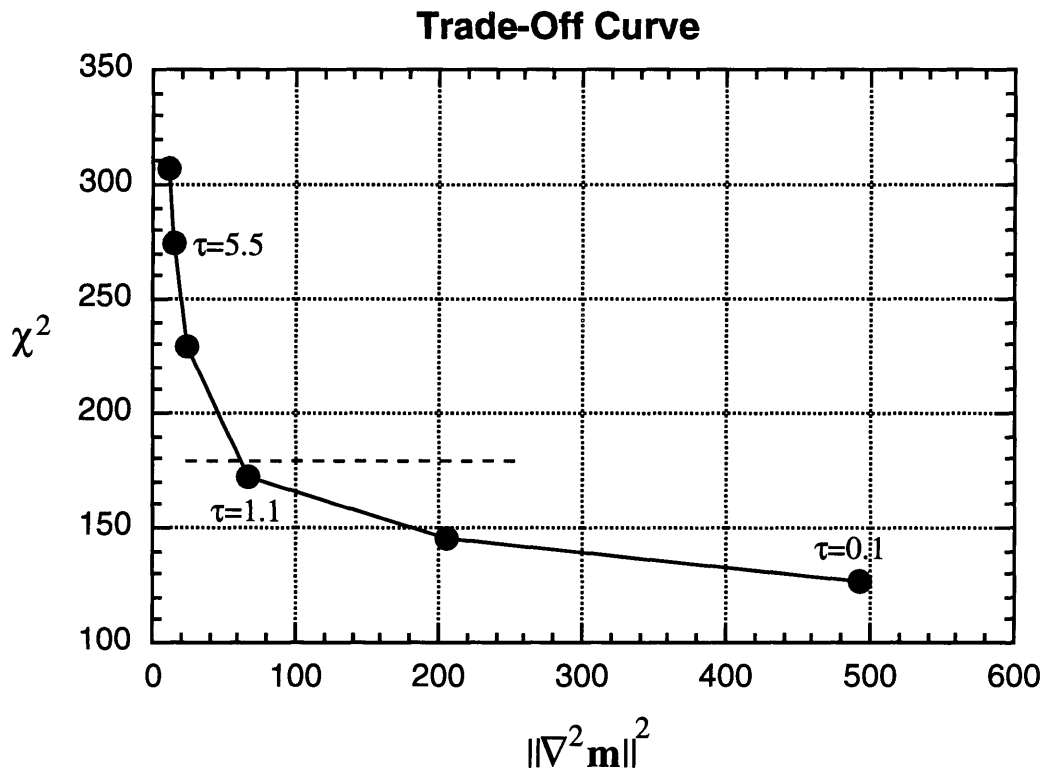
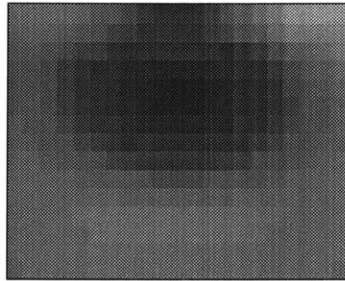


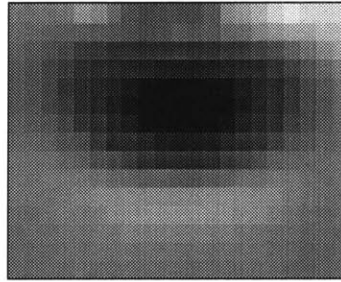
Figure 2-3: This trade-off curve shows how the data misfit balanced by the model roughness. If the model is too smooth, it can not fit the data well. Over-fitting the data will result in a rough model which contains incorrect surface anomalies. An optimum choice is to fit  $\chi^2$  to the number of independent data which, in this case, is 180, indicated by the dashed line.

**Min. Laplacian Solutions Controlled by  $\tau$**

$\tau = 5.5$



$\tau = 1.1$



$\tau = 0.1$

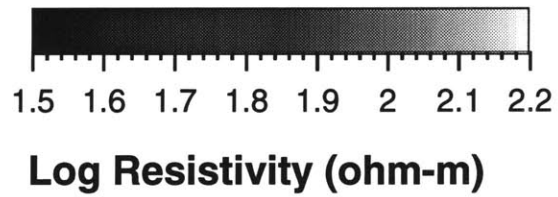
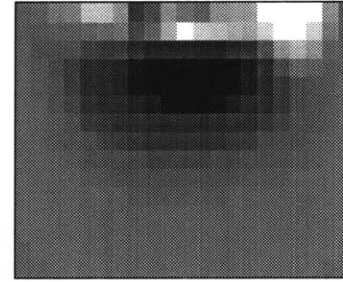


Figure 2-4: Resistivity inversion model for three values of the regularization parameter  $\tau$ .

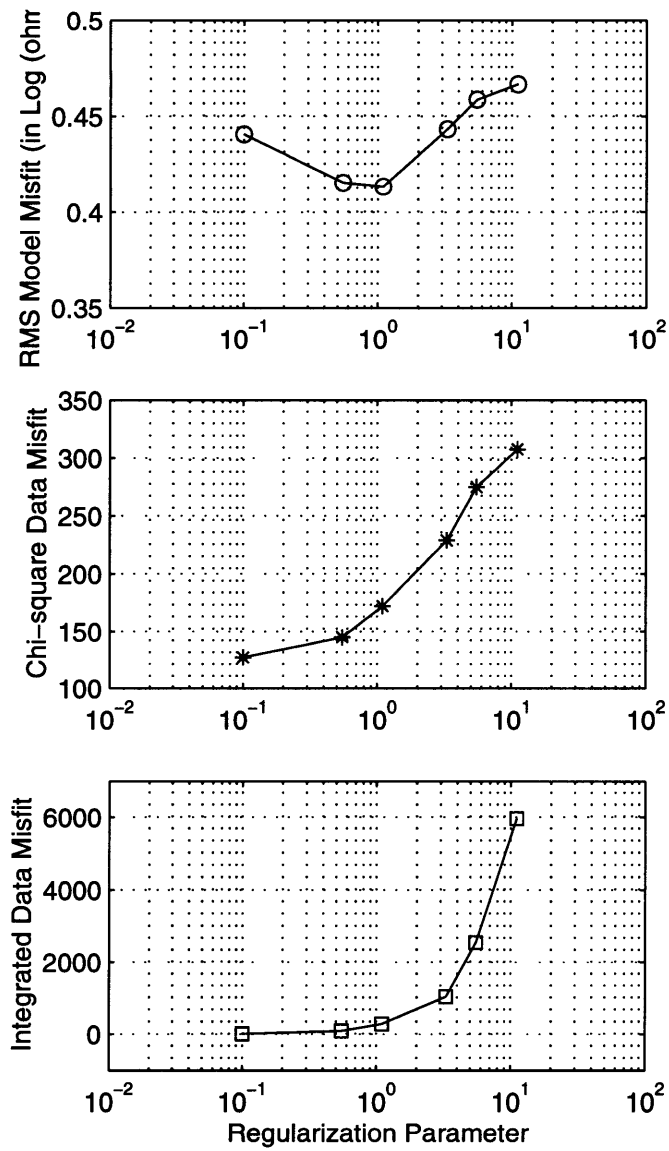


Figure 2-5: A minimum model misfit with the corresponding value of  $\tau = 1.1$  is found in the RMS model misfit curve (top). This  $\tau$  is considered to be an optimum choice. There is a slope change in the data misfit curve (middle). This slope change becomes more clear when the  $\chi^2$  data misfit is integrated with respect to  $\tau$  (bottom).

## Solutions by Three Different Stabilizing Functionals

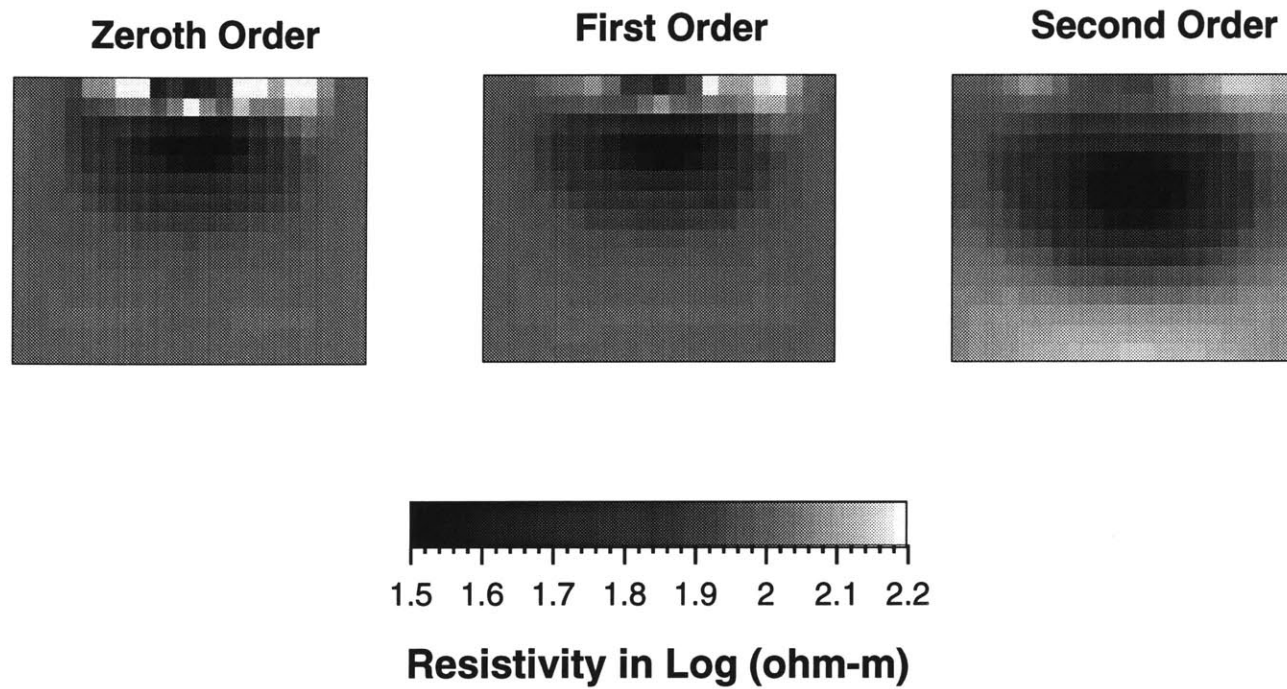


Figure 2-6: Resistivity inversion model for three regularization operators.

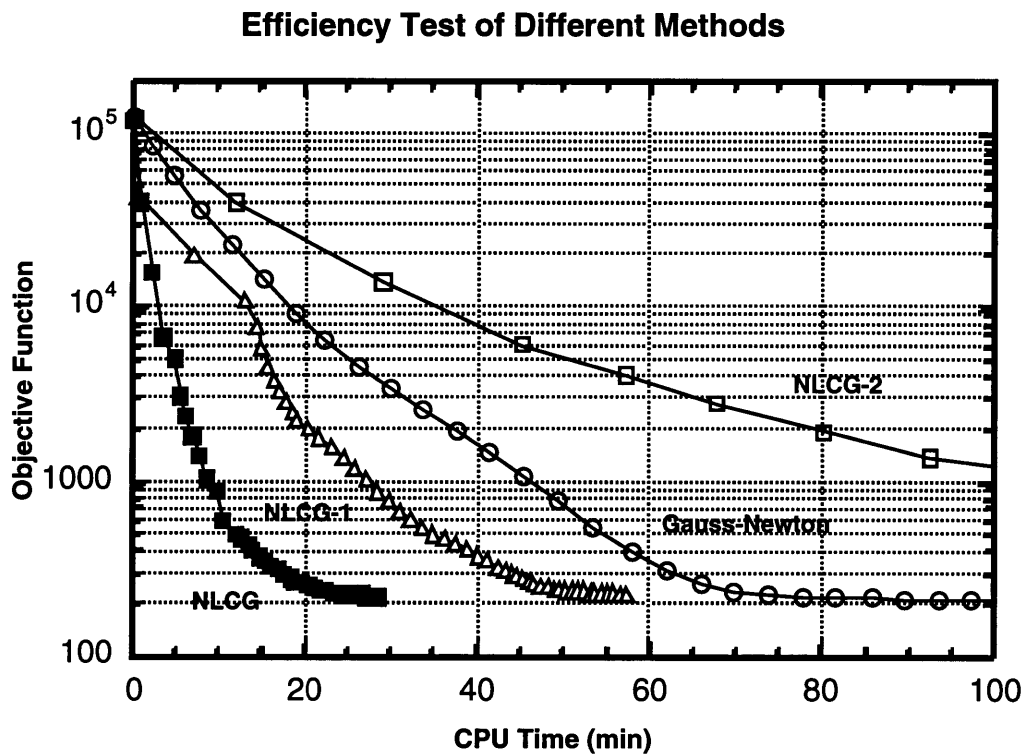


Figure 2-7: NLCG is the most efficient method compared to NLCG-1, NLCG-2, and Gauss-Newton method. NLCG-2 is the least efficient method. The Gauss-Newton method interpolates between them. The initial model for this test is  $m_o = 200\Omega.m$ .

### Solutions by Different Algorithms

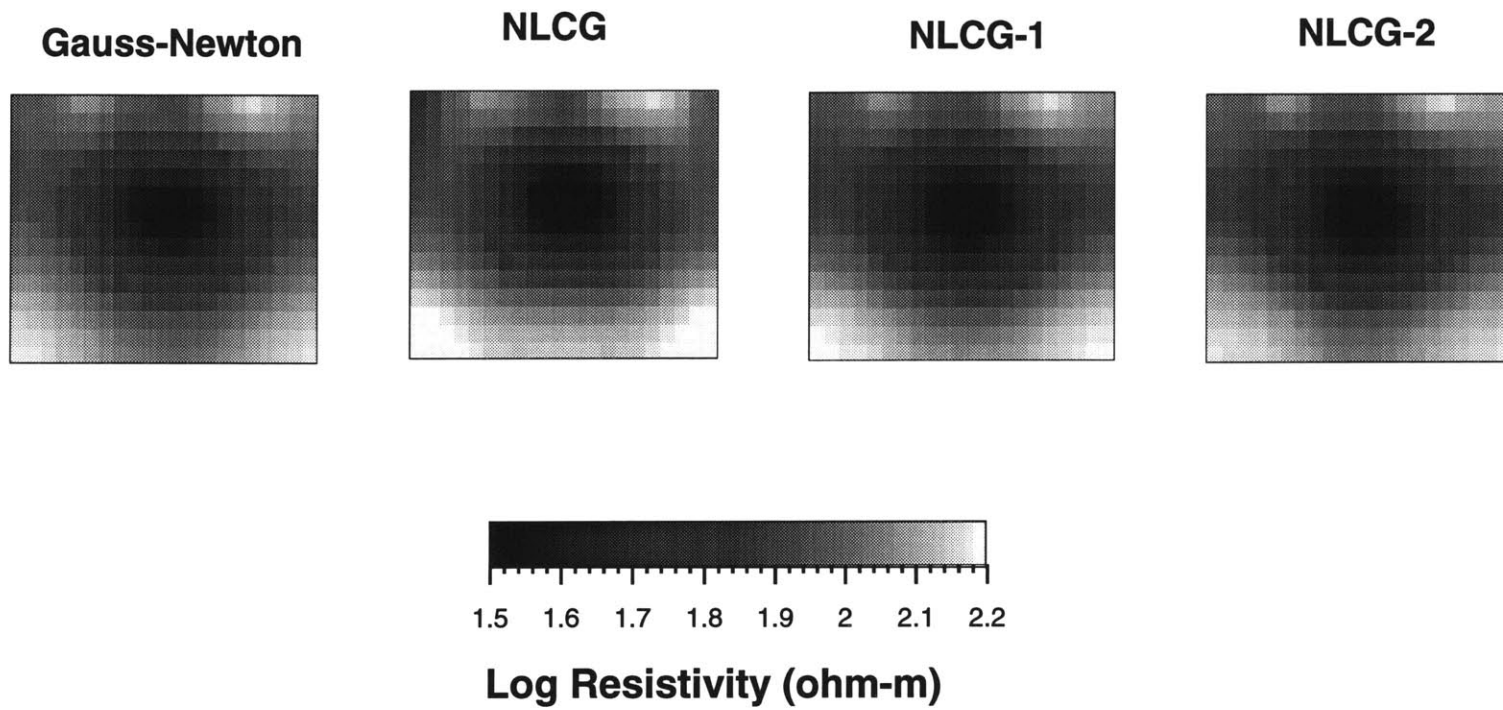


Figure 2-8: All of the algorithms find the same solution using an initial model  $m_o = 200\Omega.m$ . In all of these example,  $\tau = 1.1$ .



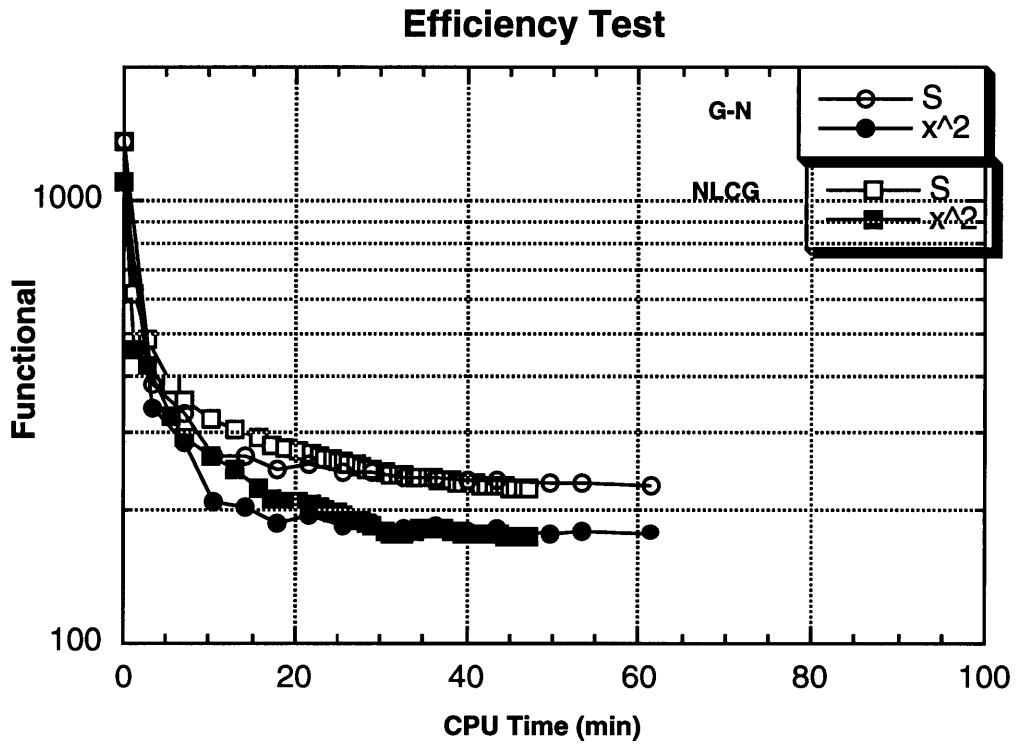


Figure 2-9: When the initial guess is close to the true model, the Gauss-Newton method is about as efficient as the NLCG method. Where 'S' denotes the objective function, and 'x2' denotes the  $\chi^2$ . The initial model for this test is  $m_o = 100\Omega.m$  for the background, and  $m = 50\Omega.m$  for the target.

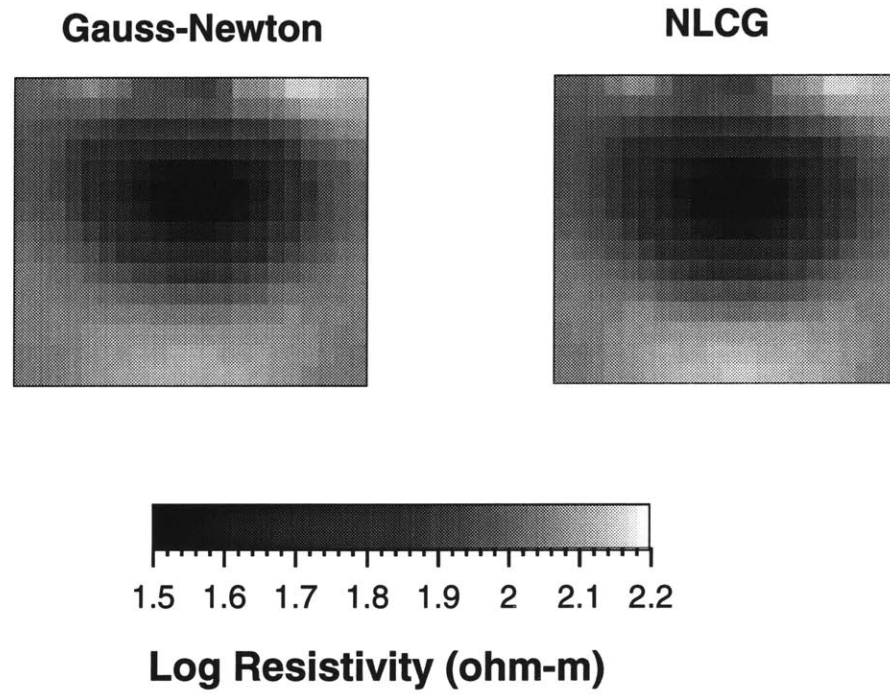


Figure 2-10: All of the algorithms find the same solution using an initial model  $m_o = 200\Omega.m$ .

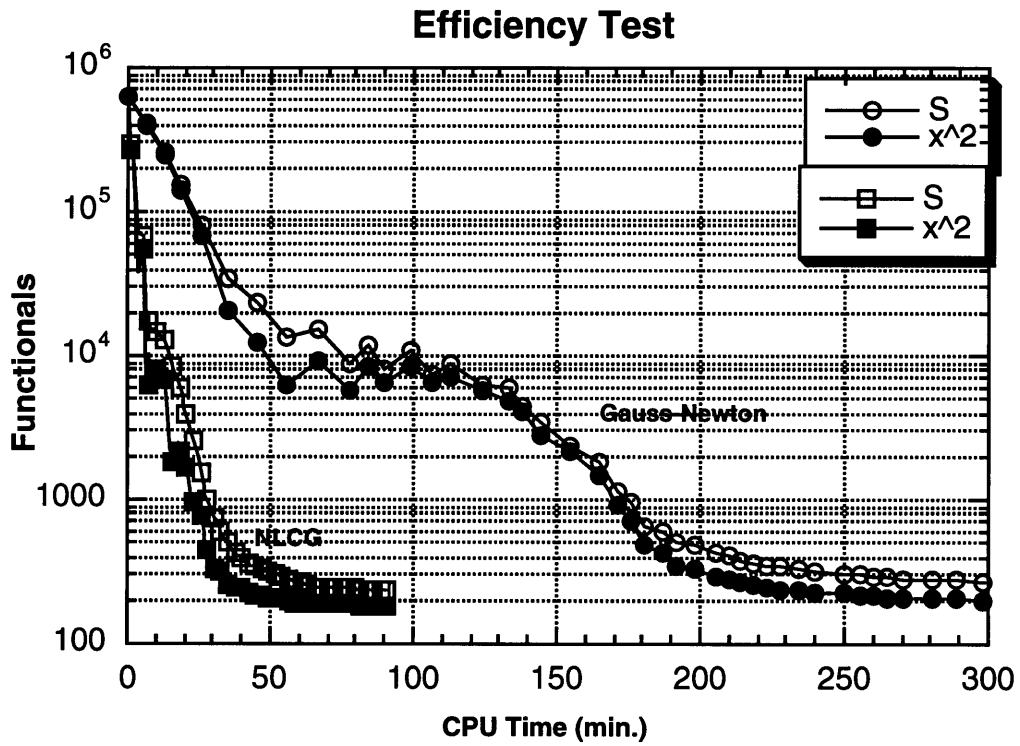


Figure 2-11: For a starting model far from the solution, NLCG is much more efficient than the Gauss-Newton method. The initial model for this test is  $m = 500\Omega.m$ .

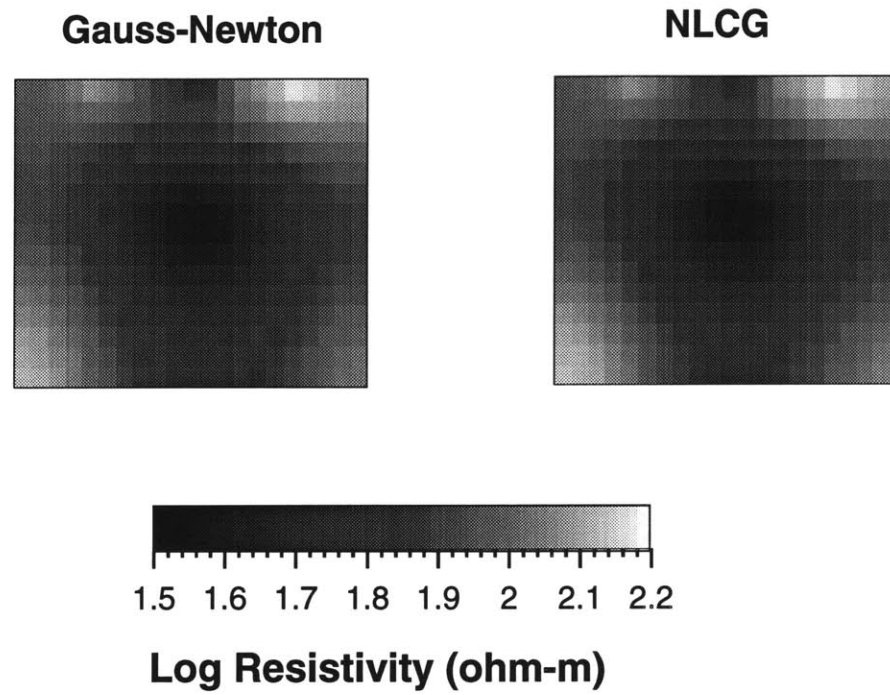


Figure 2-12: All of the algorithms find the same solution using an initial model  $m_o = 500\Omega.m$ .

# Chapter 3

## Inversion of d.c. Electrical Resistivity Data – Applications

### 3.1 Introduction

In this chapter, we demonstrate the practical value of our inversion algorithm developed in chapter 2 by applying it to various field data. The first data sets are collected from an Environmental Protection Agency (EPA) superfund in Woburn, Massachusetts. Using the homogeneous initial model based on surface measurement at selected points, we are able to invert the data for underground resistivity structure. The information is correlated with the ground penetrating radar data and the cone penetrometer. The second experiment is performed in Larderello Geothermal Field in Italy. The objective is to relate the variations in resistivity with position and time to the water re-injection history. In this example, since we are interested in the electrical resistivity change between different times during the re-injection, we modify the inversion procedure to efficiently calculate the resistivity change through the linearization

about a base model. We then compare the inversion result to the ones obtained by a nonlinear inversion procedure. The third experiment is performed in Barbados, West Indies. The objective of the study is to detect underground limestone caves in an effort to understand the cavern structure and thus facilitate surface construction activities. We invert data from this experiment and show that our resistivity tomography technique can be very useful for mapping caves or other underground facilities mapping. The results not only recover the existing cave locations and sizes but also indicate some new undiscovered cavern systems in the area.

## **3.2 Imaging Aberjona Contamination Site**

### **3.2.1 Introduction**

The Aberjona Watershed is located in eastern Massachusetts (Figure 3-1) in the town of Woburn. The area has a history of industrial contamination dating back to the beginning of the century. Industries, including leather tanning, metal cleaning and automobile salvage yards, dumped waste into the ground and contaminated the ground water with high concentrations of chemicals, including chloroform, perchloroethylene (PCE), trichloroethane, and trichloroethylene (TCE). The area was designated as a U.S. Environmental Protection Agency superfund site in 1982, and has become the focus of numerous environmental investigations.

The subsurface geology of the Aberjona Watershed is characterized by glacial outwash and till deposits. The Aberjona Valley was formed by glacial movement and runs beneath the main branch of the Aberjona River. The valley that forms the transmissive regions of the aquifer to a depth of over 100 feet is filled with glacial outwash consisting of fine to medium sands with traces of silt at shallow depth, and

medium to coarse sand and gravel as the depth increases. Previous studies also indicated a peat layer overlaying the stratified sand deposits extending over a large area with thickness ranging from 2 to 7 feet (U.S.G.S., 1989).

Our study site (marked inside the square in Figure 3-1) is located near the Well H region of the Aberjona River. Our interest focuses on characterizing the soil around the river in an effort to understand the transport mechanisms been involved in the contamination of drinking water. Before our resistivity survey, other geophysical investigations were conducted in the area, including ground penetrating radar and cone penetrometer surveys (Zeeb *et al.*, 1994). The goal of the resistivity survey is to correlate soil properties with those investigations and to extend the sparse ground truth information into a 3-D map of the stratigraphy of the region.

We performed the electrical resistivity survey at the site in March 1995. Figure 3-2 shows the electrode configuration for the experiment. There are 80 electrodes placed at 25 ft intervals in an 8x10 array on the surface, covering a 175 ft by 225 ft area. Electric current is injected one at a time into 30 of the electrodes with the negative end of the current placed 1000 feet south of the Well H. Potential differences are measured between each of the remaining electrodes and a point adjacent to the current electrode. A total of 2340 potential differences are thus obtained.

### **3.2.2 Inversion Results**

Our 3-D inversion model is defined over a 26x24x20 grid of cells covering a volume beneath the electrode array. To construct a starting model, surface resistivity information is used. As one can see from Figure 3-2, a part of the Aberjona River meanders its way southward about 100 feet west of the Well H. The river is built into the starting model by assigning an initial resistivity value of 10  $\Omega\text{m}$  to cells traversed

by the path of the river. In the rest of the area resistivity values of surface soil samples are measured and their mean value,  $65 \Omega\text{m}$ , is assigned to the remaining cells of the starting model. The NLCG algorithm is used to compute a minimum-Laplacian, 3-D model that fits the data. The NLCG algorithm requires less than two hours of computing time on a DEC alpha workstation to find the solution. We regenerate the same solution with the Gauss-Newton algorithm, which required more than ten hours of CPU time. The efficiency of the computation using the Gauss-Newton method and the Nonlinear Conjugate Gradient is shown in Figure 3-3.

Figure 3-4 and Figure 3-5 show our 3-D resistivity inversion model as vertical and horizontal cross-sections. The results depict a resistive zone at 20 feet below the surface, dipping from southeast to northwest. Above the resistive zone is a bowl-shaped conductive zone. To verify the robustness of this bowl-shaped zone, we take a 2-layer model as our *a priori* model and see if the inversion results will be consistent with this chosen model. We see that the model shown in Figure 3-6 reveals a similar bowl-shaped structure in the upper half of the model. This common property shared by both models should be given high confidence.

In order to interpret the physical soil types, a vertical cone penetrometer profile obtained at a site 75 feet west of Well H is used to correlate the resistivity results. The penetrometer results are shown in Figure 3-7. The cone penetrometer response indicates somewhat more detailed soil types at shallow depth. Except for a region of organic peat layers directly below the surface, there is a section comprising brown, spongy material that has a high water content (80% water by weight) and contains almost no organic matter. This section is found to be diatomaceous earth which consists primarily of siliceous skeletons of diatom-microscopic. Because of high porosity (generally 70–90%) resulting in high water content, the diatomaceous earth section appears to be very conductive. Adjacent to the bowl-shaped lower boundary of the diatomaceous earth is, as expected, a glacial sand layer which is quite resistive. The



boundary between the conductive zone (peats and diatomaceous earth) and the resistive zone (sand), as indicated by the 3-D resistivity inversion model, is strongly consistent with the cone penetrometer results. However, due to their limited resolving power (e.g. interval between each of the electrodes is 25 ft), the resistivity data cannot delineate heterogeneity within the conductive zone, i.e. different thin peat layers and the diatomaceous earth section.

The resistivity results are in strong agreement with GPR (ground penetrating radar) experiments at the site (Cist *et al*, 1995). Figure 3-8 and Figure 3-9 compare two vertical GPR sections with a corresponding vertical cross-section of the 3-D resistivity inversion model. From these plots, one can see that the shape of the boundary between the diatomaceous earth and the sand layer is in good agreement between the two experiments. Below this interface, the GPR section is dominated by ringing effects of the antennas, whereas the resistivity model detects vertical and lateral variations in electrical resistivity. This result indicates that the resistivity method has great advantages in resolving structures at depths unattainable by either GPR method or cone penetrometer.

### **3.2.3 Conclusion**

We have successfully applied our 3-D resistivity inversion algorithm to an actual resistivity field survey in the Aberjona Watershed, Woburn, Massachusetts. Our 3-D resistivity image indicates two major layers of the site: a shallow conductive layer composed of thin peat beds and diatomaceous earth overlying a resistive layer of glacial sands. The top of the sand layer is approximately 20 feet deep and dips from southeast to northwest. These results are strongly correlated with other geophysical data from the site such as cone penetrometer and GPR measurements. Thus, the resistivity experiment succeeds in extending these sparse measurements into a 3-D

stratigraphic model, which adds valuable information about the transport of contaminants in the Aberjona Watershed.

## 3.3 Imaging Larderello Geothermal Field

### 3.3.1 Introduction

The Valle Secolo geothermal region in the Larderello Geothermal Field (Figure 3-10) in Tuscan region of Italy is a vapor-dominated, hydrothermal type that produces steam primarily from shallow, highly fractured Tuscan Anhydrites at a depth of a few hundred to 3000 meters (Allegrini *et al.*, 1995; Dini, 1989; Batini *et al.*, 1985; Ferrara *et al.*, 1985; Block, 1991). Intensive exploitation in this area caused a sharp decline in the fluid storage of the reservoir and depleted the reservoir pressure. For environmental and economic reasons, starting in 1984, re-injections of water discharged from power plants became an important part of the exploitation strategy for this area. It has been confirmed that a large portion of the re-injected water has been converted into super-heated steam, with a significant increase in both the steam flow-rate and the reservoir pressure (Cappetti *et al.*, 1995).

In the last few years the re-injection rate has been steadily increased. Whether such an increment of re-injection is sustainable, or if it could gradually modify the natural hydrostatic equilibrium provoking liquid phase storage inside the reservoir, remains a question. In order to monitor the re-injection, and particularly to locate the possible presence of liquid accumulation caused by the re-injection, geoelectrical monitoring surveys have been performed by ENEL (Ente Nazionale per L'Energia Elettrica) of Italy.

The surveys were carried out in a two-phase procedure. Phase 1, which took place in the winter of 1991, was carried out under the existing conditions of re-injection and exploitation. Phase 2, which took place 18 months later, was carried out with the same layouts of electrodes, following a steady increment of re-injections in the period between phase 1 and phase 2.

The purpose of this work is to present the results of the geoelectrical monitoring survey by applying a 3-D electrical resistivity tomography technique.

### **3.3.2 Geoelectrical Survey at Larderello-Valle Secolo**

The electrical resistivity data are collected in the vicinity of injection wells 138, 140, 94, 119, etc., inside a 2.2 x 2.8 ( $km^2$ ) area. Figure 3-11 shows the study area, the locations of the nearby wells, and the coordinates that will be used in the later inversion analysis.

A vertical cross-section, displayed in Figure 3-12, shows the local geological stratigraphy. Under the recent sediments, the geological structure is primarily characterized by a three-layer model. The main upper layer is a thick flysch. The middle layer, overlain by a high permeable zone, is a Tectonic Wedges complex mainly constituted by Anhydrites and limestones. The deepest layer is the metamorphic basement consisting of Phyllites and quartzites.

Three types of electrical measurements are conducted in both phase 1 and phase 2:

- Electrical potential measurements between the injection well 140 and the surrounding area, with a dipole current source located at S. Dalmazio 4 and well 134.

- Electrical potential measurements between the injection well 140 and the surrounding area, with a dipole current source located at Colline 3 and well 134.
- Electrical apparent resistivity measurements between wells and at the surface on a ‘rectangle’ configuration. The dipole current source is located at Colline 3 and S. Dalmazio 4.

Field instrumentation is calibrated carefully in order to reduce any internal and external sources of noise. The total percentage error of the measurement is estimated to be no greater than 4 percent (ENEL report, 1995). We present here a portion of the electrical potential and apparent resistivity measurements results Figure 3-13, Figure 3-14, and Figure 3-15.

Between the 1991 and 1993 surveys, a large decrease of about 15-20% in potential values are observed. There is also a strong reduction of the apparent resistivity values across the entire area under examination. In the next section we will describe how these data can be inverted to recover a three dimensional subsurface resistivity distribution by using a 3-D resistivity inversion technique.

### 3.3.3 Inversion Procedure

Resistivity surveys inject current into the ground via a positive and negative electrode and the source current density can be written

$$j(x, y, z) = J_0 [e_+(x, y, z) - e_-(x, y, z)] \quad (3.1)$$

where  $J_0$  is the total source current and where  $e_+$  and  $e_-$  represent the spatial distribution of the two electrodes. Typically, each electrode is small compared to the spacing between electrodes and  $e_+$  and  $e_-$  are each taken to be concentrated at a

point, e.g.,

$$e_+(x, y, z) = \delta(x - x_0)\delta(y - y_0)\delta(z - z_0) \quad (3.2)$$

where  $(x_0, y_0, z_0)$  is the electrode position, and  $\delta$  is the Dirac distribution. In the present study, some of the data are obtained using steel well-casings as electrodes. Since the well casings extend to several hundred meters or more in depth, we model them as vertical line distributions of finite length, e.g.

$$e_+(x, y, z) = \delta(x - x_0)\delta(y - y_0) [H(z - z_1) - H(z - z_2)] / (z_2 - z_1) \quad (3.3)$$

where  $H$  is the Heaviside function,  $z_1$  and  $z_2$  are the minimum and maximum depth of the casing, respectively.

Similarly, a potential field measurement,  $d$ , is the difference between the voltages sampled by two “receiver” electrodes:

$$d = \int e_+(x, y, z)v(x, y, z) dx dy dz - \int e_-(x, y, z)v(x, y, z) dx dy dz \quad (3.4)$$

where again  $e_+$  and  $e_-$  denote electrode distributions. As with the source, the receiver electrodes are usually concentrated at points, but in the present study, some are well casings. In the latter case,  $e_+$  and  $e_-$  are taken as vertical line distributions as in Equation 3.3.

In the present study we have two data sets,  $d^{(1)}$  and  $d^{(2)}$ , corresponding to two resistivity surveys at different times. The resistivity models for the two surveys,  $m^{(1)}$  and  $m^{(2)}$ , may be different. Of particular interest is the change in resistivity between the two surveys, i.e.,

$$\delta m(x, y, z) = m^{(2)}(x, y, z) - m^{(1)}(x, y, z) = \log \frac{\rho^{(2)}(x, y, z)}{\rho^{(1)}(x, y, z)}. \quad (3.5)$$

Here we outline two methods for estimating  $\delta m$ . Both methods assume that a non-linear inversion of the first data set is performed to yield a model  $\widehat{m}^{(1)}$ :

$$\|d^{(1)} - \mathbf{G}(\widehat{m}^{(1)})\|^2 + \tau \|\mathbf{L}\widehat{m}^{(1)}\|^2 = \text{minimum}. \quad (3.6)$$

The methods differ in how they obtain a second model,  $\widehat{m}^{(2)}$ , and the model change,  $\widehat{\delta m}$ .

**Method 1: Separate, Nonlinear Inversion.** In this method, we simply perform a nonlinear inversion of the second data set to obtain a second model,  $\widehat{m}^{(2)}$ , and then let  $\widehat{\delta m} = \widehat{m}^{(2)} - \widehat{m}^{(1)}$ . Thus, the second model satisfies

$$\|d^{(2)} - \mathbf{G}(\widehat{m}^{(2)})\|^2 + \tau \|\mathbf{L}\widehat{m}^{(2)}\|^2 = \text{minimum}. \quad (3.7)$$

**Method 2: Coupled, Nonlinear Inversion.** The model  $\widehat{m}^{(2)}$  resulting from Method 1 is constrained to be smooth but is not directly constrained to be similar to  $\widehat{m}^{(1)}$ . In Method 2 we modify the model roughness penalty function to include  $\widehat{m}^{(1)}$  as a *a priori* model. The minimization criterion is

$$\|d^{(2)} - \mathbf{G}(\widehat{m}^{(2)})\|^2 + \tau \|\mathbf{L}(\widehat{m}^{(2)} - \widehat{m}^{(1)})\|^2 = \text{minimum}. \quad (3.8)$$

Note, this approach is only valid if the time interval between measurements is small compared to a characteristic time scale for change in the flow system.

**Linearization** If  $\delta m$  is not too large, the above methods can be performed with the forward modeling operator,  $\mathbf{G}$ , replaced by its first order approximation about  $\widehat{m}^{(1)}$ . Let  $\mathbf{A}^{(1)}$  be the first-order derivative of  $\mathbf{G}$  evaluated at  $m = \widehat{m}^{(1)}$ . Then the first order approximation is

$$\mathbf{G}(\widehat{m}) \approx \mathbf{G}(\widehat{m}^{(1)}) + \mathbf{A}^{(1)}(\widehat{m} - \widehat{m}^{(1)}). \quad (3.9)$$

Using this approximation, the minimization problems in Methods 1 and 2 reduce to the solution of linear systems.

When the linear approximation in Equation 3.9 is used, it is natural to re-couch each method in terms of a minimization with respect to  $\widehat{\delta m}$ . For Method 1, we have

$$\|d^{(2)} - \mathbf{G}(\widehat{m}^{(1)}) - \mathbf{A}\widehat{\delta m}\|^2 + \tau\|\mathbf{L}(\widehat{m}^{(1)} + \widehat{\delta m})\|^2 = \text{minimum.} \quad (3.10)$$

For Method 2:

$$\|d^{(2)} - \mathbf{G}(\widehat{m}^{(1)}) + \mathbf{A}\widehat{\delta m}\|^2 + \tau\|\mathbf{L}\widehat{\delta m}\|^2 = \text{minimum.} \quad (3.11)$$

### 3.3.4 Inversion Results and Interpretation

Our 3-D inversion model is defined over a 26x36x17 grid of cells covering a volume of 2.2x2.8x1.5  $km^3$  beneath the injection area. A three-layer starting model for the inversion iterations is developed using available geologic data. In this Larderello application we input *a priori* information into the final inversion via the MT measurement. These include the bottom topography of the flysch layer, and the average resistivity values for each of the layers (i.e.,  $\rho_0 = 20\Omega.m$  for the flysch;  $\rho_0 = 200\Omega.m$  for the Tectonic Wedges;  $\rho_0 = 200\Omega.m$  for the metamorphic basement) obtained from an MT survey (Rieven *et al.*, 1995; Fiordelisi *et al.*, 1995).

Figure 3-16 shows our 3-D resistivity inversion model as vertical and horizontal cross-sections of phase 1. The primary resistivity variations in the Larderello-Valle Secolo geothermal field seem to be of structural origin. However, the results depict a conductive zone at a depth of 700 meters, starting from the location of well 140, diffusing towards the north-west direction. This feature is not structurally related and therefore may indicate a zone of high permeability or high water saturation assumed to be related to the injection history.

Inversions of resistivity using data from the phase 2 survey are computed by the two inversion methods described in the last section. Figure 3-17 and Figure 3-18

present the results of the changes in resistivity between the two surveys. The results clearly indicate a large decrease of the resistivity values across the northeastern part of the survey area. Most resistivity changes have taken place either inside the flysch or at the interface between the flysch and the Tectonic Wedges. Little or no variation is observed below a depth of 750 m where the transition to the Tectonic Wedges is complete. The correlation of high conductive anomalies near the northern part of the survey area from phase 1 to phase 2 suggests that this area may have high permeability, and/or high water saturation. Comparison of the anomaly in Figure 3-16, Figure 3-17, and Figure 3-18 indicates a change of the diffusion directions from phase 1 to phase 2. This feature most likely relates to the increment of the re-injection, indicating a possible modest water accumulation in this area.

### **3.3.5 Conclusions**

We have presented a method for monitoring changes in subsurface electrical resistivity caused by the movement of water and the conversion of water to steam in the Larderello-Valle Secolo geothermal field. Comparisons of the resistivity anomalies obtained from two surveys conducted in 1991 and 1993 indicate a correlation between the changes in resistivity and the water re-injection history. The results show that it is possible to evaluate and detect the re-injection of fluid through the systematic observation of electrical resistivity at the site.



## **3.4 Imaging A Limestone Cavern System in Barbados, West Indies**

### **3.4.1 Introduction**

Delineation of underground cavities has been a challenging problem for exploration geophysicists. The problem continues to be relevant today as the discovery of more underground cavities or tunnels is important to domestic and military interests. Many geophysical methods have been employed for cave structure investigation including the electrical resistivity method. Traditionally, electrical resistivity surveys were designed with soundings, profilings, or pseudo-section interpretations. These methods cannot yield a complete or accurate image of the subsurface structure. Today, faster computer resources and the development of robust inversion techniques have made the use of tomography technology possible, this advance can, in theory, improve the recovery of the complete underground structure. In this section, we will apply the resistivity tomography to map an underground limestone cave system in Barbados, West Indies.

Barbados is a small island located in the east of the Caribbean Sea (Figure 3-19). The island has been formed by progressive uplifting of a great thickness of sediment. Most of the island is covered by coral limestone with a thickness about 90 meters. Harrison cave is located in the center of the island. The purpose of the geophysical survey in this area is to investigate the structure of the caves, and to delineate any unknown caverns that might be suitable for future public development.

### 3.4.2 Data Acquisition

A 2-D resistivity tomography survey employs a series of electrodes laid out in a straight line with a constant electrode spacing. We used the ELREC T resistivity meter produced by IRIS Instruments for data recording. The resistivity meter is connected to an intelligent node system in which the active electrodes can be selected automatically to vary source and receiver dipole spacing for each measurement. The measurement is made automatically through the control of a microprocessor, automatic self potential correction, and temporal stacking signal enhancement. The internal memory store the electrical data as well as station number and position of electrode.

A total of three electrical resistivity tomography lines were acquired (Figure 3-20). Line A is 90 meters long, located in the general vicinity of the Cascade Pool. Line B is on top of the Great Hall with a length of approximately 80 meters long. Line C is about 160 meters and is perpendicular to line B. Line A and line B contain 20 electrodes placed at 5 meter intervals. Line C deploys two sets of 20 electrode arrays which are overlapped by 30 meters to cover a total length of 160 meters. The data acquisition was performed on a dipole-dipole tomographic electrode configuration (see Chapter 7). This data acquisition geometry guarantees an evenly distributed sensitivity across the whole region. The inversion model for each electrode array is defined over a 46x26 grid of cells covering a cross-section beneath the electrode array. A homogeneous starting model was chosen for the inversion.

### 3.4.3 Inversion Results

Figure 3-21 shows the resistivity inversion results of line B. This is our best calibrated line because there is a borehole connecting the Great Hall next to our survey line.

The resistivity image shows two large cave systems possibly connected by a narrow route. Because this line is known to be directly over the Great Hall by existing borehole data, the cave on the left is confirmed to be the Great Hall by comparison with actual shape of the cave. Notice the indication in the resistivity image of a fracture or a high porosity path (on the left corner) rising toward the surface.

As shown earlier, in order to obtain a stable solution the minimum structure approach employs a spatial smoothness constraint in the inversion. Such an approach results in diffused or blurred boundaries between the cavern system and the surrounding environment. To better establish true cave shapes we employ a method that qualitatively predicts the anomaly's geometry suggested by Beard and Morgan (1991). This method determines a cut off resistivity value. Any resistivity value less than the cut off value is shaded by blue, and resistivity values higher (resistive zone) than the cut off value is shaded by yellow. The cut off resistivity value  $\rho_{cut}$  is determined by,

$$\rho_{cut} = 10^{x_h - \Delta x} \quad (3.12)$$

and

$$\Delta x = (x_h - x_l)/a \quad (3.13)$$

where  $x_h$  and  $x_l$  denote the highest and the lowest logarithmic resistivity values respectively, and  $a$  is a coefficient which controls the size of the shaded anomaly. Resistive anomalies associated with a large  $a$  tend to have more compressed shape than the ones that are associated the a small  $a$ . An optimal  $a$  is usually obtained by numerical exercise. Through numerical tests using identical data acquisition and model geometry, we find that  $a = 8$  gives the best estimate of a resistive anomaly's size for our case. Using this approach, our best estimate of sizes and locations of caverns in line B is displayed also in Figure 3-21.

Recall that line C is perpendicular to line B. The resistivity data of line C is

gathered in two overlapping sections and then combined in a single image. The inversion result (Figure 3-22) shows a broad region of high resistivity, however, three distinct cave systems can be identified. The cave to the left is probably a cross-over of the cave system going out to the Rotunda Room. The anomaly in the middle is assumed to be the passage of the known cave system. The large anomaly to the right in the figure is in close proximity to the natural entrance system. One interpretation is that there is a large significant cave at this position. These assumptions can only be tested through a more intensive survey which will be planned for the future. Note the distinct high resistivity features extending from the top of the large cave toward the surface. We interpret these as high porosity chimneys connecting the cave with the surface or near-surface. These anomalies are far too high in amplitude to be considered artifacts.

The location of line A has a very complicated topographic feature, our survey line is sited almost at the bottom of a valley. This line has a possible connection to another cavern system, the Cole's cave, which is in the west of the Harrison's cave. The inversion result (Figure 3-23) depicts a conductive feature centered at a high resistivity region shown on the right. There is also a small feature in the upper left, it is hoped that future investigations will clarify these anomalies.

#### **3.4.4 Conclusion**

The d.c. resistivity tomography has been applied to the delineation of a limestone cave system in Barbados. The inversion successfully identifies the known caves, and a new, previously undiscovered cave. However, from our known knowledge of Harrison's cave the inversion suffers from a bias which tends to locate the caves at a shallower depth and to exaggerate their size. Improvements can be made by combining resistivity with other geophysical methods, such as gravity, GPR or seismic methods.

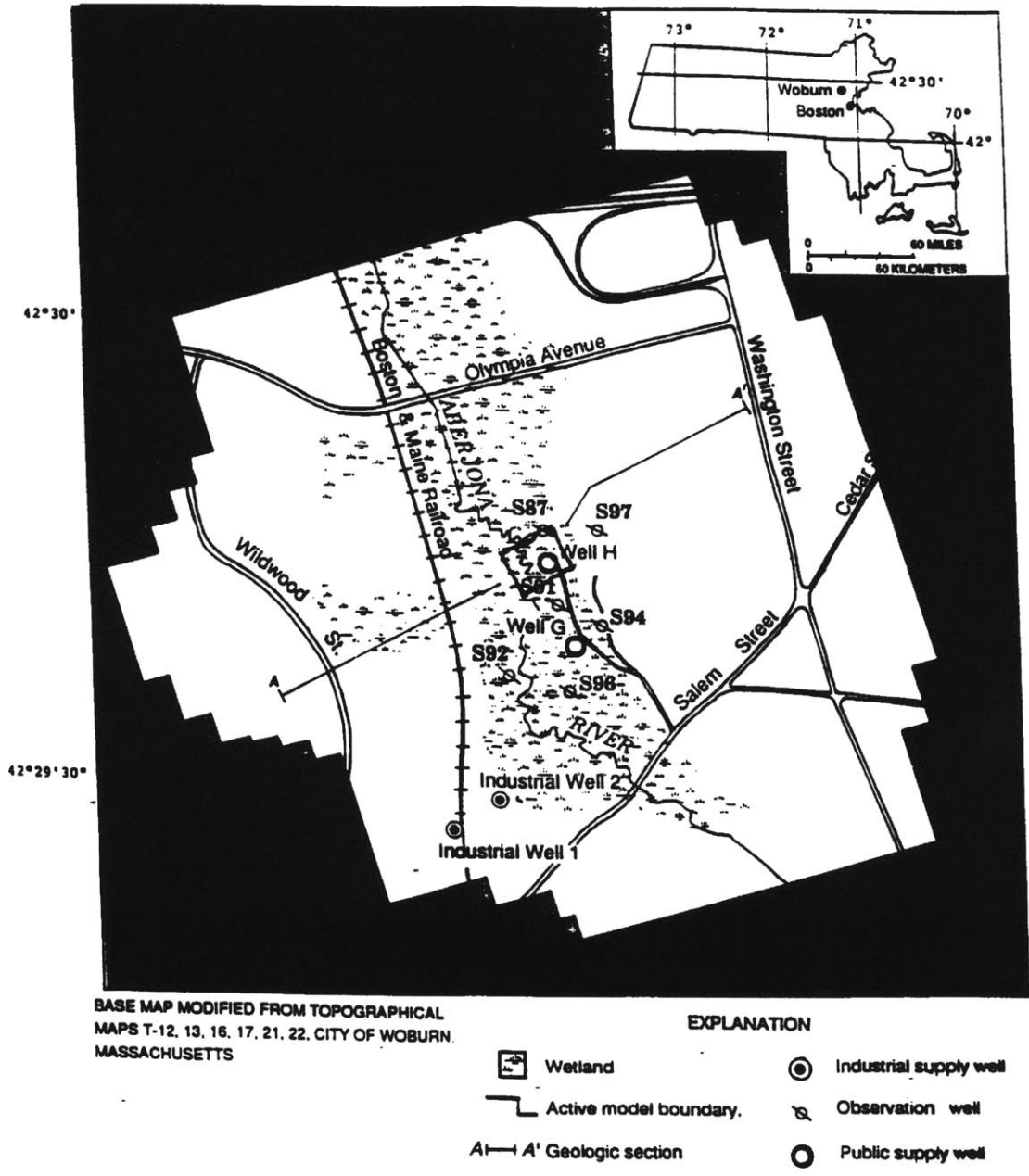


Figure 3-1: The Aberjona Watershed is located in eastern Massachusetts. Our experiment site (indicated by the small square) is located near the Well H region of the Aberjona River in the town of Woburn, ten miles north of Boston (Modified from USGS report, 1989).

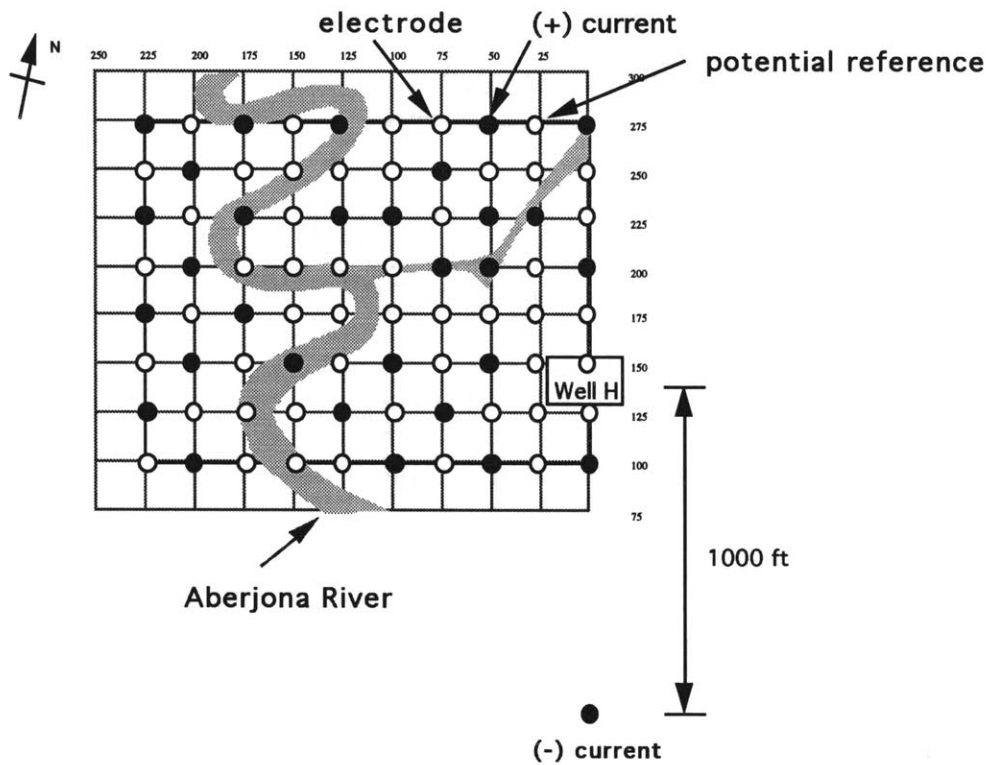


Figure 3-2: The resistivity experiment deploys 80 electrodes in the Well H region, 30 of them are used as the current electrodes. The negative current electrode is 1000 ft south of the Well H. The potential differences are measured with respect to a point which is adjacent to the current electrode

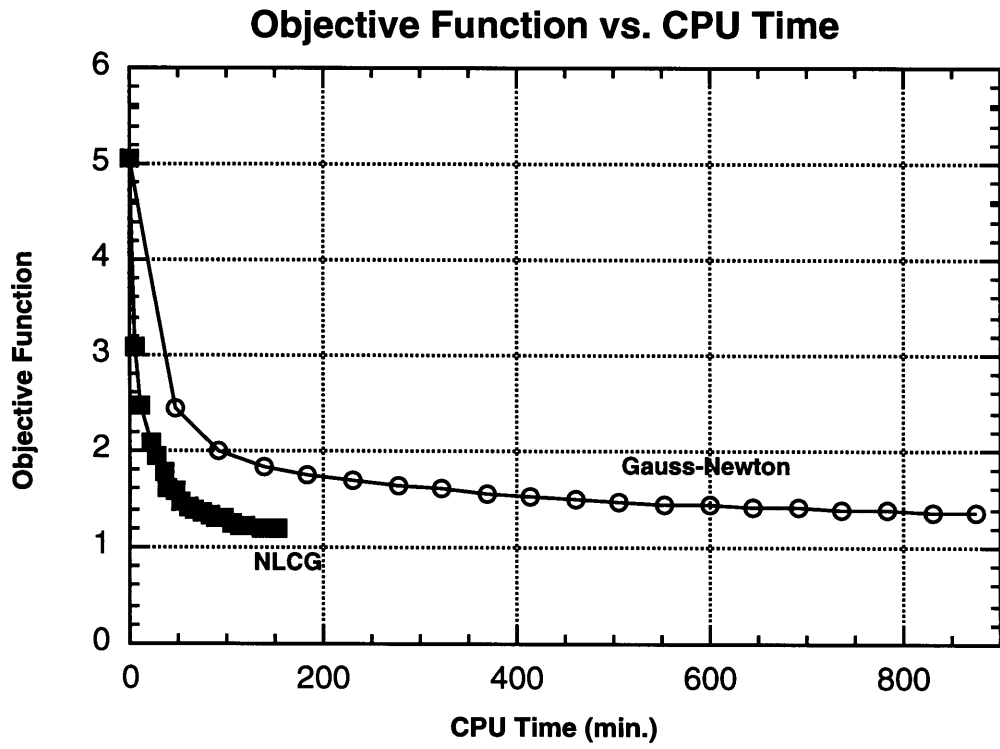


Figure 3-3: NLCG is ten times faster than the Gauss-Newton method for the Aberjona data set.

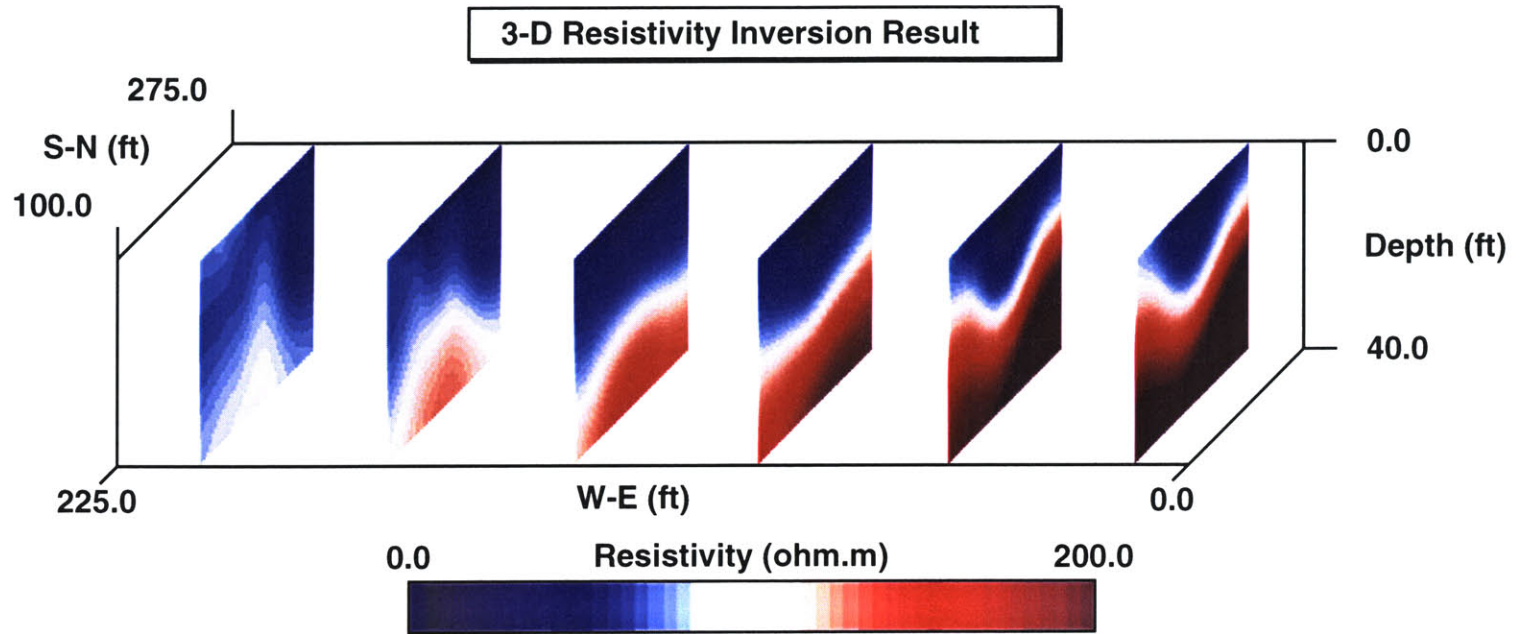


Figure 3-4: 3D resistivity inversion model (vertical slices) for the Aberjona contamination site. The resistive zone at depth dipping from east to west is interpreted to be a sand formation underlying more conductive diatomaceous earth.



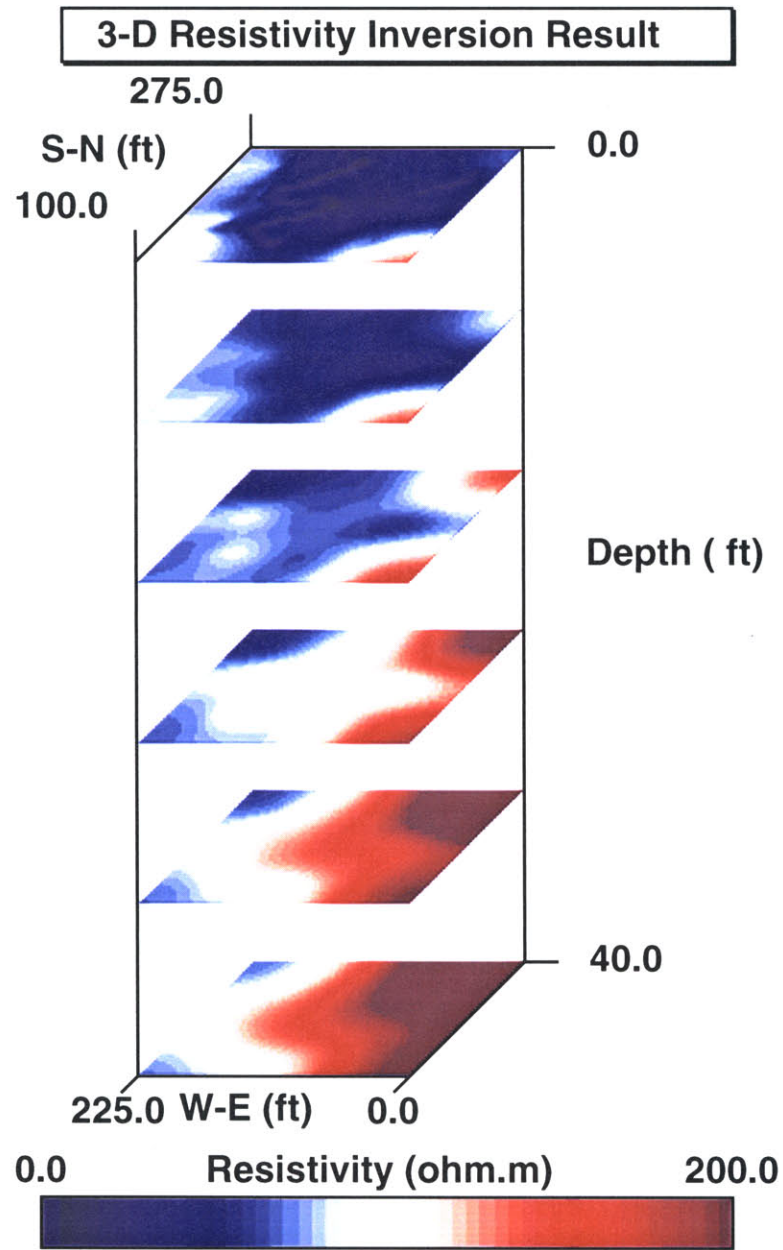


Figure 3-5: 3D resistivity inversion model (horizontal slices) for the Aberjona contamination site. The resistive zone at depth dipping from east to west is interpreted to be a sand formation underlying more conductive diatomaceous earth.

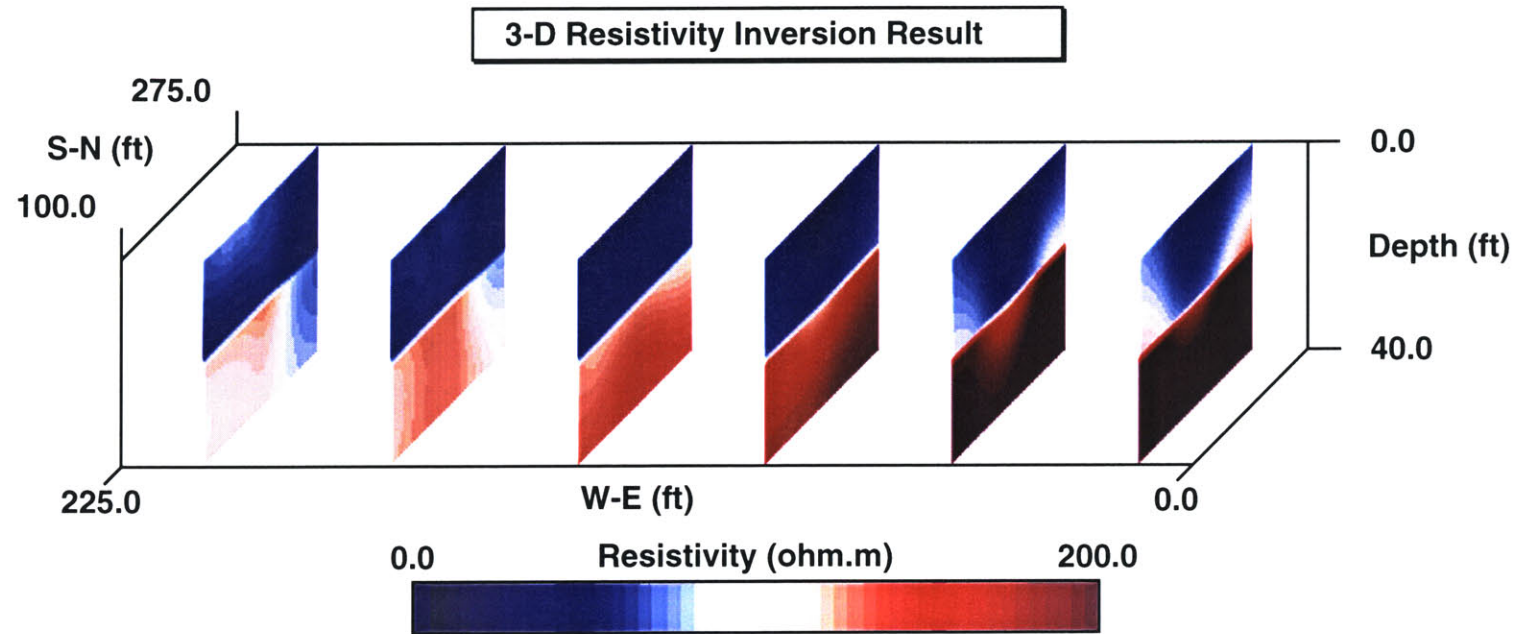


Figure 3-6: 3D resistivity inversion model (vertical slices) for the Aberjona contamination site. At this time, a 2-layer model is chosen to be the *a priori* model. The inversion model reveals similar structure with respect to the previous inversion in Figure 3-4.

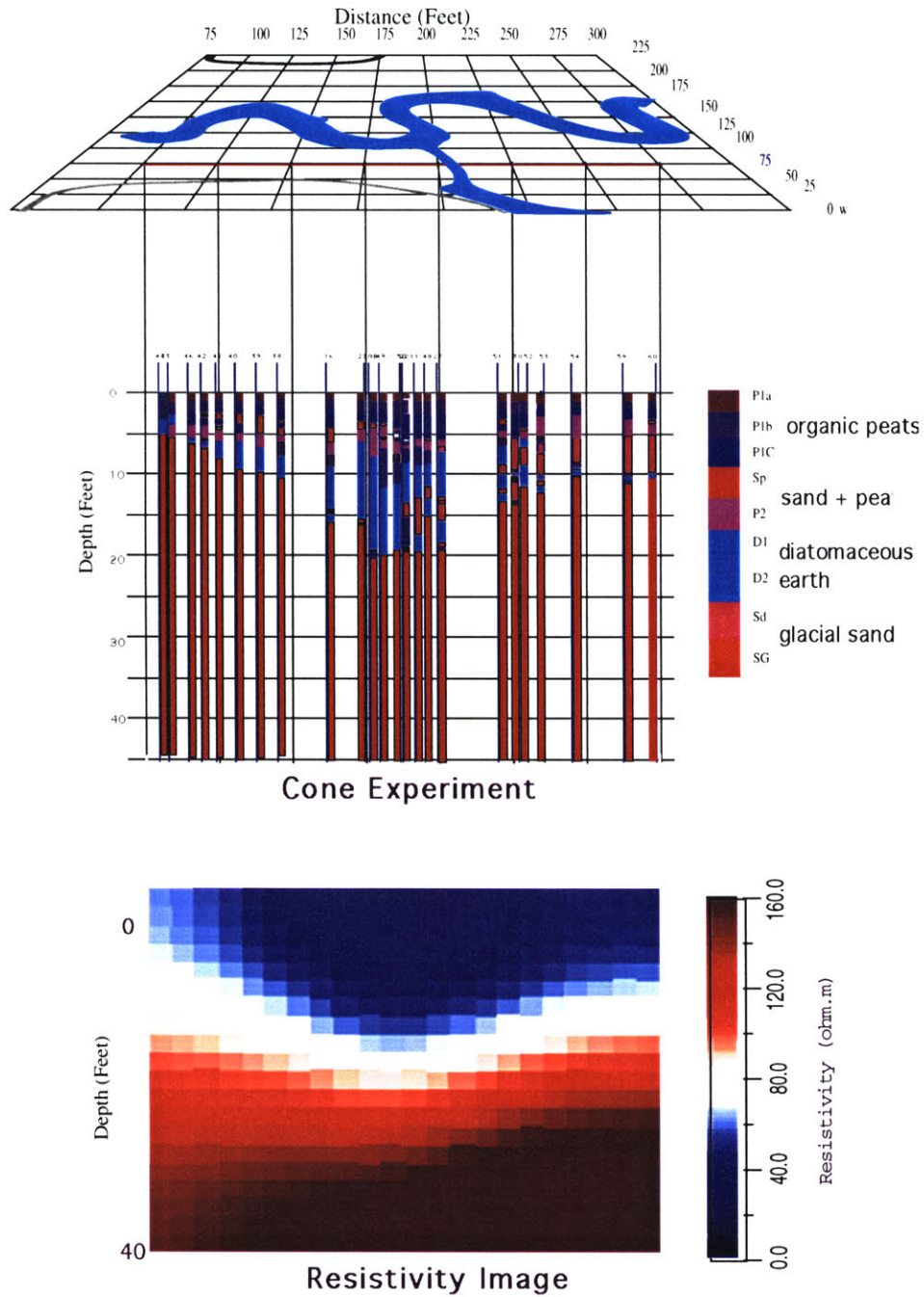


Figure 3-7: Correlating the 3-D resistivity inversion model with the Cone penetrometer response. Note, the bowl-shaped lower boundary of the diatomaceous earth is in good agreement with the resistivity inversion method.

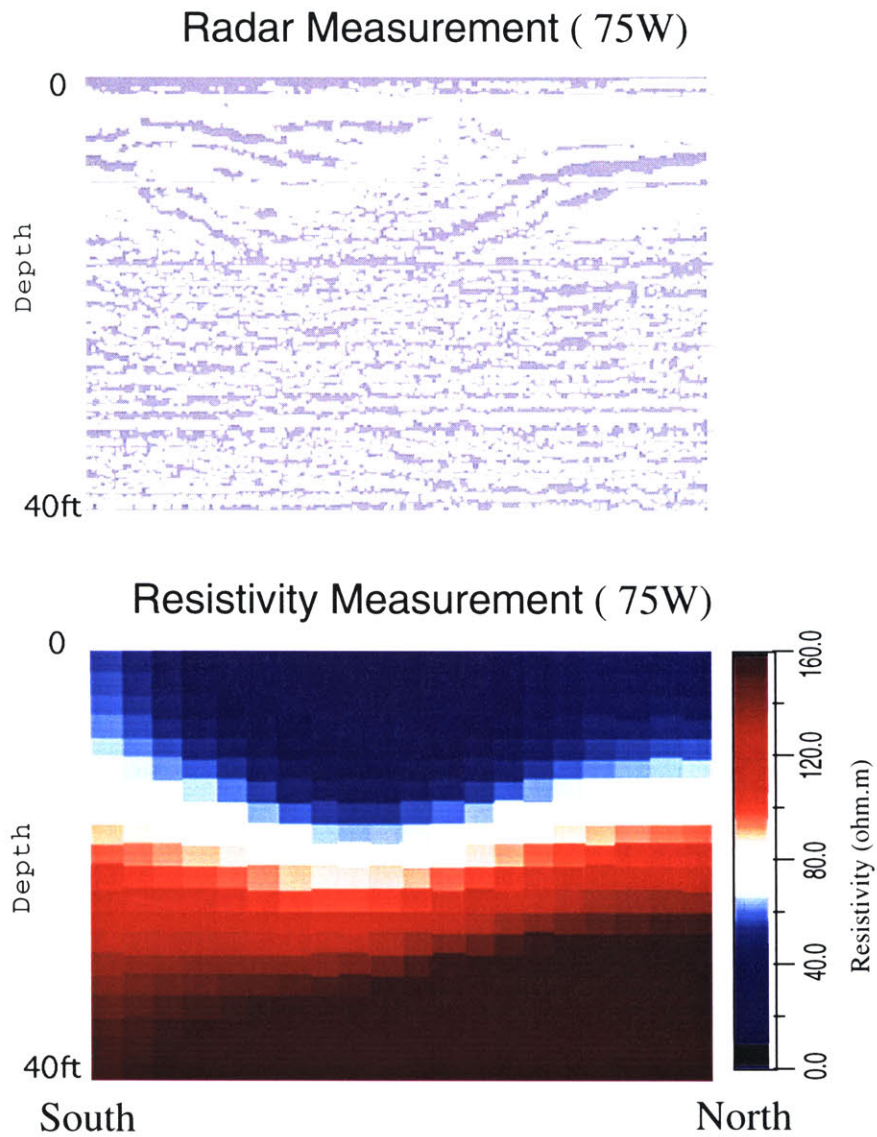


Figure 3-8: Comparison of resistivity inversion model with a GPR section located at 75 ft west of Well H. The shape of the boundary between the diatomaceous earth and the sand layer is in good agreement.

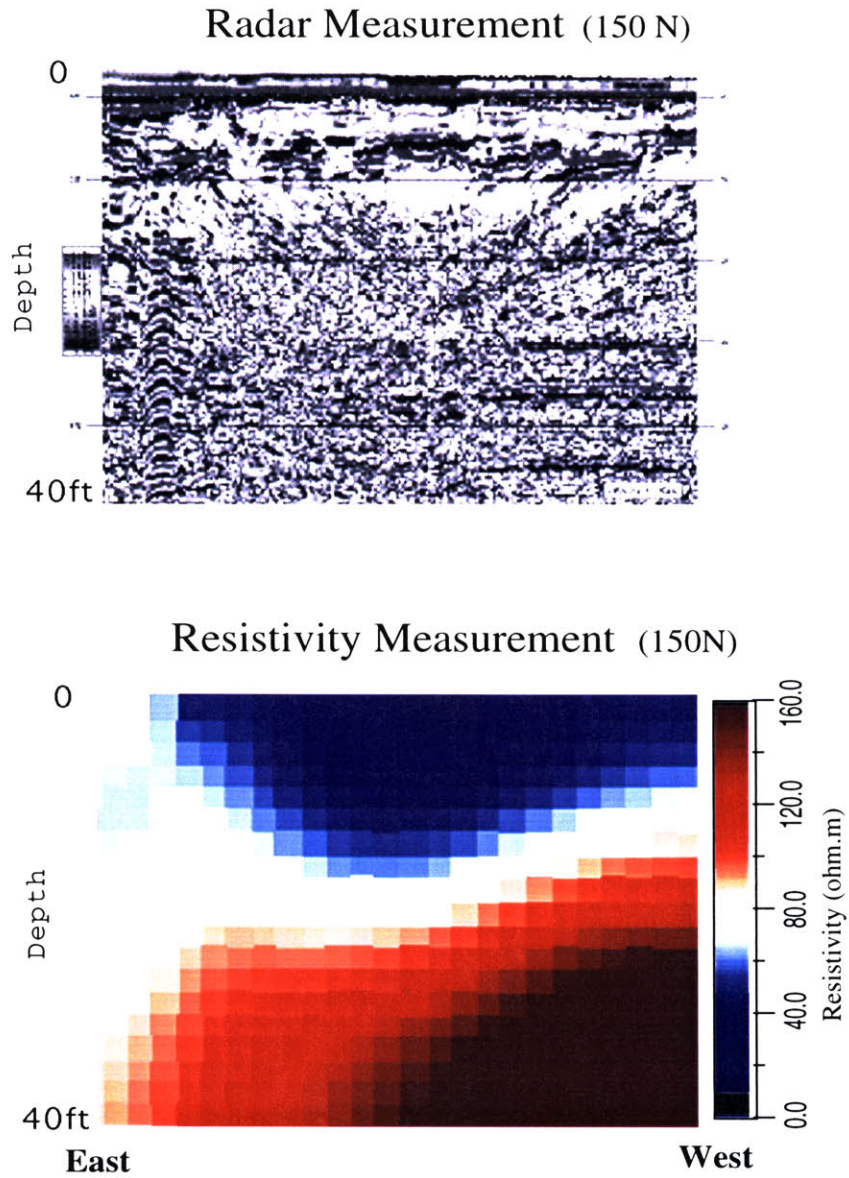


Figure 3-9: Comparison of resistivity inversion model with a GPR section located at 150 ft north of Well H. The shape of the boundary between the diatomaceous earth and the sand layer is in good agreement.

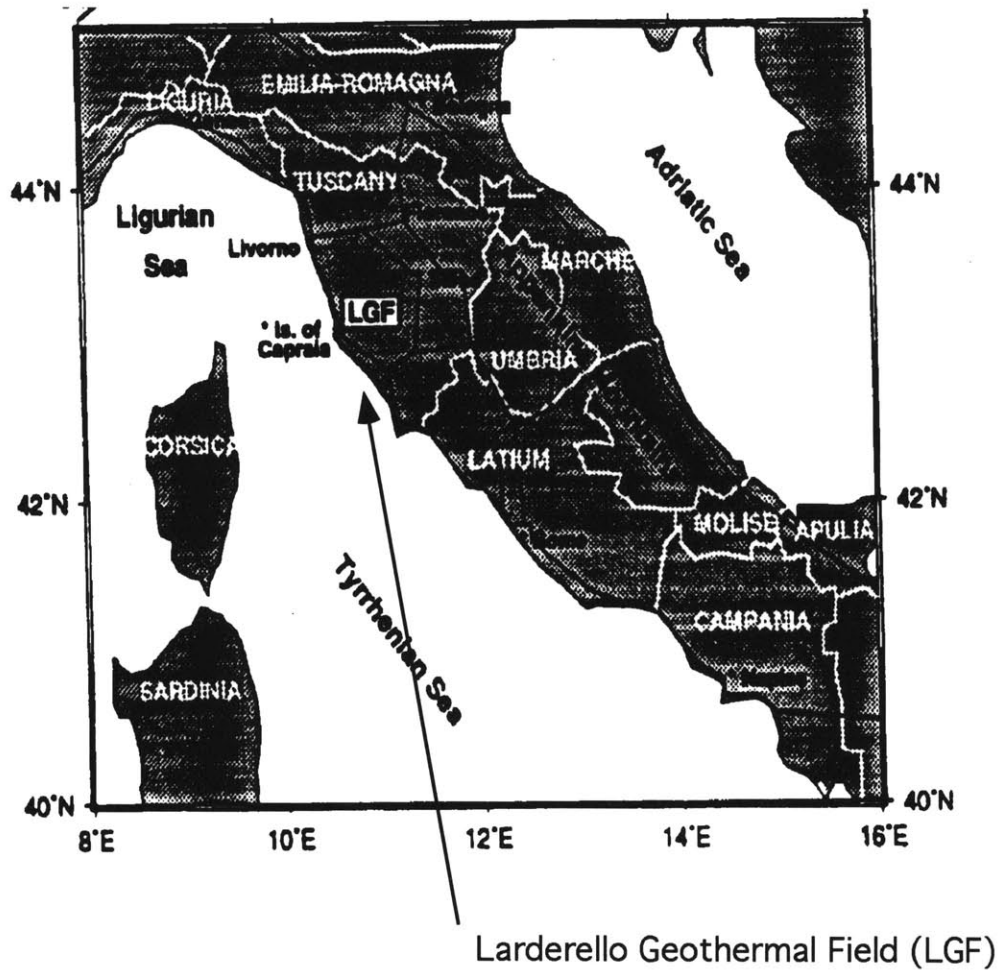


Figure 3-10: The geographic location of Larderello Geothermal Field.

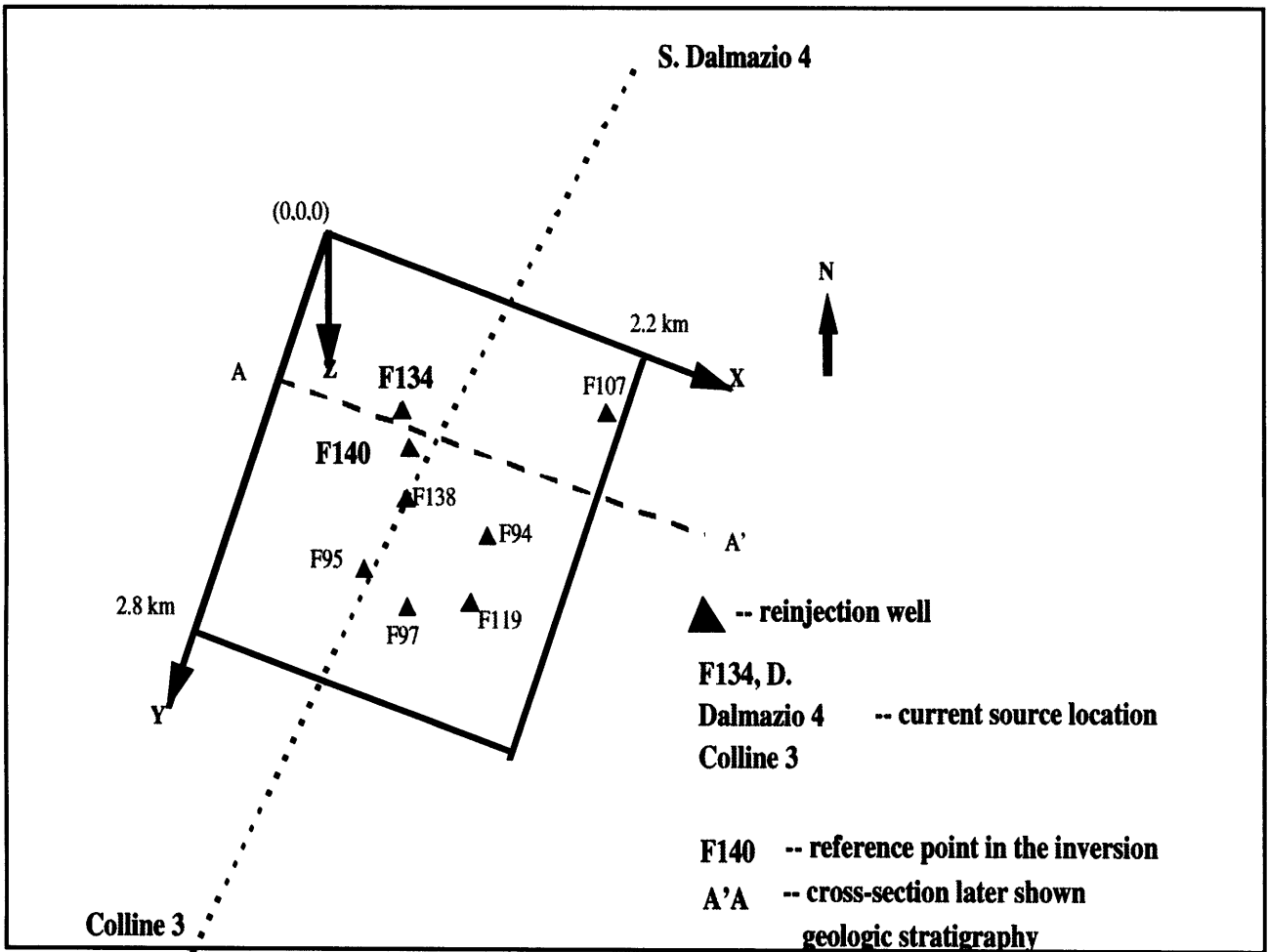


Figure 3-11: The relative position of the major injection wells are shown with the rectangular survey area and the inversion coordinate system.

- **Flysch Layer (0-500 m)**
- **Tectonic Wedges Complex (500-1000 m)**
- **Metamorphic Basement (1000 +)**

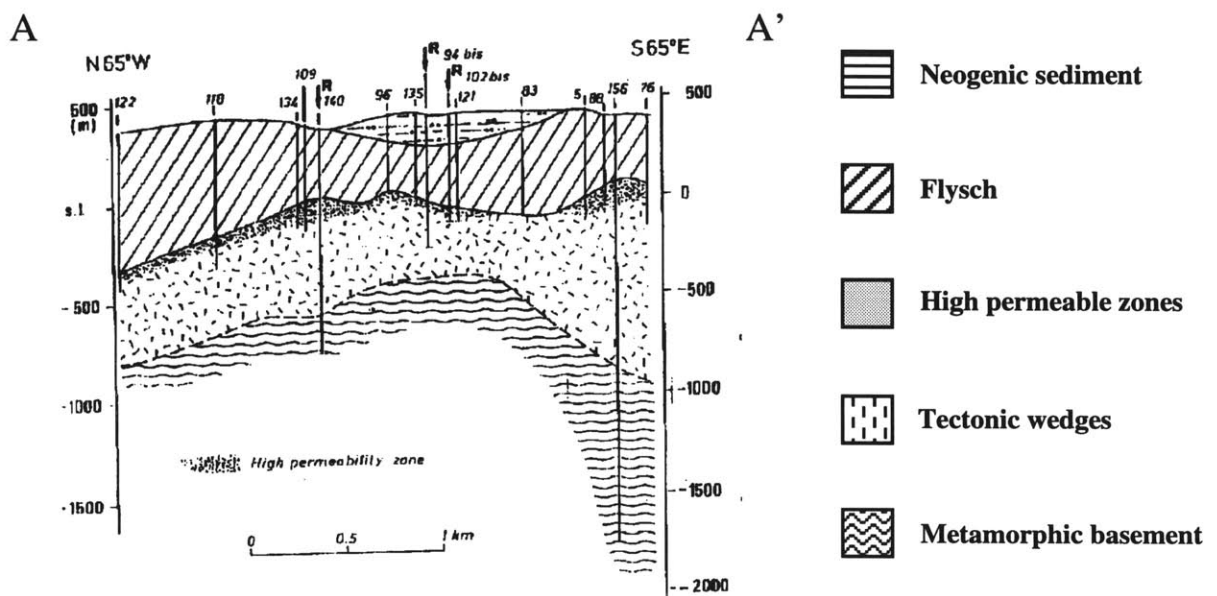


Figure 3-12: Cross-section depicting the three layers characterizing the geologic stratigraphy in the Larderello-Valle Secolo geothermal field, (section A-A' from (Figure 3-11)).



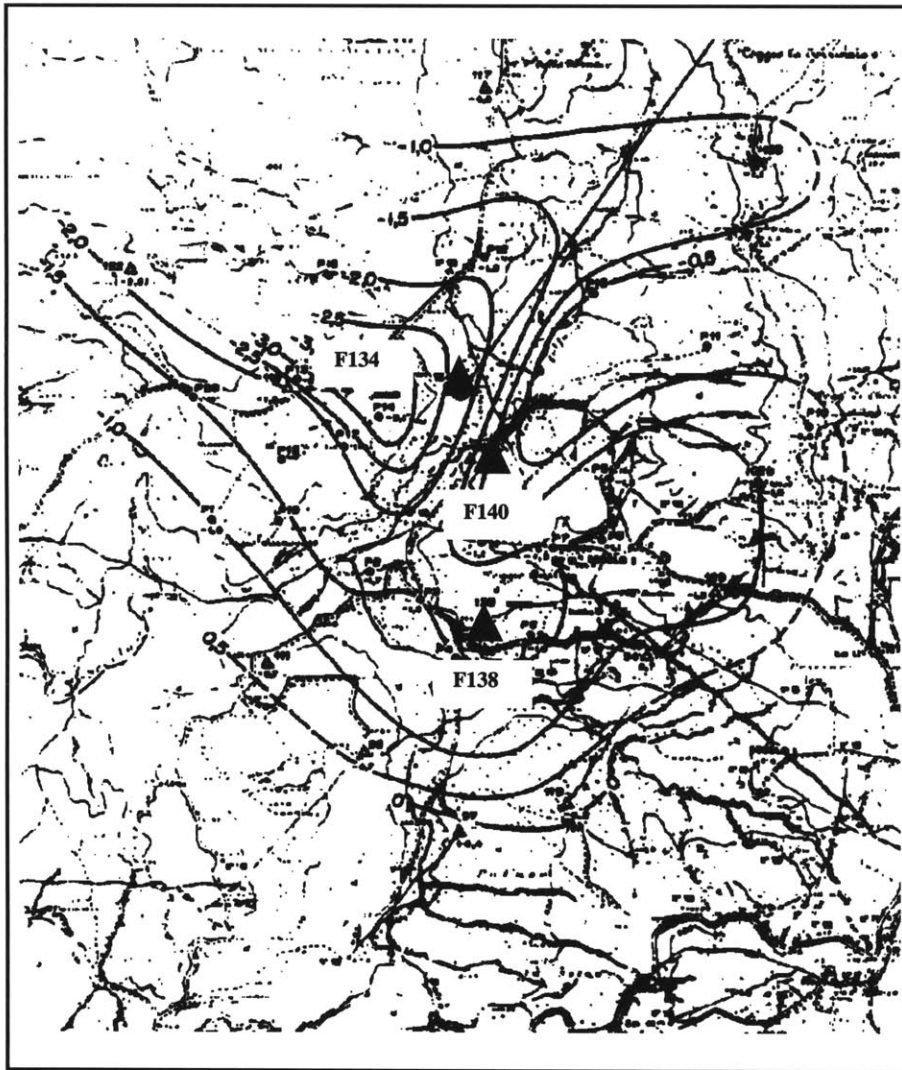


Figure 3-13: Contour plot of the potential variations (in the unit of mv) between phase 1 and phase 2. The current sources were located at well 134 and S. Dalmazio.

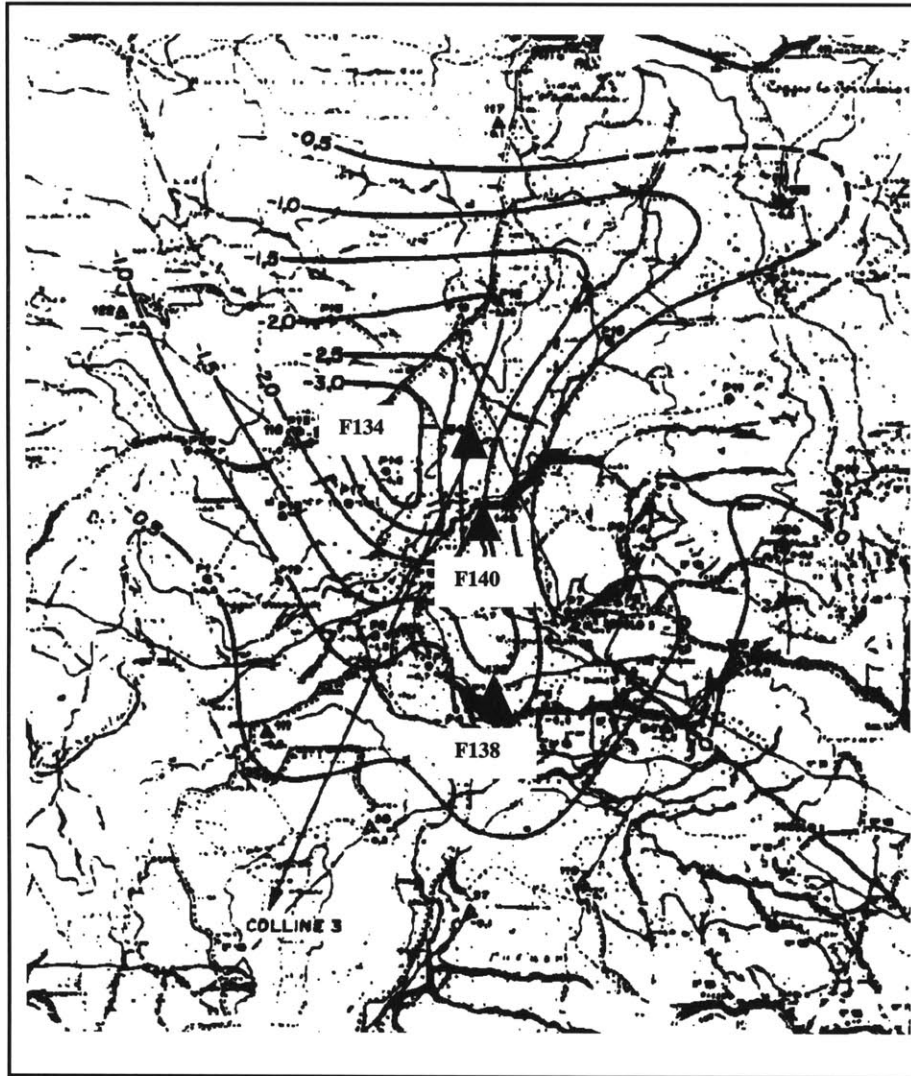


Figure 3-14: Contour plot of the potential variations (in the unit of mv) between phase 1 and phase 2. The current sources were located at well 134 and Colline 3.

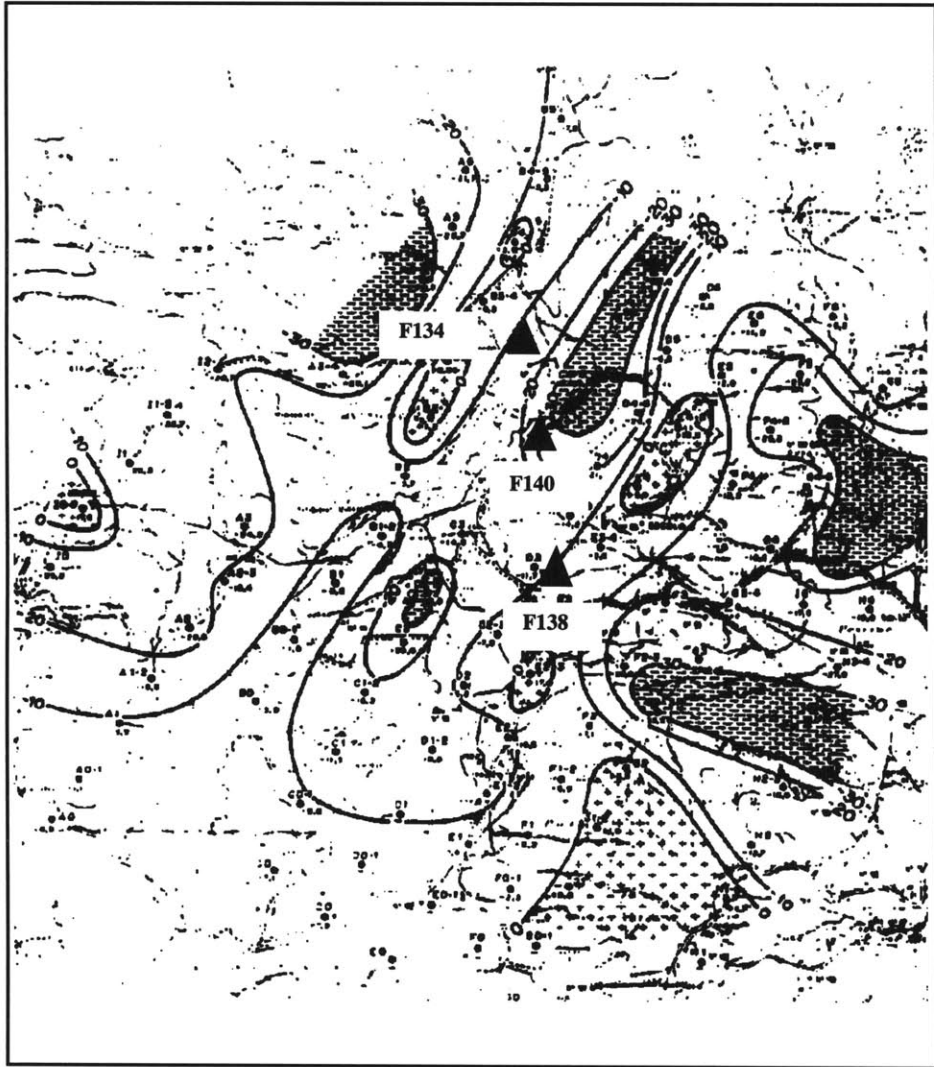


Figure 3-15: Contour plot of the apparent resistivity variations between phase 1 and phase 2. The measurement was conducted on a 'rectangle' configuration, and the current sources were located at Colline 3 and S. Dalmazio.

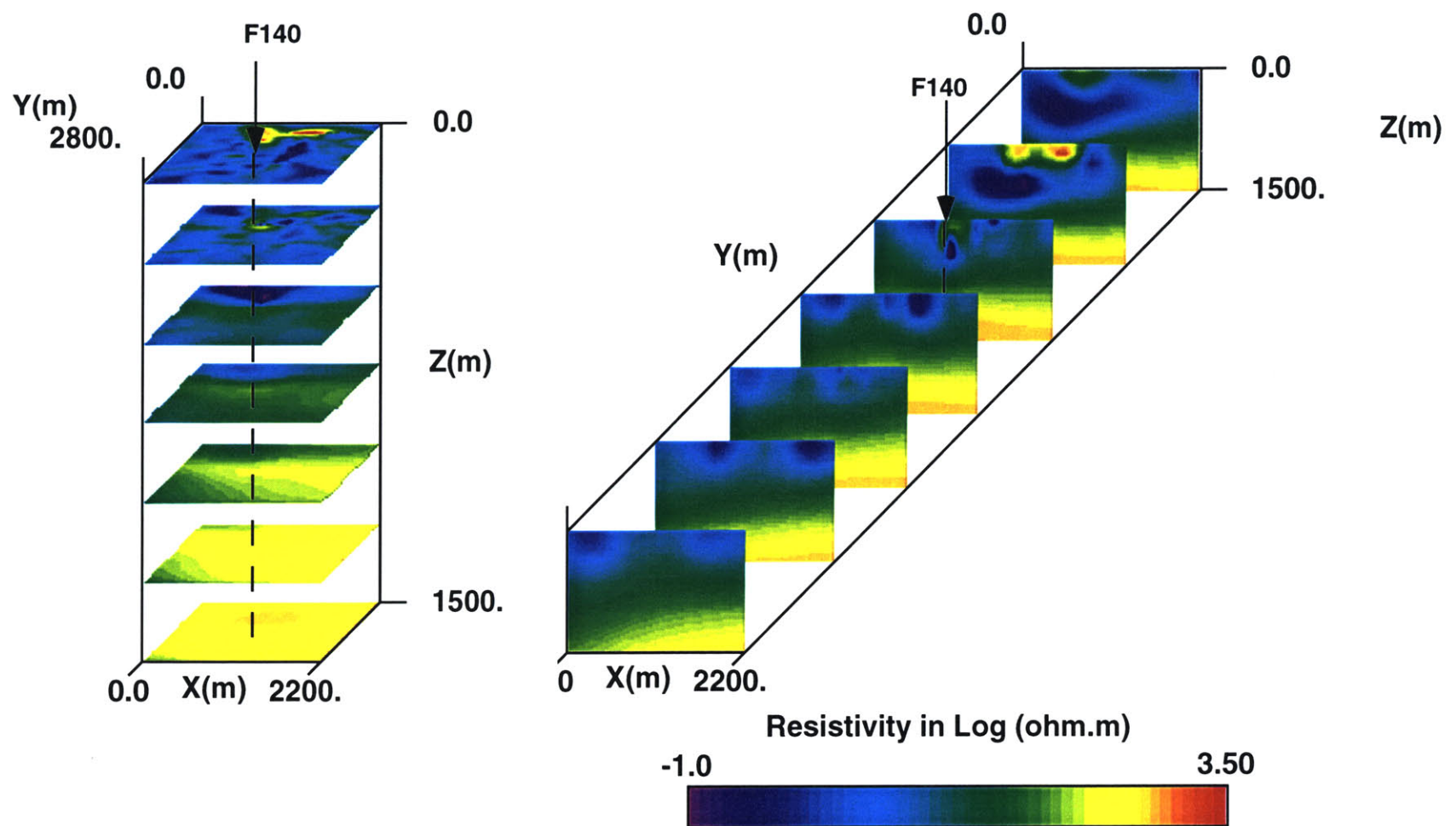


Figure 3-16: The vertical and horizontal slices of the 3-D resistivity inversion results of phase 1. The results depict a conductive zone at a depth of 700 meters near well 140. This feature is not structural and therefore may indicate a zone of high permeability of high water saturation. It is related to the re-injection.

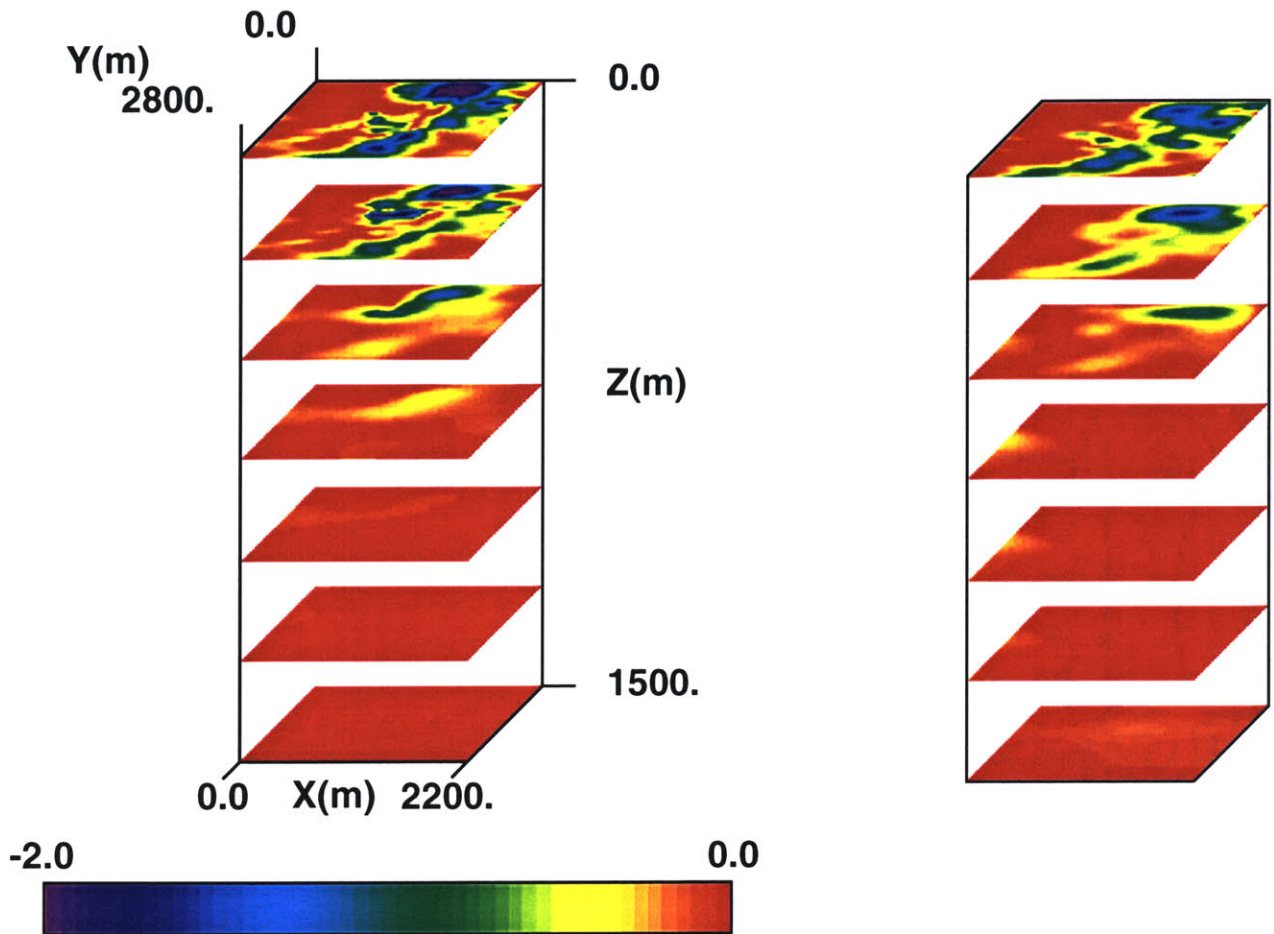


Figure 3-17: This figure presents the change in resistivity between the two surveys computed by the two methods. The results are displayed on horizontal cross-section. A large decrease of the resistivity values (about 100 times less) are observed in the northern part of the survey area, particularly in the north east side of well 140. Method 1 (left) shows stronger anomaly than Method 2(right).

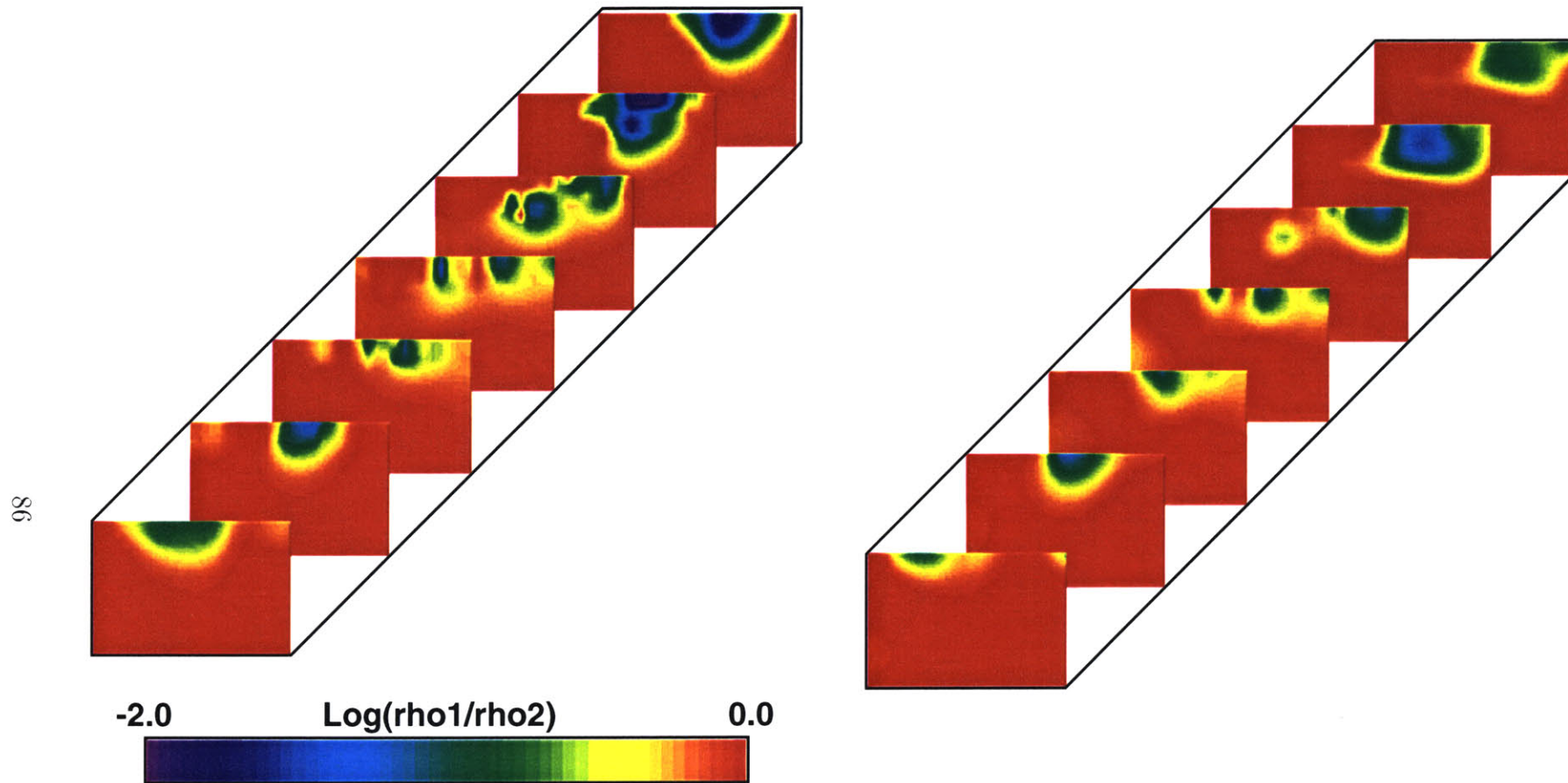


Figure 3-18: This figure presents the change in resistivity between the two surveys computed by the two methods described in section 3.3.3. The results are displayed on vertical cross-section.

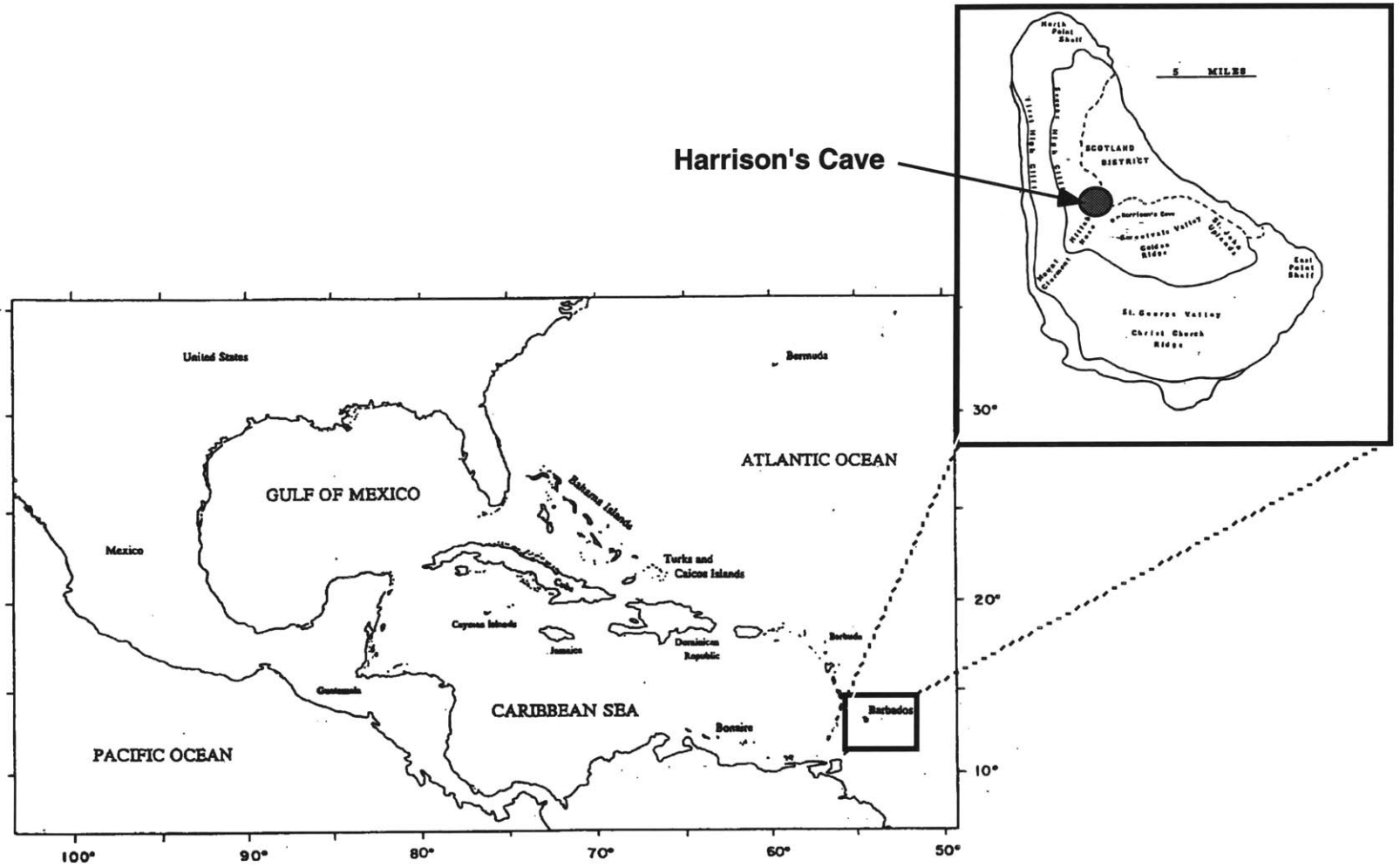


Figure 3-19: Locations of the Barbados island and the Harrison's cave.

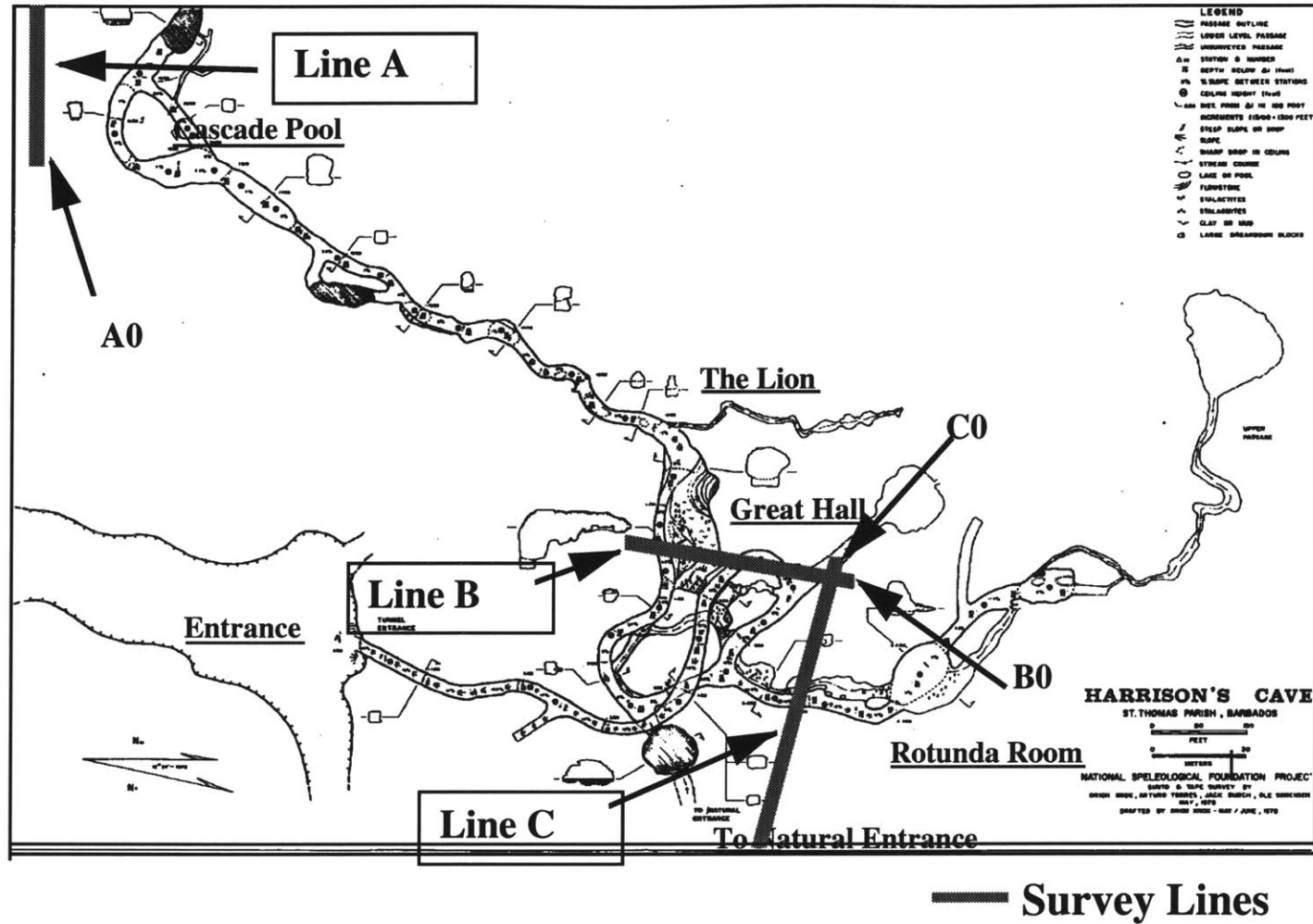


Figure 3-20: Map of Harrison's cave, showing locations of survey lines and the features discussed in the survey (modified from Hobbs, 1994).



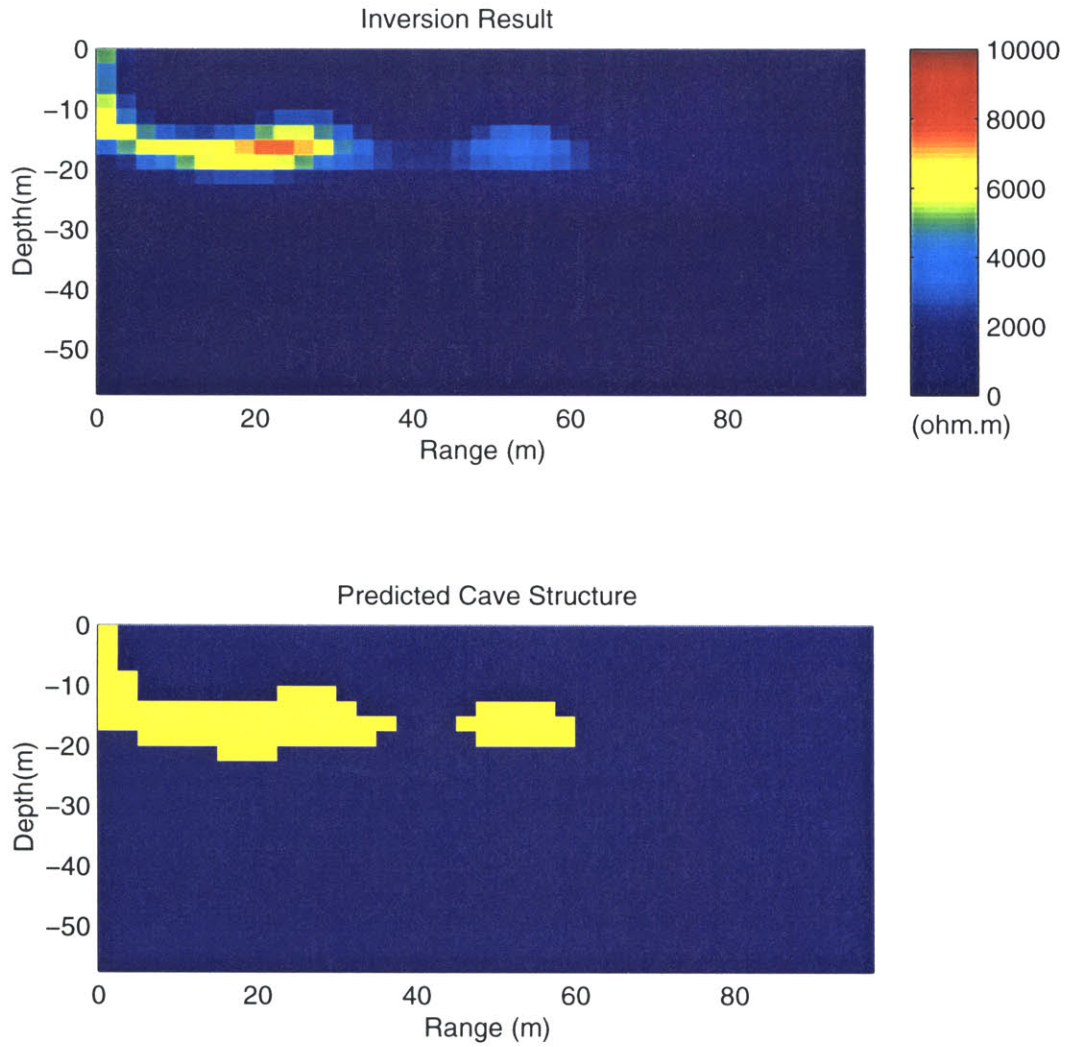


Figure 3-21: Resistivity inversion results of line B show two caves possibly connected by a narrow route. The top figure shows the inversion results, while in the bottom figure, a simple method which qualitatively predicates the cave's geometry is used.

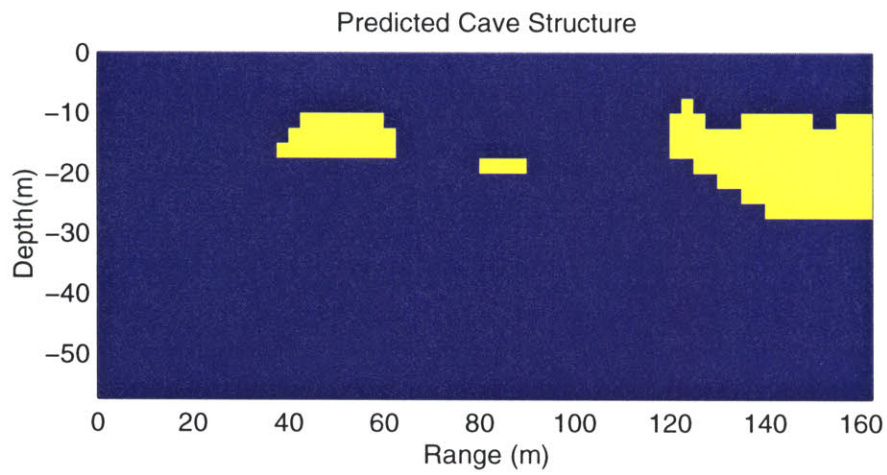
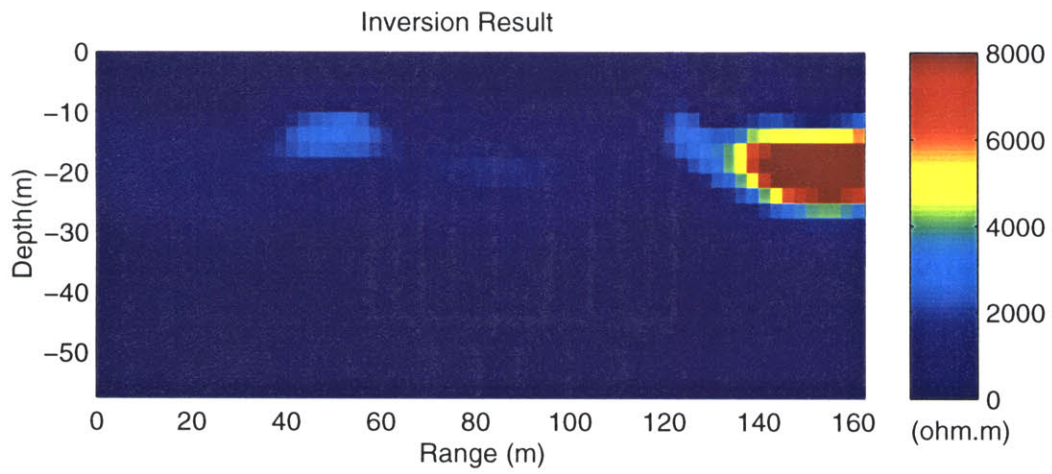


Figure 3-22: Resistivity inversion results of line C depict three distinct caves.

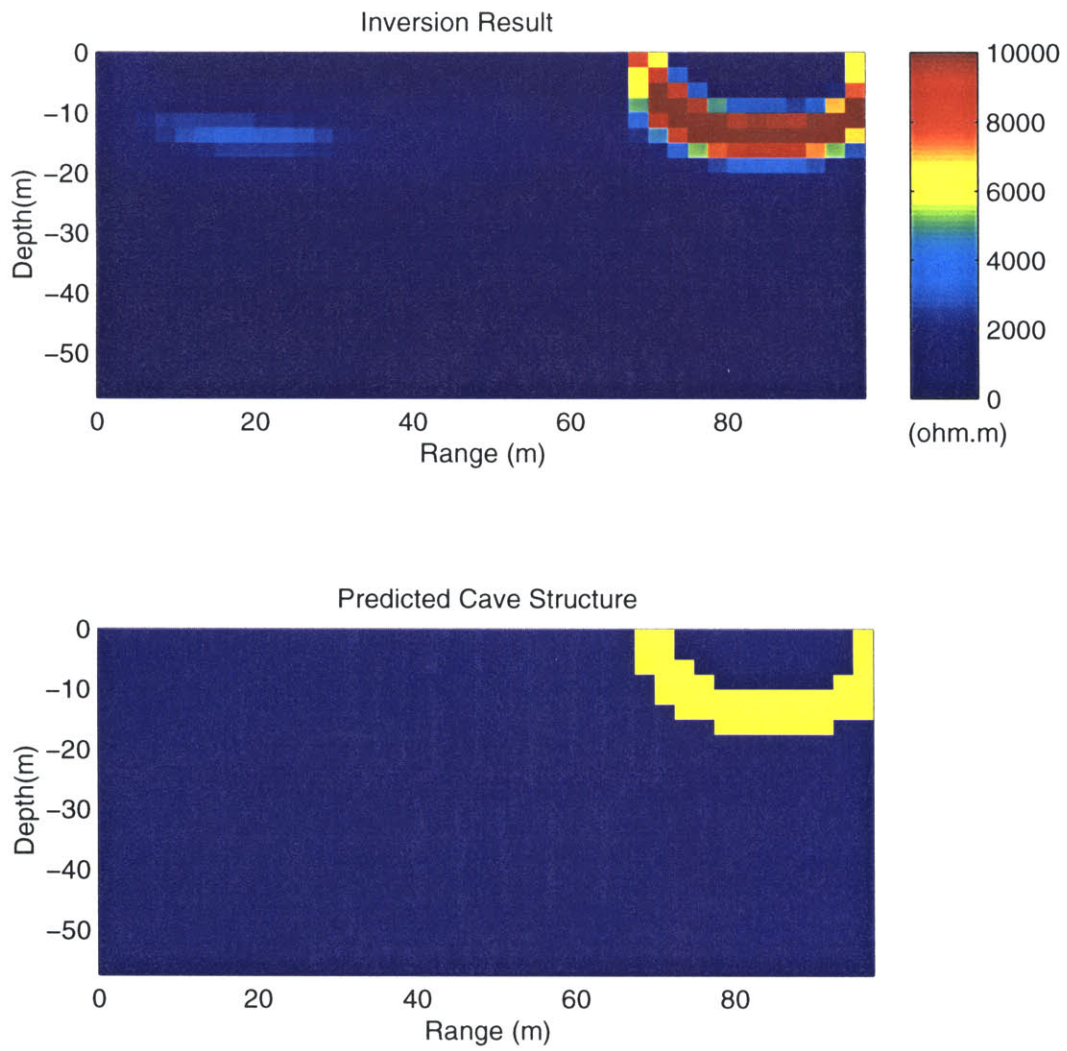


Figure 3-23: Resistivity inversion results of line A.

# Chapter 4

## Inversion of Electrical Induced Polarization Data

### 4.1 Introduction

The most common electrical and electromagnetic method used in exploration geophysics measures the d.c. electrical resistivity of the subsurface. There are two other electrical techniques which utilize different electrical properties than simply resistivity. These are (1) the electrical induced-polarization (IP) method and (2) the electrical self-potential (SP) method. The IP and SP methods both attempt to measure effect where electro-chemical phenomena play an important role. The following two chapters will address issues of measurement and inversion techniques for the IP and SP methods.

The IP response is a current-stimulated electrical phenomenon observed as a delayed voltage response in earth materials. Excellent reviews on the IP method and case histories can be found in Sumner (1976), Fink *et al.* (1990), Bertin and Loeb

(1976), and Madden and Cantwell (1967). The basic mechanisms of the IP response is mainly driven by the electro-chemical processes, where some of the chemical energy is stored because of (a) variation in the mobility of ions in fluids associated with mineral surface and (b) variations between ionic and electronic conductivity where metallic minerals are present. The first of these effects is known as *membrane* or *electrolytic polarization*, the second is known as *electrode polarization* or *over-voltage*. Conventionally the IP method has been most applied to mineral exploration. Recently, the method has been extended to application of the delineation and characterization of groundwater contaminants.

It has been indicated that the IP method is a more effective means of detecting and mapping ground water contaminants in many situations where d.c. resistivity has been ineffective. In many groundwater contaminant plumes, the concentrations of contaminants is very low so that they do not significantly change the conductivity of the saturating solution. Therefore, they do not cause a measurable resistivity anomaly. Although the contaminant concentrations are too low to be detected using conventional resistivity methods, they are still very toxic to humans. The acceptable drinking water limits for most toxic substances are orders of magnitude less than the concentrations that can be detected using conventional resistivity. Therefore, conventional resistivity only provides enough sensitivity to detect levels of contamination which are relatively high. The IP response of rocks and soils is controlled by surface chemical effects which are very sensitive to the solution chemistry. Even small amounts of contaminant can significantly effect the surface properties of a sample.

Measurement of the IP effect can be made either in the time or the frequency domains. In the time-domain method a square wave current source is applied and the transient (decay or buildup) electrical potential is sampled at the receiver electrodes as a function of time. Superficially the transient voltage behavior in the time domain measurement resembles the discharge and charge effects of a capacitor through a finite

resistance, but the charge and decay curves are logarithmic rather than exponential (as in the R-C circuit) and do not commence at the static potential limits, 0 and  $V_c$  (Figure 4-1). In the frequency-domain method, the current is harmonic and the amplitude and phase lag of the potential is measured over a spectrum of source frequencies.

Although surveying with the IP method is, in principle, similar to d.c. resistivity (measuring potential difference between two points on the surface of the earth or in the bore hole), the interpretation of IP data is considerably more complex. Until recently, IP interpretation was mainly a qualitative exercise. As the measurement techniques for detecting the IP effect fall into two classes, the time domain and the frequency domain methods, the parameters that are used to interpret the IP effect also fall into two categories. In the time domain measurement, the most commonly measured parameter is the apparent *chargeability*,  $\eta$ , defined as the area beneath the decay curve over a certain time interval ( $t_1 - t_2$ ) normalized by the steady-state potential  $V_c$ , e.g.  $\eta = \frac{1}{V_c(t_2-t_1)} \int_{t_1}^{t_2} V(t)dt$ . IP results are then displayed in simple profiles of chargeability plotted against station location. In the frequency domain, the apparent *percentage frequency effect*, defined as a normalized percentage difference between the apparent resistivity measured at two frequencies, or, the *metal factor* defined as the *percentage frequency effect* times a fixed factor, are plotted against station location.

Recently quantitative interpretations have been found in the literature. In these works, most authors adopt a method given by Seigel (1959) that the ultimate effect of a chargeable body alters its effective conductivity. As such, the IP and DC resistivity problems are intimately linked, and the inversion of IP data is a two-step process (Oldenburg and Li, 1994). In the first step, the DC potentials are inverted to recover the background conductivity  $\sigma_b$ . The second step recovers the perturbed conductivity so that a chargeability can be recovered. This procedure may be suited for the forward modeling problem, but for the inversion it is not practical because of

the measurement inaccuracy and errors in numerical computation which result in instabilities in the inversion. Except for the interpretation based on chargeability, more complicated approaches have been taken by few authors. One of the approaches is the Cole-Cole method (Cole and Cole, 1941) in which the IP effect is characterized by four parameters, the d.c electrical resistivity, the intrinsic chargeability, the time constant and the frequency dependent constant. Pelton *et al.* (1978) study mineral IP effects using Cole-Cole method. They employ the Marquardt least-square method to fit the apparent Cole-Cole parameters. This method provides useful information for a homogeneous medium, but it cannot handle situations where the Cole-Cole parameters are functions of position. A different method to recover the Cole-Cole model is accomplished by Johnson (1990). He uses a master curve fitting to back out the Cole-Cole parameters for a simple medium. A more recent work by Yuval and Oldenburg (1997) extends the time-domain approach by using samples of the potential fields  $V$  at discrete times,  $t_k$ , to infer d.c. resistivity and chargeability vs.  $t_k$  and position, then from the chargeability curve estimates of the Cole-Cole parameters as a function of position are made.

Extending the work of d.c. electrical resistivity inversion theory, an alternate IP inversion technique, based on frequency domain measurements, is presented in this chapter. This technique is based on the assumption that the resistivity value of the subsurface is complex. Complex resistivity results in a complex electrical potential observed on the surface of the earth and recorded as the amplitude of the electrode potential and the phase shift from the injected current signal. A general algorithm to simulate the response of an arbitrary 2-D or 3-D distribution of complex resistivity to arbitrary arrays of current and receiver electrodes and its inversion procedure is developed.

## 4.2 Formulation of the Problem

The induced polarization phenomenon is usually modeled macroscopically as a generalization of Ohm's law in which voltage  $V(t)$  is linearly related to current  $I(t)$  through convolution with an impedance response function  $R(t)$ :

$$V(t) = \int_0^{\infty} R(t') I(t - t') dt' \quad (4.1)$$

Treating the earth as a continuum, we have at each point

$$\mathbf{E}(t) = \int_0^{\infty} \rho(t') \mathbf{J}(t - t') dt' \quad (4.2)$$

where  $\mathbf{E}$  is the electric field,  $\mathbf{J}$  is the current density, and  $\rho$  is the electrical resistivity. The function  $\rho(t)$  is taken as the superposition of an instantaneous response and a decaying memory function. We write this as

$$\rho(t) = \rho_0 \left[ (1 - \eta_0) \delta(t) - \frac{d}{dt} \eta(t) \right] \quad (4.3)$$

where  $\rho_0$  is the d.c. resistivity,  $\eta_0$  is the total chargeability, and  $\eta(t)$  is a decay function.  $\eta_0$  is a number between zero and one; the function  $\eta$  is equal to  $\eta_0$  for  $t \leq 0$  and decays to zero as  $t \rightarrow \infty$ . The Fourier transform of  $\rho(t)$  defines a complex resistivity as a function of frequency,  $\rho(\omega)$ , such that

$$\mathbf{E}(\omega) = \rho(\omega) \mathbf{J}(\omega). \quad (4.4)$$

For low frequencies, electromagnetic induction can be ignored and  $\mathbf{E}$  is the gradient of a potential field  $V$  that is determined by the current conservation law

$$\nabla \cdot \left( \frac{1}{\rho(\mathbf{x}, \omega)} \nabla V(\mathbf{x}, \omega) \right) = -\mathbf{I}(\mathbf{x}, \omega) \quad (4.5)$$

where  $I$  is the source current. In the IP method, the difference between  $V$  at two point electrodes is measured, as generated by a source ( $I$ ) comprising current injected at two other electrodes. In the time-domain method, a transient signal is obtained



by shutting off a steady current. In the frequency-domain method, the amplitude and phase lag of  $V$  is measured with respect to  $I$  for a set of source frequencies. The inverse problem is to use such measurements, for many different current and potential field electrode locations, to infer the complex resistivity function  $\rho(\mathbf{x}, \omega)$  or, alternatively, the d.c. resistivity function  $\rho_0(\mathbf{x})$  and chargeability function  $\eta(\mathbf{x}, t)$ .

The inversion method of Li and Oldenburg (1994) uses time-domain IP data to infer two parameters of the medium as a function of position: the d.c. resistivity,  $\rho_0(\mathbf{x})$ , and total chargeability,  $\eta_0(\mathbf{x})$ . Yuval and Oldenburg (1997) extend the time-domain approach by using samples of the potential fields  $V$  at discrete times,  $t_k$ , to infer  $\rho_0(\mathbf{x})$  and  $\eta(\mathbf{x}, t_k)$ . (They fit the sampled medium response at each point  $\mathbf{x}$  with Cole-Cole parameters as an additional step.) In this paper we develop a frequency-domain approach. Complex potential field measurements at discrete frequencies,  $\omega_k$ , are used to infer the complex resistivity in the earth at these same frequencies,  $\rho(\mathbf{x}, \omega_k)$ .

### 4.3 Forward Modeling

Given a complex resistivity function  $\rho$ , the predicted IP response of the earth for a given source  $I$  and frequency  $\omega$  is obtained by solving Equation 4.5 (with suitable boundary conditions). IP data are samples of  $V$  at various electrode locations. It is clear that the forward problem separates with respect to  $\omega$ , i.e. the IP data for a particular frequency depends on the earth's resistivity only at that frequency.

We discretize (Equation 4.5) on the transmission network introduced earlier in the d.c. electrical resistivity problem with current and potentials defined at each node and a complex impedance on the branch connecting each node. This method, like finite differences, entails sampling  $\rho$  and  $V$  spatially on a dense, 3-D grid and then

solving a linear system of equations,

$$\mathbf{K}v = s \tag{4.6}$$

where  $\mathbf{K}$  is a matrix depending on the resistivity function  $\rho$  and grid geometry;  $v$  is a vector containing the potential field samples at grid points; and  $s$  is a source vector determined by integrating the current distribution  $I$  over grid elements. The resulting equations are precisely those for d.c. resistivity modeling but with  $\mathbf{K}$ ,  $v$  and  $s$  complex, instead of real, quantities. The matrix  $\mathbf{K}$  is complex symmetric, not Hermitian.

We solve the system (Equation 4.6) using a complex bi-conjugate gradient method (e.g. Jacobs, 1986). Given that  $\mathbf{K}$  is symmetric, the bi-conjugate gradient method reduces to a special form which is very similar to the (real) conjugate gradient method extended to complex numbers. This simplification makes solving an IP forward model no more computationally different than a d.c. resistivity forward modeling. Although the bi-conjugate gradient method for complex symmetric systems is not guaranteed to converge (Jacobs, 1986), our experience to date has not encountered convergence problems, probably owing to the fact that for the types of earth materials we have considered, the imaginary part of  $\rho$ , and hence  $\mathbf{K}$  and  $v$ , are much smaller than its real part.

## 4.4 Extension of Nonlinear Inverse Theory to the Complex Domain

Let us define a complex vector  $d_k$  to contain all the complex potential measurements associated with a fixed frequency  $\omega_k$ . Each component of  $d_k$  corresponds to a single source and receiver electrode configuration. We let  $m$  denote a model function

that defines the complex resistivity in the subsurface as a function of position and frequency. In this paper, we use

$$m(\mathbf{x}, \omega) = \log \rho(\mathbf{x}, \omega). \quad (4.7)$$

Therefore, the real part of  $m$  is the log amplitude of the complex resistivity ( $\log |\rho|$ ) while the imaginary part of  $m$  is the phase of resistivity.

We may state the frequency-domain IP inverse problem as determining the function  $m$  from the equations

$$d_k = \mathbf{G}(m; \omega_k) + e_k, \quad k = 1, 2, \dots, n \quad (4.8)$$

where  $G$  represents the forward modeling operator, defined implicitly by Equation 4.5, and each  $e_k$  is a (complex) error vector. In this paper we do not address the interpolation of  $m$  with respect to  $\omega$  via parameterization (e.g. Cole-Cole) or smoothing. Instead, because the forward problem separates by frequency, we approach Equation 4.8 as  $n$  separate inverse problems with the objective of inferring  $m$  only at the observation frequencies,  $\omega_k$ . That is, we solve

$$d_k = \mathbf{G}(m_k) + e_k, \quad k = 1, 2, \dots, n \quad (4.9)$$

where  $m_k(\mathbf{x}) = m(\mathbf{x}, \omega_k)$ . (Note that, if the source is independent of frequency,  $G$  does not depend explicitly on  $\omega$ .)

Our inversion algorithm solves the inverse problem for each frequency  $\omega_k$  separately. Accordingly, in this section we drop the subscript  $k$  on the data vector  $d$  and model function  $m$ .

The IP inverse problem (for a given frequency) is ill-posed because  $m$  is a function of continuous position while  $d$  is finite-dimensional. In practice,  $m$  is sampled on a grid and is thus finite-dimensional, but the grid is intentionally dense and the ill-posed nature of the problem remains. To obtain stable solutions of the inverse problem, we

employ the method of Tikhonov regularization, following the implementation of the previous chapter for d.c. resistivity inversion. That is, we define solutions in terms of an optimization problem where an objective function,  $\Psi(m)$ , is minimized. We write  $\Psi$  as

$$\begin{aligned} \Psi(m) = & (d_r - \mathbf{G}_r(m))^T R_r^{-1} (d_r - \mathbf{G}_r(m)) + (d_i - \mathbf{G}_i(m))^T R_i^{-1} (d_i - \mathbf{G}_i(m)) \\ & + \tau_1 m_r^T \mathbf{L}^T \mathbf{L} m_r + \tau_2 m_i^T \mathbf{L}^T \mathbf{L} m_i \end{aligned} \quad (4.10)$$

where  $d = d_r + id_i$  denotes the complex electrical potential data,  $m = m_r + im_i = \log(\rho)$  the complex resistivity model ( $m_r$  representing the logarithmic amplitude of the complex resistivity,  $m_i$  representing the phase),  $\mathbf{G} = \mathbf{G}_r + i\mathbf{G}_i$  the complex forward modeling operator,  $R_r$  and  $R_i$  the covariance matrices corresponding to the real and the imaginary part of the data,  $\mathbf{L}$  a linear operator taken to be the Laplacian ( $L = \nabla^2$ ), and  $\tau_1$  and  $\tau_2$  are positive numbers (the “regularization parameter”).

The objective function  $\Psi$  defined above presumes that the real and imaginary parts of  $d$  have an independent covariance matrix. Therefore, a different coefficient of the smoothness constraint is required, in principal, to apply to the real and imaginary parts of  $m$ . However, in practice, the imaginary component of the complex resistivity is always much smaller than the real part,  $m_i \ll m_r$ , and the imaginary component of the data is always much smaller than the real part,  $\mathbf{G}_i \ll \mathbf{G}_r$ . Further, because the forward modeling operator  $G$  is analytic, it satisfies the Cauchy-Riemann equation,

$$\frac{\partial \mathbf{G}_r}{\partial m_r} = \frac{\partial \mathbf{G}_i}{\partial m_i} \quad (4.11)$$

$$-\frac{\partial \mathbf{G}_r}{\partial m_i} = \frac{\partial \mathbf{G}_i}{\partial m_r}, \quad (4.12)$$

which implies that the contribution of the real model component to the real data component is equal to the contribution of the imaginary model component to the imaginary data component. The cross-dependency also has an equal magnitude which

is very small. Therefore, it is reasonable to assume a common regularization term,

$$R_r \tau_1 = R_i \tau_2 = \tau \mathbf{I} \quad (4.13)$$

With this definition, the objective function can be written in a more compact format,

$$\begin{aligned} \Psi(m) &= \|d - \mathbf{G}(m)\|^2 + \tau \|\mathbf{L}m\|^2 \\ &= (d - \mathbf{G}(m))^H (d - \mathbf{G}(m)) + \tau m^H \mathbf{L}^T \mathbf{L} m \end{aligned} \quad (4.14)$$

where  $H$  denotes the conjugate transpose, or Hermitian (note  $\mathbf{L}$  is real).

Because the forward modeling operator  $G$  depends nonlinearly on  $m$ ,  $\Psi$  in Equation 4.14 is not a quadratic functional, and an iterative or search algorithm is needed to find its minimum. A commonly used iterative method is the Gauss-Newton method. It starts with an initial guess,  $m_0$ , and at the  $k$ th iteration step finds a model  $m^{k+1}$  that minimizes an approximate version of  $\Psi$ , defined by linearizing  $G$  at the current model,  $m_k$

$$\mathbf{G}(m^k + \delta m) = \mathbf{G}(m^k) + \mathbf{A} \delta m \quad (4.15)$$

where  $\mathbf{A}$  is the complex sensitivity matrix defined as

$$\mathbf{A} = \mathbf{A}_r + i \mathbf{A}_i \quad (4.16)$$

with

$$\mathbf{A}_r = \frac{\partial \mathbf{G}_r}{\partial m_r} = \frac{\partial \mathbf{G}_i}{\partial m_i} \quad (4.17)$$

$$\mathbf{A}_i = -\frac{\partial \mathbf{G}_r}{\partial m_i} = \frac{\partial \mathbf{G}_i}{\partial m_r} \quad (4.18)$$

both of which are real quantities.

Substituting Equation 4.15 - Equation 4.18 into Equation 4.14, we obtain

$$\begin{aligned} \Psi(m^k + \delta m) &= (d - \mathbf{G}(m^k) - \mathbf{A} \delta m)^H (d - \mathbf{G}(m^k) - \mathbf{A} \delta m) \\ &\quad + \tau (m^k + \delta m)^H \mathbf{L}^T \mathbf{L} (m^k + \delta m) = \text{Minimum} \end{aligned} \quad (4.19)$$

Let

$$\delta m = \delta m_r + i\delta m_i \quad (4.20)$$

Then  $\Psi(m^k + \delta m) = \text{Minimum}$  requires

$$\begin{aligned} \frac{\partial \Psi}{\partial \delta m_r} &= -2\mathbf{A}_r^T [d_r - G_r(m^k)] - 2\mathbf{A}_i^T [d_i - G_i(m^k)] + 2\tau \mathbf{L}^T \mathbf{L} m^k + \\ &\quad 2(\mathbf{A}_r^T \mathbf{A}_r + \mathbf{A}_i^T \mathbf{A}_i + \tau \mathbf{L}^T \mathbf{L}) \delta m_r \\ &= \text{Re}\{-2\mathbf{A}^H [d - \mathbf{G}(m^k)]\} + 2\tau \mathbf{L}^T \mathbf{L} m^k + 2(\mathbf{A}_r^T \mathbf{A}_r + \mathbf{A}_i^T \mathbf{A}_i + \tau \mathbf{L}^T \mathbf{L}) \delta m_r \\ &= 0 \end{aligned} \quad (4.21)$$

$$\frac{\partial \Psi}{\partial \delta m_i} = \text{Im}\{-2\mathbf{A}^H [d - \mathbf{G}(m^k)]\} + 2(\mathbf{A}_r^T \mathbf{A}_r + \mathbf{A}_i^T \mathbf{A}_i + \tau \mathbf{L}^T \mathbf{L}) \delta m_i = 0 \quad (4.22)$$

Putting them together,

$$\begin{aligned} (\mathbf{A}^H \mathbf{A} + \tau \mathbf{L}^T \mathbf{L})(\delta m_r + i\delta m_i) &= \text{Re}\{\mathbf{A}^H [d - \mathbf{G}(m^k)]\} + \tau \mathbf{L}^T \mathbf{L} m \\ &\quad + i\text{Im}\{\mathbf{A}^H [d - \mathbf{G}(m^k)]\} \end{aligned} \quad (4.23)$$

i.e.

$$(\mathbf{A}^H \mathbf{A} + \tau \mathbf{L}^T \mathbf{L}) \delta m = \mathbf{A}^H [d - \mathbf{G}(m^k)] + \tau \mathbf{L}^T \mathbf{L} m^k \quad (4.24)$$

We solve this equation by the complex bi-conjugate gradient method. Because  $\mathbf{A}^H \mathbf{A} + \tau \mathbf{L}^T \mathbf{L}$  on the left hand side of this equation is a Hermitian matrix, the complex bi-conjugate gradient method becomes the general conjugate gradient with the complex form, as expected.

The Gauss-Newton method thus constructs a sequence of models with

$$m^{k+1} = m^k + \delta m \quad (4.25)$$

until the model converges.

## 4.5 Bi-Conjugate Gradient Method

In the preceding section, we defined the induced polarization forward problem to solve equation Equation 4.5 and the inverse problem to construct a sequence of models with increment defined by equation Equation 4.24, both are systems of complex matrices. Since, in practice, a moderate 3-D complex resistivity model always involves a large number of model parameters, solving these systems is numerically intensive. A fast method known as the complex-bi-conjugate gradient method can be used to solve these problems.

The elements of the bi-conjugate gradient method were first introduced by Lanczos (1952) for obtaining the eigenvalues of nonsymmetric real matrices. The method was later extended by Jacobs (1986) to treat complex non-symmetric matrix equations. To solve a complex matrix equation such as  $\mathbf{A}x = b$ , the complex bi-conjugate gradient method defines the following recurrence,

$$(a) \quad \text{Choose } x_0, \quad \text{set } r_0 = b - Ax_0 = p_0$$

$$\text{set } w_0 = \bar{r}_0, \text{ and } q_0 = \bar{p}_0$$

$$(b) \quad \text{For } k=1,2, \dots \text{ do}$$

$$z_k = c^{-1}r_k$$

$$\alpha_k = \frac{\langle \bar{r}_k, z_k \rangle}{\langle \bar{p}_k, Ap_k \rangle} = \frac{\bar{r}_k^H z_k}{p_k^H Ap_k}$$

$$(c) \quad x_{k+1} = x_k + \alpha_k p_k$$

$$r_{k+1} = r_k - \alpha_k Ap_k$$

$$w_{k+1} = w_k - \bar{\alpha} A^H q_k$$

$$(d) \quad p_{k+1} = z_k + \beta_k p_k$$

$$q_{k+1} = \bar{z}_k + \bar{\beta}_k q_k$$

$$\text{where } \beta_k = \frac{\langle \bar{r}_{k+1} \cdot z_{k+1} \rangle}{\langle \bar{r}_k \cdot z_k \rangle} = \frac{\bar{r}_{k+1}^H z_{k+1}}{\bar{r}_k^H z_k}.$$

The differences between this algorithm and the conventional conjugate gradient method is that the number of unknowns are doubled. However, for a complex symmetric matrix, i.e.  $A^T = A$  which is the case in the induced polarization forward problem Equation 4.6, the above algorithm can be simplified as follows:

$$(a) \quad \text{Choose } x_0, \quad \text{set } r_0 = b - Ax_0 = p_0$$

$$(b) \quad \text{For } k=1,2, \dots \text{ do}$$

$$z_k = c^{-1} r_k$$

$$\alpha_k = \frac{\langle \bar{r}_k \cdot z_k \rangle}{\langle \bar{p}_k \cdot Ap_k \rangle} = \frac{\bar{r}_k^H z_k}{\bar{p}_k^H Ap_k}$$

$$(c) \quad x_{k+1} = x_k + \alpha_k p_k$$

$$r_{k+1} = r_k - \alpha_k Ap_k$$

$$(d) \quad p_{k+1} = z_k + \beta_k p_k$$

$$\text{where } \beta_k = \frac{\langle \bar{r}_{k+1} \cdot z_{k+1} \rangle}{\langle \bar{r}_k \cdot z_k \rangle} = \frac{\bar{r}_{k+1}^H z_{k+1}}{\bar{r}_k^H z_k}$$

If  $A$  is Hermitian, i.e.  $A^H = A$  which is the case in solving the induced polarization inverse problem (Equation 4.23), the above complex bi-conjugate gradient algorithm becomes the complex form of the basic conjugate gradient algorithm, as expected.



## 4.6 Example

To illustrate the inversion method we invert synthetic data taken over a contaminated plume model shown in Figure 4-2. The model consists of a 70x70x40 meter plume embedded in a homogeneous background. The complex resistivity parameters of the background medium are based on laboratory data from Berea sandstone cores saturated with 0.01M *NaCl* solution with a pH value of 8, while data from 0.0096M *BaCl<sub>2</sub>* solution saturated cores are used to model the contamination plume parameters. The laboratory measurements used are from Frye *et al.* (1998). Data from five different frequencies used for the inversion with each model parameter at each frequency are shown in Table 4.1 and plotted in Figure 4-3. The IP data responses are simulated on a 5x5 electrode array and comprise 24 potential measurements for each of 9 current sources at frequency  $f = 0.01(Hz)$ ,  $f = 0.1(Hz)$ ,  $f = 1(Hz)$ ,  $f = 10(Hz)$ , and  $f = 100(Hz)$ , respectively.

The inversion results are shown in Figure 4-4, Figure 4-5, Figure 4-6, and Figure 4-7. The inversion results depict the plume in both the amplitude and phase frames. The frequency dependence of the plume resistivity is clearly detected. Although both the amplitude and phase values of the anomaly reveal somewhat under-determined natures, the variations of both values with frequencies are certainly almost identical to the "true" model's frequency response. Additionally, in this example we only consider IP response at five single frequencies, but the inversion method is general and by repeating the inversion procedure we can obtain more complete complex electrical properties of the sample over a large frequency band.

## 4.7 Conclusion

We have developed algorithms for forward modeling and inversion of spectral IP data in 3-D media. The algorithms accommodate a general earth model with a complex electrical resistivity as a function of frequency and 3-D spatial position. Given a complex resistivity structure, the forward modeling which predicts the complex electrical potential distribution is solved by a bi-conjugate gradient method. Because the linear system of the equation for the forward modeling has a complex symmetric conductance matrix, the bi-conjugate gradient method is simplified to a special form which is comparable to the (real) conjugate gradient method that is used in the d.c. resistivity forward modeling. Regularization and optimization techniques are employed to obtain stable solutions to the nonlinear inverse problem. In practice, because the imaginary part of both data and model are much smaller than their real parts, the inversion can be formulated in a compact form and solved completely in the complex domain. Such an approach achieves an efficient IP inversion. We have successfully applied our inversion technique to synthetic data from a known model, demonstrating the feasibility of interpreting spectral IP data directly in the frequency domain.

Sample Material	Frequency (Hz)	Amplitude ( $\Omega.m$ )	Phase (mrad)
Berea Sandstone + NaCl	0.01	12060	-6.42
Berea Sandstone + NaCl	0.1	11960	-8.35
Berea Sandstone + NaCl	1	11815	-7.69
Berea Sandstone + NaCl	10	11693	-7.11
Berea Sandstone + NaCl	100	11577	-7.10
Berea Sandstone + BaCl <sub>2</sub>	0.01	10327	-4.00
Berea Sandstone + BaCl <sub>2</sub>	0.1	10244	-5.14
Berea Sandstone + BaCl <sub>2</sub>	1	10164	-4.77
Berea Sandstone + BaCl <sub>2</sub>	10	10094	-4.30
Berea Sandstone + BaCl <sub>2</sub>	100	10027	-4.16

Table 4.1: Complex resistivity parameters of the model

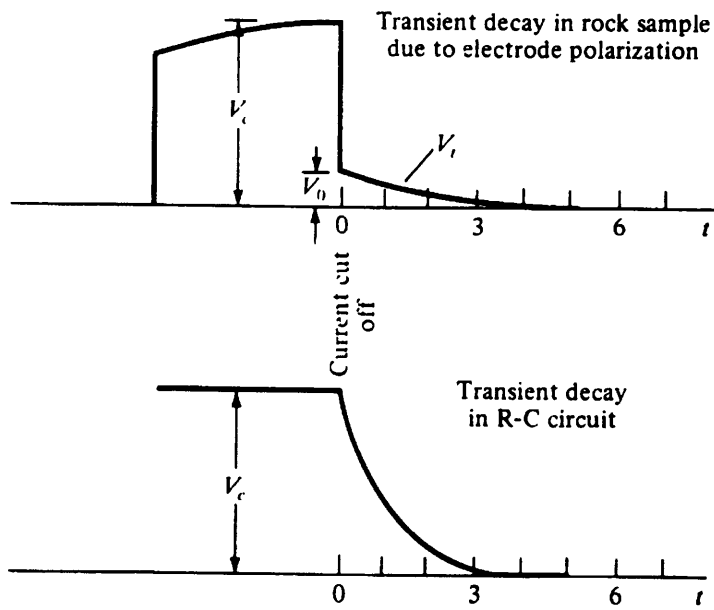


Figure 4-1: Comparison of IP and R-C decay curves.

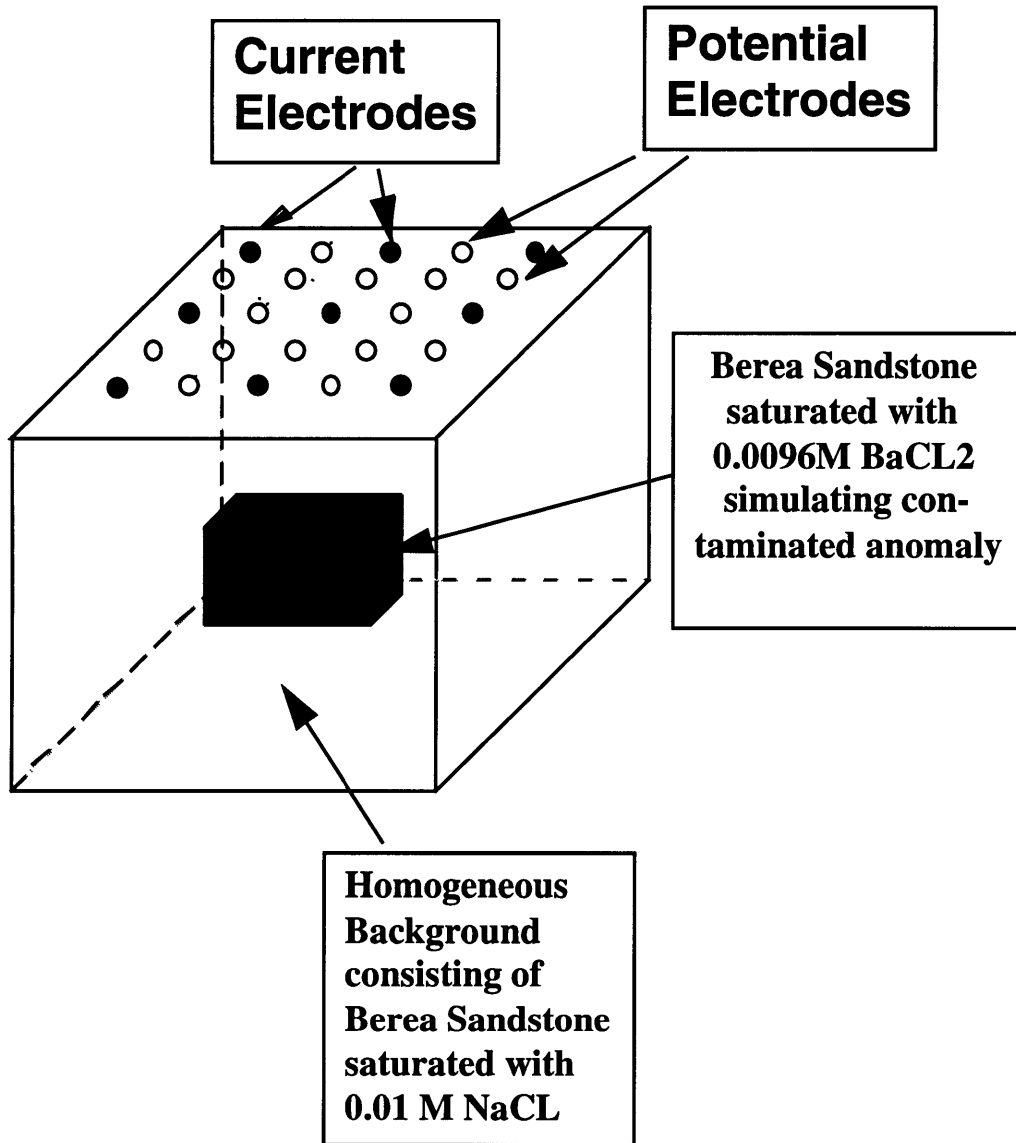


Figure 4-2: Simple model of a contaminated plume embedded in a homogeneous background. The complex resistivity parameters as a function of frequency are based on the laboratory results. Synthetic IP data were computed for the electrode array at the surface.

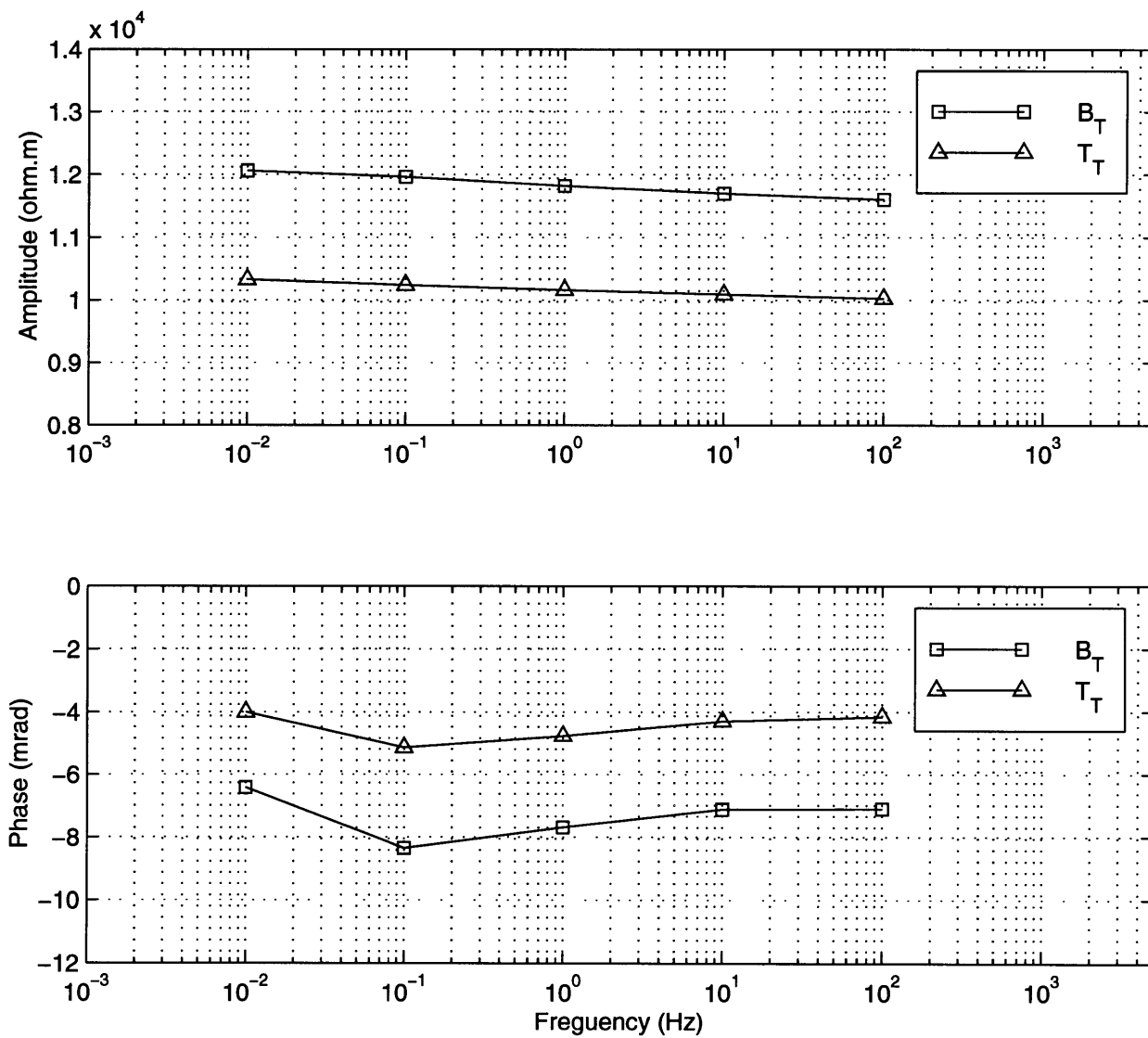


Figure 4-3: Frequency variations of amplitude and phase for the two materials (Berea sandstone saturated with  $0.01M NaCl$ , and Berea sandstone saturated with  $0.0096M BaCl_2$ ).

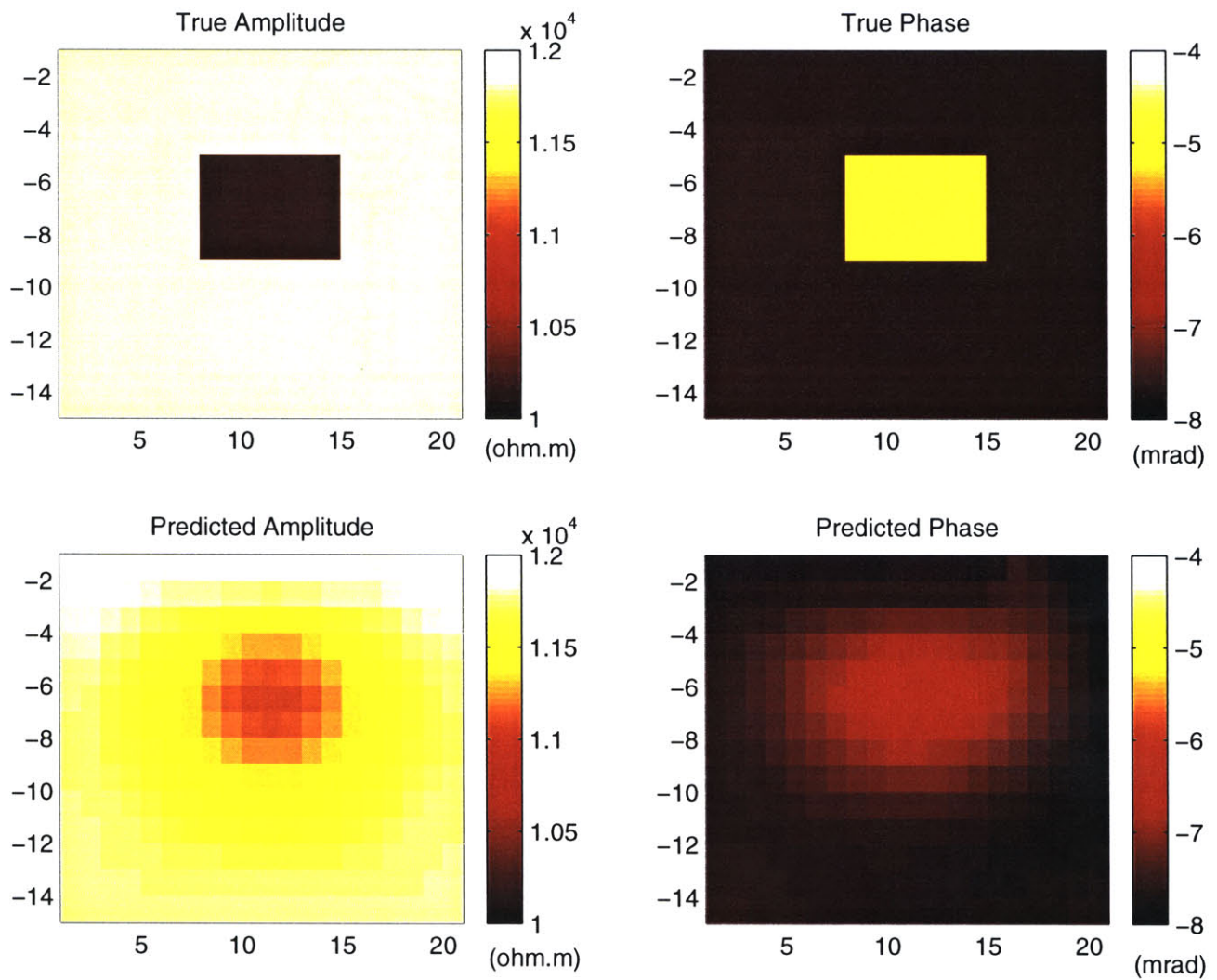


Figure 4-4: Inversion images for  $f=1$  hz (bottom) are compared to the "true" model (top). Each frame shows a cross-section through the center of the 3-D model. The amplitude of the complex resistivity is shown on the left, and the phase is shown on the right.

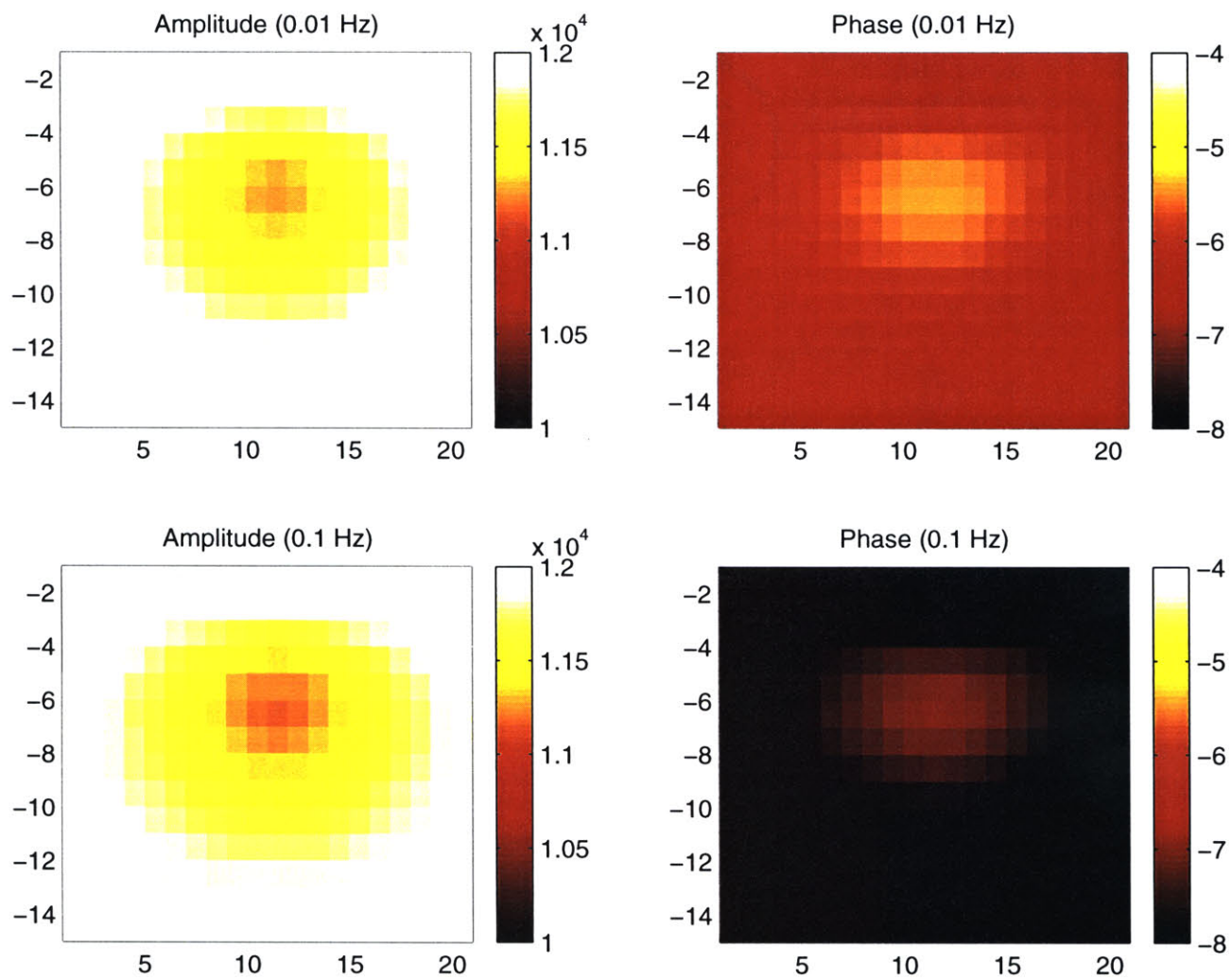


Figure 4-5: Inversion images for  $f=0.01$  hz (top) and  $f=0.1$  hz (bottom). The amplitude of the complex resistivity is shown on the left, and the phase is shown on the right.

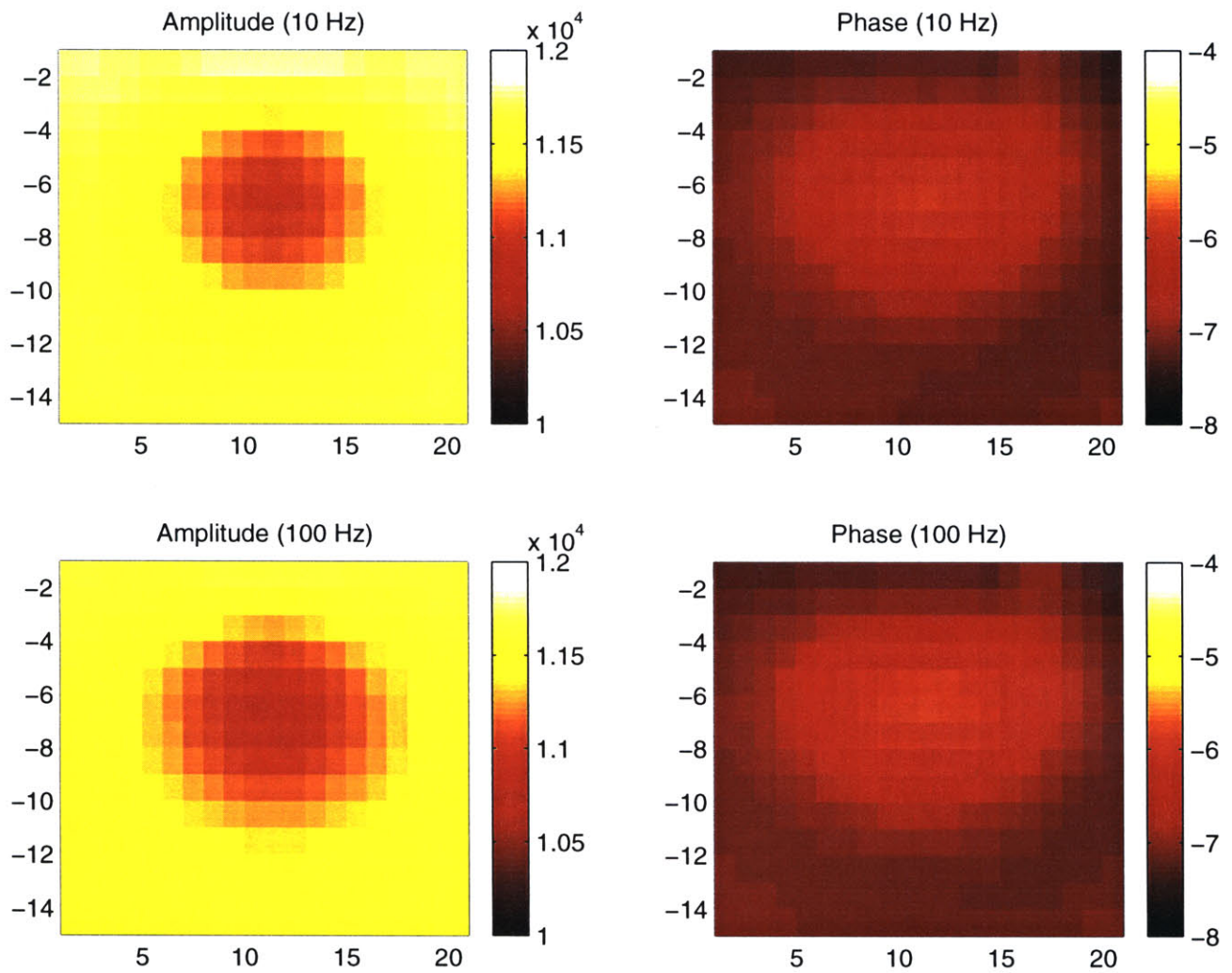


Figure 4-6: Inversion images for  $f=10$  hz (top) and  $f=100$  hz (bottom). The amplitude of the complex resistivity is shown on the left, and the phase is shown on the right.



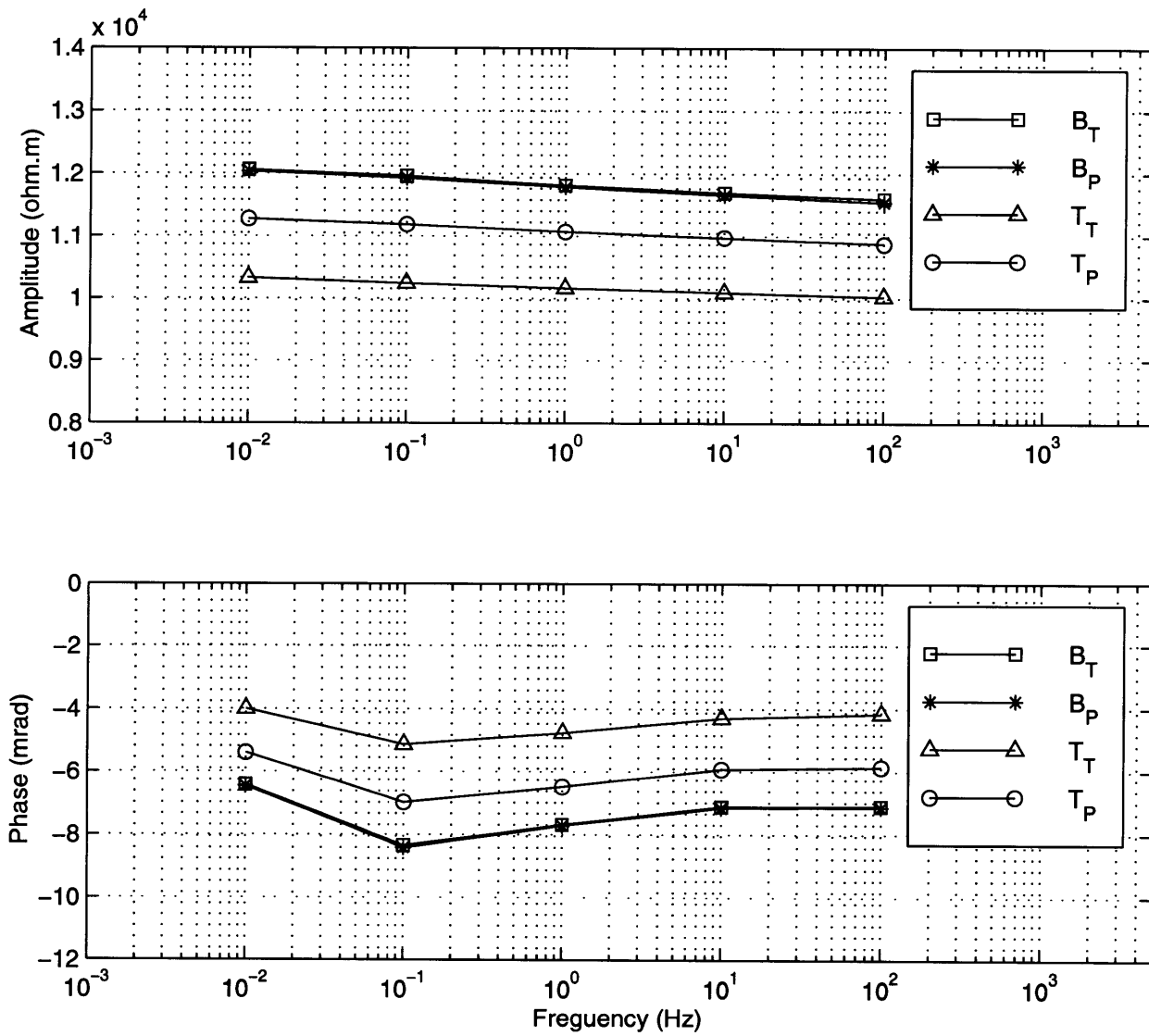


Figure 4-7: Comparison of the true and the inverted frequency variations of the amplitude and phase of the two materials (Berea sandstone saturated with 0.01M  $NaCl$ , and Berea sandstone saturated with 0.0096M  $BaCl_2$ ).

# Chapter 5

## Inversion of Electrical Self-Potential Data

### 5.1 Introduction

Self-Potential (SP) refers to a naturally induced electrical field from a source in the subsurface of the earth. There are four principal mechanisms producing these potentials (Telford *et al.*, 1990). Electrokinetic potential, also known as streaming potential, is observed when a fluid is forced through a porous medium. The resultant potential depends on the product of the pressure gradients, the electrical resistivity structure of the material, and the cross-coupling coefficients between the fluid flow and the electrical properties. The diffusion potential is caused by the difference in mobilities of various ions in solutions of different concentration and is proportional to the logarithm of the solution concentrations. The shale potential, which also is proportional to the logarithm of the solution concentrations, is caused by immersing two identical metal electrodes in a solution with different concentrations at the two

electrodes. The mineralization potential, which is especially pronounced in metallic zones such as sulfides, graphite, and magnetite, is caused by an oxidation reaction on the mineral bodies.

The SP method is based on measurements of the surface electrical potential field, and from these measurements locations of subsurface current source are inferred. Because the SP anomalies are associated with subsurface fluid flow, heat transfer, and the movement of ions, the use of the SP method has a great advantage in characterizing sources associated with these phenomena. The SP method was first introduced in mineral exploration (Sato and Mooney, 1960) and recently the method has been increasingly employed in the investigation of underground water movement (Sill, 1983) and monitoring the migration of environmental contaminants (Vichabian, 1997). Because the method offers relatively rapid field data acquisition it is a cost effective means for reconnaissance and initial field investigation of an area prior to more extensive geophysical studies.

Quantitative interpretation of SP data is difficult. In the early years, interpretations of SP data was done mostly qualitatively. The shape of the SP anomaly and its extent were indicated by the contour map of equal-potentials. The depth of the SP source was approximated as the same order of half the distance of the total width of the anomaly at half the maximum magnitude. The attitude of the source body also was obtained from the symmetry of the anomaly profile. Such qualitative interpretation has proven useful in many cases where the SP data primarily were used to indicate locations for more detailed geophysical investigations. In order to help provide more information about the depth, location, and configuration of anomaly sources, the use of geometric interpretation techniques were later developed by many authors (Corwin *et al.*, 1981; Fitterman, 1979, 1984). Geometric interpretation involves the use of calculated curves and contours, generated by relatively simple SP source models, to match the observed field data. Available models include polar-

ized points, lines, cylinders, spheres, sheets, and other geometric forms (Corwin *et al.* 1981). Although these techniques are useful, they have limitations when source structure becomes complex, especially in the presence of a complex resistivity distribution. The use of these techniques becomes extremely difficult and impractical under these conditions.

In this chapter, a new technique for modeling and inverting the SP data to recover a 3-D subsurface electrical current source distribution is presented. The technique is based on the idea that the subsurface electrical current sources can be considered as multi pairs of dipole current sources with arbitrary intensity, orientation, and spatial extent. Therefore the SP voltages are produced by such distributed current sources with the current passing through the specific subsurface resistivity structure. Using this technique for SP problems provides a new flexibility in the interpretation of SP data.

Once the inversion procedure is established, another major difficulty in the interpretation of SP data is the problem's non-unique nature. The second objective of this chapter is to investigate the non-uniqueness and possible reduction in non-uniqueness by appropriately constraining the resistivity structure and the source location, magnitude, and dimensions.

## 5.2 Formulation of the Forward Modeling

The electrical SP forward problem is to solve the surface electrical potential field given the surface electrical resistivity structure and source current distribution. The source current distribution is governed by the conservation of current law,

$$\nabla \cdot \left( \frac{1}{\rho(\mathbf{x})} \nabla v(\mathbf{x}) \right) = -j(\mathbf{x}) \quad (5.1)$$

where  $j(\mathbf{x})$  is the current source,  $\rho(\mathbf{x})$  is the resistivity of the media, and  $v(\mathbf{x})$  is the electric potential field. In the problem of resistivity inversion, one is interested in recovering the resistivity structure, however the goal of the SP inversion is to recover the current source distribution  $j(\mathbf{x})$ . Using the network analogy, a linear system of equations is constructed,

$$\mathbf{K}v = s \quad (5.2)$$

where  $v$  is a vector of the potentials at the network nodes,  $s$  is the current source vector, and  $\mathbf{K}$  is a real, symmetric, and positive-definite matrix which depends on the resistivities and dimensions of the network cells. On the surface of the earth, it is necessary to use the Neumann boundary condition,  $\partial v / \partial \hat{n} = 0$ , where  $n$  is the direction normal to the boundary. On portions of the boundary inside the earth, an exact boundary condition is not available but various approximate boundary conditions including Dirichlet and mixed boundary conditions can be used (see chapter 3, section 1). A linear conjugate gradient algorithm implemented with the incomplete Cholesky preconditioning is used to efficiently solve the forward problem. Comparing this forward modeling with the forward modeling of d.c. electrical resistivity, one finds that, except for the fact that the source nature is different, the forward modeling procedures are identical.

A synthetic test model is designed to demonstrate the forward modeling algorithm. The test model is constructed of a horizontal dipole current source inside a 50x50 square meter homogeneous background ( $\rho = 1000\Omega m$ ). The surface electrical potential responses are calculated for various dipole current source depth locations (Figure 5-1). The results show that the deeper the current source is buried, the broader and less sharp the surface anomaly becomes. Although this example is based on a single dipole source inside a homogeneous earth model, the forward modeling itself is capable of computing the surface potential for cases with randomly distributed multi-current sources in inhomogeneous earth models.

### 5.3 Inversion Method

A practical electrical SP inverse problem may be defined as follows: given a finite set of electrical potential measurements  $d = (d_1, d_2, \dots, d_M)$  made at the earth's surface, determine the intensity and location of subsurface current sources  $s$ . The relation between  $d$  and  $s$  may be written via the standard inverse problem,

$$d = \mathbf{G}(s) + e \quad (5.3)$$

where  $\mathbf{G}$  represents the forward modeling operator that maps a current source vector to a theoretical data vector, and  $e$  is an error vector. Like most ill-posed geophysics inverse problems, the SP inverse problem is inherently non-unique. Solution of the inverse problem also is made by incorporation of the Tikhonov regularization where a solution is defined to jointly minimize the data misfit and a "stabilizing functional,"

$$\psi = (d - \mathbf{G}(s))^T R_{dd}^{-1} (d - \mathbf{G}(s)) + \tau \|W(s - s_0)\|^2 \quad (5.4)$$

where  $\Psi$  is the objective functional to be minimized,  $R_{dd}$  the data covariance matrix,  $W$  a linear operator,  $\tau$  a regularization parameter, and  $s_0$  the *a priori* model. The first term in the objective function measures the data misfit, it is the likelihood function when noise contaminating each observed data has Gaussian distribution with zero mean and variance  $R_{dd}$ . The second term defines the stabilizing functional as a regularization term which helps to constrain the model. Due to high sensitivities in the region near the surface, the SP inversion tends to find the solution that depicts the current sources near the surface. In order to overcome this problem, knowledge from geologic information and other geophysical data can be introduced to constrain the current source intensity or location through a proper choice of  $W$ , in the following combinations,

*No constraint*

$$W = 0 \quad (5.5)$$

*Uniform damping*

$$W = Identity \quad (5.6)$$

*Spatial constraint, while( $s_0 = 0$ )*

$$W = W(x, y, z) \quad (5.7)$$

*Source constraint, while( $s_0 \neq 0$ )*

$$W = W(x, y, z) \quad (5.8)$$

Since the surface potential data is linearly dependent on the subsurface current source, the inversion is linear and can be solved by a one step Gauss-Newton method. Assuming the starting model in  $s_0$ , the final model can be written as

$$s = s_0 + \delta s \quad (5.9)$$

with

$$\delta s = (A^T R_{dd}^{-1} A + \tau W^T W)^{-1} [A^T R_{dd}^{-1} (d - G(s)) + \tau W^T W (s_0 - s)] \quad (5.10)$$

## 5.4 Non-uniqueness

To study the non-uniqueness of the SP inversion, a synthetic model is designed. The model contains a dipping dipole located at about 100 m below the surface. The medium has a homogeneous background ( $100\Omega.m$ ) with a resistive layer ( $1000\Omega.m$ ) at the near surface. There are 60 electrodes deployed in the medium, with 30 placed on the surface and 30 in boreholes. The SP data are generated by forward modeling with a 1% random noise added (Figure 5-2).

In the beginning of the test, only the surface SP data are used for the inversion. The results of the SP inversion for the synthetic model are found to be extremely

non-unique. In fact one can obtain perfect data fits by appropriately adjusting the location, magnitude of current source and source dimensions. Without knowing the resistivity structure and without using any constraint, the inversion finds a solution which depicts the current dipole at the surface with a perfect data fit (Figure 5-3) (top). The current distribution is unsymmetric due to the near surface resistivity inhomogeneity. When the correct resistivity structure is applied, the inversion result (Figure 5-3) (bottom) gives a somewhat more symmetric, better current source distribution on the surface, but the perfect data fit still remains.

By using both the borehole and the surface data in the inversion, the inversion result places the current source at a more accurate depth location but exaggerates the size (Figure 5-4). However, because of the high sensitivities near the surface, the inversion still tends to place part of the current sources on the surface area. To further constrain the inversion result, we employ a depth constraint by imposing a depth varying operator,  $W(x, y, z) = W(z)$ , to the objective function. Specifically, we use  $W(z) = 1.0e + 7$  when  $z \leq 100m$  and  $W(z) = 0$  when  $z > 100m$ . With this constraint, the inversion returns a source distribution with a more accurate size (Figure 5-5). We then further impose a magnitude constraint on the current source, i.e. we force the magnitude of the source to be  $|s| = 1$ , the inversion finds a solution which is identical to the true model (Figure 5-6). These exercises show that with additional constraints the nonuniqueness can be reduced to some extent. However, a complete elimination of the nonuniqueness is extremely difficult, it requires further constraints. These constraints may be attainable in practice.



## 5.5 Field Example

In the spring of 1996, a SP survey was conducted to investigate the groundwater contamination associated with fuel leakage at the Massachusetts Military Reservation (MMR).

The MMR is located in western Cape Cod, about 60 miles south of Boston. There are various Department of Defense (DOD) operations housed at the reservation including the US Coast Guard, the US marine Corps, the National Guard, the US Army, and the US Air Force. In 1986, the National Guard Bureau's Installation Restoration Program was initiated to investigate suspected contaminant plumes at the MMR.

Our investigation was conducted at the FS-12 jet fuel plume. The source area of FS-12 is at the intersection of Green way road and the western entrance of the L-firing range, about 3000 ft north of Snake pond (Figure 5-7). Leakage from an underground fuel pipeline during 1972 resulted in an estimated spill of 70000 gallons, mainly aviation gasoline and JP-4 jet fuel. The pipeline which was built in the early 1960s, transports fuel from the Cape Cod canal to the National Guard flight line. The contaminants of greatest concern are Benzene and Ethylene Dibromide (EDB) because they are the ones with the greatest potential health hazard. The direction of the plume migration is south-southeast-ward (HAZWRAP, 1995).

Figure 5-8 shows the extent of the Benzene contamination. The greatest level of contamination in the source area is 2000 ppb, at depth of 100 feet. In the down gradient, the maximum plume concentration is shifted to 150 feet. The vertical geologic cross-section and the relative plume location (Figure 5-9) show that the subsurface of FS-12 consists of outwash sands and gravel with discontinuous lenses of sand, silt, and clay down to at least a depth of 130 ft below the water table. The

majority of the aquifer is confined by deep clay layers, or bedrock. The surface soil is about 2-5 feet, on average. The interval typically consists of silty clay or clay silt, with a mixture of fine sand or organic matter. A layer of sand and gravel outwash deposit lies below. The sand and gravel serve as a primary aquifer for municipal and residential water supply wells.

A Soil Vapor Extraction (SVE) system and an Air Sparging (AS) system are currently in operation to remove fuel at the source area of FS-12. The components of systems include vacuum pumps, control valves which adjust air flow, pressure gauges, flow meters at well heads, air-liquid separation, and air treatment. The AS system is accomplished by injecting air under pressure below the water table. It is expected that contaminants located within air flow pathways will volatilize or biodegrade. The SVE system began operation on Oct 23, 1995, the AS began on Feb 21, 1996. As of Feb 1997, an estimated 19,147 kilograms of product had been removed from the site. At the time of our SP measurements, the entire system was shut down. On all other days, the system is in operation.

Figure 5-10 shows the location of electrodes deployed in seven lines at FS-12. Each electrode is placed at a 25 ft interval, with potential measured with respect to a point far away from the source area. A large negative anomaly with a maximum value of 600 mv, covering a range of 300 ft down gradient from Green Road was observed (Figure 5-11). The estimated depth of the water table in this region is around 100 ft deep from the well log information. A Wenner array sounding is performed and the corresponding apparent resistivity data are shown in Figure 5-12. A 1-D resistivity inversion was then carried out and the inversion results are shown in Figure 5-12. The resistivity data shows a small decreasing resistivity as the depth approaches the water table and then a gradually increasing resistivity as the depth crosses the water table. This increase in resistivity is caused by the highly resistive contaminant plume. The resistivity value starts to decrease as it passes the contaminant plume and then

increases again as the depth approaches bedrock.

A 3-D model consisting of 26x20x15 grid cells covering 624x480x300 ( $ft^3$ ) is chosen for the inversion. All the electrodes are placed on the surface layer, the observations of SP on these electrodes are inverted to reconstruct the subsurface electrical current source. The input resistivity values for each cell is obtained from our 1-D resistivity inversion results. A homogeneous current model ( $s = 1 \text{ Am}$ ) is chosen as a starting model for the SP inversion.

We first conduct an inversion without any spatial constraint. As expected, the inversion results shown in Figure 5-13 depict all the current source anomalies on the surface. This is certainly unrealistic. We then use the information of the depth location of the contaminant plume from other sources of measurement such as the the well log data and the apparent resistivity data, as mentioned earlier, to constrain the location of the plume. Specifically, we add a spatially varying damping coefficient which permits the majority of the electrical current source variation to take place below the water table. With this depth constraint, the inversion locates an egg-shaped anomaly below the water table with a spatial extent of 160 ft in range and 50 ft in depth (Figure 5-14). The center point of this current anomaly has a magnitude of  $-15(am)$ . This inversion result is compared to the previously measured concentration information of Benzene, shown in Figure 5-8. A comparison of the results shown in Figure 5-15 and Figure 5-16 at a vertical and a horizontal cross-section cutting through the groundwater monitor well GMW-51 reveal a coherent match. The actual electrochemical cause of the SP anomaly is not fully understood and is currently under study.

## 5.6 Conclusion

In this chapter, we develop a methodology for the inversion of 3-D electrical Self-Potential data. By measuring the electrical potential on the earth surface or boreholes, the distribution of subsurface electrical current, induced by underground mechanical and electrochemical activities, is recovered. This inversion is inherently non-unique. In fact one can obtain a perfect data fit by appropriately adjusting the location, magnitude and dimension of the electrical current sources. To reduce the nonuniqueness, the regularization constraints are justified and extended to a broader range of formulation including constraints on the resistivity structure and constraints on position, orientation, magnitude, and dimension of the SP source geometry. With these constraints, the nonuniqueness can be reduced to some extent, however, it is difficult to completely eliminate the nonuniqueness. In practice, the success of SP inversions is highly dependent on one's knowledge of the resistivity structure and reasonable estimation of the geometry and location of the source.

We conduct a 3-D electrical Self-Potential tomography to investigate a groundwater contamination associated with a jet-fuel leakage at Massachusetts Military Reservation in Cape Cod, Massachusetts. With the information of the possible location of the contaminant plume, the inversion describes a shape of the contaminant plume which matches the results of the concentration information obtained by monitoring wells.

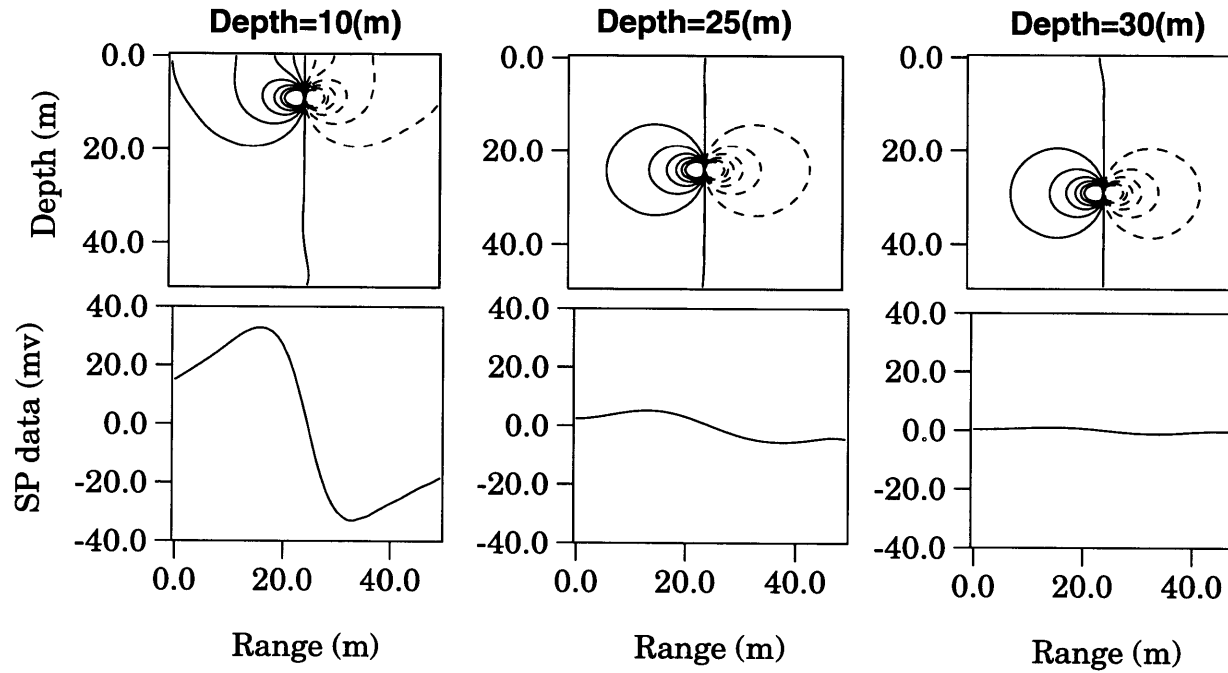


Figure 5-1: The surface electrical potential responses computed by the forward modeling for a dipole current source located at a depth of 10 m (left), 25 m (middle), and 30 m (right). The results show that the deeper the current source is buried, the broader and less sharp the surface anomaly becomes.

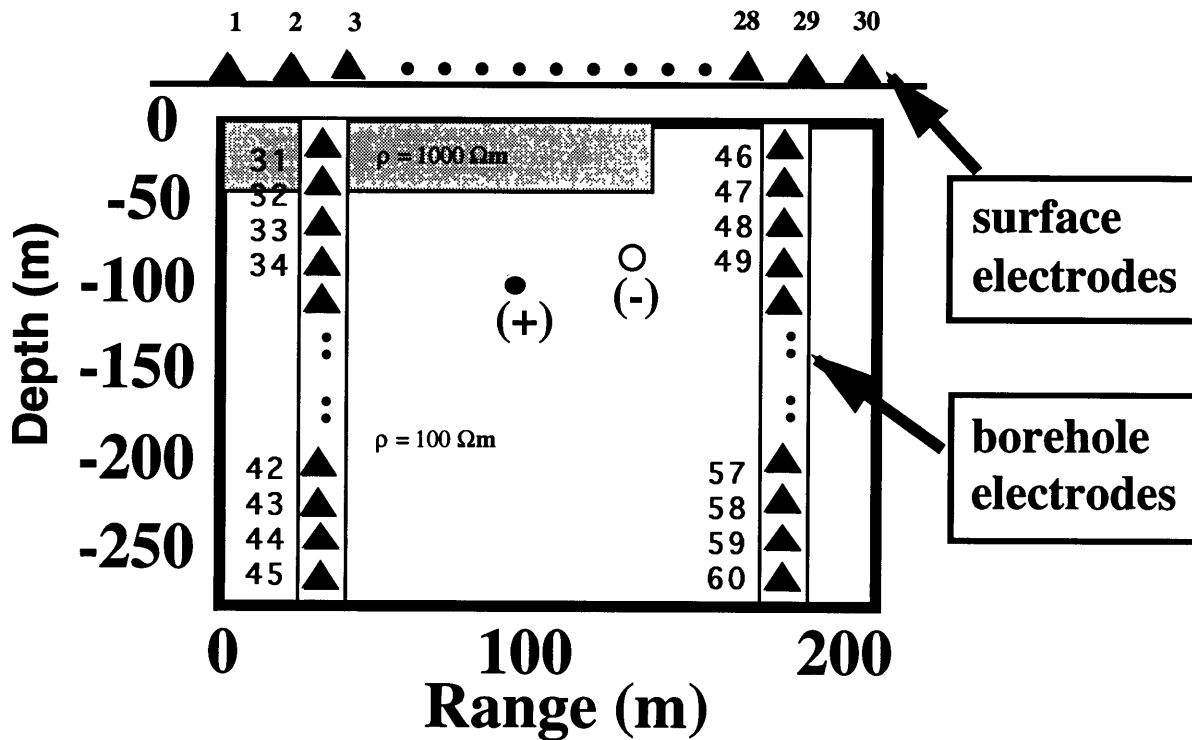


Figure 5-2: The synthetic model consists of a dipping dipole located at about 100 m below the surface. The medium has a homogeneous background and a resistive layer near the upper left corner. There are 60 electrodes deployed in the medium, with 30 placed on the surface and 30 in boreholes. The SP data are generated by forward modeling with 1% random noise added.

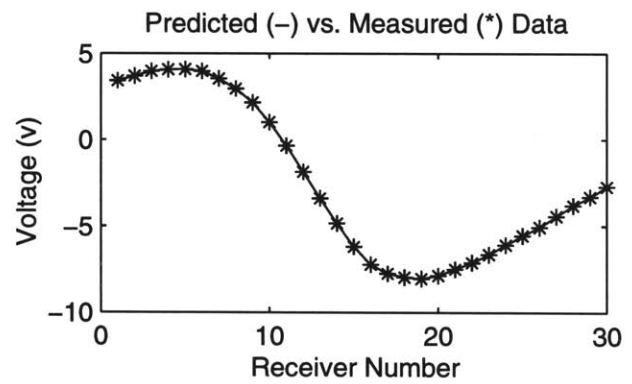
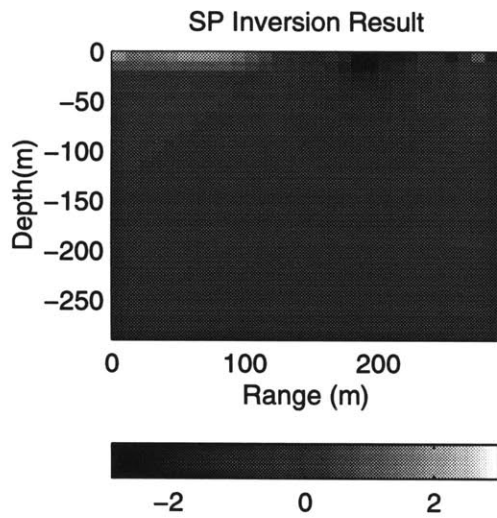
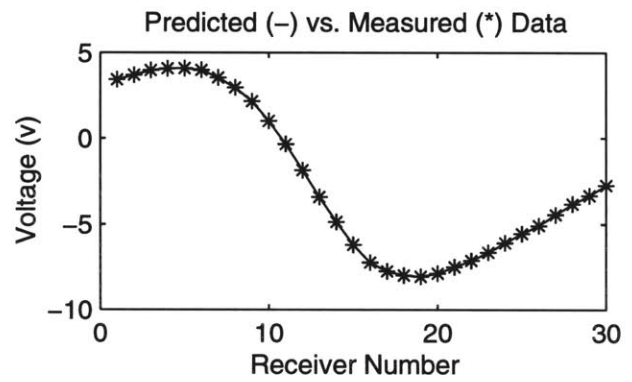
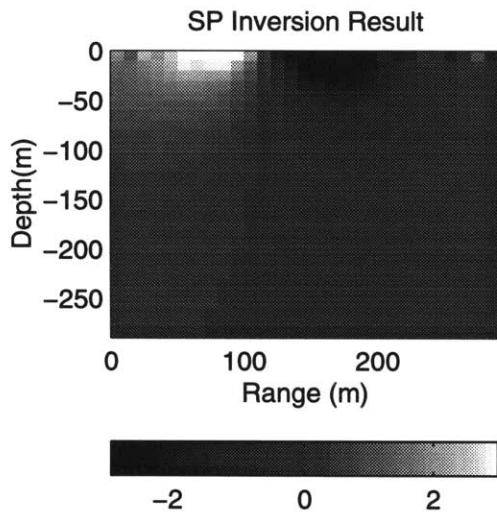


Figure 5-3: The inversion results obtained by using only the surface data. Both results, with (bottom) and without (top) the resistivity constraint, depict the current anomalies near the surface. The unit of the color scale is (mA).

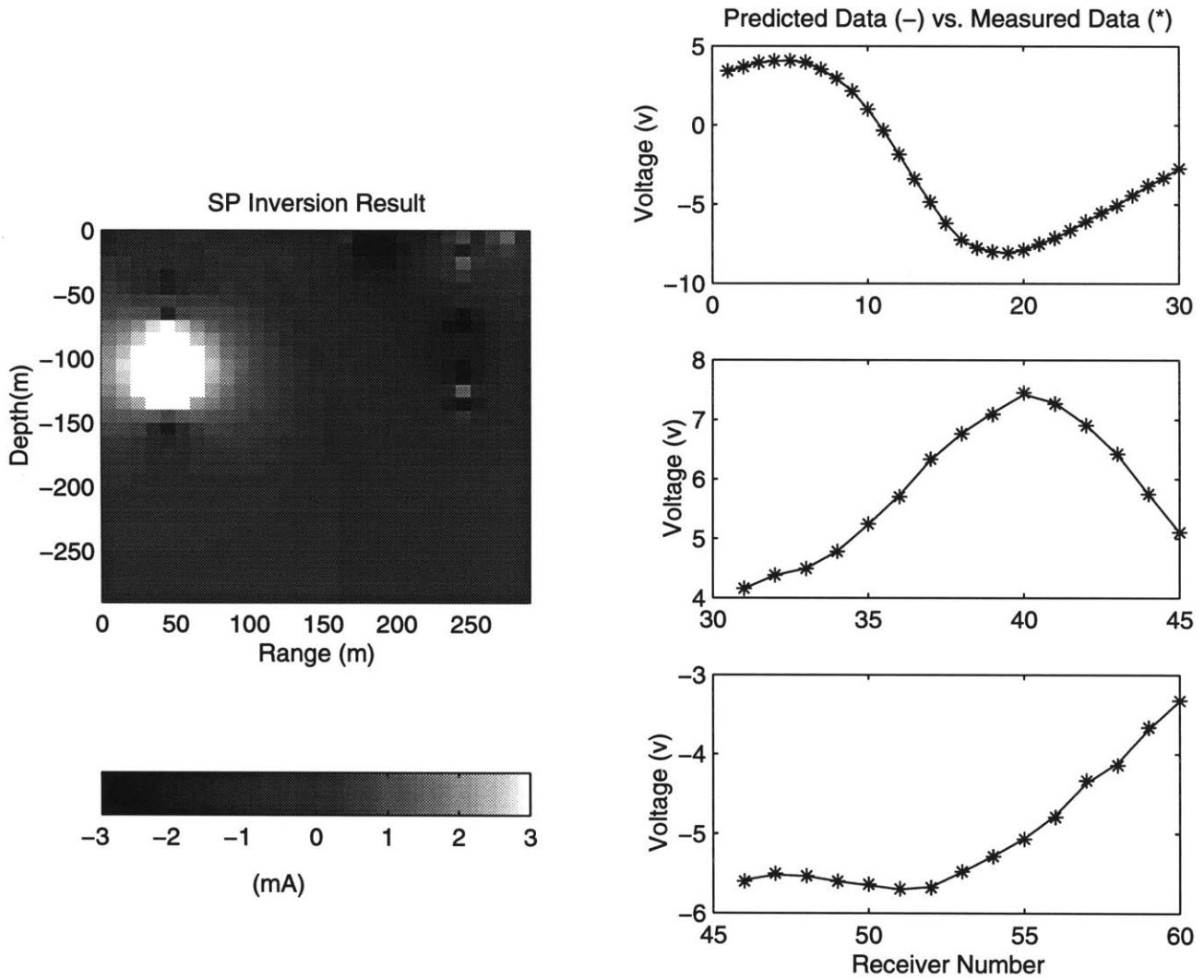


Figure 5-4: The inversion obtained using both the surface data and the borehole data. The current anomalies are mapped to the places near the surface and the places near the boreholes.



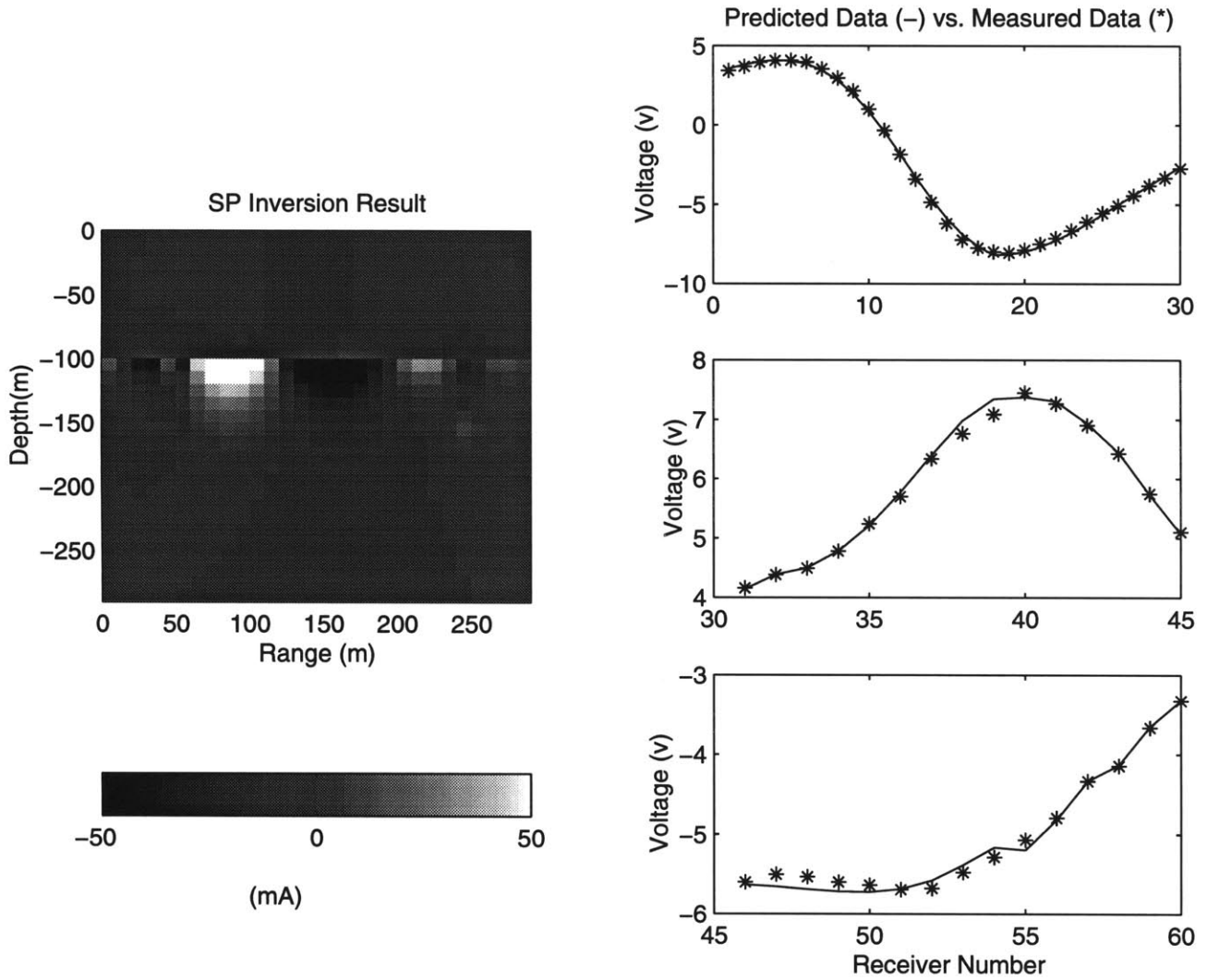


Figure 5-5: The inversion results obtained using both the surface data and the bore-hole data. A depth constraint is applied to this inversion.

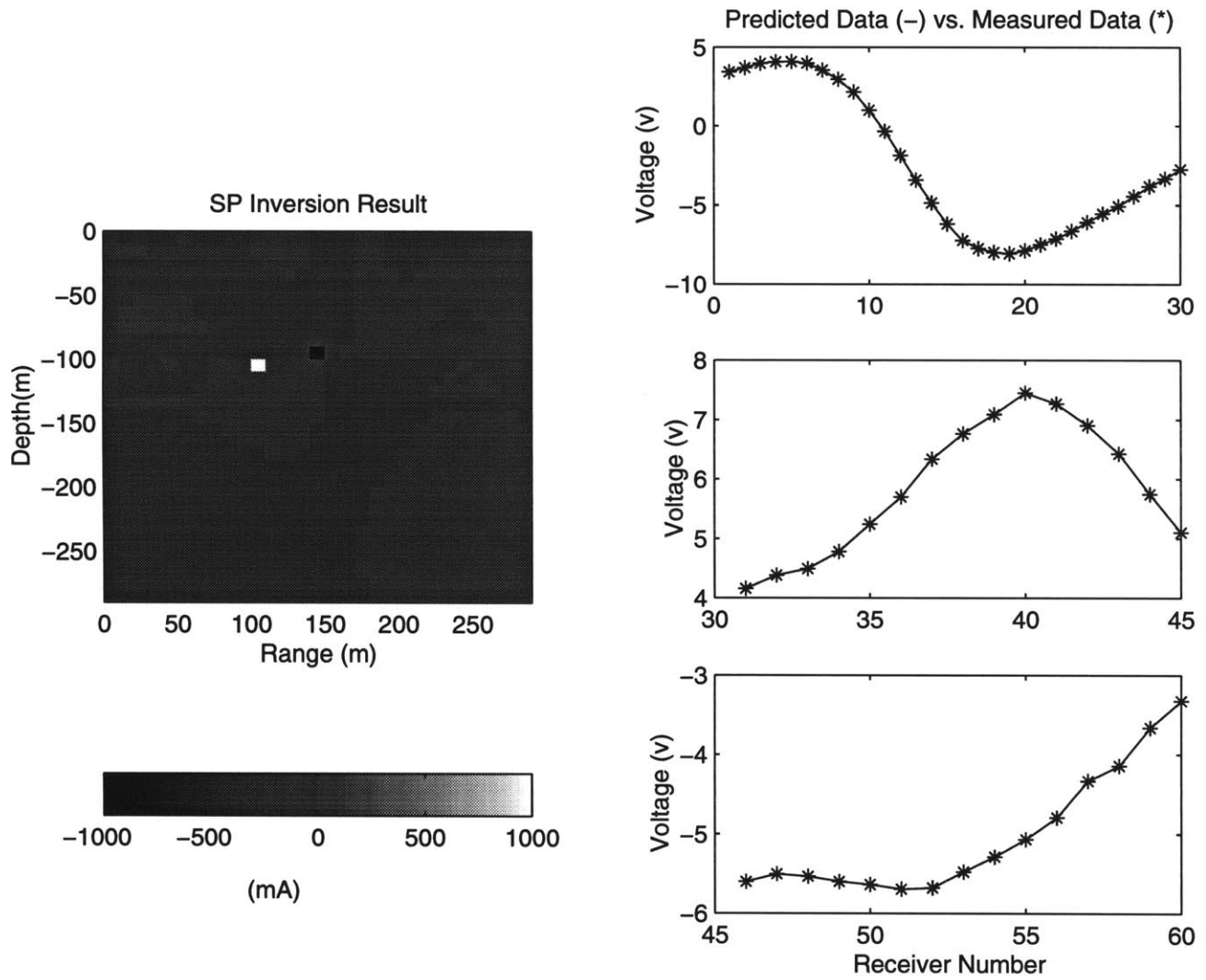


Figure 5-6: The inversion results obtained using both the surface data and the bore-hole data. A magnitude constraint is applied to this inversion.

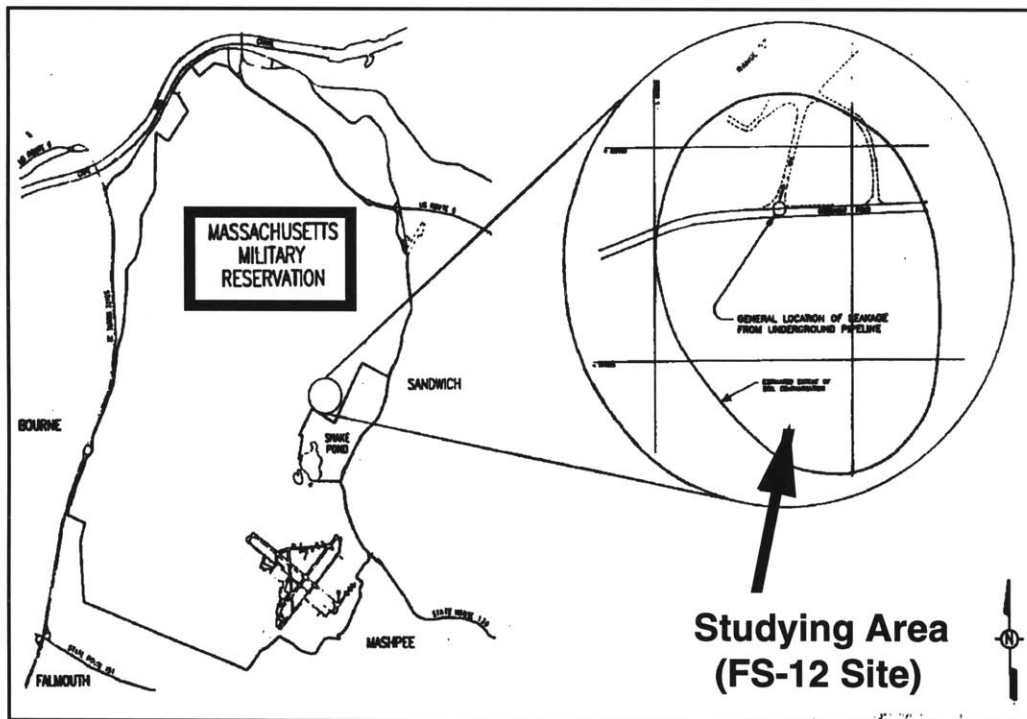


Figure 5-7: Our study area is located at the FS-12 fuel plume at the Massachusetts Military Recreation (MMR), Cape Cod, Massachusetts.

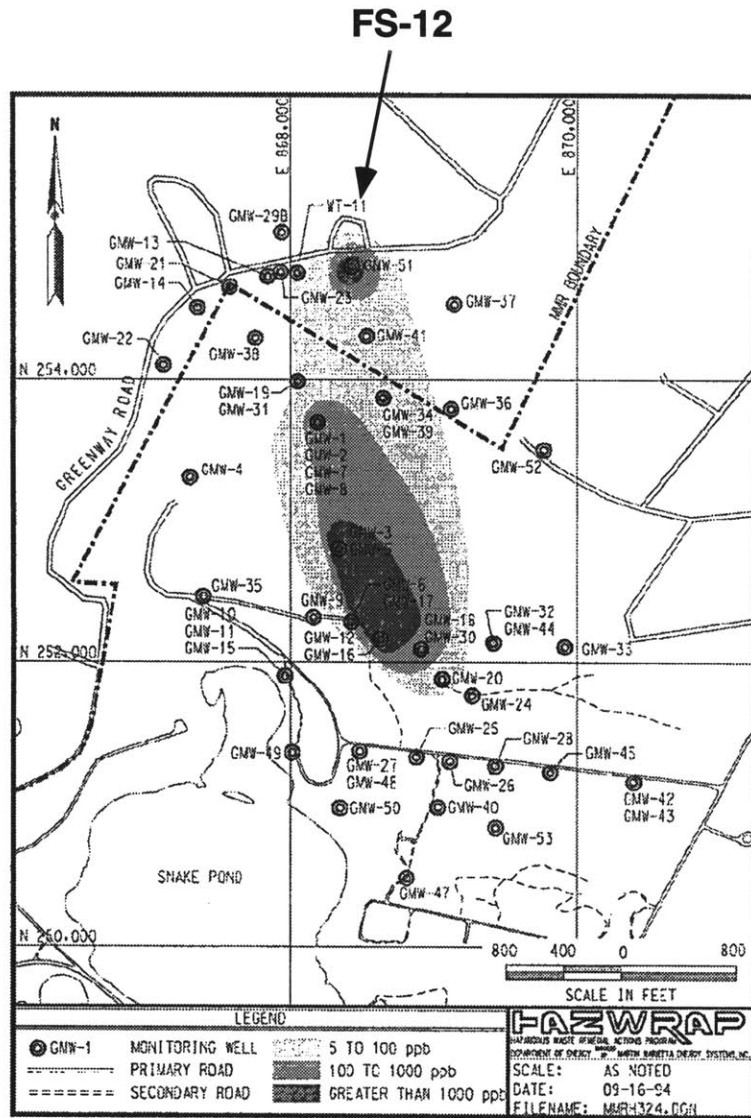


Figure 5-8: Extent of contamination of Benzene at the FS-12 study area (modified from HAZWRAP (1995)).

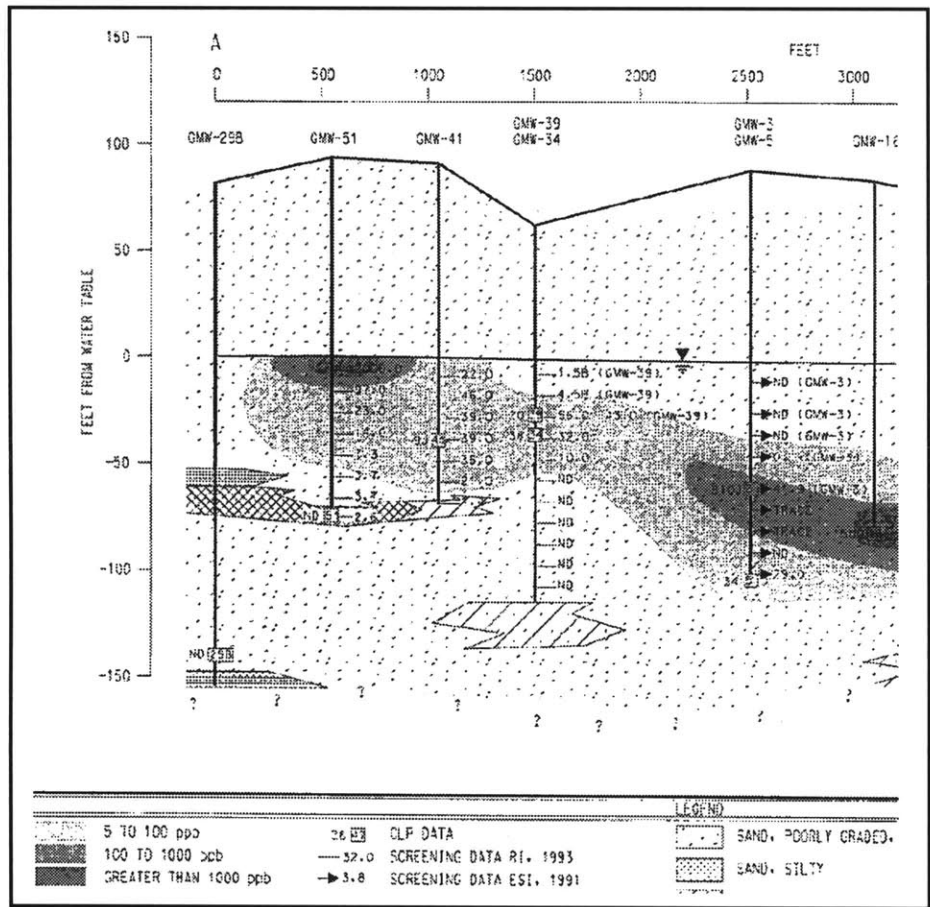
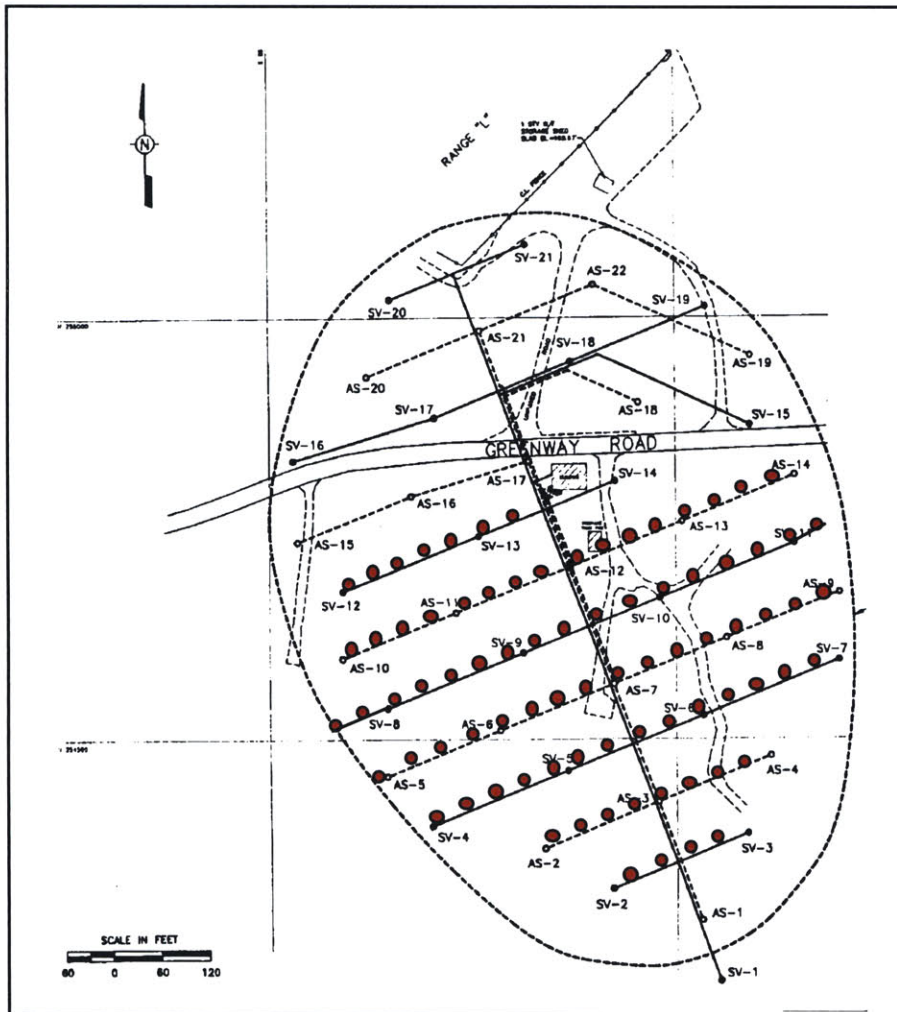


Figure 5-9: Vertical geology and the extent of contamination of Benzene at the FS-12 study area (modified from HAZWRAP (1995)).



- Air Sparging Wells (AS)
- Soil Venting Wells (SV)
- Electrodes

Figure 5-10: The experiment site and the surface electrode configuration. There are a total of seven lines of electrodes deployed on the surface. Each survey line is laid along the same line as of the soil venting wells and the air sparging wells.

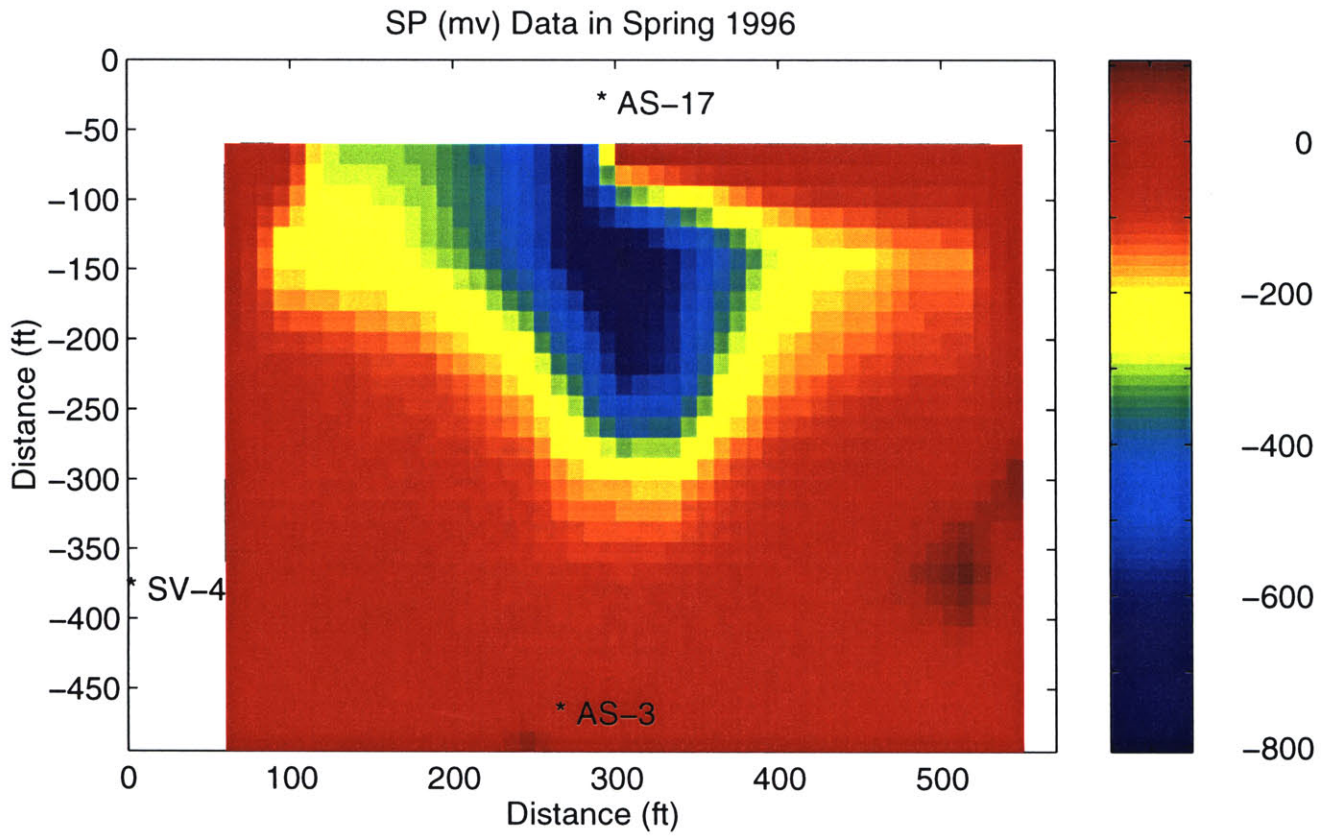


Figure 5-11: A strong SP anomaly with the approximate extent of  $300 \times 200$  ( $ft^2$ ) is found in FS-12 studying area. The x-z position of (300,0) on this plot is the position point where the Green way Road crosses the vertical center line of our surveys, as indicated in Figure 5-10.

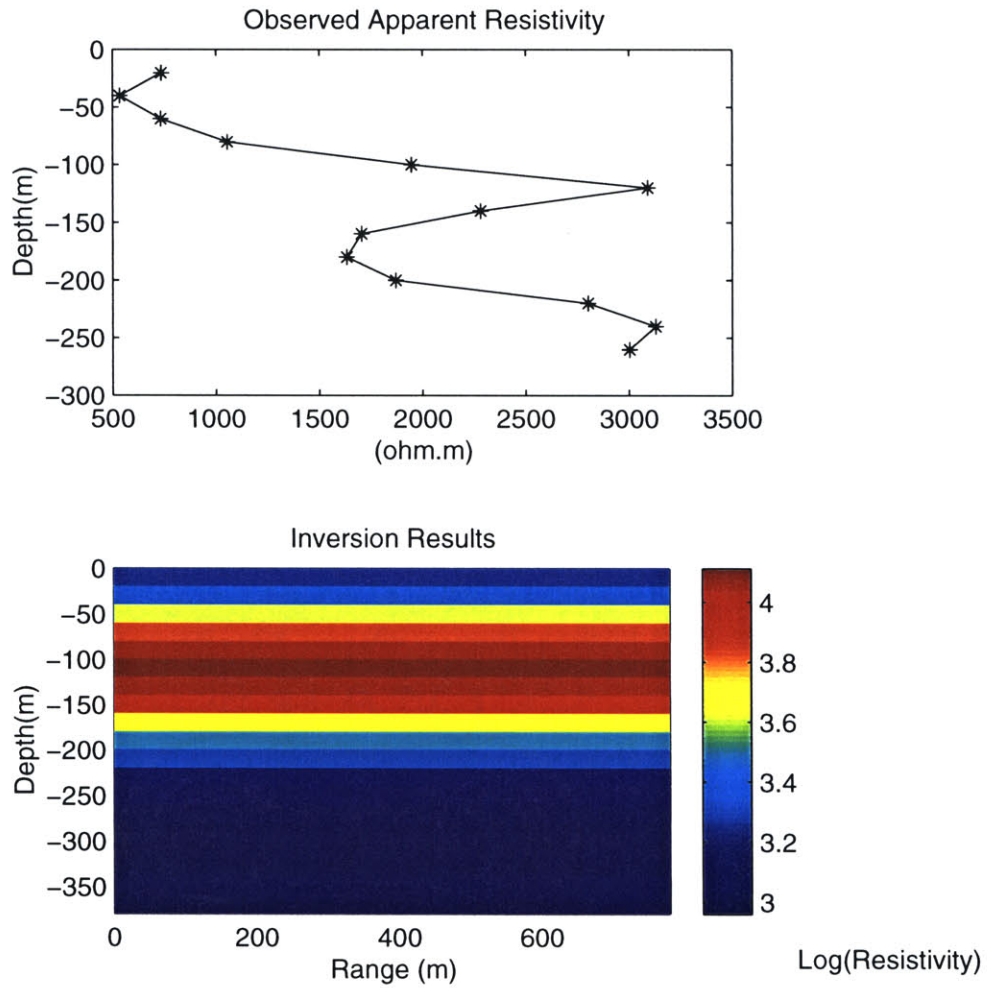


Figure 5-12: The apparent resistivity (top) and the inverted resistivity based on a 1-D earth model (bottom). The resistivity data reaches a maximum value when the depth crosses the water table which is approximately 100 ft deep in this area. The deeper resistive anomaly on the apparent resistivity probably corresponds to the location of 'bedrock'.



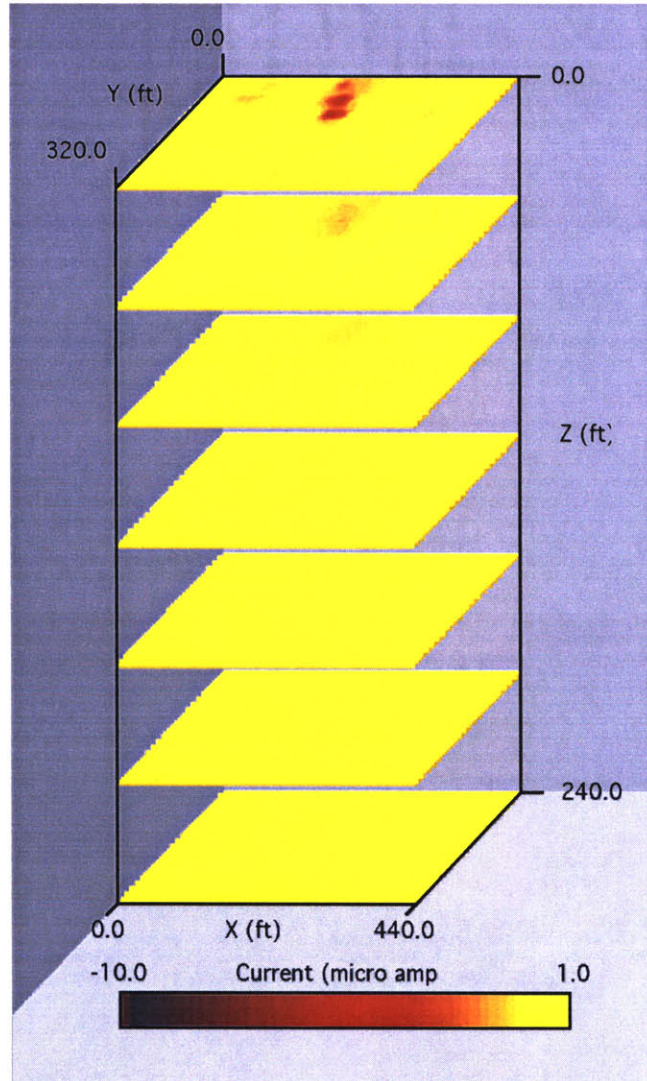


Figure 5-13: The inversion results without any constraint depicts all the anomalies near the surface. The apparent resistivity data is used to construct a layered resistivity structure for the inversion. The inversion starts from a homogeneous model with  $s = 1(ma)$ .

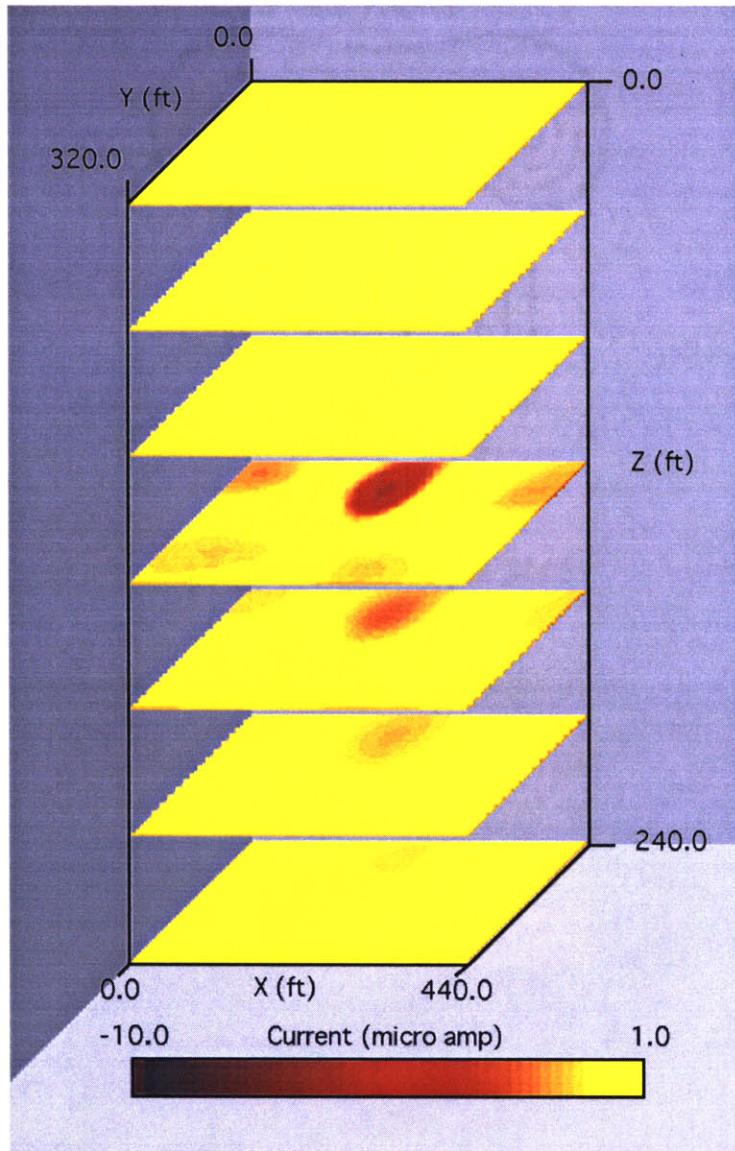


Figure 5-14: The inversion results with the depth constraint locate and describe an egg shaped current source anomaly below the water table.

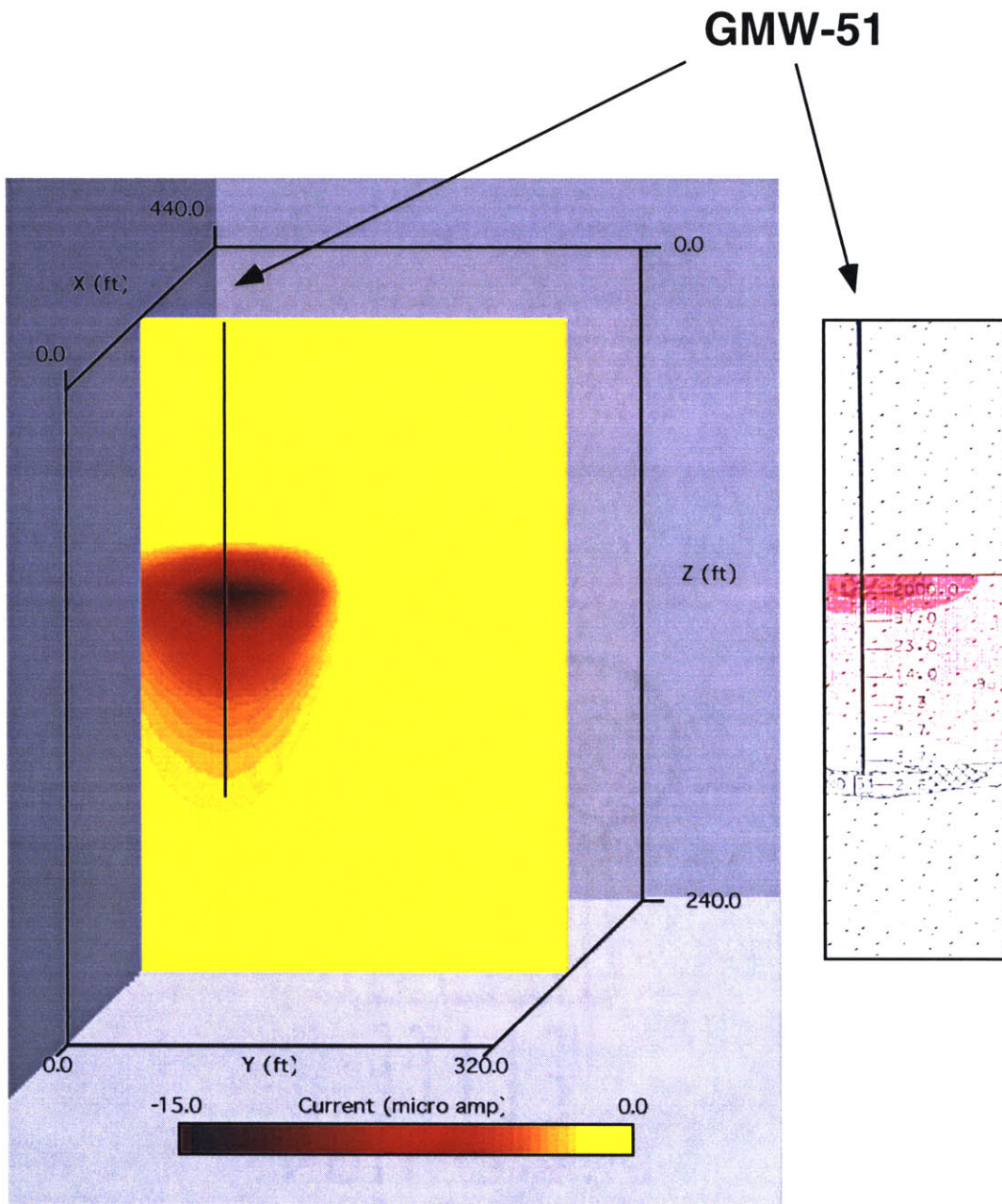


Figure 5-15: The SP inversion results are compared to the concentration extent of Benzene. The inversion result shown on the left figure is a vertical cross-section cutting through the location of the groundwater monitoring well GMW-51. Results are taken from a vertical cross-section cutting through the groundwater monitoring well GMW-51. The concentration extent of Benzene is from a report by HAZWRAP (1995).

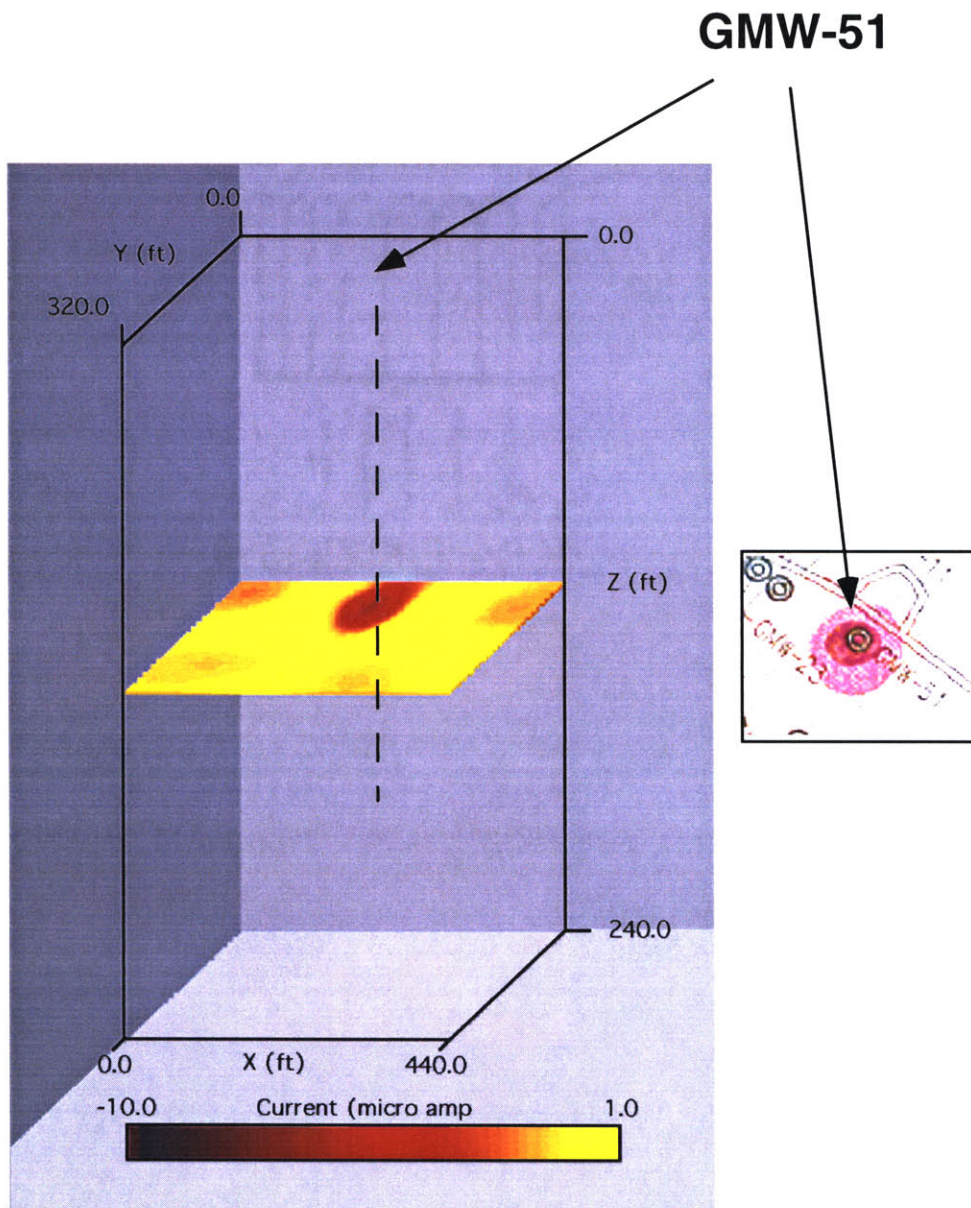


Figure 5-16: The SP inversion results (left) are compared to the concentration extent of Benzene. Here a horizontal cross-section cutting through the groundwater monitoring well GMW-51 is taken for the comparison. The concentration extent of Benzene is from a report by HAZWRAP (1995).

# Chapter 6

## Uncertainty and Resolution Analysis

### 6.1 Introduction

When analyzing a geophysical inverse problem, obtaining an optimal model is usually not sufficient. Normally we also wish to have an estimation of uncertainties and resolutions in the information content of the images. In other words, we wish to know to what degree the inversion results represent the actual structure. Any inversion procedure is considered to be incomplete without the uncertainty or resolution analysis in the results. In general, because the theory linking data with model parameters is often nonlinear, it may be multimodal in the model space, which thus makes the uncertainty or resolution analysis extremely difficult. For nonlinear inverse problems, there has been no great success in analyzing the uncertainty and resolution. Therefore, inversion results often are provided without accuracy information. Three popular approaches to resolution and uncertainty analysis among geophysicists are:

the method of Backus-Gilbert (Backus and Gilbert, 1968,1970), Bayesian parameter estimation (Tarantola, 1987; Duijndam, 1988), and Monte Carlo sampling (Press, 1968; Tarantola, 1987).

The Backus-Gilbert method poses uncertainty in terms of 'spread', a measure of a kernel which describes the spatial average of the parameter, and variance. The basic premise is that since a finite set of data cannot resolve details in earth structure on an arbitrarily small scale, only averages over a finite spatial extent can be estimated, i.e. the geophysical data depend on earth structure in a simple way, they act like simple low-pass filters to the spatial variations of earth structure. The spread, defined as a quantity which measures the spatial resolution, is intended to indicate the spatial scale over which a given estimator resolves earth structure. Furthermore, the averaging extent of an estimate varies inversely with the degree to which the estimate is contaminated by noise, i.e. there is a trade-off between the spatial resolution and statistical variance of earth structure estimates. The Backus-Gilbert method obtains an optimal linear estimator of the model parameter at a given position in the earth through a joint minimization of spread and variance.

Another appealing approach is Bayesian parameter estimation. In the Bayesian approach, parameters are estimated by combining information from data with a *a priori* information on the parameters. The first type of information is reflected in the likelihood function, the second in the *a priori* probability density function (pdf). The product of the two determines the *a posteriori* pdf, which is the solution to the inverse problem. The shape of this pdf gives the full picture of uncertainties of parameters. Three types of quantities that relate to the uncertainty or resolution analysis can be extracted from the *a posteriori* probability density function. They are the standard deviation, the covariance matrices, and the eigenvalue spectra. Standard deviations can be computed from taking the square root of the diagonal elements of the covariance matrix as overall uncertainty measures of the parameters. Covariance

and related matrices give more detailed information on spatial correlations between model parameters that are resolved by inversion. An eigenvalue or principal component analysis allows the inspection of essential linear combinations of the parameters.

Both methods mentioned above, however, are only realistic and relevant to the linear inversions. There has been no great success in the assessment of the resolution associated with practical data as the result of a highly nonlinear inverse problem. The Backus-Gilbert method is limited strictly to linear inverse problems. For nonlinear inverse problems, which are the general case in geophysics, where data determine nonlinear spatial averages of the structural parameters, the Backus-Gilbert framework breaks down. Although through the works by Snieder (1991) and Rodi (1989) the Backus-Gilbert method was extended to nonlinear problems based on small perturbations, two requirements must be satisfied for the set of models to adequately explain the data: (1) the forward problem must be expanded in a regular perturbation series and (2) models within the set must differ only by a fine length scale. Therefore, the usefulness of the theory for practical problems depends on the strength of nonlinearity. The validity of this approach for a very nonlinear problem such as resistivity and IP is unknown and needs to be verified.

In Bayesian formulation, questions of resolution are answered via the *a posteriori* probability density. The *a posteriori* probability density distribution contains all information about the parameterized physical system that can be derived from the available sources. Unfortunately, this distribution is multidimensional and is, therefore, hard to analyze and display, especially for highly nonlinear inverse problems such as resistivity and IP. For this class of inverse problems, the *a posteriori* distributions are typically multimodal, and traditional techniques for analyzing error and resolution properties of unimodal problems break down. Under this circumstance, computing standard derivations or covariances may be meaningless if the *a posteriori* probability density is far from Gaussian, which is always the case for highly nonlinear

problems. On the other hand, an exact computation of the *a posteriori* probability density would involve an extensive exploration of the *a posteriori* pdf through the whole parameter space. This is too computationally demanding for all but the most trivial cases.

The Monte Carlo method, where a large number of randomly generated models are tested against the data, *conceptually* can be used to assess the uncertainty or resolution analysis for both the linear and nonlinear inversions. By extensively sampling the model space, the Monte Carlo method avoids entrapment in local minima, and therefore provides a useful way to attack highly nonlinear inverse problems. Early geophysical examples of solving inverse problems by means of the Monte Carlo method are usually made by simple uniform samplings, or a crude Monte Carlo method (Keilis-Borok and Yanovskaya, 1967, Press, 1968). The method has been used for 1-D resistivity (Sternberg, 1979) and 1-D magnetotellurics (MT)(Jones and Hutton, 1979b) soundings in an attempt to characterize all models that agree with the observations. However, this approach is only ideal for problems with low dimensionality. For problems with high dimensionality, the crude Monte Carlo sampling is computationally infeasible. It is therefore necessary to severely restrict the number of samplings, as compared to the exhaustive search. One way to improve the sampling of the model space is by combining the Monte Carlo method with the Bayesian estimation. The basic idea behind this approach was described by Tarantola (1987). One can use the Monte Carlo method to invert random data vectors and random model vectors generated according to the data variance and the *a priori* model distribution for many realizations until the *a posteriori* model covariance can be reasonably well approximated. Mosegaard and Tarantola (1995) have shown a synthetic example of using of the Monte Carlo method to derive uncertainty estimates by sampling the *a posteriori* probability density functions without resorting to a Gaussian approximation for this probability. However, one of the problems raised by these authors was that the Bayesian approach requires an explicit formula for the *a priori* model



distribution, which is difficult to attain in practice. As an example, consider a resistivity survey. In such a situation one may have a fairly accurate idea of resistivity values of targets (for instance, resistivities of caverns and certain minerals are known accurately). However, the depth and the length scale of the resistivity variation is to a large extent unknown. This implies that our knowledge of the earth's interior is rather poor, especially where it concerns the *a posteriori* correlation length of the model (Scales and Snieder, 1997).

In this chapter, we will develop a methodology to assess the resolution and uncertainty capabilities of the inversion algorithms developed in Chapter 2. Considering the enormous difficulty encountered in the resolution and uncertainty analysis for the nonlinear inverse problem, we will explore possibilities and take into account the factors that may help to understand and estimate the properties of resolution and uncertainty. Specifically, we achieve our goal by the following procedures. We will first describe approaches to the uncertainty analysis within the framework of Bayesian parameter estimation combined with the Monte Carlo method. Secondly, we will discuss the feasibility of adapting Bayesian's *a posteriori* covariance to the nonlinear geoelectrical inversion in the concept of Tikhonov regularization. Third, we will justify the approach for Tikhonov regularization by incorporating a sensitivity analysis to give a reasonable estimate of the uncertainty bounds or 'error bars' on the model parameters. Then we will perform resolution analysis through the estimation of the *a posteriori* model correlations. Finally we further quantify the resolution length of the inversion method via a spectrum analysis method - the Modulation Transform Function (MTF).

## 6.2 Uncertainty Analysis via Bayesian Parameter Estimation and Monte Carlo Method

In Bayesian formulation the solution to the inverse problem is the *a posteriori* probability density  $\sigma(m)$  on the space of models  $m$  with the form (Tarantola 1987):

$$\sigma(m) = \kappa \rho(m) \varphi(m) \quad (6.1)$$

where  $\kappa$  is an appropriate normalization constant. The *a posteriori* probability density  $\sigma(m)$  equals the *a priori* probability density  $\rho(m)$  times a "likelihood function"  $\varphi(m)$  which measures the fit between observed data and data predicted from the model  $m$ . We assume that all uncertainties are Gaussian, thus the likelihood function  $L(m)$  is proportional to

$$L(m) \propto \exp\left[-\frac{1}{2}(d - \mathbf{G}m)^T \mathbf{R}_{dd}^{-1}(d - \mathbf{G}m)\right], \quad (6.2)$$

while the *a priori* model distribution  $\rho(m)$  is proportional to

$$\rho(m) \propto \exp\left[-\frac{1}{2}(m - m_{prior})^T \mathbf{C}_M^{-1}(m - m_{prior})\right] \quad (6.3)$$

where  $\mathbf{G}$  is the forward modeling operator that predicts the observations given a discretized model  $m$  of the subsurface,  $d$  is the observed resistivity or IP data,  $\mathbf{R}_{dd}$  is the data covariance matrix,  $m_{prior}$  is the a priori model, and  $\mathbf{C}_M$  is the model covariance matrix.  $\mathbf{R}_{dd}$  and  $\mathbf{C}_M$  incorporate the uncertainties in the data (numerical and observation errors) and uncertainties related to the model.

As mentioned earlier, in Bayesian inference, all questions of uncertainties and resolution are addressed via the *a posteriori* probability density  $\sigma(m)$  expressed in Equation 6.1. Because of the complicated nature of this function due to the nonlinearity, one approach is to resort to Monte Carlo integration or sampling procedures (Gouveia and Scales, 1997; Mosegaard and Tarantola, 1995) to extract confidence

sets or other measures of resolution from  $\sigma(m)$ . Considering the dimensionality and the high computational cost of the modeling algorithms for the d.c. resistivity or IP inversion, a complete search of the whole model space using Monte Carlo methods are not feasible for this problem without vastly greater computational resources than were available to us. As a compromise, the maximum likelihood point of the *a posteriori* probability density,  $m_{map}$ , is often calculated. The computation of  $m_{map}$  corresponds to the optimization problem minimizing the exponential component of the  $\sigma(m)$  in Equation 6.1,

$$\begin{aligned}\Psi(m_{map}) &= (d - \mathbf{G}m_{map})^T \mathbf{R}_{dd}^{-1} (d - \mathbf{G}m_{map}) + (m_{map} - m_{prior})^T \mathbf{C}_M^{-1} (m_{map} - m_{prior}) \\ &= \textit{minimum}\end{aligned}\tag{6.4}$$

A local analysis of  $\sigma(m)$  in the vicinity of  $m_{map}$  gives the *a posteriori* covariance matrix  $C'_M$  by

$$C'_M = (\mathbf{A}_{m_{map}}^T \mathbf{R}_{dd}^{-1} \mathbf{A}_{m_{map}} + \mathbf{C}_M^{-1})^{-1}\tag{6.5}$$

where  $\mathbf{A}_{m_{map}}$  is the Fréchet derivative of  $G$  evaluated at  $m_{map}$ . Note that for non-linear and non-Gaussian problems, Equation 6.5 is only an approximation of the *a posteriori* covariance matrix. The problem has to be linear enough for the approximation to be accurate. If it is not, the computed matrix still may be useful because it describes the curvature of the *a posteriori* pdf around the maximum likelihood point.

Tarantola (1987) suggested that when the validity of the linearization estimation of the covariance is uncertain, one can use Monte Carlo methods to generate Gaussian random data vectors with mean  $d$  and covariance operator  $\mathbf{R}_{dd}$  and Gaussian random model vectors with mean  $m_{prior}$  and covariance operator  $\mathbf{C}_M$ , solve the nonlinear inverse problem for each realization, and compute a statistics of the results. Specifically, in Equation 6.4, if we take the data to be  $\sim N(0, \mathbf{R}_{dd})$  with null correlations (i.e.,  $\mathbf{R}_{dd} = \sigma_d^2 I$ ), and the *a priori* model to be  $\sim N(0, \mathbf{C}_M)$  with null correlations

(i.e.,  $\mathbf{C}_M = \sigma_m^2 I$ ), Equation 6.4 then becomes,

$$\begin{aligned} \Psi(m_{map}) &= \sigma_d^{-2}(d - \mathbf{G}m_{map})^T(d - \mathbf{G}m_{map}) + \\ &\quad \sigma_m^{-2}(m_{map} - m_{prior})^T(m_{map} - m_{prior}) \end{aligned} \quad (6.6)$$

The Monte Carlo method then proceeds by constructing  $K$  random data vectors  $d_k$  and randomized the *a priori* model vectors such that

$$d_k = d + e_k, k = 1, 2, \dots, K, \quad (6.7)$$

where  $e_k \sim N(0, \sigma_d^2)$ , i.e.,  $\sigma_d^2$  is the variance of the uncorrelated Gaussian errors of data. In addition, we construct  $K$  random model vectors with  $m_{prior}$  as their mean such that

$$m_{prior}^k = m_{prior} + \epsilon_k, k = 1, 2, \dots, K, \quad (6.8)$$

where  $\epsilon_k \sim N(0, \sigma_m^2)$ , i.e.,  $\sigma_m^2$  is the variance of the uncorrelated Gaussian errors of the *a priori* model. For each of the  $K$  realizations, we then perform the full nonlinear inversion to determine the  $k^{\text{th}}$  regularized solution  $\widehat{m}_k$  by minimizing the following objective function:

$$\Psi(\widehat{m}_k) = \sigma_d^{-2}(d_k - \mathbf{G}\widehat{m}_k)^T(d_k - \mathbf{G}\widehat{m}_k) + \sigma_m^{-2}(\widehat{m}_k - m_{prior}^k)^T(\widehat{m}_k - m_{prior}^k) \quad (6.9)$$

and then,

$$\Delta m_k = \widehat{m}_k - m_{map} \quad (6.10)$$

is the model residual for the  $k^{\text{th}}$  random realization. From these  $K$  solutions, we can compute the *a posteriori* covariance  $C'_M$ ,

$$C'_m = \frac{1}{K} \sum_{k=1}^K \Delta m_k (\Delta m_k)^T \quad (6.11)$$

The above derivation is based on performing  $K$  nonlinear inversions to obtain an accurate estimate of the *a posteriori* covariance. However, considering the amount of

computational effort required for each nonlinear inverse problem, such a procedure is computationally highly demanding, and therefore one also can linearize the inversion about the solution to get an approximated estimate of the *a posteriori* covariance. Specifically, we randomly generate  $K$  realizations of the data perturbations and then solve for the linearized inversion solution associated near that point via the stationary condition

$$\sigma_d^{-2}(A|_{m_{map}})^T(A|_{m_{map}}\Delta m_k - e_k) + \sigma_m^{-2}(\Delta m_k - \epsilon_k) = 0. \quad (6.12)$$

Comparing the *a posteriori* covariance matrix  $C'_M$  obtained by a linearization around  $m_{map}$  in Equation 6.5 and by the Monte Carlo method in Equation 6.11, the computation of  $C'_M$  via the Monte Carlo method has two advantages: (1) the Monte Carlo method serves a much broader search over the model space, therefore,  $C'_M$  in Equation 6.11 represents a much more accurate estimate of the *a posteriori* covariance matrix provided a sufficient number of realization are performed and (2) the time required to calculate the *a posteriori* covariance matrix in Equation 6.5 via the conjugate gradient matrix inversion is proportional to the square of the number of model parameters, which may be quite large. While using the Monte Carlo method, the accuracy of the estimate of  $C'_m$  depends only on the number of realizations. Specifically, to obtain an estimate of the model variance that is precise to 25% at 95% confidence requires  $K = 100$  realizations. Given  $K = 1000$  realizations, we can be 95% confident that our estimate of the variance is within 10%. Typically, the time to compute a realization depends linearly on the model discretization. Given the realizations, calculation of the covariance with respect to a point in the model requires negligible computer time.

Once the covariance matrix is established, the most trivial quantity that can be extracted is the standard deviation, which is computed from taking the square root of the diagonal elements of  $C'_M$ . The standard deviations can be interpreted as overall uncertainty bounds or 'error bars' on the model parameters when the *a posteriori* pdf

does not deviate too much from the Gaussian form.

### 6.3 Uncertainty Analysis via Tikhonov Regularization and Monte Carlo Method

In this section we will explore the feasibility of adapting the previously discussed Monte Carlo procedure to analyze uncertainty in the concept of Tikhonov regularization. Such an approach was also attempted by Matarese (1995) for the nonlinear travelttime tomography.

In Tikhonov regularization, the inversion solution is obtained by a joint minimization of data misfit and a model roughness

$$\Psi(m) = (d - \mathbf{G}m)^T \mathbf{R}_{dd}^{-1} (d - \mathbf{G}m) + \tau \|\mathbf{L}m\|^2 \quad (6.13)$$

where  $\mathbf{L}$  is a linear operator to regularize a minimum structure solution, in our case a Laplacian, and  $\tau$  is the regularization coefficient. The first term measures data misfit, the second term introduces model roughness.

Matarese (1995) suggested that the uncertainty analysis developed within a Bayesian framework by using the Monte Carlo method can be theoretically adapted to the Tikhonov Regularization. If we let  $\sigma_h = \tau^{-1/2}$ , we can rewrite Equation 6.13 as

$$\Psi(m) = \sigma_d^{-2} (d - \mathbf{G}m)^T (d - \mathbf{G}m) + \sigma_h^{-2} (0 - \mathbf{L}m)^T (0 - \mathbf{L}m), \quad (6.14)$$

This objective function can be interpreted as the joint minimization of the data misfit  $(d - \mathbf{G}m)$  subject to the data variance  $\sigma_d^{-2}$  and the roughness misfit  $(0 - \mathbf{L}m)$  subject to the roughness “variance”  $\sigma_h^{-2}$ . A small value for  $\sigma_h$  favors models with less variability in the local roughness. This is equivalent to choosing a large value for  $\tau$  to emphasize

model smoothness. Large values for  $\sigma_h$  (low values of  $\tau$ ) allow rougher models in fitting the data.

It seems that Equation 6.14 can be directly related to Equation 6.9 because of their similar formulation. Therefore, Matarese suggested that one can generate  $K$  random data vectors and  $K$  random roughness vectors  $h_k$  with variance  $\sigma_h^2$  to calculate the *a posteriori* covariance using the concept of Tikhonov regularization, i.e., for each random realization, we solve the following optimization problem:

$$\Psi(\widehat{m}_k) = \sigma_d^{-2}(d_k - \mathbf{G}\widehat{m}_k)^T(d_k - \mathbf{G}\widehat{m}_k) + \sigma_h^{-2}(h_k - \mathbf{L}\widehat{m}_k)^T(h_k - \mathbf{L}\widehat{m}_k) = \min. \quad (6.15)$$

Because of the extensive computational demand in solving for  $K$  nonlinear inverse problems, Matarese solved a nonlinear regularization problem only once to obtain the regularized solution  $\widehat{m}$  and then linearized the solution about  $\widehat{m}$  and solved the following equation given by the stationary condition.

$$\sigma_d^{-2}(A|_{\widehat{m}})^T(A|_{\widehat{m}}\Delta m_k - e_k) + \sigma_h^{-2}\mathbf{L}^T(\mathbf{L}\Delta m_k - h_k) = 0. \quad (6.16)$$

Matarese's approach suffers from the following shortcomings. Although comparison of the Tikhonov regularization formulations in Equation 6.13, to Equation 6.15 with those of the Bayesian formulations reveals that the Tikhonov regularization mathematically resembles that of Bayesian inference (if we incorporate smoothness into the Bayesian problem as the *a priori* covariance matrix  $\mathbf{C}_M^{-1} = \tau\mathbf{L}^T\mathbf{L}$ ), the goals and interpretations of the two methods are rather different. In Tikhonov regularization, we solve the inverse problem by determining the maximum model smoothness that allows for data fitting without incorporating *a priori* information about the models, and estimate the resolution in terms of the degree of model smoothness implied by the data. In the Bayesian inversion, however, we compute a probability distribution of models that are consistent with the data and the *a priori* information. This distribution is then used to assess the resolution provided by the inverse procedure. In fact,  $\mathbf{C}_M^{-1}$  and  $\tau\mathbf{L}^T\mathbf{L}$  never can be equal because the inverse of  $\mathbf{L}^T\mathbf{L}$  is not well-posed;

thus the corresponding *a priori* covariance  $\mathbf{C}_M$  would be infinite and meaningless. It is impossible to perform a Monte Carlo random search which can sample all possible solutions in the model space. By perturbing the roughness term  $\mathbf{L}m$  only as shown in Equation 6.15 instead of perturbing the *a priori* model directly, we essentially test the stability of the minimum structure solution against the local roughness. This is not equivalent to randomly sampling the whole *a priori* model space, such an approach cannot be served as a complete method for the uncertainty and resolution analysis of the Tikhonov regularization inversion. More effort must be taken to accomplish this goal.

## 6.4 Augmented Uncertainty Analysis In Tikhonov Regularization

For many geophysical inverse problems, it is often true that some model parameters can be resolved deterministically and others only can be resolved statistically. Assuming we have a set of models that fit the data, it may happen that all the models give the same value for the model parameters which are resolved deterministically. Such parameters are well constrained by the data, and their inverse problems are "well-posed" using old terminology. On the contrary, it may happen that all the models give absolutely different answers for model parameters which are poorly constrained by the data. To determine whether a model parameter is resolved deterministically or statistically, we introduce a sensitivity analysis.

Sensitivity analysis is a procedure to quantify an overall electric potential response to a small perturbation in each model parameter. It can be carried out by computing the sensitivity matrix which is a measure of how the surface potential measurement changes with respect to a unit perturbation in the model parameter, and then sum-



ming over the source numbers and the receiver numbers. The method of calculating the sensitivity matrix on a network formulation can be efficiently obtained by incorporating reciprocity into the inversion theory. Many works have demonstrated the efficiency of reciprocity. (Rodi, 1976; Tripp *et al.*, 1984; Park *et al.*, 1991; Mackie and Madden, 1993; Zhang *et al.*, 1995).

According to Ohm's law and conservation of current, the forward response of a resistivity model is calculated by solving linear system of equations

$$\mathbf{K}v^{is} = s^{is} \quad (6.17)$$

where  $v^{is}$  is a vector of the potentials at the network nodes due to source  $is$ ,  $s$  is the  $is$ -th current source vector, and  $\mathbf{K}$  is a real, symmetric, and positive-definite matrix which depends on the resistivities and dimensions of the network cells.

For a potential measurement,  $Q_{ir}^{is}$ , due to a source number,  $is$ , at a receiver number,  $ir$ , we can write,

$$Q_{ir}^{is} = C_{ir}^{is}v^{is} \quad (6.18)$$

where  $C_{ir}^{is} = (0, \dots, 0, 1, 0, \dots, 0)$ , the non-zero component '1' is the  $ir$ -th component which corresponds to the location of the receiver. The source term  $s^{is}$  is independent of model parameters. Thus after taking the partial differential on both sides of Equation 6.17 with respect to a model parameter, i.e. the logarithmic resistivity  $\log(\rho_j)$  of cell ( $j$ ), we obtain

$$\frac{\partial Q_{ir}^{is}}{\partial \log(\rho_j)} = -C_{ir}^{is}\mathbf{K}^{-1}\frac{\partial \mathbf{K}}{\partial \log(\rho_j)}v^{is} \quad (6.19)$$

This equation shows that the sensitivity of the potential at the receiver  $ir$  to a change of  $j$ th resistivity at depth is equal to the response at the receiver site due to a source term  $\frac{\partial \mathbf{K}}{\partial \rho_j}v^{is}$ , which represents a collection of sources placed at the  $j$ th resistivity

position. The sensitivity matrix for the source number  $is$  is thus defined as,

$$\mathbf{A}^{is} = \begin{pmatrix} \frac{\partial Q_1^{is}}{\partial \log(\rho_1)} & \frac{\partial Q_1^{is}}{\partial \log(\rho_2)} & \frac{\partial Q_1^{is}}{\partial \log(\rho_3)} & \cdots & \frac{\partial Q_1^{is}}{\partial \log(\rho_n)} \\ \frac{\partial Q_2^{is}}{\partial \log(\rho_1)} & \frac{\partial Q_2^{is}}{\partial \log(\rho_2)} & \frac{\partial Q_2^{is}}{\partial \log(\rho_3)} & \cdots & \frac{\partial Q_2^{is}}{\partial \log(\rho_n)} \\ \vdots & & & & \\ \frac{\partial Q_m^{is}}{\partial \rho_1} & \frac{\partial Q_m^{is}}{\partial \log(\rho_2)} & \frac{\partial Q_m^{is}}{\partial \rho_3} & \cdots & \frac{\partial Q_m^{is}}{\partial \log(\rho_n)} \end{pmatrix} \quad (6.20)$$

To calculate the summation of the potential responses of the entire data set with respect to each model element, we simply multiply the transpose of matrix  $\mathbf{A}^{is}$  with a unit vector ' $\mathbf{I}$ ' and then sum over the source numbers, i.e.

$$\sum_{is,ir}^{ns,nr} \frac{\partial Q_{ir}^{is}}{\partial \log(\rho_j)} = \sum_{is}^{ns} \mathbf{A}^{is} \mathbf{I} = \sum_{is,ir}^{ns,nr} (-C_{ir}^{is} \mathbf{K}^{-1} \frac{\partial \mathbf{K}}{\partial \log(\rho_j)} v^{is}) \quad (6.21)$$

In diplay, since  $\frac{\partial Q_{ir}^{is}}{\partial \log(\rho_j)}$  can vary many orders of magnitude, we take the logarithmic measure of the above equation,

$$\text{Log} \sum_{is,ir}^{ns,nr} \frac{\partial Q_{ir}^{is}}{\partial \log(\rho_j)} = \text{Log} \sum_{is,ir}^{ns,nr} (-C_{ir}^{is} \mathbf{K}^{-1} \frac{\partial \mathbf{K}}{\partial \log(\rho_j)} v^{is}) \quad (6.22)$$

Given a unit change in the model parameter  $\log(\rho_j) = 1$ , Equation 6.22 estimates an overall change in the observation. If this overall change in the observation is large, it means that the parameter  $\log(\rho_j)$  is well constrained by the data. A poorly constrained model parameter will result in a small sensitivity.

The sensitivity analysis can be incorporated with the Tikhonov regularization to calibrate the estimation of the uncertainty bounds, or 'error bars'. Once the geometry of sources and receivers is given, the sensitivity analysis can be performed over the inverted model to estimate how each model parameter is dependent on the observation. The uncertainty on each model parameter should be inversely proportional to the sensitivity, i.e. parameters which possess higher sensitivities should have lower uncertainties or smaller 'error bars'. On the other hand, parameters which possess lower sensitivities should have higher uncertainties or larger 'error bars'. Therefore, if we are able to obtain an accurate estimate of the uncertainty bounds, or 'error

bars', on well constrained model parameters, we may then extend such an estimation of uncertainty to model parameters which are poorly constrained by data via the calibration of sensitivity analysis.

To obtain an accurate estimate of the uncertainty on the model parameters which are well constrained by the data, we can simply invert a Hessian matrix defined earlier or use the Monte Carlo method based on data perturbation. Since the model parameters can be resolved deterministically, any inversion model which fits data should possess the same uncertainty information as the model parameters. Therefore, we can solve the nonlinear regularized inverse problem first to obtain a regularized solution and then calculate the *posteriori* covariance according to the stationary condition which corresponds to

$$C'_M = (\mathbf{A}^T \mathbf{R}_{dd}^{-1} \mathbf{A} + \tau \mathbf{L}^T \mathbf{L})^{-1} \quad (6.23)$$

For simplicity and to be consistent with the Tikhonov regularization method described above, we here omit the subscript of the sensitivity matrix  $\mathbf{A}$ .

An alternative way to calculate the *posteriori* covariance is to use the Monte Carlo method. But here we only need to generate  $K$  random data vectors with a known standard deviation to give a statistical estimate of the *posteriori* model covariance, as the *a priori* mean and the local roughness do not influence the inversion results for parameters that can be resolved deterministically.

## 6.5 Resolution Analysis Via Model Correlation and The Modulation Transfer Function

More detailed information can be derived from the *posteriori* covariance matrix. Particularly, correlations between parameters can be quantified by the correlation matrix

ces defined in the following equation to assess the resolution analysis:

$$c^{\alpha\beta} = \frac{C^{\alpha\beta}}{(C^{\alpha\alpha})^{\frac{1}{2}}(C^{\beta\beta})^{\frac{1}{2}}} \quad (6.24)$$

If the correlation between parameters  $m^\alpha$  and  $m^\beta$  is close to zero, the *a posteriori* uncertainties are uncorrelated. If the correlation is close to 1, the uncertainties are highly correlated. A strong correlation of uncertainties indicates that the two parameters have not been independently resolved by the data set and that only some linear combination of the parameter are resolved.

The computation of the model correlations (Equation 6.24) requires the performance of  $K$  inversions on randomly generated data based on the Monte Carlo method. A more direct means of quantifying the resolution of the inversion is the method of the Modulation Transfer Function (MTF).

The MTF is a measure of quality with which an imaging system like the inversion algorithm constructs images of the subsurface whose resistivity distribution can be described by sinusoidal functions. It measures characteristics of the inversion algorithm that determine contrast sensitivity in terms of spatial frequency. Although the origin of the MTF lies in the evaluation of the resolution ability of optical imaging instruments (Born and Wolf, 1964; Perrin 1969), the methodology is suitable for geophysical tomography. The inversion exhibits inaccuracies at a variety of spatial scales owing to the discretized data sampling and the diffusive nature of the electrical method. Structure on a spatial scale finer than some critical level will be impossible to resolve. This critical scale is called the resolution length which is identified by the MTF.

To calculate the MTF function, a series of 'delta-function' resistivity perturbations can be placed in a synthetic medium. The forward model is used to calculate the resultant surface data, then the inversion code is run, using the surface data as input, to produce an image of the original delta-function. The resultant image of the

delta-function perturbation and its width are an indication of the smearing introduced by the inversion process. A Fourier transform is then conducted on both the original delta-function and the response of the delta-function which is the reconstructed model. The spectral results are plotted as a function of a spatial wave number. The MTF is defined as the ratio of the spectrum which corresponds to the reconstructed model to the spectrum of the delta-function. Therefore, the MTF quantifies at what spatial frequency (i.e. resolution length) the contrast sensitivity is lost.

Study of the resolution capabilities of the inversion algorithm through the MTF function can be accomplished by a succession of tests on synthetic data sets. Resolution capabilities will be evaluated by comparing an original synthetic resistivity distribution with the image calculated by the inversion algorithm through the use of the MTF. Since the resolution length would be expected to vary from place to place within the model, conceptually, the ideal synthetic medium would be a stochastic distribution of resistivity which would contain the complete spectrum of spatial frequencies. However, this ideal approach is probably not practical because of the nonlinear nature of the problem. The resolution in some parts of the medium is dependent on the medium's overall resistivity distribution. For example, if we reconstruct the resistivity imaging from a so called 'checker-board' test (Lévêque *et al.*, 1993), the deeper anomalies would be masked by the shallower structure, the resulting image would therefore misrepresent the resolution of the deeper structure. This means we must seek a more specific approach taking into account the typical target distribution and its variability. Therefore the synthetic test data sets would contain variations in range and depth for typical features which are expected in the application.

## 6.6 Numerical Results

This section presents numerical results of uncertainty and resolution analysis on synthetic data sets. To facilitate computations, a 2-D synthetic model containing two resistivity anomalies (Figure 6-1) is discretized onto a  $40 \times 20$  grid covering  $80 \times 40$  square meters. In order to eliminate the boundary effect, we add three model cells on each side of the lateral extended boundaries, which makes the total number of discretized model parameters  $46 \times 20$ . There are 20 electrodes deployed on the surface at a 4-meter interval, and they are arranged in a dipole-dipole configuration. Each dipole current source pair has a fixed length of 4 meters. In total, there are 150 dipole potential observations, each generated via a d.c resistivity forward modeling calculation and with 5% noise added.

We perform a nonlinear inversion to recover the subsurface electrical resistivity structure and analyze uncertainties that are associated with the inversion. By solving an optimization problem defined by the Tikhonov regularization, we obtain a minimum structure solution (the corresponding optimal regularization coefficient  $\tau = 0.4$ , and the data misfit  $\chi^2 = 122$ ) and display the inversion result and the associated model residual (i.e.  $m_{true} - m_{predicted}$ ) in Figure 6-2. The inversion result depicts a resistive anomaly in the center of the model and embedded inside a homogeneous background. Comparing the inversion result with the true model, we find that there is little indication of the second resistive anomaly which is located near the left-side boundary. From the residual plot, we see that the inversion result poses higher variances near the corners of the rectangular object, the lower corners display larger errors.

The objective of the uncertainty analysis is to give an estimation of the inversion result's accuracy, or in a more direct sense, to derive 'error bars' on the inversion solution. By this definition, we would expect to see that our inversion result should

fall within the 'error bars,' given that the estimation of the 'error bars' is correct. This concept is, in fact, a simple way to check whether our final estimation of the uncertainty makes sense.

Our first calculation is the inversion of  $(\mathbf{A}^T \mathbf{R}_{dd}^{-1} \mathbf{A} + \tau L^T L)$ , as described in Equation 6.23 to obtain the linearized *a posteriori* covariance matrix. As mentioned above, the *a posteriori* covariance may not accurately represent the true *a posteriori* covariance as it is only a local approximation of the *a posteriori* on the maximum likelihood solution point. However, for the parameters that are well constrained by the data, this *a posteriori* covariance should give the correct answer for uncertainties of the model parameter. We use a conjugate gradient method for the task of the matrix inversion. The standard deviation of each model parameter is then extracted by taking the square-root of the diagonal terms in the *a posteriori* covariance matrix. The result, shown in Figure 6-3 (top), indicates that the uncertainty is not uniform across the model. In the vicinities of the sources and receivers, the standard deviations appear to be minimal ( $\text{Log} \rho = 0.2$  on average). Locations farther from the sources and receivers display larger standard deviations. The highest standard deviations appear at the boundaries of our model. In the area where the center anomaly is located, the standard deviations reveal a relatively higher value than the surrounding area. Comparing the standard deviations of model parameters located at the lower part of the model to the parameters near the region of the sources and receiver, there is no significant change. Variations of the standard deviations, ranging from 0.2 (on the surface) to 0.8 (near the side boundaries), is too small to include the true model residual calculated in Figure 6-2. Thus the *a posteriori* standard deviations calculated from the expression in Equation 6.23 cannot yield an accurate estimation of the uncertainty on all model parameters.

Next, we perform a calculation of the standard deviation based on the Monte Carlo method by generating many realizations of random perturbation on the data

vector. In the uncertainty analysis 1000 data error realizations were computed from which the *a posteriori* covariance was computed. This number of realizations made it possible to achieve a sample deviation within 5% of the true deviation. The bottom plot in Figure 6-3 shows the *a posteriori* standard deviation as a function of model position by using the Monte Carlo sampling on data vectors. Since the perturbation is only performed on the data vector, the standard deviation calculated via this method only provides information on how the data uncertainties propagate into the model uncertainties. In other words, assuming that the total model uncertainties are determined by two terms, the data term and the regularization term, this calculation only takes into account the uncertainties in the data. In fact, in the surface area where the model parameters can be resolved deterministically, the two methods give equivalent results.

We then carry out a sensitivity analysis via Equation 6.22. The top left figure in Figure 6-4 displays the sensitivity as a function of position. The highest sensitivity is found in the vicinity of the sources and receivers. The sensitivity decreases as the depth increases, and also decreases approaching the left and right sides of the boundaries. Using this sensitivity information, we calibrate the *a posteriori* standard deviations obtained in Figure 6-3 to give a more accurate estimate of the model standard deviations. Specifically, we take the average value of the model standard deviation calculated by (1) using the Monte Carlo sampling on data vectors and (2) inverting matrix  $(\mathbf{A}^T \mathbf{R}_{dd}^{-1} \mathbf{A} + \tau \mathbf{L}^T \mathbf{L})$ , and multiply it with the normalized diagonal elements of the sensitivity matrix. This gives the calibrated *a posteriori* standard deviations, which are displayed in the top right figure in Figure 6-4. This new standard deviation reveals a much broader range in variation of the standard deviation. The true model residual displayed in Figure 6-2 falls inside the 'error bars.' We further add this standard deviation to the inversion solution shown in Figure 6-2 to give an estimate of high bounds of the inversion solution. This result, together with low bounds of the inversion solution by subtracting the standard deviation from the inverted model, is



shown in the bottom of Figure 6-4. Between these two figures is a range of resistivity models all of which will fit the surface potential data well. Although these results do not give an exact measure of errors between the inverted model and the true model (because the true model is unattainable in practice), they provide a range of possible solutions within which the true model is contained. Because of the broad range of solutions which fit the data, one sees the limitation of a specifically chosen survey geometry. This means more sophisticated and improved data acquisition geometry should be incorporated into the surveys if better accuracy is to be determined.

Perhaps the more interesting result of the *a posteriori* covariance is with regard to the model correlations. For the three selected points in the model (i.e. a shallow point, a deeper point, and a point near the right side of the boundary), Figure 6-5 “maps” the corresponding rows and columns of the model correlation matrix calculated via the Monte Carlo method. Two fundamental characteristics define the correlations: (1) positive correlations with the highest values (i.e. +1) in the selected point and a gradually decreasing correlation in the regions near by and (2) correlations are not uniform over the entire area. At the near surface and center, the correlations tend to peak higher than at the deeper and boundary areas. As mentioned earlier, if the correlation is close to 1, the parameters are highly correlated. A strong correlation of uncertainties means that the two parameters have not been independently resolved by the data set and only some linear combination of the parameter is resolved. The correlation results in Figure 6-5 thus indicate that the inversion poses a better resolving power under the center line of the surface electrodes than near the boundary and deeper areas. These results translate into acquisition guidelines which would locate the target as close as possible to a trustworthy region of the inversion.

In the previous examples, the anomalies are chosen to be resistive. For conductive anomalies, one would expect to see a relatively lower variance in the center of the conductive anomalies because they have the highest electrical current concentration

and thus pose a relatively high sensitivity. For the same reason, one would expect a relatively poor resolution and higher variance in the areas located below the conductive bodies. The shape of the conductive bodies would be less well resolved compared to the conductive bodies because the current tends to be absorbed by the conductive anomaly but travels around the region of the resistive anomaly. To verify this result, the resistive bodies in the previous examples are replaced by conductive bodies, with each anomaly having the resistivity of  $20 \Omega.m$ . The reconstructed model and associated standard deviation estimation, displayed in Figure 6-6 and the correlation map, displayed in Figure 6-7, verifies this behavior. As we can see in Figure 6-7, a more extended model correlation for the selected point below the conductive anomaly has been observed.

The resolution certainly can be improved by performing denser measurements. To perform denser measurements, we place double the number of electrodes on the surface, with each pair of electrodes occupying a 2 meter interval instead of a 4 meter interval. With the same dipole-dipole configuration, the dense survey yields a total of 703 data points. Figure 6-8 shows the *a posteriori* model correlation at the selected points. Model correlations at the selected points appear to be more condensed than the previous results (Figure 6-5), indicating a better resolution capability.

To further quantify model resolutions as a function of position, we perform the MTF estimation. To facilitate computations, synthetic models containing recurrent step-functioned anomalies at different depths are discretized onto a  $40 \times 20$  grid. There are 40 electrodes deployed on the surface using dipole-dipole configuration and potential distributions are measured by pseudo-section data gather. The nonlinear inversion reconstructs the subsurface resistivity structure using a homogeneous background as a starting point.

Figure 6-9 shows the inversion results of reconstruction and the MTF functions

calculated from anomalies located at shallower depths. This reconstruction indicates that the anomalies are well resolved with a resolution length estimated to be the same as that of the anomaly at this depth.

For deeper anomalies, the resolution decreases substantially (Figure 6-10) - (Figure 6-11). When the depth reaches 20 meters (for this specific background, i.e.  $\rho = 200\Omega \cdot m$ ) the resolution length is close to 40 meters. The resolution abilities of the data warn us to be skeptical of the deeper information, since the true length scale of these anomalies may be much less than the resolving length.

## 6.7 Conclusions

This chapter developed a method for measuring uncertainty and resolution associated with the nonlinear regularized inverse problem. It appeals to the Bayesian framework whereby both variance and resolution are inferred from the *a posteriori* covariance associated with Tikhonov regularization. To implement an uncertainty analysis within the Bayesian framework, one can employ the Monte Carlo method to the inversion where many realizations of perturbed data and the *a priori* model are inverted to obtain the *a posteriori* covariance and then from which the standard derivation and model correlation can be extracted. Such an approach, however, cannot be directly implemented with the Tikhonov regularization because the inverse of the regularization operator, which corresponds mathematically to the *a priori* model defined in the Bayesian framework, is ill-posed and not well defined. To overcome this problem, we developed a new methodology based on a sensitivity analysis. This new methodology measures the uncertainty resolution associated with the regularized nonlinear inverse problem and involves the following procedures. First, we solve the nonlinear regularization problem to obtain an optimal minimum structure solution. The *a posteriori*

covariance matrix linearized about this inversion solution is then calculated by inverting the Hessian matrix of this solution. The resulted *posterior* covariance matrix does not represent the true *a posteriori* covariance matrix associated with the nonlinear inversion, but it can give a correct measure of the uncertainty for the model parameters, which can be resolved deterministically in the nonlinear inversion. The Monte Carlo method, in which many realizations of perturbed data are inverted to obtain the *a posteriori* covariance, also can be used to give a correct measure of the uncertainty with respect to the deterministic model parameters. Then, a sensitivity analysis is carried out by adding together the responses of observations to a unit perturbation on each model parameter. The resulting sensitivity of each model parameter can give a quantitative measure of how well the model parameter be determined by the data. By incorporating the sensitivity information with the previously obtained the *a posteriori* covariance matrix, calibrated uncertainty bounds, or 'error bars' can be obtained for each model parameter. Although these results do not give an exact measure of errors between the inverted model and the true model, they provide a range of possible solutions within which the true model is contained. More sophisticated and improved data acquisition geometry should be incorporated into the surveys if better accuracy is to be determined.

To measure the resolution of the inversion result, we used the Monte Carlo method to generate random perturbations on the data vector and invert the perturbation data to give an estimate of model correlation. To further quantify the resolution length with respect to any position in the model, the MTF method is used in which a series of 'delta-function' resistivity perturbations are inverted and the spatial resolution is extracted through spectral analysis. Our approach yields results that behave properly for simple numerical problems.

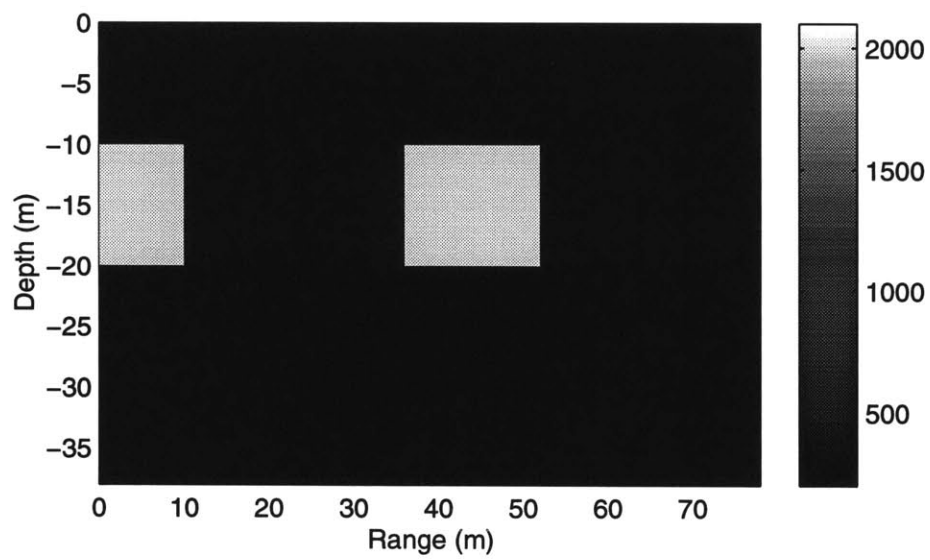


Figure 6-1: A synthetic model generated for uncertainty and resolution analysis. The model contains two resistive anomalies ( $\rho = 2000\Omega.m$ ) buried in a homogeneous background ( $\rho = 200\Omega.m$ ).

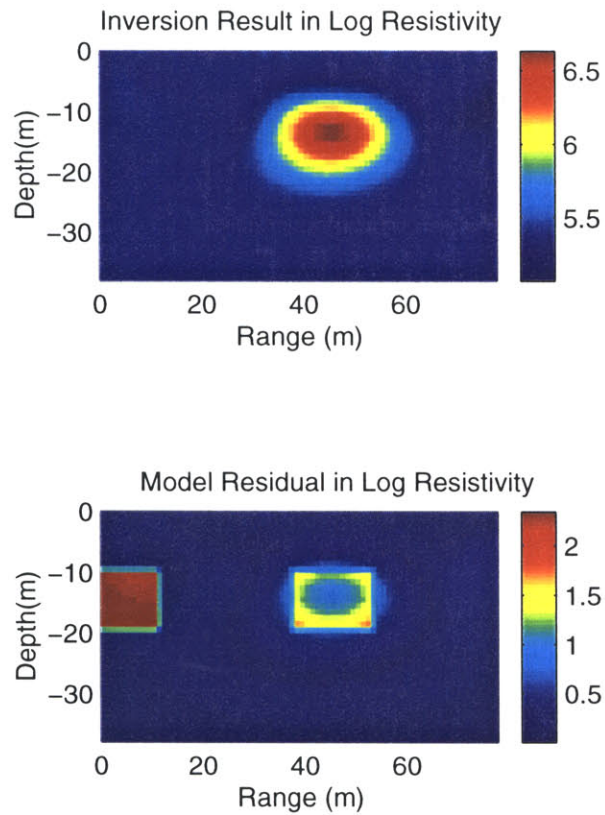


Figure 6-2: The constructed model (top) and the model residuals (bottom) as a function of position. The reconstructed model only depicts the anomaly that is located in the center of the model due to the uneven spatial sensitivity of this data configuration. The model residuals vary spatially, with the maximum value appearing to be at the anomaly located near the boundary.

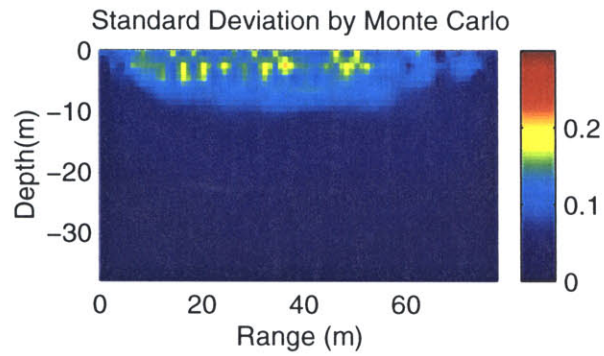
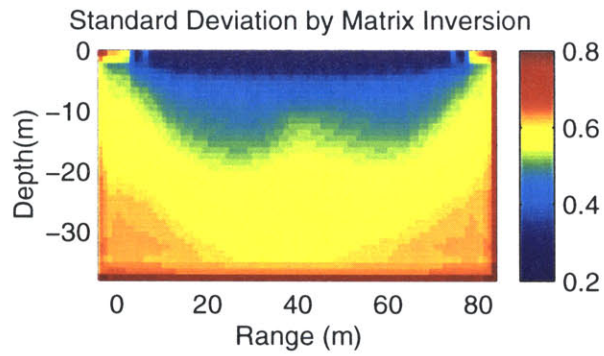


Figure 6-3: The standard deviation of logarithmic resistivity calculated by inverting the Hessian matrix of the optimal solution (top), and by a Monte Carlo method based on data perturbation (bottom). Note, units of all model standard deviations are  $\text{Log}(\Omega.m)$ .

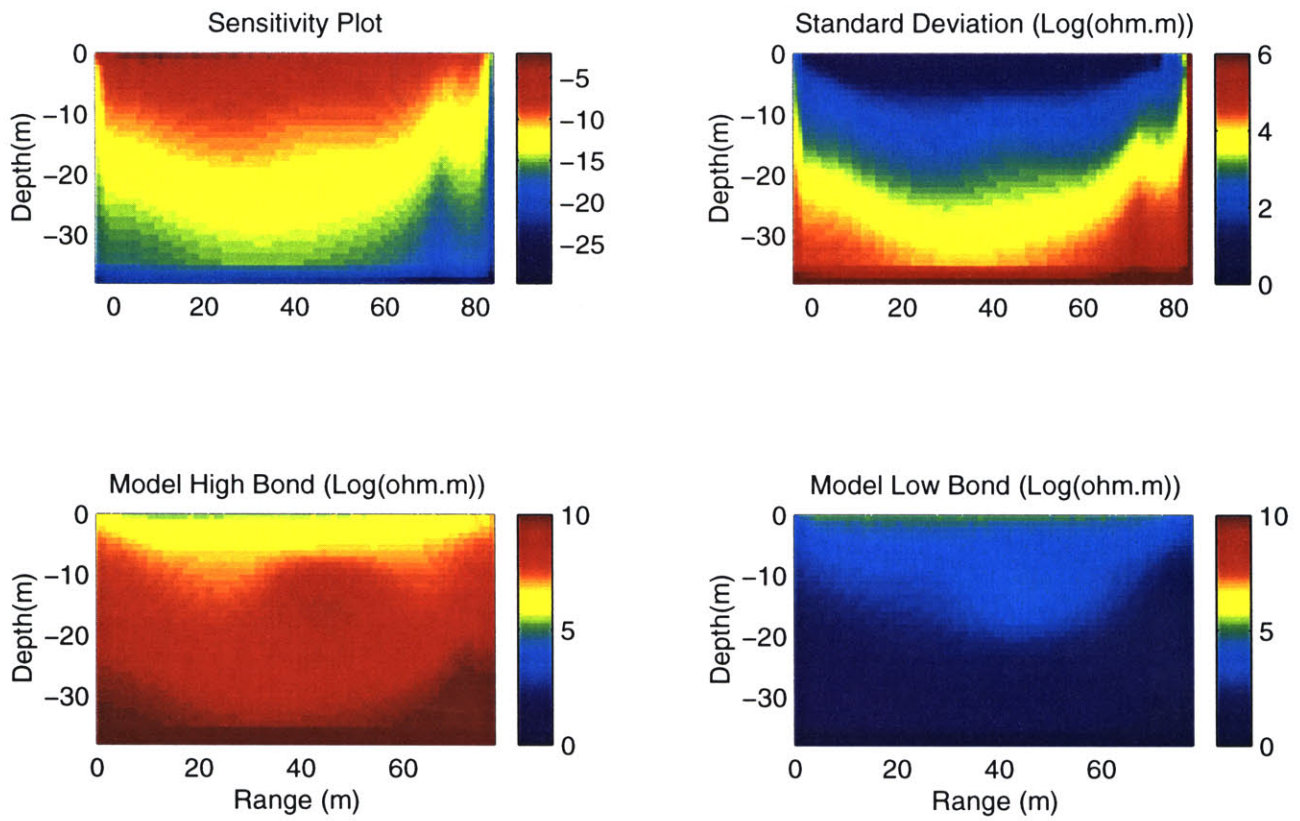


Figure 6-4: The model sensitivity as a function of position (top left) and the calibrated standard deviation (top right). The high and low bonds of model are shown in the bottom figures, respectively. Note, units of model standard deviations and model bonds are  $Log(\Omega.m)$ .



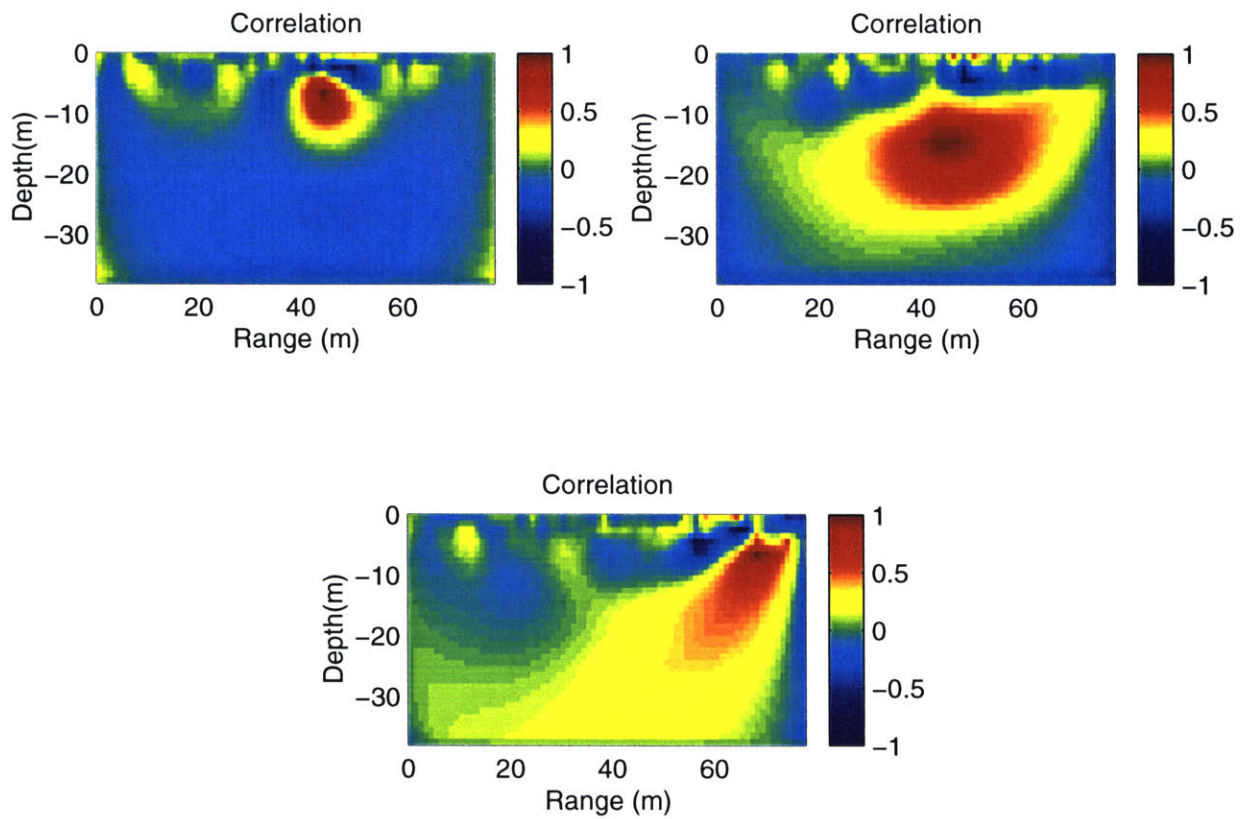


Figure 6-5: The model correlations at three selected points reveal a better resolving power below the center line of the surface electrodes than the places near the boundary and deeper areas.

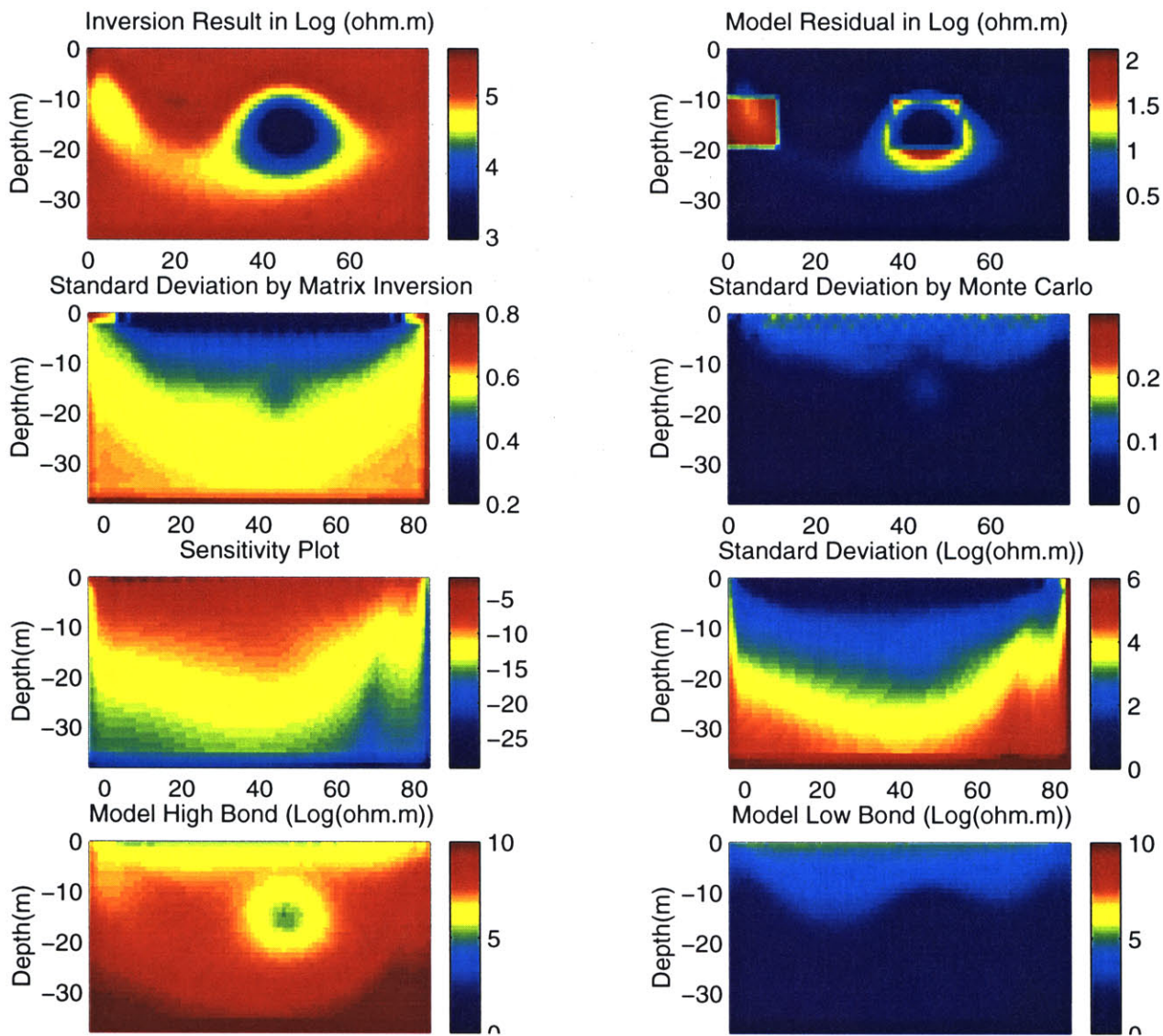


Figure 6-6: The constructed model the associated standard deviations as a function of position for the conductive anomalies. Note, units of all model standard deviations are  $Log(\Omega.m)$ .

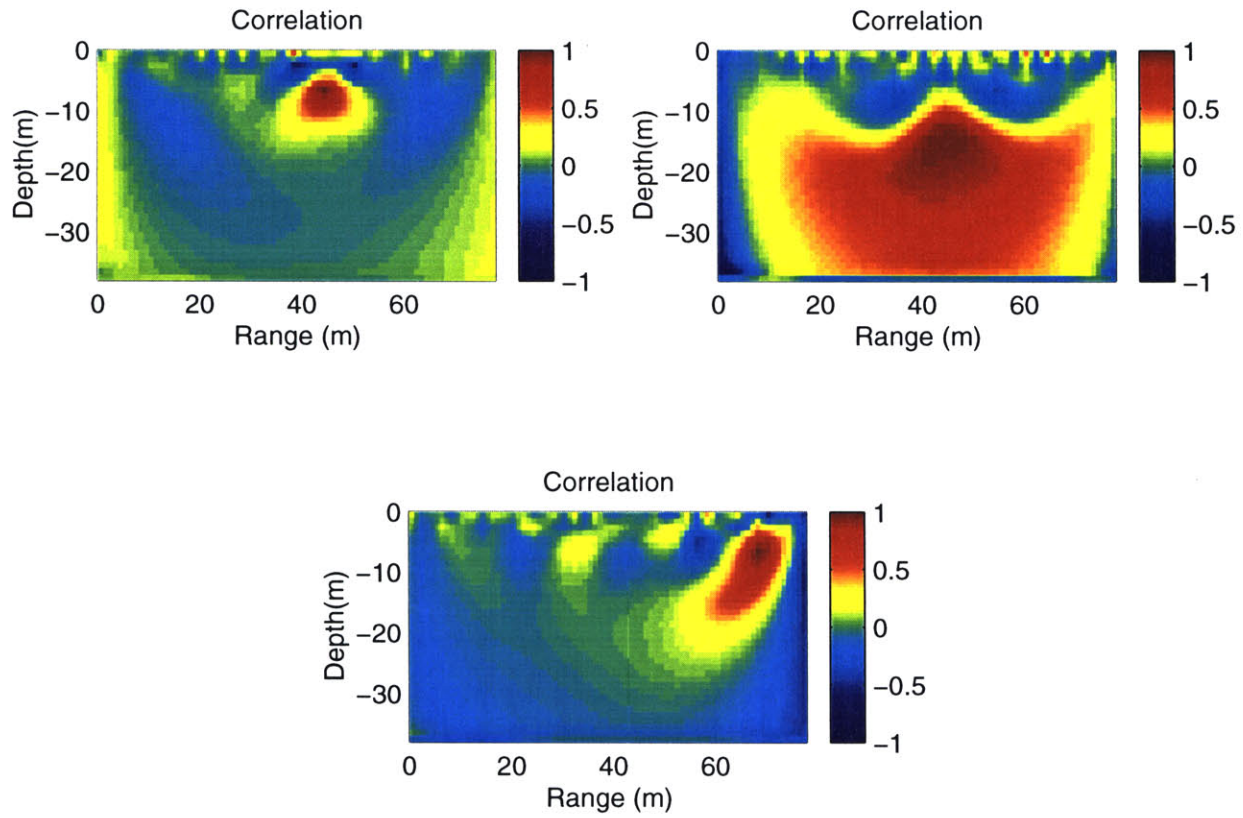


Figure 6-7: The model correlations at three selected points for the conductive anomalies indicate a poorer resolution below the conductive anomalies.

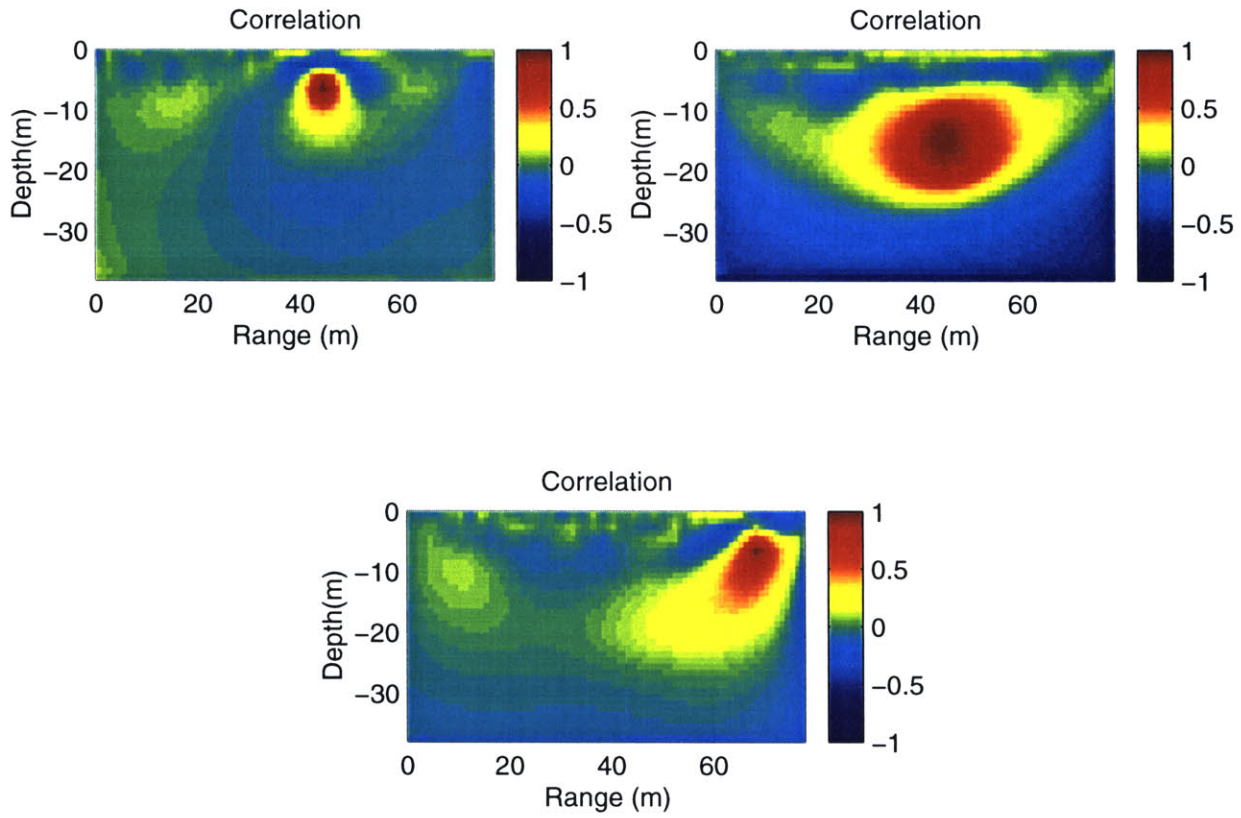


Figure 6-8: The model correlations at three selected points for a dense array reveal better resolution, overall.

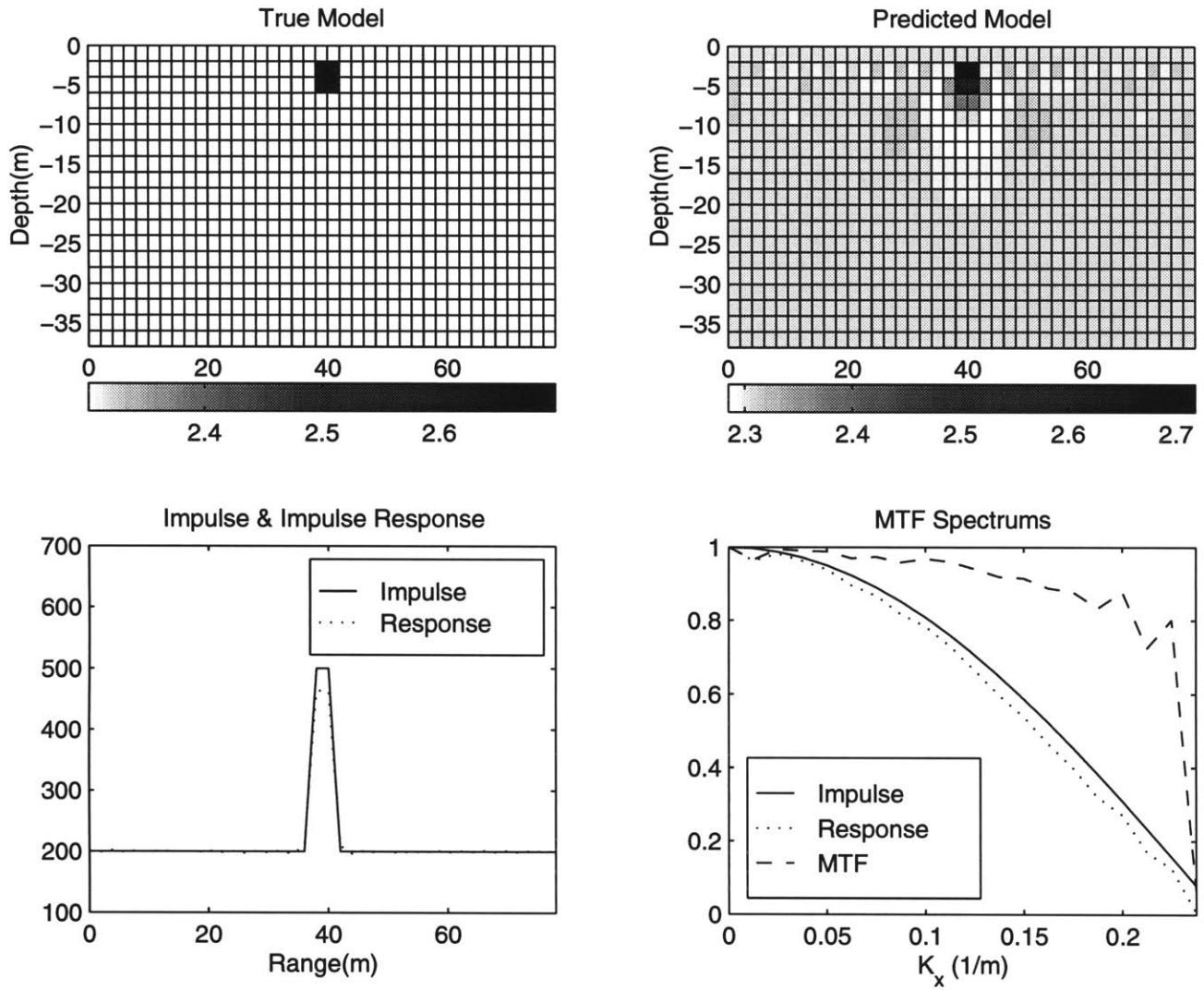


Figure 6-9: Inversion results and the MTF function obtained for an anomaly located at shallow depth. The reconstruction well resolves the anomaly.

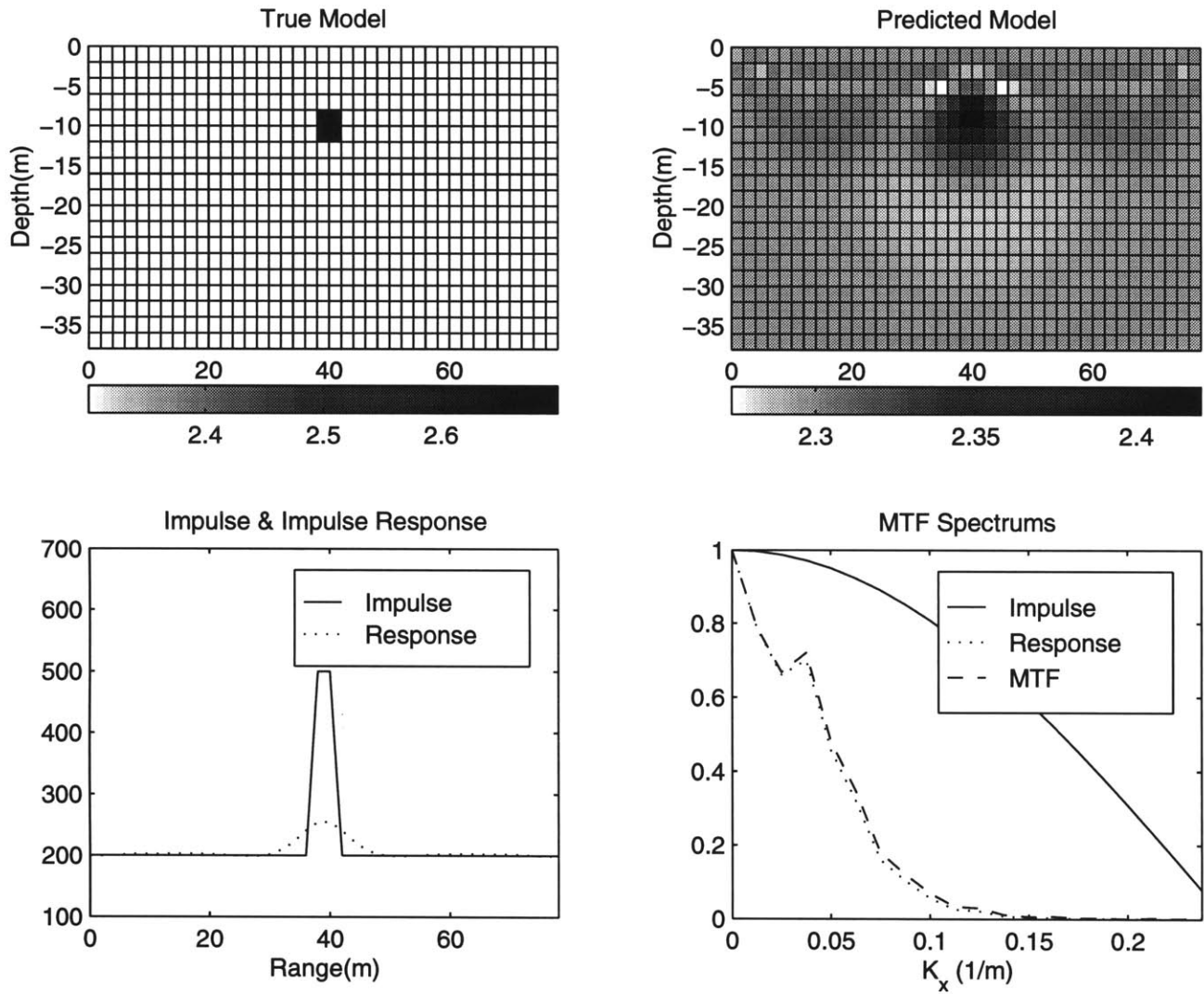


Figure 6-10: Inversion results and the MTF function obtained for an anomaly located at a deeper depth. The reconstruction shows a smeared anomaly.

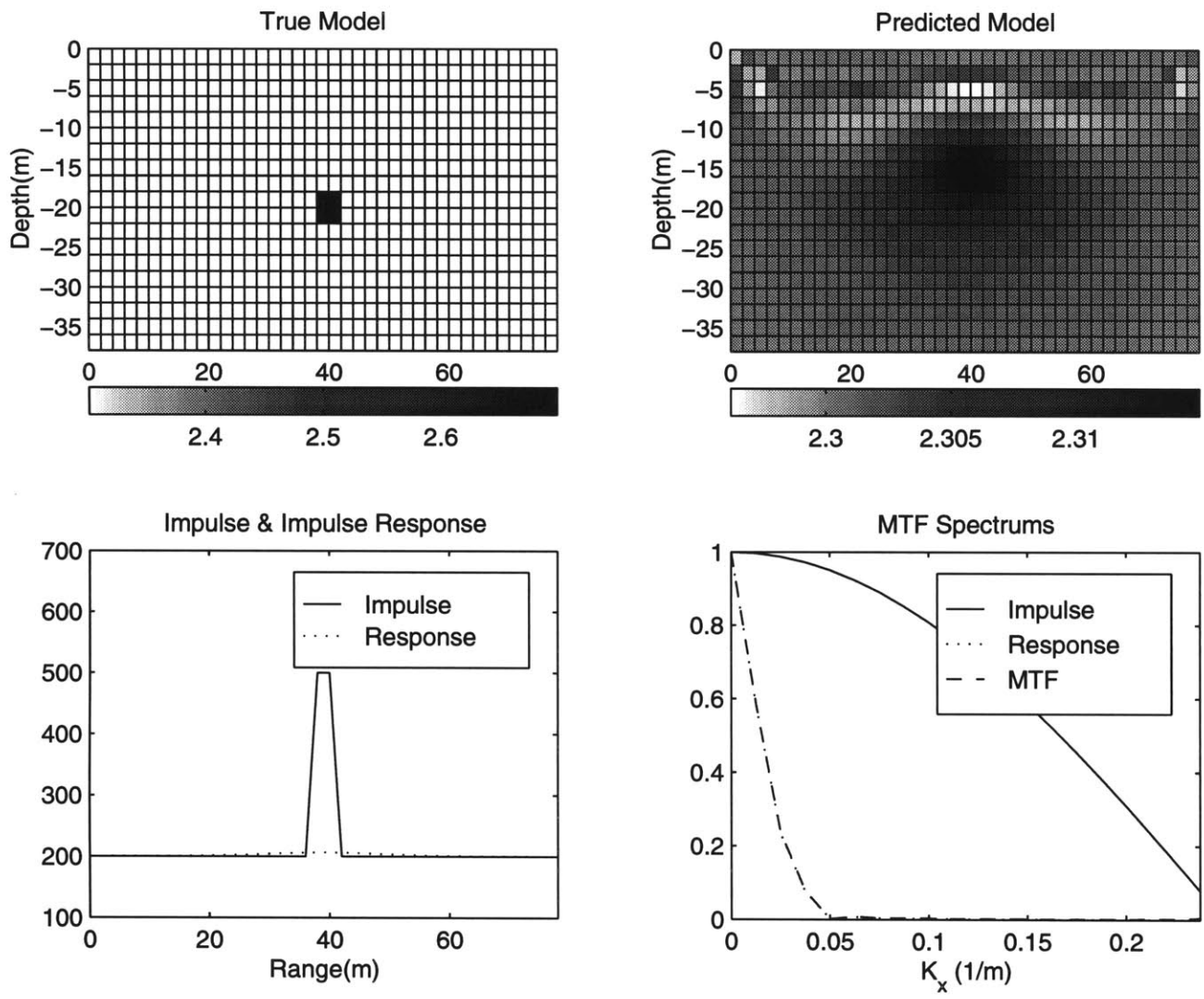


Figure 6-11: Inversion results and the MTF function obtained for an anomaly located even deeper than the previous two examples. The reconstruction indicates a substantially decreased resolution power.

# Chapter 7

## Optimizing The Electrical Survey

### 7.1 Introduction

The effectiveness and efficiency of the geoelectrical imaging method is highly dependent on the electrode configuration. An optimal electrode configuration should bring the maximal response and the highest resolution of the subsurface target inhomogeneity with the least amount of data acquisition. A number of studies have investigated various data acquisition geometries over geologic structures. A general conclusion is that the pole-pole array enables the greatest depth of investigation at the expense of vertical resolution (Roy and Apparao, 1971). The pole-dipole and the dipole-dipole arrays have the best sensitivity to anomalies (Coggon, 1973; Beard and Tripp, 1995) and are clearly superior to the pole-pole array. The dipole-dipole array appears to hold a slight advantage over the pole-dipole array (Beard and Tripp, 1995).

Traditionally, when the dipole-dipole array is used, a common approach for the acquisition geometry is the pseudo-section measurement in which the length of the current dipoles and the potential dipoles remains constant and data are plotted at



the intersection of lines sloping at 45 degrees from the center of the potential and current electrode pairs (Figure 7-1). It has been found that this method does not demonstrate capabilities of fully recovering underground structure. Thus, a more appropriate survey methodology is required to optimize the capability of the inversion technologies available.

The following sections outline a new data acquisition method which will increase the accuracy of resistivity tomography results. The sections includes a demonstration of this new data acquisition geometry with a comparison to results of the traditional, pseudo-section data gather on both a numerically generated synthetic test model and a field model. They also include an investigation of analytical approaches to estimate the sensitivity and accuracy of the new data acquisition geometry with a comparison to the pseudo-section data gather.

## **7.2 Tomographic Data Acquisition Geometry**

A 2-D resistivity tomography survey consists of a series of electrodes deployed in a straight line over the expected anomaly with a constant electrode spacing. A new geometry to obtain tomographical data is shown in Figure 7-2. This method is designed to achieve higher resolution than can be obtained with a pseudo-section gather. The measurement starts with injecting current into the ground at electrode number 1 with the common current sink located at the  $n$ th electrode. Potential differences are measured along the line of electrode pairs. Then the current is injected into the electrode number 2, and the measurements are repeated. This procedure continues until all the electrodes have been excited. The entire procedure is then repeated after reversing the geometry of the source dipole, (the current sink is moved to the number 1 electrode, and the source is scanned starting from the  $n$ th electrode).

## 7.3 Tomographic Vs. Pseudo-Section Acquisition

To illustrate the effectiveness of the spatially varying source dipole data acquisition, a numerically generated, synthetic model is designed. The synthetic model consists of two resistive prisms ( $\rho = 2000\Omega.m$ ). One is located in the middle of the model, and the other is near the edge. Both are buried in a homogeneous background ( $\rho = 20\Omega.m$ ). Results from the inversion of pseudo-section data reveals the anomaly located in the middle of the model, while the spatially varying source dipole data acquisition system leads to solutions revealing both anomalies (Figure 7-3). In practice, this new method is of interest for imaging of subsurface structures that have extended lateral anomalies. Therefore, this method can be more effective when little is known about the location, shape or extent of the anomalies.

The comparison of the two data acquisitions is also made on a field example. Recall in Chapter 3, in the field application of electrical resistivity tomography technique to the mapping of Harrison's cave in Barbados, West Indies, two caves in line B were indicted by the inversion results (Figure 3-21). The data acquisition geometry used to produce these results was the spatially varying source dipole tomographic data gather. On the same line, a pseudo-section data gather was also conducted, and the resulting image is compared to the results obtained with tomographic data gather techniques (Figure 7-4). The results indicate that the pseudo-section data acquisition geometry is only capable of depicting the cave located below the central area of the survey line. The large cave located near the left edge of the survey line is not resolved.

## 7.4 Sensitivity Analysis

In the investigations above, the study of a particular electrode array's effectiveness was carried out by a comparison between the inversion results and the true models. A more direct way to analyze the optimum of the electrode configuration is to investigate the variation of the sensitivities and model correlations with respect to each array.

Sensitivity analysis has been described in Chapter 6 for the uncertainty and resolution analysis. It is carried out by computing the sensitivity matrix and then adding together all the sources and receivers:

$$\text{Log} \sum_{is,ir}^{ns,nr} \frac{\partial Q_{ir}^{is}}{\partial \log(\rho_j)} = \text{Log} \sum_{is,ir}^{ns,nr} \left( -C_{ir}^{is} \mathbf{K}^{-1} \frac{\partial \mathbf{K}}{\partial \log(\rho_j)} v^{is} \right) \quad (7.1)$$

where  $is$  and  $ir$  are indexes numbers of sources and receivers, respectively.  $\mathbf{K}$  denotes a real, symmetric, and positive-definite matrix which depends on the resistivities and dimensions of the network cells.  $\rho$  is the model resistivity.  $v^{is}$  is a vector of the potentials at the network nodes due to source number  $is$ .  $C_{ir}^{is} = (0, \dots, 0, 1, 0, \dots, 0)$  where 1 is  $ir$ th the component which corresponds to the location of the receiver.

To compare the two survey geometries, a test model is designed for the sensitivity analysis and is chosen to be similar to Figure 7-3 but without the two anomalies. The focus is on the distribution of the sensitivity pattern caused only by the electrode configurations. 20 electrodes are placed on the surface at intervals of 4 meters. The sensitivities for both the pseudo-section gather and the spatially varying source dipole gather, as defined by Equation 6.22, are calculated and the results are displayed in Figure 7-5. The choice of a specific array geometry of source and receiver electrodes in order to yield the maximal response from a target inhomogeneity depends not only on the array configuration but also on the location of the target anomaly (e.g. for a deep target, the optimal array should have the ability to focus its energy in the zone of the target. Other places will not be important). If no such information is available,

finding an optimal array is irrelevant. In this case, the criteria for an optimal array is that the sensitivities are uniformly distributed throughout the elements of the entire model. The spatially varying source dipole data gather yields more uniformly distributed sensitivities which makes the method more effective in detecting structure with lateral extended anomalies.

## 7.5 Model Correlation Analysis

As shown in Chapter 6, the *a posteriori* correlation matrix can be extracted from the *a posteriori* covariance to inspect the relationship between the model parameters. If the model parameter is better resolved, the correlation matrix of that parameter tends to be more peaked. Conversely, a spreading correlation matrix indicates a poor resolution. This approach can be applied to distinguish an optimal electrode configuration. As seen in Figure 7-6 and Figure 7-7, the *a posteriori* model correlation at selected points gathered by the pseudo-section data acquisition tends to peak more at a point near the center than the one near the boundary. In the case of the spatially varying source dipole configuration, reconstruction of the model is more accurate. As seen in Figure 7-7 the model correlation at the boundary point is more peaked than that of the pseudo-section data gather, and spreading of the model correlation is similar to the one near the center, indicating that the entire area shares the same model correlations. These results translate into acquisition guidelines which would provide the ability to resolve targets with a high degree of accuracy.

## 7.6 Conclusion

This chapter is dedicated to the development of a methodology for investigating the optimization of electrode configuration to achieve higher resolution through sensitivity and model correlation analysis. Through this analysis it is clear that, for mapping subsurface geoelectrical structures, the spatially varying source dipole tomographic data acquisition geometry holds a more uniformly distributed sensitivity and leads to higher resolution than the traditional pseudo-section data gather. The idea of the spatially varying source geometry can be extended further. For example, one can put one of the current electrodes farther from the survey line and move it around so that more electric current can be injected into the depth. Such a performance can achieve a high resolution at depth. The idea can also be extended to 3-D electrical surveys. By spatially changing current source dipoles and moving them along different directions, one can obtain increased resolutions both laterally and with depth.

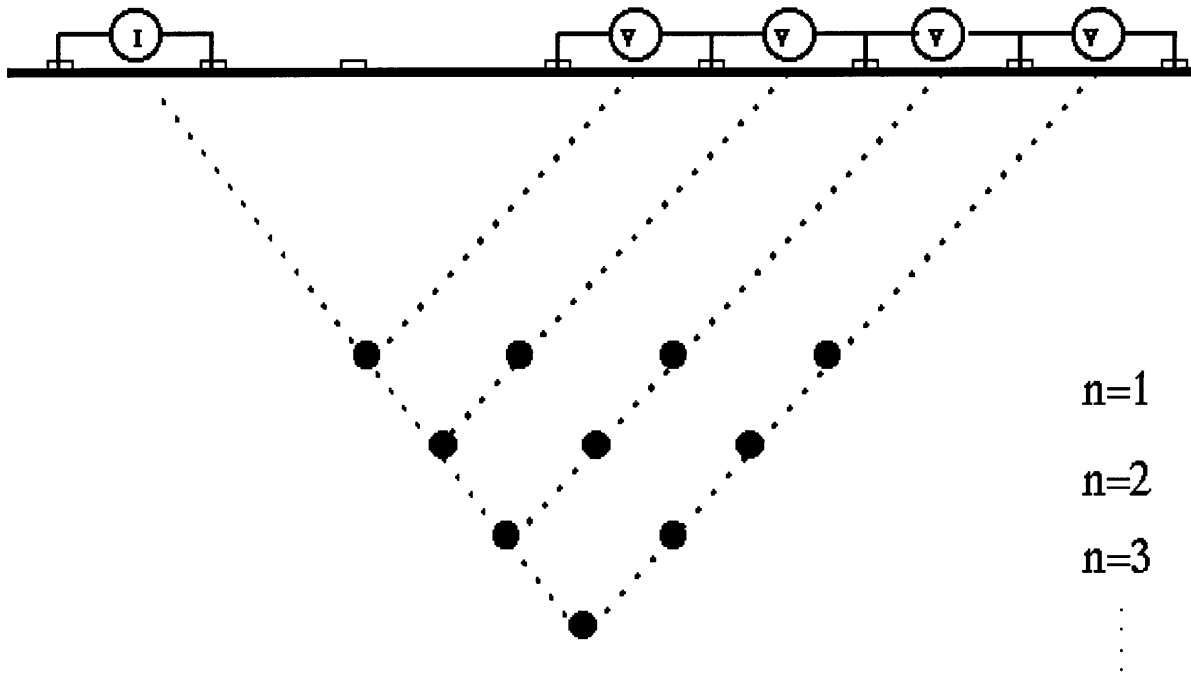


Figure 7-1: Diagram of the pseudo-section data gather in which the length of the current dipoles and the potential dipoles remain constant and data are plotted at the intersection of lines sloping at 45 degrees from the center of the potential and current electrode pairs.

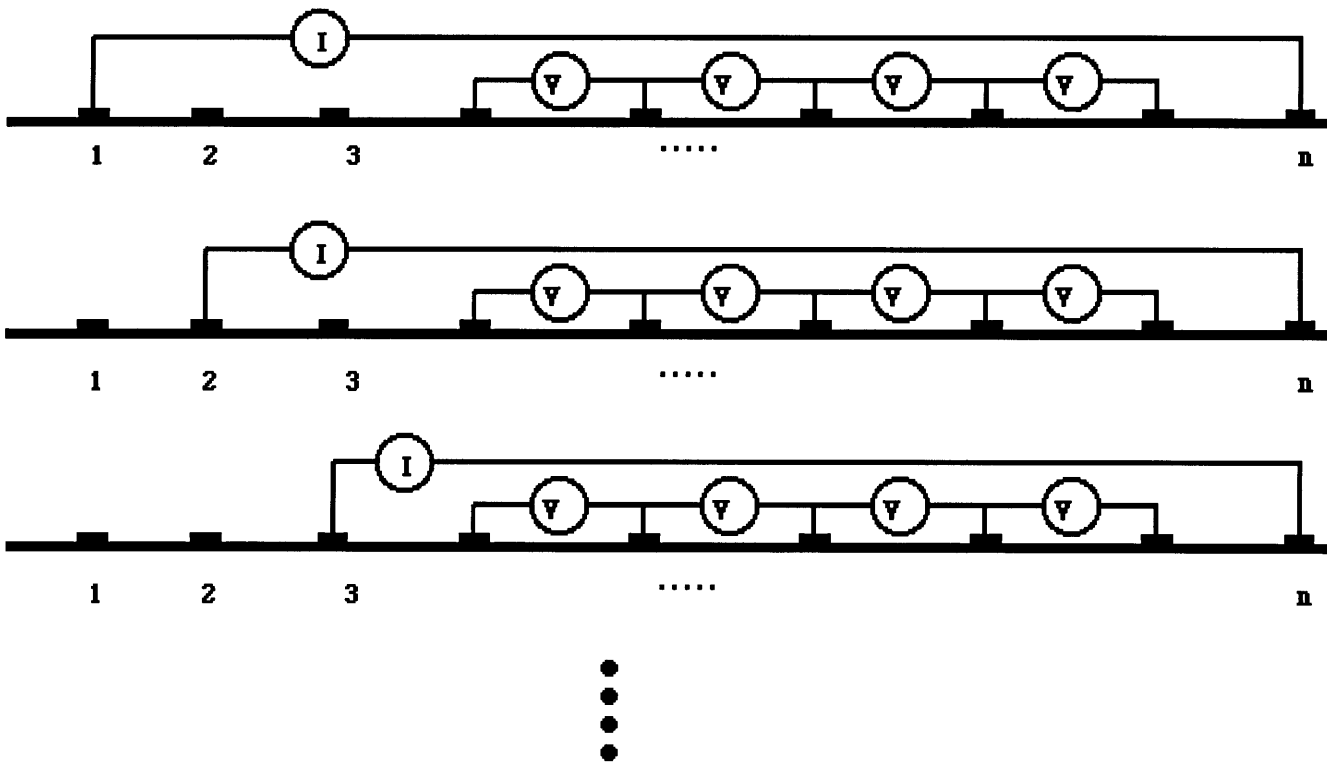


Figure 7-2: Diagram of a spatially varying source dipole tomographic data acquisition geometry.

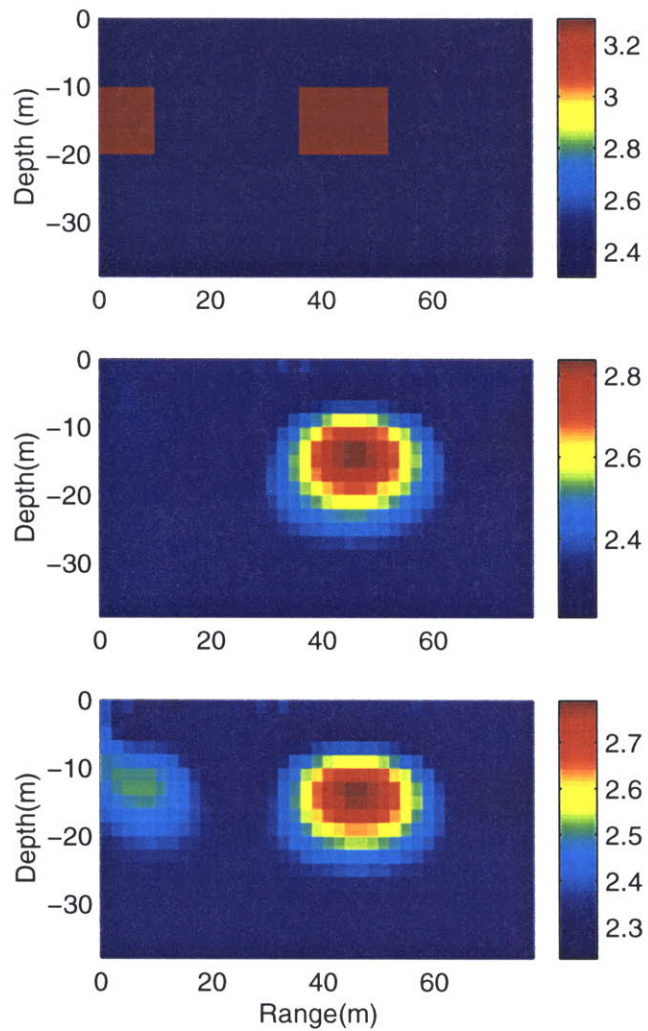


Figure 7-3: The synthetic model consists of two resistive prisms ( $\rho = 2000\Omega.m$ ) buried in a homogeneous background ( $20\Omega.m$ ) (top). Results from the inversion of pseudo-section data only reveals the anomaly located in the middle of the model (middle). Results from inversion of spatially varying source dipole data reveals both anomalies (bottom).



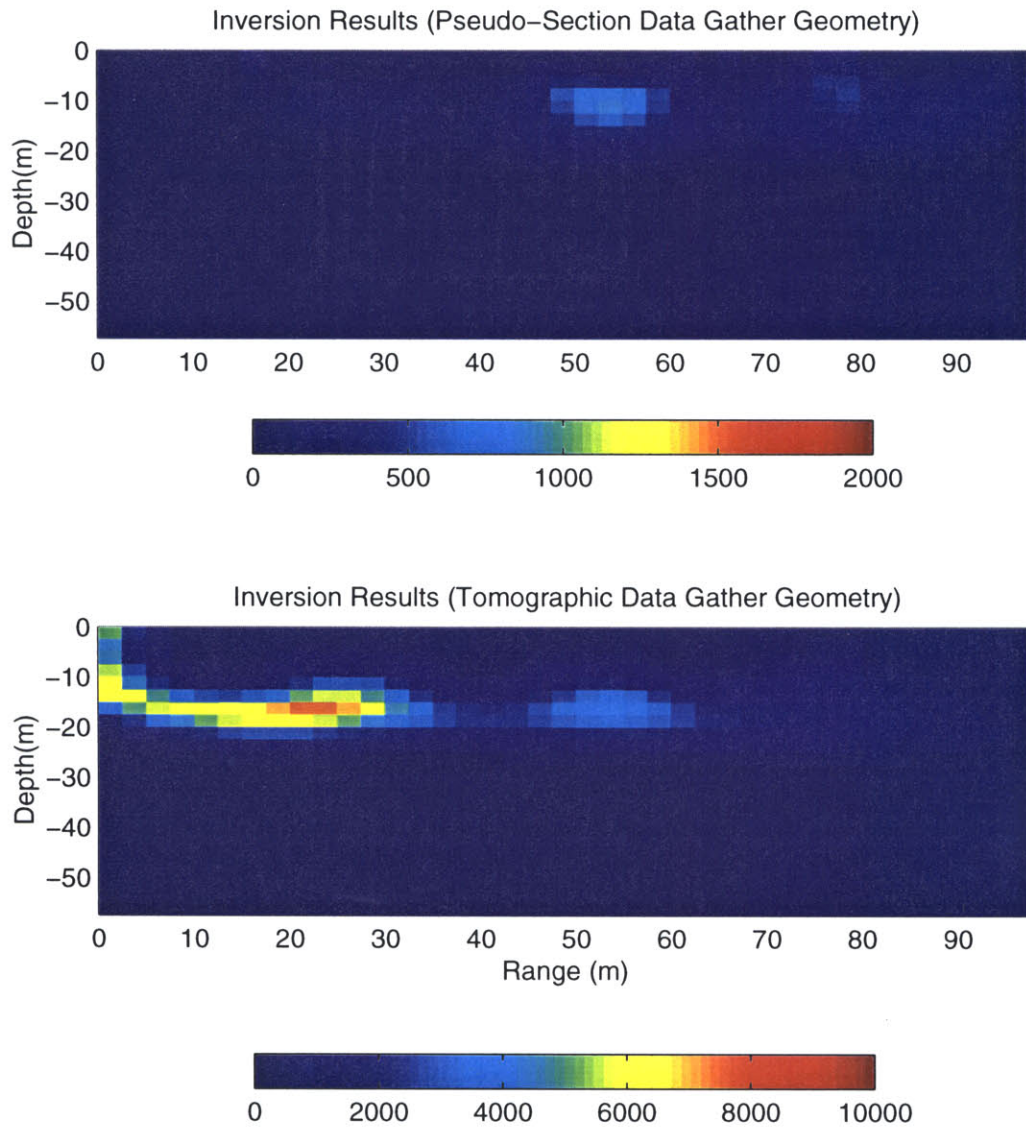


Figure 7-4: Results from inversion of pseudo-section data in Barbados Site, line B reveals only a small cave located in the middle of the model (top). Results from inversion of spatially varying source dipole data in Barbados Site, line B not only reveal the anomaly located in the middle of the model, but also indicate a large cave located near the left boundary of the model (bottom).

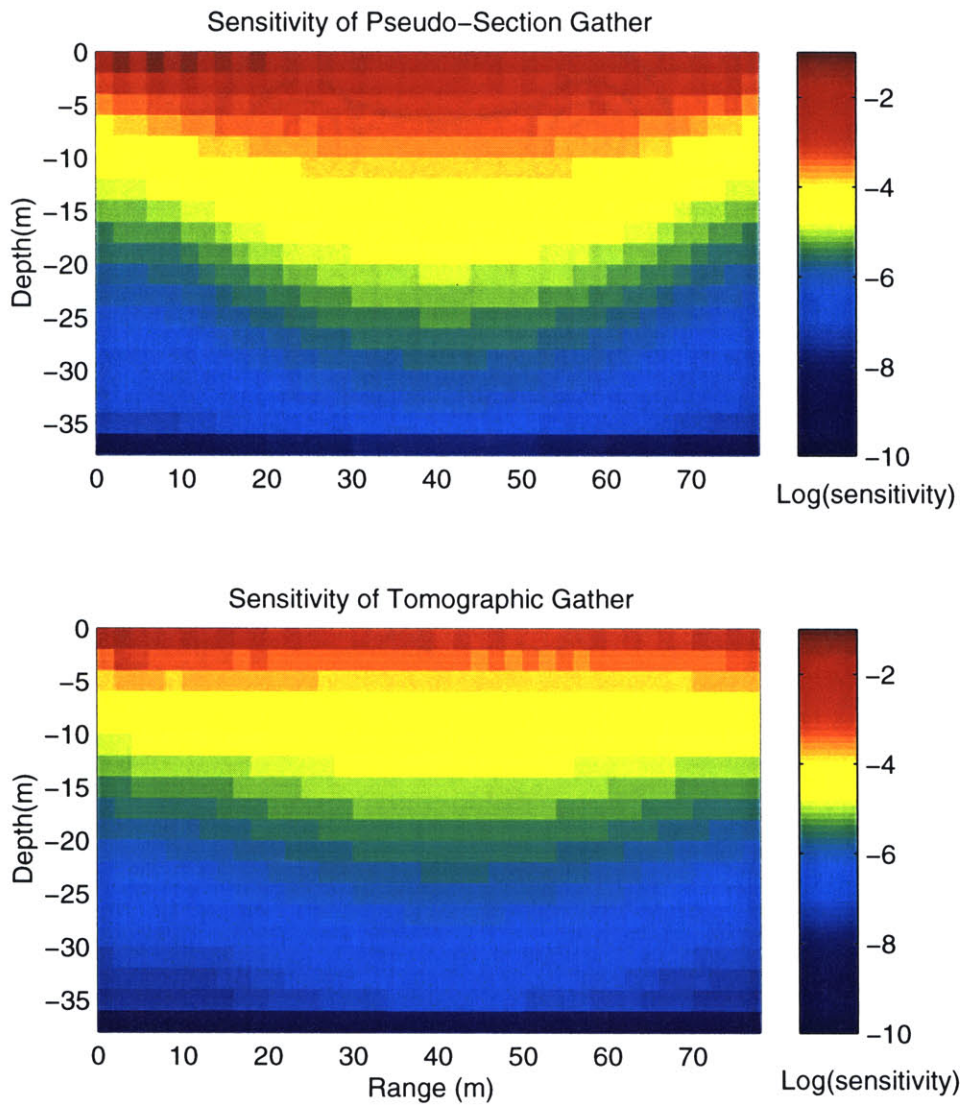


Figure 7-5: The sensitivities of the pseudo-section data gather shows a bowl-shaped distribution (top), while the sensitivities of the spatially varying tomographic data gather shows a more uniformly distributed pattern (bottom).

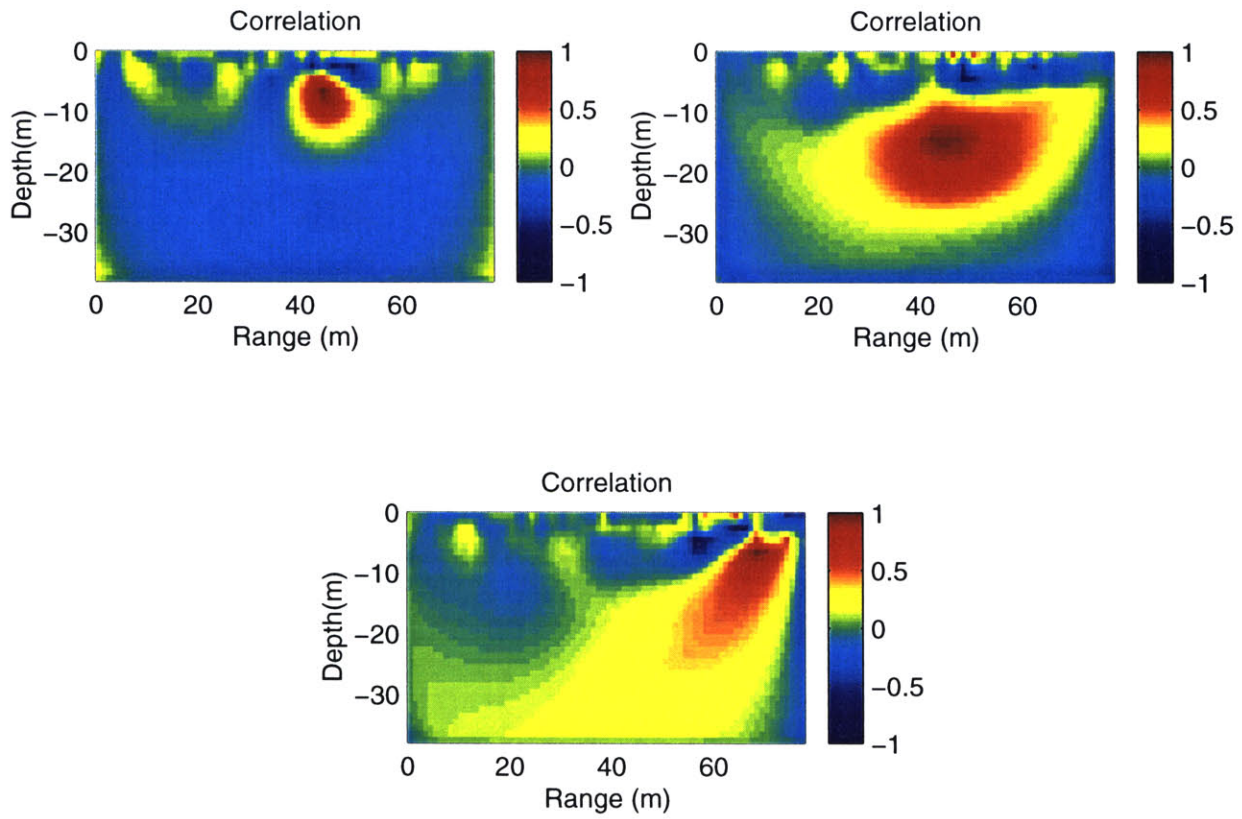


Figure 7-6: Model correlations for a selected point near the center area (top) and a point near the boundary (bottom) based on the pseudo-section data acquisition geometry.

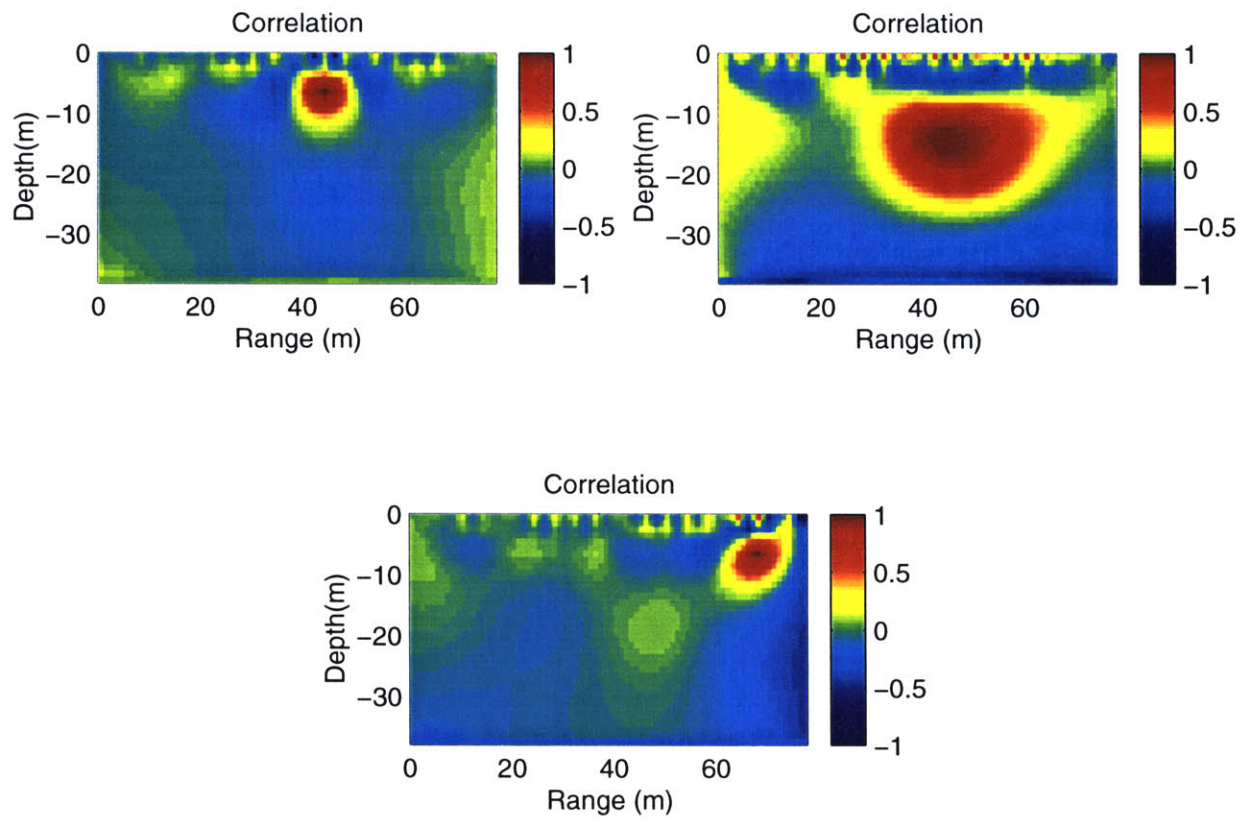


Figure 7-7: Model correlations for a selected point near the center area (top) and a point near the boundary (bottom) based on the spatially varying source dipole tomographic data acquisition geometry.

# Chapter 8

## Summary and Conclusions

### 8.1 Conclusions and Contributions

This thesis has developed a theory for the modeling and inversion of geoelectrical data based on Tikhonov regularization and the nonlinear conjugate gradient method. We have applied this theory to three important geoelectrical inverse problems: 3-D d.c. electrical resistivity, 3-D electrical Induced Polarization, and 3-D electrical Self-Potential. The primary purpose of this thesis is to develop an integrated geoelectrical methodology which includes a more physically meaningful inversion method, a more efficient algorithm to solve the inversion, a way to assess the resolution and uncertainty of the inverse solution, and a more effective survey geometry for the high resolution geoelectrical tomography. To demonstrate the applicability and the value of this inversion method to the real world, several geophysical field measurements have been conducted and the inversion results have been analyzed. Throughout the accomplishment of these goals this thesis has made the following contributions and conclusions.

Like many other geophysics inversion problems, the geoelectrical inversion is inherently nonunique. There are two reasons for the nonuniqueness: the intrinsic lack of data, and the uncertainties caused by the numerical and experimental errors. Mathematically, such an inverse problem is referred to as an 'ill-posed' problem of which the solution is neither unique nor stable. It is necessary to introduce *a priori* assumptions to the unknown model parameters in order to get a more unique and stable solution. This thesis has taken an approach of choosing a model that has the minimum structure to fit the data. Any variation of the model parameter is only required by the data. This approach is significant in that it obeys a fundamental tenet of modern science, known as Occam's razor, which states: hypotheses should be neither unnecessarily complicated nor unnecessarily numerous. This approach is a conservative way of interpreting data and provides a lower bound of model complexity.

The minimum structure solution has been constructed by using Tikhonov regularization by which the solution to the inverse problem is defined as a joint minimization of data misfit and model roughness. The minimization problem has been solved efficiently by a nonlinear conjugate gradient method with proper preconditioning. An optimal preconditioner which resembles the property of the Hessian matrix but requires far less computational power has been found. This nonlinear conjugate gradient method has resulted in a tremendous time savings over the conventional Gauss-Newton approach.

When Tikhonov regularization is applied to geoelectrical problems, it has the following justifications. (1) For the d.c resistivity problem it is necessary to apply the Laplacian operator as the smoothness constraint in order to stabilize the inversion and eliminate the surface artifacts. The 0-th order partial differential operator simply is a least square damping, it cannot diminish the surface roughness due to the singularities at the source and receiver positions. The first order partial differential operator (i.e. the gradient) can diminish some of the surface roughness but cannot

fully eliminate the surface singularity. For this reason, the Laplacian operator used as the smoothness constraint is the preferred technique. (2) For the induced polarization problem, the Laplacian operator is also necessary for stabilization. However, when applying the Tikhonov regularization method to IP problem, it is possible to use different smoothness coefficients on the real and the imaginary components of the model for a better constraint of the inversion because the real and the imaginary parts of the solution have different orders of magnitude and independent errors. In practice, because the imaginary part is much smaller than the real part, we found it is reasonable to use the same smoothness coefficient for both the real and the imaginary part of the solution. Under these circumstances, the objective function can be constructed in a complex form and solved in a straight forward scheme in the complex domain. Each step of the inversion procedure now can be related directly to the d.c resistivity inversion. From a synthetic example of the application of the inversion process, we have demonstrated that such an inversion is capable of identifying even slight changes of complex resistivity with changes in frequency. The variation of the amplitude and phase of the complex resistivity as a function of frequency has been clearly reconstructed. (3) In the problem of Self-Potential inversion, one is interested in the reconstruction of subsurface current sources from a surface electric potential anomaly. The inversion has more nonuniqueness difficulties than d.c resistivity and IP. When the Tikhonov regularization method is applied to the SP problem, the definition of the regularization operator must be justified and extended. A more flexible version of the regularization operator should be defined to reduce the nonuniqueness. For example, one can regularize the resistivity structure, the position, orientation, and magnitude of the SP anomaly, depending on the *a priori* knowledge of such information. When these constraints are applied to the inversion, the nonuniqueness can be reduced to some extent; however, it is difficult to completely eliminate the nonuniqueness. In practice, the success of SP inversions is highly dependent on one's knowledge of the resistivity structure and a reasonable estimation of the geometry

and location of the source.

Once the stabilizing functional is established, the amount of smoothing done is controlled by the regularization coefficient  $\tau$ . The optimal value of  $\tau$  is determined by plotting the RMS  $\chi^2$  data misfit curve against  $\tau$  and picking a value of  $\tau$  at the place where the slope of the curve starts to change.

We have developed a methodology to characterize the uncertainty and resolution capability of the geoelectrical inversion. We perform an uncertainty analysis to quantify the resolution and variance as a function of position in the model. We appeal to the Bayesian framework whereby both variance and resolution are inferred from the *a posteriori* covariance associated with our reconstruction. A direct extension of using the Monte Carlo method to calculate the *a posteriori* covariance is not available because the inverse of the regularization operator, which corresponds mathematically to the *priori* model defined in the Bayesian framework, is ill-posed and not well defined. Therefore, a new method which consists of the following procedures is proposed. We first calculate the corresponding *a posteriori* covariance matrix on an optimal non-linear regularization solution to give an accurate measure of the uncertainty. This uncertainty is associated with the model parameter and can be resolved deterministically by the data. Through sensitivity analysis, the obtained uncertainty is calibrated to measure uncertainty for the other model parameters. To measure the resolution power of the inversion technique, the Monte Carlo method is used, and many realizations of perturbed data are inverted to obtain the *a posteriori* model correlation. For computational efficiency, the resolution is analyzed through the Modulation Transfer Function, borrowed from the optical imaging community. The numerical analysis on synthetic data demonstrates that the method gives resolution and variance information that behaves correctly with regard to the electrical current coverage and the character of the associated reconstruction.



We have also developed a new survey geometry for the geoelectrical method. This method employs a spatially varying source dipole and obtains more complete subsurface information. We have used sensitivity analysis and model correlation estimation to demonstrate the advantages of this new geometry. Our synthetic example and the field example of mapping limestone caves in Barbados have shown that the new acquisition geometry is more effective than the traditional pseudo-section acquisition geometry in cases where structure has an extended lateral variation.

We have applied our inversion techniques to various geoelectric field measurements. With these modern inversion methods, we can revolutionize our subsurface imaging capability. We have demonstrated that the geoelectrical inversion technique can be used successfully for several purposes: (1) to characterize subsurface properties and structure, (2) to map underground caverns or facilities which are important to both domestic and military applications, (3) to monitor re-injection history in geothermal fields, and (4) to map and characterize environmental contamination. Although this thesis has provided limited examples, the application of geoelectrical inversion certainly can be used for many other geophysics problems. It is the author's belief that this advanced modeling and inversion technique will help the geoelectrical method evolve as a more general technique which can be applied to many complicated structures.

## 8.2 Future Work

While working on this thesis, we found that the following issues require more concentrated investigation in the future.

A better smoothness operator should be investigated. Although the Laplacian operator can successfully constrain the surface roughness and stabilize the solution, the

overall reconstructed imaging is overly smoothed compared to the original medium. Future focus should consider methods to increase the resolution ability of the geoelectrical inversion technique or to yield a more accurate reconstruction of the subsurface. A possible approach is using the fractional partial derivative as the smoothness operator.

In this thesis, regularization is applied to the model space to emphasize the spatial correlation of each model parameter. In the future, it would help to develop a regularization technique in terms of spatial interpolation which can be applied to the data space. There are two advantages: first, since each datum contains random experimental noise, regularizing data through the spatial interpolation can average the noise and, essentially, increase the data accuracy; second, by regularizing data, additional information may be added to the inversion. Any earth material should obey certain spatial continuity and geoelectrical energy also has a diffusive nature; therefore, any abrupt spatial change in data is not realistic. Geophysical data should follow spatial continuity in the places that are nearby. Using data regularization, one hopes to retrieve such spatial correlation. Thus more information about the medium can be extracted from the existing data and can be added to positions where there is no electrode coverage.

Investigation on the interpretation of IP data is still in a premature state. This thesis has theoretically developed an inversion methodology to invert the frequency domain IP data for the complex resistivity structure. Whether such a method can be applied successfully to the real field data is not verified. Field experiments need to be conducted to demonstrate the applicability of the inversion technique. Another important direction for the future work on IP inversion is the investigation of IP parameters as they relate to solving real geophysics problems such as delineation of environmental contamination plumes and prospecting for mineral deposits.

The inversion of SP data can be extended to the characterization of electrokinetic, electrochemical, thermoelectrical sources. Current emphasis is made on the purely electrical problem, ignoring the sources that cause the SP effects. In the future, a more direct inversion can be developed including the cross-coupling effect. The inversion thus can be proposed as a two-step process. For instance, in the problem of streaming potential, one first can invert the electrical potential data to recover the location and magnitude of subsurface electrical current sources, then on the same grid system one can perform an inversion to solve for the hydrodynamic term that causes the electrical Self-Potential anomaly.

Finally, the joint inversion concept is an important approach to develop in the future. Because the resolution power of each individual method is limited, a combined survey and a joint inversion between different geophysics surveys is promising for obtaining more accurate images of subsurface structure. Any joint inversion technique requires a more sophisticated inversion method and more computational effort. With further development of the inversion technique and the advancing computational potential, it will become a practical method and will result in more detailed information than is possible with a single technique.

# Bibliography

- [1] Allegrini, G., Cappetti, G., and Sabatelli, F., 1995, Geothermal development in Italy, country update report, Proceedings of the World Geothermal Congress, 201-208.
- [2] Bache, T. C., Rodi, W. L., and Harkrider, D. G., 1978, Crustal structures inferred from Rayleigh-wave signatures of NTS explosions, *Bull. Seism. Soc. Am.*, **68**, 1399-1413.
- [3] Backus G., and Gillbert F., 1967, Numerical application of a formalism for geophysical inverse problems, *Geophys. J. Roy. Astron. Soc.*, **13**, 247-276.
- [4] Backus G., and Gillbert F., 1968, The resolving power of gross earth data, *Geophys. J. Roy. Astron. Soc.*, **16**, 169-205.
- [5] Backus G., and Gillbert F., 1970, Uniqueness in the inversion of inaccurate gross earth data, *Phil. Trans. R. Soc. London Soc., A*. **266**, 123-192.
- [6] Beard, L. P., and Hohmann, G. W., 1992, Subsurface imaging using approximate IP inversion, 62nd Ann. Internat. Mtg., Soc. Expl. Geophys. Expanded Abstracts, 427-430/
- [7] Beard, L. P., and Morgan, F. D., 1991, Assessment of 2-D resistivity structures using 1-D inversion, *Geophysics*, **56**, 874-883.

- [8] Beard, L. P., and Tripp, A. C., 1995, Investigating the resolution of IP arrays using inverse theory, *Geophysics*, v. 60, p. 1326-1341.
- [9] Beasley, C. W., and Ward, S. H., 1986, Three-dimensional mise-a-la-masse modeling applied to mapping fracture zones, *Geophysics*, **51**, 98-113.
- [10] Bertin, J., and Loeb, J., 1976, Experimental and aspects of induced polarization, Vol. 1 and 2., Gerbruder Borntraege.
- [11] Bertini F., Bertini G., Dianelli G., Pandeli E., Puxeddu M., Villa I. 1985b. Deep structure, age and evolution of the Larderello-Travale geothermal field, *Transactions of the Geothermal Resources Council*, Vol. 9-Part I.
- [12] Bevc, D., and Morrison, H.F., 1991. Borehole-to-surface electrical resistivity monitoring of a salt water injection experiment, *Geophysics*, **56**, 769-777.
- [13] Black, W. E., and Corwin, R.F., 1984, Application of self-potential measurements to the delineation of groundwater seepage in earth-fill embankments, 54th Ann. Internat. Mtg., Soc. Expl. Geophys., Expanded Abstracts, 162-164.
- [14] Block L. and Royden, L., 1991 Core complex geometries and regional scale flow in the lower crust, *Tectonics*, **9**, 557-567.
- [15] Blum, R. 1989, Geoelectrical mapping and groundwater contamination in detection of subsurface flow phenomena, ed. G-P Merker, Springer, Berlin Heidelberg, 253-260.
- [16] Bogoslovsky, V. A. et al, 1979, Geophysical methods for controlling the seepage regime in earth dams, *Bull. Int. Ass. of Geol.*, **20**, 249-251
- [17] Bogoslovsky V, V., and Ogilvy, A. A., 1973, Deformations of natural electric fields near drainage structures, *Geophys. Prosp.*, v. 21, p. 716-723.
- [18] Born, M., and Wolf, E., 1964, "Principles of optics", Macmillan, New York.

- [19] Burger, H. R., 1992, *Exploration Geophysics of the shallow surface*, Prentice Hall.
- [20] Buselli, G. B., et al, 1991, Detection of groundwater contamination near waste disposal sites with transient electromagnetic and electrical methods, in *Investigations in Geophysics no. 5, Geotechnical and Environmental Geophysics, II*, SEG, Tulsa, 27-39.
- [21] Cappetti, G., Parisi, L., and Stefani, G., 1997, Fifteen years of reinjection in the Larderello-Valle Secolo area: Analysis of the production data, *Proceedings of the World Geothermal Congress*.
- [22] Carpenter, P. J., et al, 1990, Use of resistivity soundings to determine landfill structure, *Ground Water*, **28**, 569-575.
- [23] Cist, D.B., Mackie, R.L., Zeeb, P.J., and Toksöz, M.N., 1995, Correlating GPR and resistivity surveys with cone penetrometer and shallow coring studies along the Aberjona River, *Proceedings, SAGEEP*, Orlando, Florida, Environmental and Engineering Geophysical Society, 87-96.
- [24] Coggon, J. H., 1971, Electromagnetic and electrical modeling by the finite element method, *Geophysics*, **36**, 132.
- [25] Coggon, J. H., 1973, A comparison of IP electrode arrays, *Geophysics*, **38**, 737-761.
- [26] Cole, K. S., and Cole, R. H., 1941, Dispersion and absorption in dielectrics, *J. Chem. Phys.*, **9**, 341.
- [27] Constable, S.C., Parker, R. and Constable, C.G., 1987, Occam's Inversion, A practical algorithm for generating smooth models from electromagnetic sounding data, *Geophysics*, **52**, 289-300.

- [28] Corry, C. E., 1985, Spontaneous polarization associated with porphyry sulfide mineralization, *Geophysics*, **50**, 1020-1034.
- [29] Corwin, R. F., DeMouly, G. T., and Harding, R.S. Jr., 1981, Interpretation of self-potential survey results from the East Mesa geothermal field, California, *J. Geophys. Res.*, **86**, p. 1841-1848.
- [30] Corwin, R. F., and Hoover, D. B., 1979, The self-potential method in geothermal exploration, *Geophysics*, , **44**, p. 226-245.
- [31] Corwin, R. F., and Morrison, H. F., 1977, Self-potential variations preceding earthquakes in central California, *Geophys. Res. Lett.*, **4**, p. 171.
- [32] Corwin, R. F., 1990, The self potential method for environmental and engineering applications, Edited by Ward, S. *in* Geotechnical and environmental geophysics, SEG.
- [33] Dey, A., Morrison, H. F., 1979, Resistivity modeling for arbitrary shaped three-dimensional structures, *Geophysics*, **44**, 753-780.
- [34] deGroot-Hedlin, C., and Constable, S., 1990, Occam's inversion to generate smooth, two-dimensional models from magnetotelluric data, *Geophysics*, **55**, 1613-1624.
- [35] de Witte, L., 1948, A new method of interpretation of self potential data, *Geophysics*, **13**, p. 600-608.
- [36] Dini, I., 1989, Structural model of the Larderello geothermal field; main geophysical lineaments of the metamorphic basement, *U.N.G. Geominerario Uff. Esplorazione, internal report*, ENEL, Pisa, Italy.
- [37] Duijndam, A.J.W., 1988. Bayesian estimation in seismic inversion. Part II, Uncertainty Analysis. *Geophysical Prospecting*, **36**, 899-918

- [38] Ellis, R. G., and Oldenburg, D. W., 1994a, Applied geophysical inversion, *Geophys. J. Int.*, **116**, 5-11.
- [39] Ellis, R. G., and Oldenburg, D. W., 1994b, The pole-pole 3-D DC-resistivity inverse problem, a conjugate gradient approach, *Geophys. J. Int.*, **119**, 187-194.
- [40] Eloranta, E. H., 1986, Potential field of a stationary electric current using Fredholm's integral equations of the second kind, *Geophys. Prospecting*, **34**, 856-872.
- [41] ENEL spa, 1995, Geoelectric control of reinjection in the Larderello-Valle Secolo geothermal field, (Final Report).
- [42] Ferrara G. C., Luccioli F., Palmerini G. C., and Scappini U., 1985, Update report on geothermal development in Italy, *International Symposium on geothermal energy, International Volume, Geothermal Resources Council*.
- [43] Fink, J. B., McAlister, E. O., Sternberg, B. K., Wieduwilt, W. G., and Ward, S. H., 1990, Induced polarization, applications and case histories, Investigations in Geophysics No. 4, SEG
- [44] Fiordelisi A., Mackie M., Madden T., Manzella, A., Rieven, S., 1995, Application of the MT method using a remote-remote reference system for characterizing deep geothermal system, *Proceedings of the World Geothermal Congress*, 893- 897.
- [45] Fitterman, D. V., 1978, Electrokinetic and magnetic anomalies associated with dilatent regions in a layered earth, *J. Geophys. Res.*, **83**, p. 5923.
- [46] Fitterman, D. V., 1970, Calculations of self-potential anomalies near vertical contact, *Geophysics*, **44**, p. 195-205.
- [47] Fitterman, D. V., 1979, Calculations of self-potential anomalies near vertical contacts, *Geophysics*, **44**, p. 195-205.



- [48] Fitterman, D.V., 1984, Theroelectrical self-potential anomalies and their relationship to the solid angle substenced by the source region, *Geophysics*, **49**, p. 165-170.
- [49] Fletcher, R., and Reeves, C. M., 1959, Function minimization by conjugate gradients.
- [50] Franklin J., N., 1970, Well-posed Stochastic Extensions of Ill-posed Linear Problems. *Math. Anal. Appl.*, **31**, 682-716.
- [51] Frangos, W., 1992, Electrical detection of leaks in lined waste disposal ponds, M.S. thesis, University of Utah.
- [52] Frye, K. M., Lesmes, D. P., and Morgan, F. D., 1998, The influence of pore fluid chemistry on the induced polarization response of rocks and soils, *Proc. SAGEEP'98*, 771-780.
- [53] Furness, P., 1993, Gradient array profiles over thin resistive veins, *Geophys. Prosp.*, **41**, 113-130.
- [54] Gouveia, W., and Scales, J., 1997, Resolution of seismic waveform inversion, Bayes versus Occam, *Inverse Problems*, **13**, 323-349.
- [55] Hallof, P. G., 1957, On the interpretation of resistivity and induced polarization field measurements, Ph.D thesis, Massachusetts Institute of Technology.
- [56] Hanneson, J. E., 1990, A model for interpreting IP/ resistivity data from areas of steep dip and thin overburden, in Fink, J. B., McAlister, E. O., Sternberg, B. K., Wieduwilt, W. G., and Ward, S. H., Eds., Induced polarization, Applications and case histories, Soc. Expl. Geophys., Investigations in geophysics No. 4, 128-149.
- [57] Hazardous Waste Remedial Actions Program (HAZWRAP), 1995, Installation restoration program remedial investigation report. Advance Science, Inc. Oak Ridge, TN.

- [58] Hobbs III, H. H., 1994, A study of environmental factors in Harrison's cave, Barbados, West Indies, report, National Speleological Foundation.
- [59] Hohmann, G. W., 1975, Three-dimensional induced polarization and electromagnetic modeling, *Geophysics*, **40**, 309-315.
- [60] Hohmann, G. W., 1990, Three-dimensional IP models, in Fink, J. B., McAlister, E. O., Sternberg, B. K., Wieduwilt, W. G., and Wark, S. H., Eds., Induced polarization, Applications and case histories, Soc. Expl. Geophys., Investigations in geophysics No. 4, 150-178.
- [61] Inman, J.R., 1975, Resistivity inversion with ridge regression, *Geophysics*, **40**, 798-817.
- [62] Jacobs, D. A., 1986, A generalization of the conjugate gradient method to solve complex systems, *IMA J. Num. Analysis*, **6**, 447-452.
- [63] Jiracek, G. R., Rodi, W. L. and Vanyan, L. L., 1987, Implications of magnetotelluric modeling for the deep crustal environment in the Rio Grande rift, *Phys. Earth Planet. Int.*, **45**, 179-192.
- [64] Johnson, I. M., 1990, Spectral IP parameters derived from time-domain measurements, in Fink, J. B., McAlister, E. O., Sternberg, B. K., Widuwilt, W. G., and Ward, S. H., Eds., Induced Polarization: Applications and case histories, SEG.
- [65] Jones, A. G., and Hutton, R., 1979, A multi-station magnetotelluric study in southern Scotland II. Monte-Carlo inversion of the data and its geophysical and tectonic implication, *Geophys. J. Roy. Astr. Soc.*, **56** 351-358.
- [66] Keilis-Borok, V. J., and Yanovskaya, T. B., 1967, Inverse problems in seismology (structure review), *Geophys. J. R. Astron. Soc.*, **13**, 223-234.

- [67] Keller, G.V., and Frischknecht, F.C., 1966, Electrical methods in geophysical prospecting, Oxford, Pergamon, 517.
- [68] Killpack, T.J., and Hohmann, G. W., 1979, Interactive dipole-dipole resistivity and Ip modeling of arbitrary two-dimensional structures, DOE/DGE rep., contract EG-78-C-07-1701, Earth Science Lab, Univ. of Utah Research Inst.
- [69] Lanczos, C., 1952, Solution of systems of linear equations by minimized iterations, *J. Res. Natl. Bureau Standards*, 49, 33-35.
- [70] L ev eque, J., Rivera, L., and Wittlinger, G., 1993, On the use of the checkerboard test to assess the resolution of tomographic inversions, *Geophys. J. Int.*, **115**, 313-318.
- [71] Mackie, R. L. and Madden, T. R., 1993, Three-dimensional magnetotellurics inversion using conjugate gradients, *Geophys. J. Int.*, **115**, 215-229.
- [72] Madden, T.R., 1972, Transmission system and network analogies to geophysical forward and inverse problems, *ONR Tech. Rep.*, **72-3**.
- [73] Madden, T.R., 1971, The resolving power of geoelectric measurements physical properties of the earth's crust, T. G. Heacock, Ed., AGU monograph 14, p. 95.
- [74] Madden, T. R., and Cantwell, T., 1967, Induced polarization, a review, in *Mining Geophysics. 2, Theory: Soc. Exp. Geophys.* 46 916-931.
- [75] Marquardt, D. W., 1963, An algorithm for least-squares estimation of non-linear parameters, *J. Soc. Ind. App. Math.*, **11**, 431-441.
- [76] Marshall, D. J., and Madden, T. R., 1959, Induced polarization, A study of its causes; *Geophysics*, **24**, p. 790.
- [77] Mase, C. W., Chapman, D. S., and Ward, S. H., 1978, Geophysical study of the Monroe-RedHill geothermal system, DOE/DGE topical rep., contract EY-76-S-07-1601, Univ. of Utah.

- [78] Matarese, J., 1995, Nonlinear Traveltime Tomography, PhD thesis, Massachusetts Institute of Technology.
- [79] Mazac, O., et al, 1990a, Determination of the extent of oil contamination in groundwater by geoelectrical methods, in *Investigations in Geophysics no. 5, Geotechnical and Environmental Geophysics*, **II**, SEG, Tulsa, 112-119.
- [80] McBrearty, D., 1993, Fracture Flow as Influenced by Geologic Fractures in the Aberjona Valley, Massachusetts, *M.S. thesis*, Massachusetts Institute of Technology.
- [81] McNeill, J.D., 1990 Use of electromagnetic methods for groundwater studies in Ward, S. H., *Geotechnical and Environmental Geophysics*; **I**, 191-218.
- [82] Medeiros, W. E. and Lima, O.A.L., 1990, Geoelectrical Investigation for groundwater in crystalline terrains of center Bahia, Brazil, *Ground Water*, **28**, 518-523.
- [83] Mosegaard, K., and Tarantola, A., 1995, Monte Carlo sampling of solutions to inverse problems, *J. Geophys. Res.*, **B7**, 12431-12447.
- [84] Mufti, I. R., 1976, Finite-difference resistivity modeling for arbitrarily shaped two-dimensional structures, *Geophysics*, **41**, 62.
- [85] Nourbehecht, B., 1963, Irreversible thermodynamic effects in inhomogeneous media and their application in certain geoelectric problems, Ph. D. thesis, Massachusetts Institute of Technology.
- [86] Ogilvy, A. A., Ayed, M. A., and Bogoslovsky, V. A., 1969, Geophysical studies of water leakages from reservoirs, *Geophys. Prosp.*, **17**, p. 36-62.
- [87] Okko, O. T., 1993, Geophysical investigations in municipal engineering - the enlargement of landfill area in Hanko city, southern Finland, in *Procs. SAGEEP 1993*, 669-676.

- [88] Oldenburg, Douglas W. and Li, Yaoguo, 1994, Inversion of Induced Polarization Data, *Geophysics*, **59**, 1327-1341.
- [89] Onsager, L., 1931, Reciprocal relations in irreversible processes I, *Phys. Rev.*, **37**, p. 405-426.
- [90] Parker, R., 1984, The inverse problem of resistivity sounding, *Geophysics*, **49**, 2143-2158.
- [91] Park, S. K. and Van, G. P., 1991, Inversion of pole-pole data for 3-D resistivity structure beneath arrays of electrodes, *Geophysics*, **56**, 951-960.
- [92] Paul, K., 1965, Direct interpretation of self-potential anomalies caused by inclined sheets of infinite horizontal extensions, *Geophysics*, **30**, p. 418-423.
- [93] Pekeris, C. L., 1940, Direct method of interpretation in resistivity prospecting, *Geophysics*, **5**, 31-42.
- [94] Pelton, W.H., Rijo, L., and Ward, S.H., 1981, Three-dimensional resistivity and induced polarization data, *Geophysics*, **43**, 788-803.
- [95] Pelton, W. H., Ward, S. H., Hallof, P. G. Sill, W. R., and Nelson, P. H., 1978, Mineral Discrimination and Removal of Inductive Coupling with Multi-frequency IP, *Geophysics*, **43**, 588-609.
- [96] Perrin, F., 1969, Method of Appraising Photographic Systems, *J. Soc. Motion Pict. Telev. Eng.*, **69**, 151-156, 239-248.
- [97] Petrick, W.R., Jr., Sill, W.R., and Ward, S.H., 1981, Three-dimensional resistivity inversion using alpha centers, *Geophysics*, **43**, 788.
- [98] Pfeifer, M-C,, and Andersen, H.T., 1995. DC-resistivity array to monitor fluid flow at the INEL infiltration test, Proceedings, SAGEEP, Orlando, Florida, Environmental and Engineering Geophysical Society, 709-718.

- [99] Pilkington, M., and Todoeschuck, J.P., 1992, Natural smoothness constraints in cross-hole seismic tomography, *Geophysical Prospecting*, **40**, 227-242.
- [100] Philips, W. S., and Fehler, M. C., 1991, Traveltime tomography: a comparison of popular methods, *Geophysics*, **56**, 1639-1649.
- [101] Pridmore, D.F., Hohmann, G W., Ward, S.H. and Sill, W.R., 1981. An investigation of finite element modeling for electrical and electromagnetic data in three dimensions, *Geophysics*, 46, 1009-1024.
- [102] Press, F., 1968, Earth models obtained by Monte Carlo inversion, *J. Geophys. Res.*, **73**, 5223-5234.
- [103] Press W. H., Teukolsky, S. A., Vetterling, W. T., and Flannery, B. P., 1992, Numerical Recipes, Cambridge Univ. Press.
- [104] Ramirez, A., Daily, W., LaBrecque, D., Owen, E., and Chesnut, D., 1993. Monitoring an underground steam injection process using electrical resistance tomography, *Water Resources Research*, 29, 73-87.
- [105] Reiter, D. T., and Rodi, W., 1996, Nonlinear waveform tomography applied to crosshole seismic data, *Geophysics*, **61**, 902-913.
- [106] Rieven, S. A., Mackie, R.L., Madden, T.R., Manella, A., Fiordelisi A., and Larson, J., 1995, A magnetotelluric survey of the Larderello geothermal field, *Proceedings of the World Geothermal Congress*, May.
- [107] Rijo, L., 1984, Inversion of 3-D resistivity and induced polarization data: 54th Ann. Internat. Mtg., Soc. Expl. Geophys., Expanded Abstracts, 113-117.
- [108] Rodi, W., 1976, A technique for improving the accuracy of finite-element solutions for magnetotelluric data, *Geophys. T. Roy. Astr. Soc.*, **44**, 483-506.

- [109] Rodi, W., 1989, Regularization and Backus-Gilbert estimation in nonlinear inverse problems, application to magnetotellurics and surface waves, PhD thesis, The Pennsylvania State University.
- [110] Roy, A., and Apparao, A., 1971, Depth of investigation in direct current methods, *Geophysics*, **36**, 943-959.
- [111] Sasaki, Y., 1992, Three-dimensional resistivity inversion using the finite-element method, Soc. Expl. Geophys., Expanded Abstracts, 423-426.
- [112] Sato, M., and Mooney, H. M., 1960, The electrochemical mechanism of sulfide self-potentials, *Geophysics*, **25**, p. 226-249.
- [113] Scales, J. A., Docherty, P. and Gersztenkorn, A., 1990, Regularization of nonlinear inverse problems, imaging the near-surface weathering layer, *Inverse problems*, **6**, 115-131.
- [114] Scales, J. A., and Snieder, R., 1997, To Bayes or not to Bayes, *Geophysics*, **62**, 1045-1046.
- [115] Seigel, H. O., 1959, Mathematical formulation and type curves for induced polarization, *Geophysics*, **24**, 547-565.
- [116] Snieder, R., 1991, An extension of Backus-Gilbert theory to nonlinear inverse problems, *Inverse Problems*, **7**, 409-433.
- [117] Shima, H., 1990, Two-dimensional automatic resistivity inversion technique using alpha centers, *Geophysics*, **55**, 682-684.
- [118] Shima, H., 1992, 2-D and 3-D resistivity image reconstruction using crosshole data, *Geophysics*, **53**, 1565-1576.
- [119] Sill, W. R., and Johng, D. S., 1979, Self potential survey, Roosevelt Hot Springs, Utah, DOE/DGE topical rep., contract DE-AC07-78ET28392, Univ. of Utah.

- [120] Sill, W. R., 1983, Self-potential modeling from primary flows, *Geophysics*, **48**, p.76-86.
- [121] Slichter, L. B., 1933, The interpretation of the resistivity prospecting method for horizontal structures, *Physics*, **4**, 307-322.
- [122] Smith, J. T., and Booker, J. R., 1988, Magnetotelluric inversion for minimum structure, *Geophysics*, **53**, 1565-1576.
- [123] Smith, N.C., and Vozoff, K., 1984, Two-dimensional DC resistivity inversion for dipole-dipole data, *IEEE Trans. Geoscience and Re. Sens.*, **GE-22**, 21-28.
- [124] Spies, B.R., and Ellis, R.G., 1995, Borehole resistivity tomography of a pilot-scale, in-site, vitrification test, *Geophysics*, **60**, 886-898.
- [125] Sternberg, B. K., 1979, Electrical resistivity of the crust in the southern extension of the Canadian shield - layered earth models: *J. Geophys. Res.*, **84**, 212-228.
- [126] Sumner, J. S., 1976, Principles of induced polarization for geophysical exploration, Elsevier Scientific Publishing Company.
- [127] Swift, C. M., Jr., 1967, A magnetotelluric investigation of an electrical conductivity anomaly in the southwestern United States, Ph. D. thesis, Massachusetts Institute of Technology.
- [128] Tarantola, A., 1987. Inverse problem theory, Elsevier.
- [129] Tarantola, A., Valette, B., 1982, Inverse Problems = Quest for information, *J. Geophys.*, **50**, 159-170.
- [130] Telford, W. M., Geldart, L. P., Sheriff, R. E., 1990, Applied geophysics, second edition, Cambridge University Press.



- [131] Thompson, D. R., 1993, Nonlinear waveform tomography: theory and application to crosshole seismic data, PhD thesis, Massachusetts Institute of Technology.
- [132] Tikhonov A., Arsenine, V., 1977, Solutions of Ill-posed Problems, Wiley.
- [133] Tripp, A.C., Hohmann, G.W., and Swift, C.M., Jr., 1984, Two-dimensional resistivity inversion, *Geophysics*, **49**, 1708-1717.
- [134] U.S.G.S., 1989, Hydrogeology and simulation of ground-water flow at superfund-site wells G and H, Woburn, Massachusetts, *Technical Report*, U.S. Geological Survey.
- [135] Van, G. P., Park, S.K., and Hamilton, P., 1992, Use of electrical resistivity monitoring systems to detect leaks from storage ponds, *SAGEEP '92*, Chicago, 629-647.
- [136] Van Nostrand, R. G., and Cook, K. L., 1966, Interpretation of resistivity data, Geological Survey Prof. Paper 499, U.S. Geol. Survey.
- [137] Vichabian, Y., 1997, An environmental application of self potential geophysics, Master's Thesis, Massachusetts Institute of Technology.
- [138] Vozoff, K., 1958, Numerical resistivity analysis: horizontal layers, *Geophysics*, **23**, 536-556.
- [139] Vozoff, K., and Jupp, D. L. B., 1975, Joint inversion of geophysical data, *Geophys. J. R. Astron. Soc.*, **42**, 977-991.
- [140] Wiggins, R. A., 1972, The general linear inverse problem: implication of surface waves and free oscillations for earth structures, *Rev. Geophys. and Space Phys.*, **10**, 251-285.
- [141] Yang, F. W., and Ward, S. H., 1985, Single and cross-borehole resistivity anomalies of thin ellipsoids and spheroids, *Geophysics*, **50**, 637-655.

- [142] Yungul, S. H., 1950, Interpretation of spontaneous polarization anomalies caused by spheroidal orebodies, *Geophysics*, **15**, p. 237-246.
- [143] Yuval, Oldenburg, D. W., 1997, Computation of Cole-Cole parameters from IP data, *Geophysics*, v. 62, p. 436-448.
- [144] Zeeb, P. 1994, The effects of Deposit Scale Heterogeneities on the Trapping and Transport of Toxic Metals in an Urban Riverine Peatland, em AGU, Spring Metting, Baltimore, **148**.
- [145] Zhang, J., Mackie, R. L., and Madden, T. R., 1995, Three-dimensional resistivity for ward modeling and inversion using conjugate gradients, *Geophysics*, **60**, 1313-1325.